Universidade Federal de Minas Gerais
Instituto de Ciências Exatas – Departamento de Química
Programa de Pós Graduação em Química

Gustavo Henrique de Magalhães Gomes

Unraveling the anomalous nature of the niobium pentoxide

Belo Horizonte
2021

Gustavo Henrique de Magalhães Gomes

Unraveling the anomalous nature of the niobium pentoxide

Tese apresentada ao Departamento de Química do Instituto de Ciências Exatas da Universidade Federal de Minas Gerais como requisito parcial para a obtenção do grau de Doutor em Ciências - Química

Orientadora: Nelcy Della Santina Mohallem

Coorientador: André Santarosa Ferlauto

Belo Horizonte
2021

Ficha Catalográfica

G633u
2021
T

Gomes, Gustavo Henrique de Magalhães
Unraveling the anomalous nature of the niobium pentoxide [manuscrito] / Gustavo Henrique de Magalhães Gomes. 2021.
169 + [20] f. : il., gráfs., tabs.

Orientadora: Nelcy Della Santina Mohallem.
Coorientador: André Santarosa Ferlauto.

Tese (doutorado) - Universidade Federal de Minas Gerais - Departamento de Química.
Inclui bibliografia.
Inclui anexos.

1. Físico-química - Teses. 2. Compostos de nióbio - Teses. 3. Óxidos metálicos - Teses. 4. Materiais nanoestruturados - Teses. 5. Rietveld, Método de - Teses. 6. Cristalografia - Teses. 7. Raios X - Difração - Teses. 8. Microscopia eletrônica - Teses. 9. Fotocatálise - Teses. 10. Cristais - Defeitos - Teses. I. Mohallem, Nelcy Della Santina, Orientadora. II. Ferlauto, André Santarosa, Coorientador. III. Título.

CDU 043

Elaborada por Sérgio Ferreira da Silva - CRB6-2719.

UNIVERSIDADE FEDERAL DE MINAS GERAIS

UFMG
Programa de Pós-Graduação em Química
Departamento de Química - ICEx

química
pós-graduação-ufmg

"Unraveling The Anomalous Nature Of The Niobium Pentoxide"

Gustavo Henrique de Magalhães Gomes

Tese aprovada pela banca examinadora constituída pelos Professores:

Profa. Nelcy Della Santina Mohallem - Orientadora
UFMG

Prof. André Santarosa Ferlauto - Coorientador
UFABC

Profa. Renata Diniz
UFMG

Prof. Anderson Dias
UFMG

Prof. Sergio da Silva Cava
UFPel

Prof. Osmando Ferreira Lopes
Universidade Federal Uberlândia

Belo Horizonte, 07 de dezembro de 2021.

Documento assinado eletronicamente por **Anderson Dias**, **Membro de comissão**, em 07/12/2021, às 18:47, conforme horário oficial de Brasília, com fundamento no art. 5º do Decreto nº 10.543, de 13 de novembro de 2020.

Documento assinado eletronicamente por **Osmando Ferreira Lopes**, **Usuário Externo**, em 07/12/2021, às 18:47, conforme horário oficial de Brasília, com fundamento no art. 5º do Decreto nº 10.543, de 13 de novembro de 2020.

Documento assinado eletronicamente por **Andre Santarosa Ferlauto**, **Usuário Externo**, em 07/12/2021, às 18:47, conforme horário oficial de Brasília, com fundamento no art. 5º do Decreto nº 10.543, de 13 de novembro de 2020.

Documento assinado eletronicamente por **Renata Diniz**, **Professora do Magistério Superior**, em 07/12/2021, às 18:47, conforme horário oficial de Brasília, com fundamento no art. 5º do Decreto nº 10.543, de 13 de novembro de 2020.

Documento assinado eletronicamente por **Sergio da Silva Cava**, **Usuário Externo**, em 07/12/2021, às 18:48, conforme horário oficial de Brasília, com fundamento no art. 5º do Decreto nº 10.543, de 13 de novembro de 2020.

Documento assinado eletronicamente por **Nelcy Della Santina Mohallem**, **Professora do Magistério Superior**, em 07/12/2021, às 19:42, conforme horário oficial de Brasília, com fundamento no art. 5º do Decreto nº 10.543, de 13 de novembro de 2020.

A autenticidade deste documento pode ser conferida no site https://sei.ufmg.br/sei/controlador_externo.php?acao=documento_conferir&id_orgao_acesso_externo=0, informando o código verificador **1128392** e o código CRC **70A84F46**.

Referência: Processo nº 23072.262580/2021-11 SEI nº 1128392

"The Nitrogen in our DNA, the Calcium in our teeth, the Iron in our Blood, the Carbon in our apple pies were made in the interior of collapsing stars.
We Are Made of Starstuff''
– Carl Sagan, Cosmos

Agradecimentos

Esse foi o último texto, em termos cronológicos, escrito na presente Tese de Doutoramento. Acredito que pela importância desse elemento pré-textual, e da dificuldade de concebe-lo. Me lembro do meu professor de Quântica da Pós-graduação, João Pedro Braga, dizendo que essa era, definitivamente, a melhor parte de todas as teses que ele leu e avaliou, pela dificuldade que encontramos de praticar a gratidão àqueles que fazem, ou fizeram, parte de nossas vidas. Nesse momento, me encontro sem dificuldades para isso, na verdade, acredito que as minhas palavras jamais poderão contemplar o significado que tais pessoas têm em minha vida, por isso, sintam-se também abraçadas.

Primeiramente, agradeço meus pais Maria da Conceição e Alberto Paulo, por terem concebido a minha vida, nutrido ela, e incentivado todos e quaisquer caminhos que eu tenha resolvido trilhar, da melhor forma que podiam e sabiam fazer. Eu não mudaria NADA. Apenas sou o que sou graças à vocês e ao mundo em que me inseriram, sintam meu mais sincero amor. Não poderia deixar de agradecer à minha família, todos primos, sobrinhos, e tios que tenho, sintam-se abraçados. Um carinho especial vai para os meus irmãos, Júlia, Glauber, Thatiana e Alexandre. Todos vocês têm um jeito único de ser, nunca mudem, e continuem sendo essas pessoas incríveis e completamente apaixonadas pela vida.

Parafraseando nosso querido poeta Belchior: "eu posso me considerar um sujeito de sorte...", pois essa jornada rumo ao conhecimento não teria sido a mesma sem os amigos que escolhi para a vida, neles cito com muito carinho meus amigos da época de adolescência, uma turma que foi crescendo, e ainda cresce. Um grupo único e distinto cujo nome é "nós somos" composto por pessoas com ideais, visões, e experiências de vida diferentes, porém unidas pelo mais lindo laço da amizade. Durante a minha caminhada, tive a sorte e privilégio de ter uma pessoa única ao meu lado, que, com seu

jeito irradiante de ser, decidiu compartilhar parte de sua vida comigo, e me mostrar que tudo pode ser mais leve, doce, e belo ao seu lado, eu te amo Camila Peres.

Aos amigos que a UFMG me deu, que levarei para vida toda, em especial um abraço do mais apertado para o Pedro Henrique, Magnum - Zinhão, Renier Arabolla, Sunday Olusegun, Luiz Fernando, e José Balena. Nossas conversas científicas foram mais do que essenciais para que eu pudesse ser o cientista que sou hoje. A forma com que toda conversa acaba descontraída, empolgante, e animadora, é sem igual. O sucesso de vocês me inspira. Agradeço também à professora responsável por grande parte desses momentos, Nelcy Mohallem. Compartilhamos do interesse científico e caminhamos juntos desde 2014. Além de uma excelente mentora, orientadora, e cientista, pude ter o privilégio de compartilhar momentos rotineiros da nossa vida, e nisso criar a admiração não só pela profissional, mas sim pela pessoa que você é, gerando uma relação excepcional. Como dizemos no nosso laboratório, a Nelcy é nossa mãe científica, e amiga querida.

Para chegar onde estou, não poderia deixar de fora os Professores, cientistas, e funcionários que fizeram parte da minha caminhada. Durante mais de 10 anos como aluno da UFMG, tive a sorte de conhecer profissionais magníficos que contribuíram para o meu crescimento pessoal e profissional, em especial para Marcelo Viana, Fabiano Vargas, Rochel Lago, Hatem Abushamala, Renata Diniz, Luciano Montoro, Alessandra Dinotte, Wladmir Teodoro, Lúcia Pimenta, Lucienir Paes, Heitor Avelino, André Ferlauto, Sérgio Ferreira da Silva, João Pedro Braga, Jarbas Magalhães, José Israel Vargas, Maria Helena de Araújo, Renata Araújo, e Luiza de Marillac.

Agradeço ao departamento de química da UFMG e todos seus funcionários, que me acolheram durante toda essa jornada. É, com certeza, um lugar especial no meu coração. Agradeço ao Centro de Microscopia da UFMG, pela disponibilização de sua estrutura. Agradeço também às agências de fomento FAPEMIG, CAPES, e CNPq pelo apoio financeiro durante essa jornada.

A todos vocês, MUITO OBRIGADO.

Resumo

O pentóxido de nióbio (Nb_2O_5) figura atualmente como um dos óxidos metálicos mais discutidos nos últimos anos. Os tópicos de discussão utilizando o Nb_2O_5 englobam áreas cruciais da ciência, como engenharia, física, química e biologia. O Nb_2O_5 provou ter capacidade extraordinária em catálise, fotocatálise, conversão de energia e utilização em dispositivos eletrônicos. Essas aplicações geram atenção por causa das propriedades diferenciadas do Nb_2O_5, com a possibilidade de obtenção de diversos polimorfos com diferentes fases cristalinas, que podem apresentar defeitos na microestrutura. A combinação das propriedades estruturais e eletrônicas do pentóxido de nióbio fez com que ele se tornasse um material emergente na classe dos óxidos metálicos. A presente tese utilizou dois métodos de síntese simples: calcinação do precursor e método Pechini. Ambos métodos são diretos, com baixo custo, e de fácil manipulação. A rota Pechini é conhecida por produzir materiais mesoporosos devido à presença de um *template* polimérico, e também tem capacidade de produzir materiais com defeitos estruturais. Nós sintetizamos nove amostras distintas, todas com comportamento cristalográfico diferente, em um total de quatro fases cristalinas. Experimentos de difração de raios X aliada com refinamento Rietveld tornou possível o entendimento do comportamento de todas as fases cristalográficas obtidas. Microscopia eletrônica de transmissão de alta resolução se mostrou uma técnica robusta para elucidar sobre a presença de defeitos na microestrutura dos materiais. Todas essas técnicas, aliadas com uma elucidação das propriedades eletrônicas, nos deu informação suficiente para propor as melhores aplicações para os materiais obtidos. O Nb_2O_5 mostrou sua capacidade superior em processos de adsorção e fotocatálise de poluentes em relação à materiais reportados na literatura, além da conversão seletiva de biomassa para produtos de interesse da indústria química. Essas descobertas estão intrinsicamente ligadas com a presença de defeitos na estrutura e o uso da fase cristalina correta. De uma forma geral, o interesse do trabalho foi a investigação das propriedades

microestruturais do Nb_2O_5 e como elas impactam nas propriedades eletrônicas e aplicações fotocatalíticas do material. Os resultados apresentados na presente tese instigam pesquisas futuras utilizando o Nb_2O_5, principalmente na obtenção desses materiais associados à defeitos estruturais.

Palavras-chave: Pentóxido de nióbio, Nanomateriais, Estrutura Cristalina, Defeitos cristalinos, Fotocatálise.

Abstract

The niobium pentoxide (Nb_2O_5) figures as one of the most spoken metal oxides in the past few years. The research topics employing niobium pentoxide encompass crucial areas of scientific knowledge, such as engineering, physics, chemistry, and biology. The Nb_2O_5 proved to have remarkable performance in catalysis, photocatalysis, energy conversion, and electronic devices. These applications stand out because the Nb_2O_5 presents an odd behavior, with the possibility to obtain several polymorphs with distinct crystalline phases, and it could present defects in its structure due to non-stoichiometric behavior. Combining all niobium pentoxide properties has made it an emergent metal oxide nowadays. The present thesis employed two simples synthetical routes: precursor burnt and Pechini method, as they are straightforward, cheap, and easy to manipulate. The Pechini route produces mesoporous materials due to the polymeric chain. There are also reports in the literature of defects in the niobium pentoxide employing the Pechini method. We synthesized nine different samples. All of them presented distinct behavior, with four crystalline phases. X-ray diffraction allied with Rietveld refinement was performed to understand the crystalline behavior of all obtained phases. High-resolution transmission electron microscopy proved to be a robust technique to understand the crystalline phase and the role of these defects in the structure. These techniques allied with an electronic structure evaluation gave sufficient information to perform the most suitable applications. The Nb_2O_5 showed its remarkable capability in the adsorption and photodegradation of pollutants and biomass conversion to chemicals with industrial interest. These findings are closely related to defects and the correct crystal structure. Overall, the interest of this research is the investigation of the Nb_2O_5 crystal structure and evaluating its impact in photocatalytic applications. The results presented are instigating further research on the Nb_2O_5, bringing the subject of defect engineering for improved performance.

Keywords: Niobium pentoxide, Nanomaterials, Crystal structure, Crystalline defects, Photocatalysis.

Abbreviation List

BAS – Bronsted acid site
BET – Brunauer-Emmett-Teller
BJH - Barrett-Joyner-Halenda
CA – Citric acid
Cb – Columbium
CBMM – Companhia Brasileira de Metalurgia e Mineração
CERN – European Organization for Nuclear Research
CIF – Crystallographic information file
CV – Crystal violet
DOI – Digital object identifier
DOS – Density of states
DRS - Diffuse reflectance spectroscopy
Eg – Band-gap energy
EG – Ethylene glycol
EPR – Electron paramagnetic resonance
EQE – External quantum efficiency
ESR – Electron spin ressonance
FFT – Fast Fourier Transform
GPA – Geometric phase analysis
HRTEM – High-resolution transmission electron microscopy
IFFT – Inverse Fast Fourier Transform
IUPAC – International Union of Pure and Applied Chemistry
LAS – Lewis acid site
LHC – Large Hadron Collider
Nb - Niobium
NbOX - $NH_4[NbO(H_2O)_2(C_2O4)_2].xH_2O$
PDF – Peak distribution function
PEG – Polyethylene glycol
ROI – Region of Interest
SAED – Selected area electron diffraction
SETOVs - Single electron trapped oxygen vacancies
SSA – Specific surface área
Ta – Tantalum
TEM – Transmission electron microscopy
U.S.A. – United States of America
UV – Ultraviolet
XPS – X-ray photoelectron spectroscopy
XRD – X-ray diffraction

Table List

Figure List

Summary

Chapter 1 - The Niobium Oxide

INTRODUCTION

The most relevant historical events related to the niobium discovery and the evolution of scientific knowledge about its properties in the materials field are present in this chapter. Several scientific breakthroughs on niobium research from the 1800s until nowadays are essential to understand better how the scientific interest increased over the years, focusing mainly on the niobium oxides. The niobium pentoxide (Nb_2O_5) materials require special attention, which present a wide range of stoichiometric and non-stoichiometric polymorphs and several applications. However, it still necessitates further studies on their structure obtainment and its relation to their properties [1].

1. A new metal: Niobium

The history of niobium dates back more than 200 years, when in 1802, Charles Hatchett (1765-1847), a British chemist and mineralogist, announced the discovery of a new element. The nineteenth-century studies were special, mainly by discovering fifty-one new elements, and niobium was the first of these elements. In the early history of niobium discovery, between 1727-1741, Sir Hans Sloane (1660-1753) was the Royal Society president in Great Britain (preceding Isaac Newton). He received from Massachusetts a collection of 600 minerals, in which he cataloged, performed notes, and displayed them at the British Museum in Montagu House [2]. In 1801, Charles Hatchett was working in the British Museum. He noticed that Sloane's sample, described as "a very heavy black stone with golden streaks ... from Nautneague. From Mr. Winthrop," was very similar to his example, described by him as a "Siberian chromate of iron." At the moment, he noted that Sloane's description was not very clear. Thus, he decides to perform a more in-depth study on the ore's composition.

Charles Hatchett extracted the fused ore using potassium carbonate, nitric acid, and water, obtaining a white residue. As he studied its properties, he noticed an

unexpected behavior, which he attributed to a new element. At the moment, he named it Columbium (Cb), from the Columbite ore [2]. Figure 1.1. shows a picture of the Columbite ore.

Figure 1. 1. Columbite ore - Evidencing the black color and the gold streaks – Image obtained from [3].

In 1802, Anders Ekeberg published an article announcing a new element named tantalum [4]. The discovery of both metals in a short period provoked some confusion. In 1809, William Wollaston used Hatchett samples to perform some tests. By comparing the obtained results with the newly discovered element Tantalum by Ekeberg, he erroneously affirms that Columbium and Tantalum were the same elements [5]. The pursuit of identifying the elements in the Columbite ore remained until 1846, where Heinrich Rose, a German chemist, was able to separate two different metals from the Columbite ore, in which one was tantalum and the other he named niobium, corroborating Hatchett's discovery in 1802 [6].

In 1864, the Swedish mineralogist Christian Wilhelm Blomstrand was the first to isolate the niobium in its pure form [7]. However, in 1866, Jean-Charles de Marignac, in his studies, finally proved that Columbium and Niobium were the same elements, and tantalum was a different element [8].

Since the two elements (Ta and Nb) demonstrated similar properties and are recurrently found together in the minerals, they named niobium in honor of Niobe, Tantalus's daughter, from Greek mythology. However, the name Columbium was

common in the U.S.A., while niobium was in Europe, and in 1949 the International Union of Pure and Applied Chemistry (IUPAC) adopted the name niobium. Nevertheless, the use of Columbium could be found in some mineralogy works and textbooks in the U.S.A. [9].

1.1. Niobium early applications

Despite niobium's early discovery by Charles Hatchett, only in 1864 could scientists obtain the metal, and its first industrial application was in 1900 as a filament metal in incandescent lamps. However, its use stopped in 1911, where the Tungsten substitutes niobium because it presents a higher melting point [10]. However, after 1915, several industries started to use niobium in steel alloys, the first granted patent in the U.S.A. in 1917 [11]. In the subsequent years, the industrial interest strongly increased in the niobium usage for steel production, considerably raising the number of granted and deposited patents. At the time, metallurgical and scientists found that small amounts of niobium in steel composition could promote mechanical, thermal, and structural improvement. These properties are suitable for the aircraft and space industry.

In the early 1950s, with the beginning of the space race, the interest in niobium alloys strongly increased due to its characteristics as the lightest refractory metal. In 1954, Eugene Kunzler and associates discovered a niobium-tin alloy (Nb_3Sn) with superconductor properties. In 1961, researchers found that niobium-tin exhibits superconductivity even at large currents and strong magnetic fields, becoming the first material for this purpose [12]. Nowadays, the niobium-tin alloy acts as superconductivity material in the Large Hadron Collider (LHC), built by the European Organization for Nuclear Research (CERN) [13].

In 1966, the IN718 alloy was introduced, consisting of Ni-Fe-Cr-Nb steel, and is still used in most modern aircraft and stationary turbines, considered a breakthrough in steel fabrication, and nowadays, 75% of niobium usage is for micro-alloyed steels [14].

1.2. The Charles Hatchett Award and the Niobium ascension

At the beginning of the 1950s, several events contributed to the niobium ascension. Before this date, niobium was considered a scarce metal, with a high cost and small amount. However, in 1953, a Brazillian civil engineer and mineralogist named Djalma Guimarães found a large pyrochlore deposit in Araxá, Minas Gerais, with suitable niobium content. By coincidence, in Oka, Canada, in the same year occurred a new Niobium deposit discovery. Those events were responsible for the rapid growth of niobium research, mainly in steel and stainless steel production and improvement, and to supply the world demand for the metal, in 1955, with the Companhia Brasileira de Metalurgia e Mineração (CBMM) foundation in Araxá, Minas Gerais. The enormous world demand for niobium caused a rise in production. The Araxá factory started production only in 1961; by 1979, the CBMM had offices and technology plants in the U.S.A., Germany, Russia, China, and Japan [15].

Those events affected the mineralogy and metallurgy fields. In 1978, the head office from CBMM in Europe, along with the Metals Society (today is Institute of Materials, Minerals & Mining), created a prize for the best published scientific work using niobium in steel, which they called the "Charles Hatchett Award," in honor of the niobium discoverer. The prize rules consisted of [16]:

1. *An award is made annually for a published paper on the use of niobium in steel.*
2. *The award might be associated with the name of Charles Hatchett.*
3. *The award should be administered on a worldwide basis by the Metals Society.*
4. *The prize would take the form of a visit to appropriate places in Brazil.*
5. *The restriction of the subject matter to the use of niobium in steel could be unduly restrictive and that it would be advantageous to widen the subject to include:*
    a. *The use of niobium (and its alloys) on its own.*

b. The relationship between niobium and other metals, e.g., vanadium normally associated with it in steel.

The first awarded work was "Effect of Deformation in the Austenite and Austenite-Ferrite Regions on the Strength and Fracture Behaviour of C, C-Mn, C-Mn-Cb, and C-Mn-Mo-Cb Steels" noticing the use of the metals former name, Columbium (Cb). The creation of this prize settled niobium's worldwide importance, where several vital countries announced niobium as a strategic mineral resource, in which this statement persists nowadays.

Despite the attention given towards niobium's use in steel production, the scientific discussion and industrial output of niobium oxides were minimal. In 1989, the CBMM founded a niobium oxides production and manufacturing unit, leading this market in the '90s, with high purity niobium oxide with an optical grade in 1997. Over 41 years of the Charles Hatchett Award's creation, only two niobium oxide work won the prize in 2018 and 2019, demonstrating a growing interest in studying these materials [15, 16].

1.3. Chemical Characteristics

Niobium is a transition metal from the d block, with atomic number 41, electronic configuration $[Kr]4d^45s^1$, paramagnetic with one unpaired electron, the relative atomic mass of 92.906, the density of 8.57 $g.cm^{-3,}$ and it belongs to the fifth group and period of the periodic table. It presents in the solid-state at 20 °C and has a melting and boiling point of 2477 and 4744 °C, respectively. It is a silvery metal, light-gray color, soft, ductile and malleable, crystallizing in a body-centered cubic lattice. Niobium presents four oxidation states: Nb^0, Nb^{2+}, $Nb^{4+,}$ and Nb^{5+}, related to the phases of Nb, NbO, NbO_2, and Nb_2O_5, respectively [1].

2. The niobium-oxygen system

The early findings on Niobium-oxygen binary system began around 1940 with Brauer. This German researcher published the first article, proposing that niobium possesses four oxidation states: Nb^0, Nb^{2+}, Nb^{4+} and Nb^{5+}, and the NbO and NbO_2

oxides had only one crystalline phase, and the Nb_2O_5 presented two polymorphs [17]. Nonetheless, Brauer published the first complete work in the niobium oxides crystal structure one year later, entitled "*Die Oxyde Des Niobs.*". The scientific community proposed six niobium oxides, Nb_2O_5, NbO_2, Nb_3O_5, Nb_2O_3, NbO, and Nb_2O. However, there was physical evidence of only three structures, the Nb_2O_5, NbO, and NbO_2 [18].

Brauer's first experiments used niobium minerals from the pyrochlore group, with 41% wt. of Nb_2O_5 content, which he obtained the niobium oxide through the sample digestion using sulfuric acid (H_2SO_4), oxygen peroxide (H_2O_2), and potassium bisulfate ($KHSO_4$). Brauer confirmed the existence, using X-ray diffraction (CuKα radiation), of only one crystalline phase for NbO and NbO_2, showing NbO crystallizes in a face-centered cubic system and NbO_2 in a tetragonal rutile-like crystalline system. However, he found that the Nb_2O_5 presents three crystalline phases and not two, as previously stated. He named the polymorphs T (*tief,* from the German, meaning low), M (*mittel,* medium), and H (*hoch*, high), according to the thermal treatment temperature.

Brauer performed powder X-ray diffraction in the samples in his studies, finding a crystallization in the T-Nb_2O_5 at 500 °C, which changes at 1000 °C, where the formation of the M- phase took place. In temperatures above 1000 °C, he observed the disappearance of M- phase diffraction lines and the H- phase formation. Figure 1.2. presents the X-ray diffraction patterns, showing the similarity between the obtained T-Nb_2O_5 and Ta_2O_5, demonstrating that the M- phase could be a transitory crystal structure between T- and H- phase. Brauer proposed that the T, M, and H phases of niobium oxide crystallized in a monoclinic system.

The scientific community believed in the existence of several Nb_2O_5 non-stoichiometric polymorphs. Brauer was also the first to propose that the niobium pentoxide's oxygen content is crucial for phase obtainment. He prepared Nb_2O_5 powders heating at high temperatures (1350-1400 °C) under a reductive atmosphere using molecular hydrogen (H_2) in different partial pressures in his experiments. Therefore, obtaining several non-stoichiometric oxides in a system ranging between

$NbO_{2.5}$ and NbO_2, providing the X-ray diffraction pattern for all samples, shown in Figure 1.3.

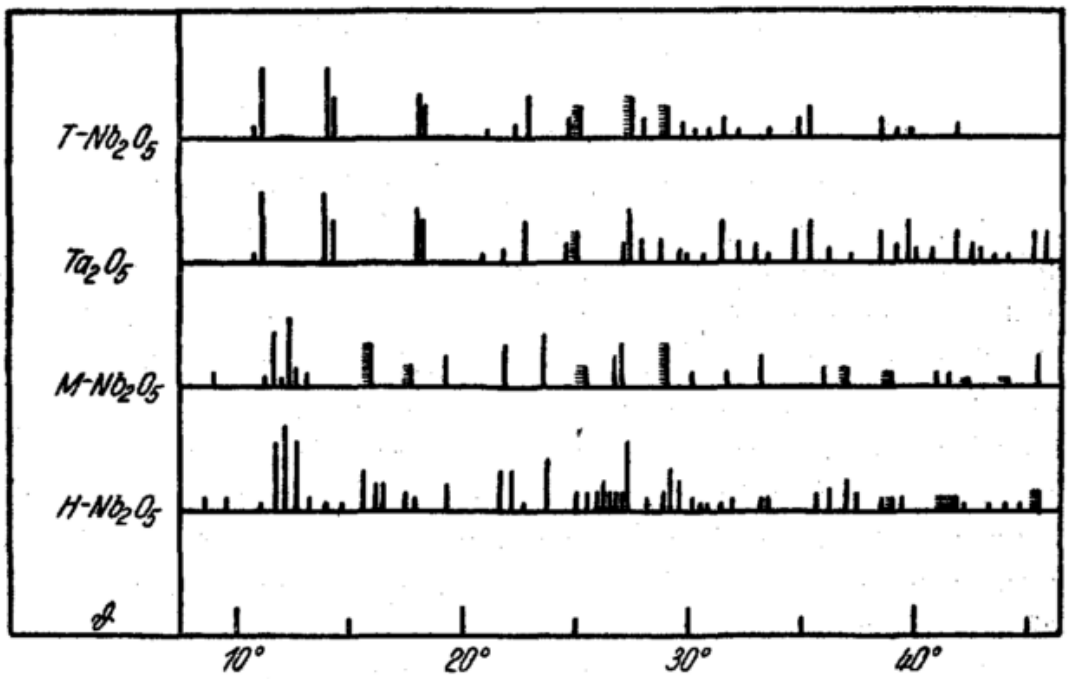

Figure 1. 2. Brauer's X-ray diffraction data for Ta_2O_5 and T-, M- and H-Nb_2O_5 phases - Image obtained from [18].

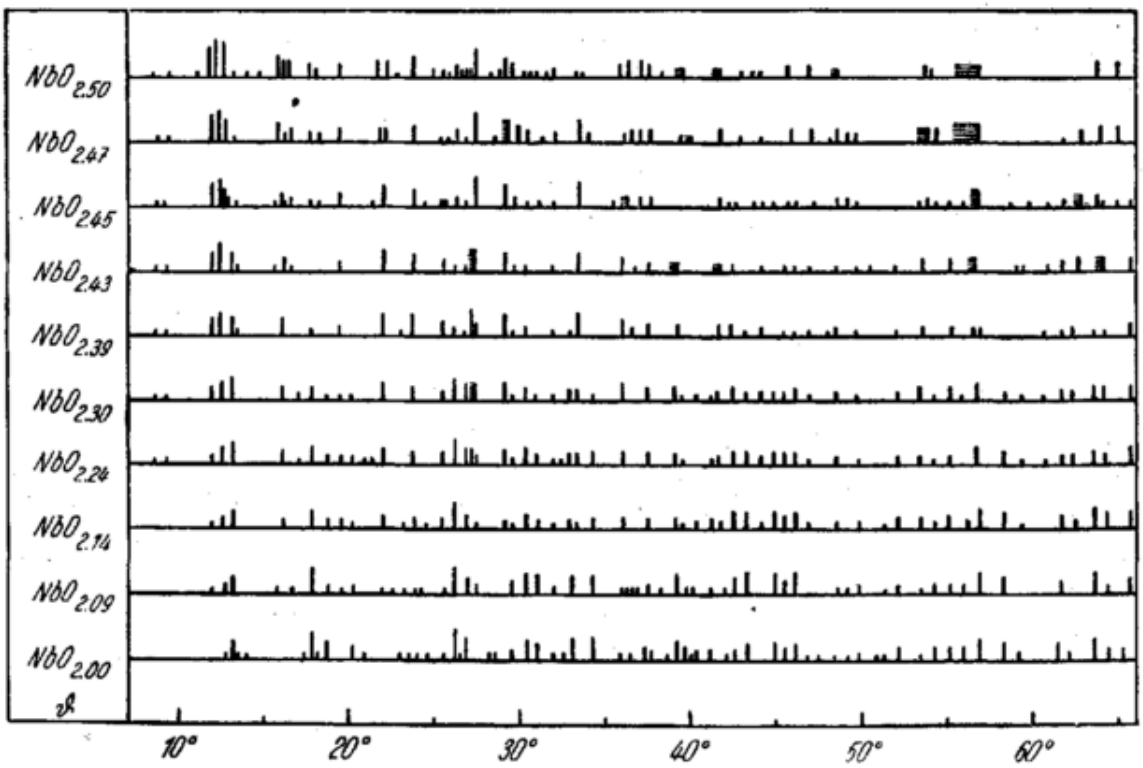

Figure 1. 3. X-ray diffraction data for $NbO_{2.5-x}$ non-stoichiometric polymorphs - Image obtained from [18].

The obtained data for the transition between Nb_2O_5 and NbO_2 showed a very complex system. Some weak diffraction lines disappear or overlap with others' reflections with decreasing oxygen content, making it challenging to analyze. Brauer instigated the scientific community to better understand the Nb_2O_5 phase formation despite the difficulties in understanding the crystal structure of those non-stoichiometric oxides. He concludes that only Nb_2O_5, NbO_2, and NbO oxides exist. The Nb_3O_5, Nb_2O_3, and Nb_2O were non-stoichiometric phases with Nb^{5+} and Nb^{4+} cations in the crystal structure and lower oxygen content.

A decade after Brauer's discoveries, the scientific interest in the niobium pentoxide was growing, and there were still misinformation and contradictions about its crystal structures and the main differences from Ta_2O_5. Hahn [19], in 1951, published data about niobium and tantalum phosphates and niobium pentoxide to provide a better understanding of stable metal phosphate salts. He performed powder diffraction and reported new values for d-spacing, which was not correlated with the known phases (T, M, or H), contradicting Brauer's results.

In 1955, Frevel and Rinn studied the tantalum and niobium pentoxide crystal structure, obtaining Ta_2O_5 by direct oxidation of metallic Ta and Nb_2O_5 from a commercial sample [20].

Frevel and Rinn reported the interplanar space and Müller index for orthorhombic Nb_2O_5 and Ta_2O_5, which presented a monoclinic system. They also performed experiments to obtain the powder diffraction pattern for the Nb_2O_5 commercial sample. They reported a new phase, described as a pseudohexagonal crystalline cell containing 0.5 molecules of niobium pentoxide per unit, and it is related structurally to columbite ore [20]. Another accounted finding is that upon heating at 700 °C for 16h, the pseudohexagonal-Nb_2O_5 converted to the T-Nb_2O_5 phase, called "low modification of Nb_2O_5". Frevel and Rinn stated that the T-Nb_2O_5 crystallizes in an orthorhombic system.

Table 1. 1. Data from the powder diffraction pattern of pseudohexagonal niobium pentoxide – Adapted from [20].

d-spacing / Å	[hkl]	$(I/Io)_f$	$(I/Io)_o$	B
3.925	001	0.90	0.60	0.25
3.124	100	1.00	1.00	0.48
2.446	101	0.40	0.39	0.42
1.962	002	0.30	0. IS	0.35
1.800	110	0.25	0.30	0.86
1.663	102	0.30	0.21	0.49
1.637	111	0.14	0.15	0.75
1.565	200	0.12	0.08	0.8
1.456	201	0.08	0.07	0.8
1.327	112	0.18	0. 10	0.8
1.309	003	0.04	Lattice Constants	
1.222	202	0.08	a	3.925 Å
1.205	103	0.06	c	3.607 Å

The most interesting fact about the pseudohexagonal phase, latterly called TT-phase (*tief-tief*), is that the data obtained by Frevel and Rinn are the first and most reliable in the literature and are the basis for this phase study. Table 1.1. shows the crystallographic data, where d spacing is the interplanar spacing, [hkl] are the Müller index, $(I/Io)_f$ is the relative integrated intensity from Norelco diffractometer data, $(I/Io)_o$ is the relative intensity from film measured with intensity scale. B is the observed angular breadth of the diffraction line at half-peak intensity.

The reported "low modification Nb_2O_5" phase caused some confusion in the scientific environment since Brauer [18] said it was a monoclinic crystal and showed weak diffraction lines for the T- phase at 500 °C, and the findings by Frevel and Rinn [20] contradicts Brauer and provide information on a phase transition between TT and T phases.

Two years later, Holtzberg et al. [21] published a work corroborating Brauer's discoveries on the T, M, and H phases, where they called γ-, β-, and α-Nb_2O_5, respectively. However, they reported a contradiction regarding Brauer's temperatures and the reversibility between γ (T) to β (M) phases. They also discussed the newly discovered "low modification Nb_2O_5" phase in their work, named the δ (TT) phase. They believed it was a less crystalline form of the γ (T) phase, as they obtained a very noise diffractogram, with peak enlargement and split, between stages, as shown in Figure 1.4.

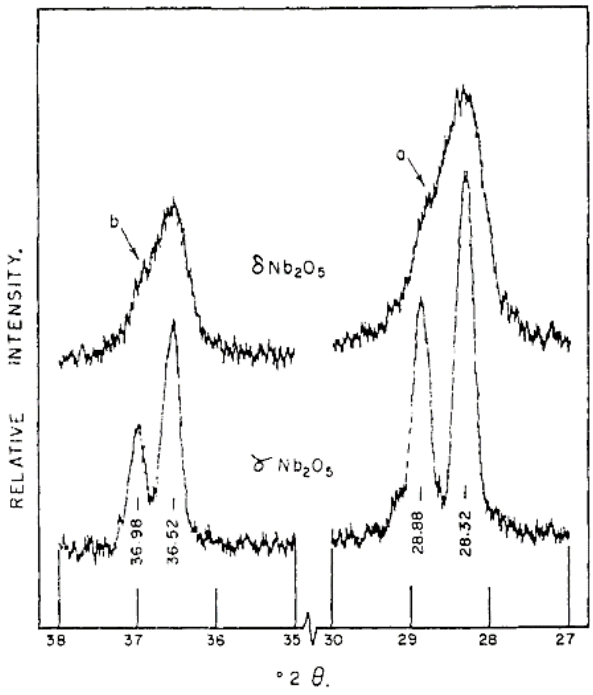

Figure 1. 4. Partial X-ray diffraction from δ (TT), and γ (T) niobium pentoxide - Image obtained from [21].

Holtzberg et al. [21] reported significant findings, like reliable powder diffraction for α (T) phase and the niobium oxide behavior in several calcination temperatures, showing that the niobium-oxygen system is very complex. Meanwhile, Schafer and Roy [22] published a work on the Nb_2O_5 polymorphism, naming the phases as low (III), medium (II), and high (I), for the T, M, and H phases, respectively. They proposed a phase diagram of the Nb_2O_5 system and pointed a contrary report from Holtzberg [21], where they could obtain Nb_2O_5 with only one crystalline phase, and stating that the Holtzberg affirmation that the T phase always is converted on a mixture of the M and H phase was incorrect.

Another two years later, Holtzberg published some further comments on the Nb_2O_5 polymorphism as a criticism for the recently reported information about the niobium oxides structures by Shafer and Roy [23].

Several scientists have pursued the niobium oxide structure elucidation despite the divergences between the research groups. In 1962, Nobuzo Terao [24] published an article discussing the Nb_2O_5 structure, reporting, and discovering a new phase, γ', latterly called the B phase. He is the first to propose that the δ (TT) phase, which was considered a poorly crystallized γ (T) phase, was, in fact, an oxide with defects. He also shows that the γ (T) phase crystallizes in an orthorhombic system, not in the monoclinic system, as believed before.

Several scientists' misinterpretation of the niobium oxides structure clarified the need to compile all gathered data in the past years. In 1966, Schäfer et al. [25] published the first work with all relevant published data in the literature, comparing their findings and settling the need for the Nb_2O_5 phase's names standardization. He stated that the misuse of several scientific notations for the Nb_2O_5 phases causes confusion and misinformation. He proposed Brauer's neutral symbols, TT, T, B, M, N, P, and H.

The Guinier photographs for all presented Nb_2O_5 phases were provided by Schäfer, as seen in Figure 1.5, showing the diffraction lines for all obtained phases in the literature, and comparing them. Discussing that several forms, such as ox I, II, III, IV, V, and VI, could be structures with different niobium or oxygen content (Nb_2O_{5-x}) and low-intensity diffraction lines in the T phase, which is not present in the TT phase. Schäfer also proposed that the TT-phase occurs due to structural defects in the crystalline system. The presence of ionic impurities (like Cl^-, SO^{4-}) could lead to phase formation when they calcinate amorphous $Nb_2O_5.H_2O$ at low temperatures (300 to 500 °C).

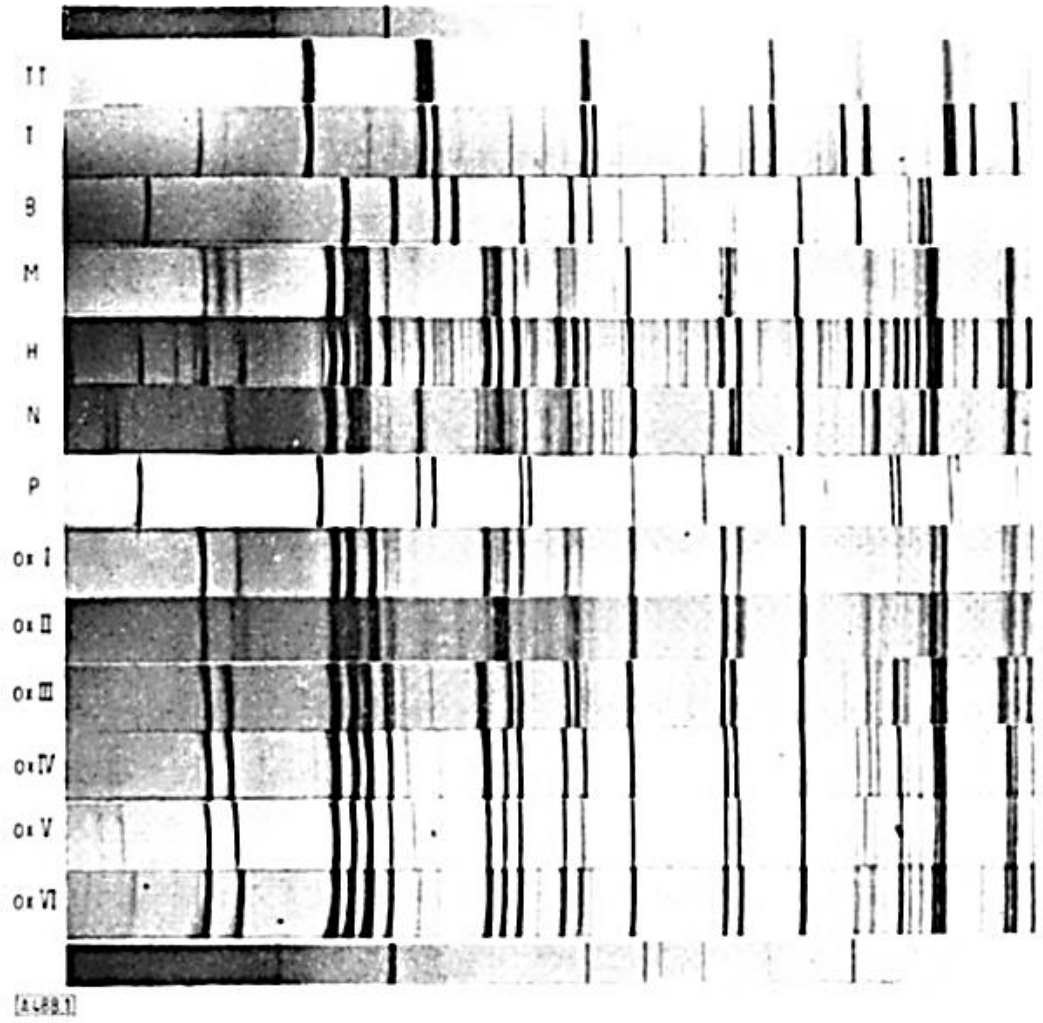

Figure 1. 5. Guinier photographs of the Nb_2O_5-phases TT, T, B, M, H, N, P, and ox I to VI. Image retrieved from [25]

Schäfer et al. proposed that the B phase occurs when there are oxygen vacancies or the presence of Nb^{4+} atoms in the crystal structure ($Nb_2O_{4.996}$, for example), reporting a blueish color from the obtained powders. The P and N phases also could be brought together with the B phase. However, several differences in the crystal shape for the three phases, which he concluded could be easy to separate. Another important finding is the oxidation of the NbO_2 under an air atmosphere, where he first obtained the TT phase, which was converted to the T phase and then to the B phase. Hence reinforcing that the crystallization path could not be standardized; however, he had reliable information that the TT phase could occur in the presence of defects or trace impurities.

The discussion about defects in the Nb_2O_5 crystalline system grows; the subsequent studies showed the defects, their formation, and which phases are correlated. Chen and Swalin [26] present a scientific report on their findings, discussing the presence of defects on the α-Nb_2O_5 (H phase), calling attention to the Nb_2O_5 non-stoichiometric nature. They proposed that the single or double charge oxygen vacancies create a metal-excess n-type semiconductor, increasing the electrical conductivity and lowering the band-gap. Meanwhile, the interest for the NbO_2 increased since its existence intrinsically correlates with better electrical properties and defects in Nb_2O_5 [27-29].

The first series of in-depth studies concerning defects in the niobium pentoxide structure has begun in the '70s. Anderson et al. published four relevant scientific articles at the time concerning how impurities in niobium oxides behave and how it allows modifications in the crystal structure [30-34]. In 1972, he published his first work as a short communication report in the Nature journal [32]. He performed high-resolution electron microscopy, obtaining direct evidence that impurities and vacancies can form extended defects in the structure. He stated that niobium pentoxide structures derived from the ReO_3 type are suitable for promoting stoichiometry changes and presenting a high degree of local order.

He proposed a block structure of NbO_6 octahedrons linked by the edge, forming a rectangular white block and black dots between the white blocks, representing the NbO_4 tetrahedral sites, shown in Figure 1.6(a). This configuration creates good flexibility in the anion/cation site ratio, providing variations in the cross-sections of column sets, which produces primarily point defects and extended defects by the intergrown columns in wrong positions. These defects create changes in the anion/cation ratio, implying fluctuations in composition, efficiently producing non-stoichiometric materials. Figure 1.6(b) shows the HRTEM image, pointing to the extended defects caused by edge-dislocations, using a JEM-100U microscope.

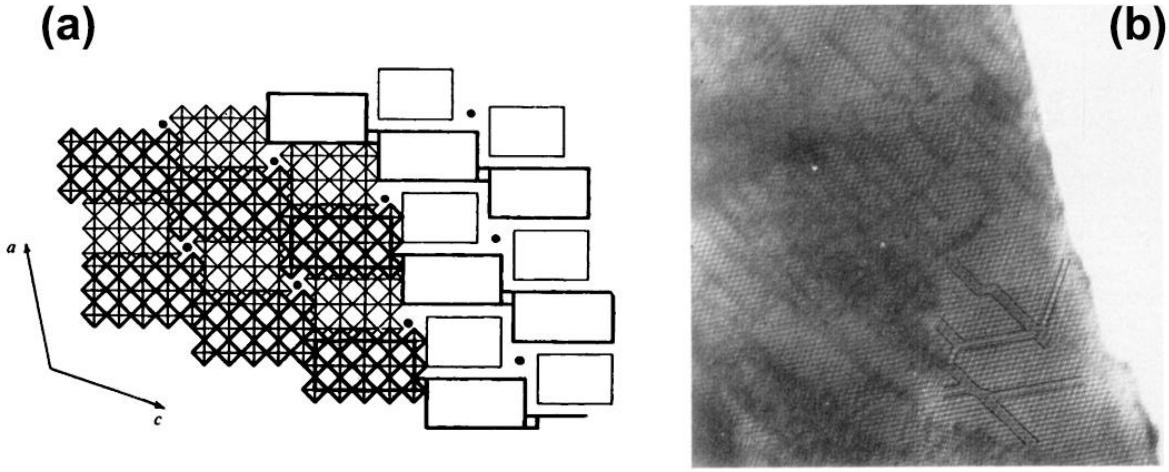

Figure 1. 6. (a) Block structures (5x3) of NbO_6 octahedrons of H-Nb_2O_5 [010] projection. (b) HRTEM image showing extended edge-dislocations defects - Retrieved from [32].

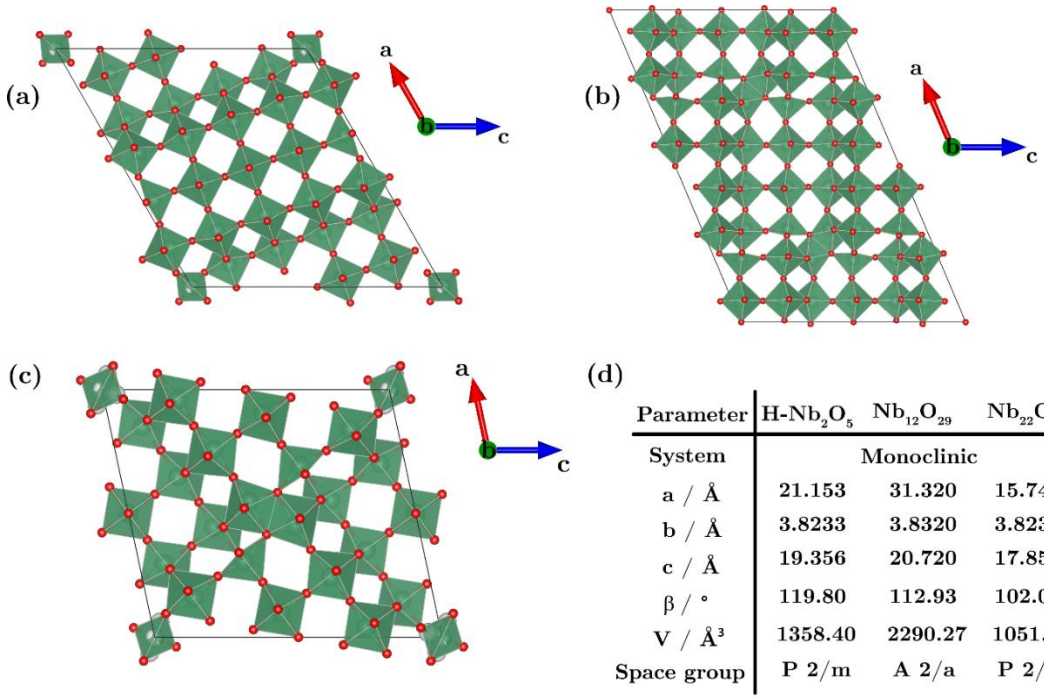

Parameter	H-Nb_2O_5	$Nb_{12}O_{29}$	$Nb_{22}O_{54}$
System	Monoclinic		
a / Å	21.153	31.320	15.749
b / Å	3.8233	3.8320	3.8236
c / Å	19.356	20.720	17.852
β / °	119.80	112.93	102.03
V / Å³	1358.40	2290.27	1051.41
Space group	P 2/m	A 2/a	P 2/m

Figure 1. 7. Crystal structure along the b-axis of (a) H-Nb_2O_5, (b) $Nb_{12}O_{29}$, (c) $Nb_{22}O_{54}$, and their (d) lattice parameters.

Anderson et al. subsequent works studied the non-stoichiometric behavior and the formation of $Nb_{25}O_{62}$ ($NbO_{2.480}$), $Nb_{22}O_{54}$ ($NbO_{2.454}$), and $Nb_{12}O_{29}$ ($NbO_{2.417}$). They proposed that the oxide structure is intermediate between $NbO_{2.5}$ and NbO_2 and occurs at phase transformations since they present a similar monoclinic system compared with H-Nb_2O_5, as shown in Figure 1.7, except for the $Nb_{25}O_{62}$ since there is no crystallographic data in the literature. They showed the extended defects in those oxides and examined the structure of the three non-stoichiometric oxides, concluding

that each of these oxides converts into H-Nb_2O_5 at adequate thermal treatment. These non-stoichiometric oxides show a structural relationship with H-Nb_2O_5, indicating the occurrence of phase formation and segregation in the presence of impurities and extended defects in the structure [34].

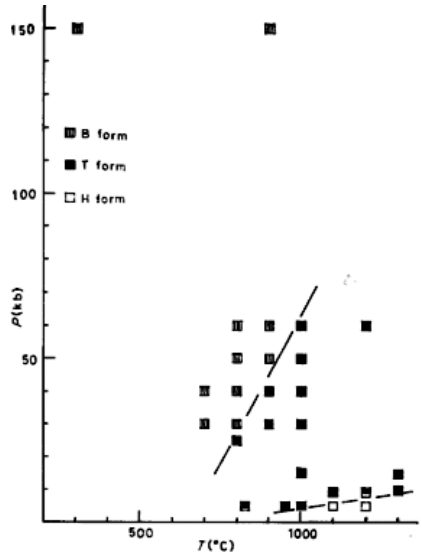

Figure 1. 8. Pression x Temperature phase diagram for Brauer's Nb_2O_5 phases - Adapted from [35]

Meanwhile, several research groups worked on the niobium oxides' structure evaluation. Tamura published a work in 1972 settling the need to understand the phase formation and obtainment in niobium oxides, where he gathered all information in the literature and proposed a sketch of the Nb_2O_5 phase diagram [35], shown in Figure 1.8.

In his work, Tamura proposed that the TT-Nb_2O_5 stabilizes in the presence of impurities, and they presented sharp X-ray diffractogram patterns, proposing that TT-phase crystallizes based on a monoclinic unit cell, with a = 7.238 Å, b = 15.70 Å, c = 7.188 Å, β = 119.5°, cell volume = 711.7 $Å^3$, and z = 8 molecules/cell. The deviation from the hexagonal unit cell proposed by Frevel and Rinn [20] occurs between the a and c axis, where the β value is close to 120° [35]. Table 1.2 shows Tamuras' X-ray diffraction results for the TT-phase compared with Frevel and Rinn.

However, no other work supported that the TT-phase presents weak diffraction lines and peak splitting, believing that Tamura obtained a TT and T phases mixture.

Table 1. 2. Comparison between crystallographic data of the TT-Nb_2O_5.

Tamura [35] TT-Nb_2O_5			Frevel and Rinn [20] TT-Nb_2O_5		
(hkl)	d / Å	I	(hkl)	d / Å	I
(030)	5.266	5			
(040)	3.948	100	(001)	3.925	90
(200)	3.136	90	(100)	3.124	100
(002)	3.118	45			
(240)	2.455	30	(101)	2.446	40
(042)	2.444	15			
(080)	1.974	30	(002)	1.962	30
$(40\bar{2})$	1.810	15	(110)	1.800	25
(202)	1.804	20			
(280)	1.670	15	(102)	1.663	30
(082)	1.667	15			
$(44\bar{2})$	1.645	10	(111)	1.637	14
(242)	1.641	10			
(400)	1.568	10	(200)	1.565	12
Monoclinic Unit cel			Pseudohexagonal Unit Cell		
a = 7.238 Å			a = 3.607 Å		
b = 15.70 Å			b = 3.607 Å		
c = 7.188 Å			c = 3.925 Å		
β = 119.5°			β = 120°		
Volume = 711.7 $Å^3$			Volume = 44.22 $Å^3$		
z = 8 molecules/cell			z = 0.5 molecule/cell		

In 1973, Kimura published findings on NbO_2-Nb_2O_5 phase equilibria, obtaining several non-stoichiometric oxide forms with a mixture of NbO_x, at x ranging from 2.418-2.496 work with Schäfer's [25, 36]. Kimura's work settled the importance of

understanding phase formation, initiating several studies in this area since Marucco stated that oxygen vacancies and interstitial niobium cations have a fundamental step before forming crystallographic shear planes [37, 38].

Naito and Matsui published a series of works concerning the phase equilibria in the niobium-oxygen system, using electrical measurements, mass spectrometric method, and thermogravimetric analysis [39-43].

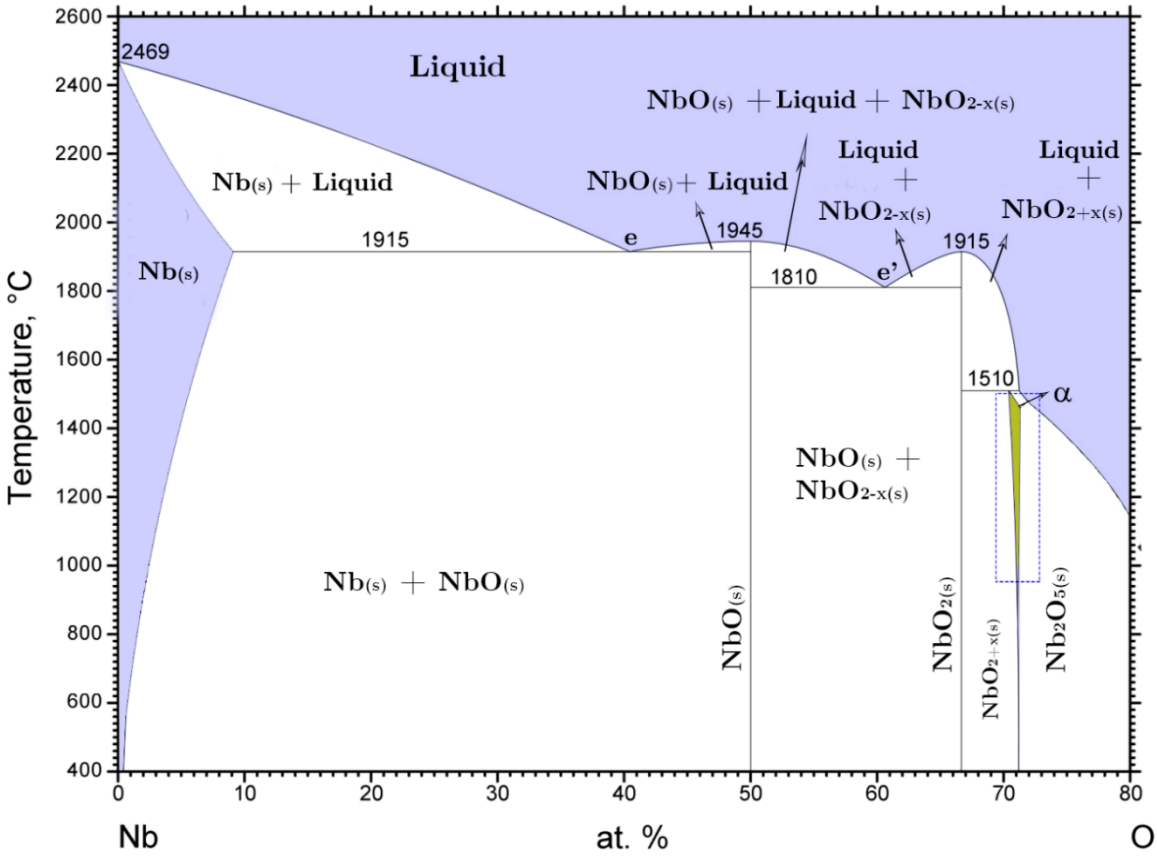

Figure 1. 9. Phase Diagram of the Niobium-oxygen system – Adapted from [40, 44].

Figure 1.9 shows the complete phase diagram for the niobium-oxygen system, adapted from Naito and Matsui's mentioned works, and the binary alloy phase diagram from ASM International [44]. The Nb-O phase diagram exhibits a complex system with several non-stoichiometric phases with increased oxygen content and temperature. There is the formation of four congruent melting points, at oxygen 0% (2469 °C), 50% (1945 °C), and 66.6% (1810 °C), and 71.2% (1510 °C). The points are related to Nb, NbO, NbO_2, and Nb_2O_5 phases. The Nb_2O_5 presents a lower melting point than pure metallic Nb, which is odd in the metal oxides class materials. The incongruent region between the (Oxygen 71,2%) NbO_2-Nb_2O_5 system is

called alpha (α), described in the literature as the region with the most distinct non-stoichiometric phases. Figure 1.10. show in detail the α region of Figure 1.9.

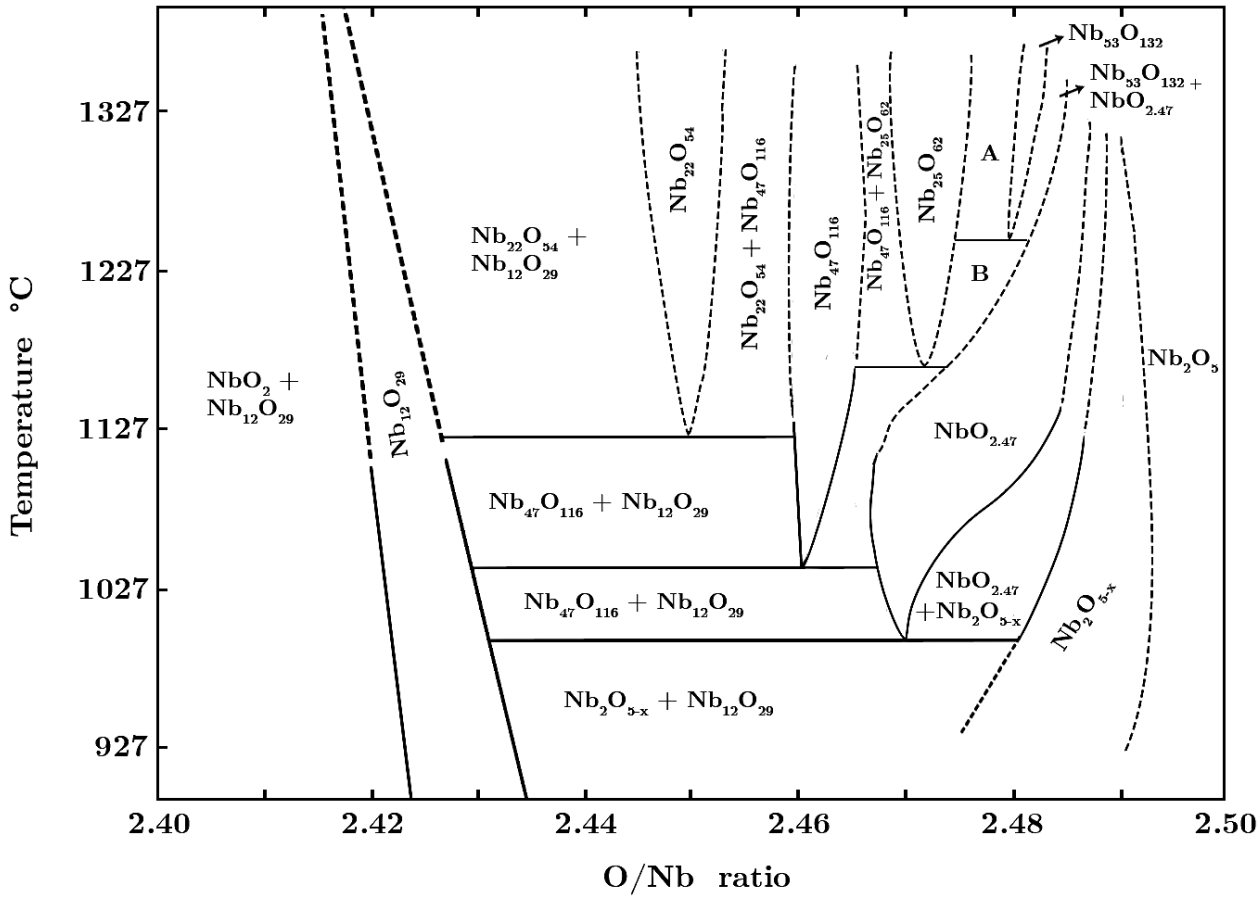

Figure 1. 10. Magnification of the alpha region in Figure 1.8. with Oxygen/Niobium ratio between 2.40-2.50. Region A: $Nb_{53}O_{132}$ + $Nb_{25}O_{62}$ and Region B: $NbO_{2.47}$ + $Nb_{25}O_{62}$. Adapted and remastered from [40].

The most common non-stoichiometric phase is the $Nb_{12}O_{29}$ ($NbO_{2.417}$), as it is present in almost all phases of the α region, and this statement is true until nowadays [1]. The presence of several non-stoichiometric phases intrigued the scientific community. The desire to understand the role of defects in the Nb_2O_5 properties has grown. Two works by Balachandran et al. present H-Nb_2O_5 (α) electrical conductivity (σ) as a function of the oxygen partial pressure (P_{O2}), showing increases in the σ with decreasing P_{O2}, indicating of a metal excess conductivity, as shown in Figure 1.11 [45, 46].

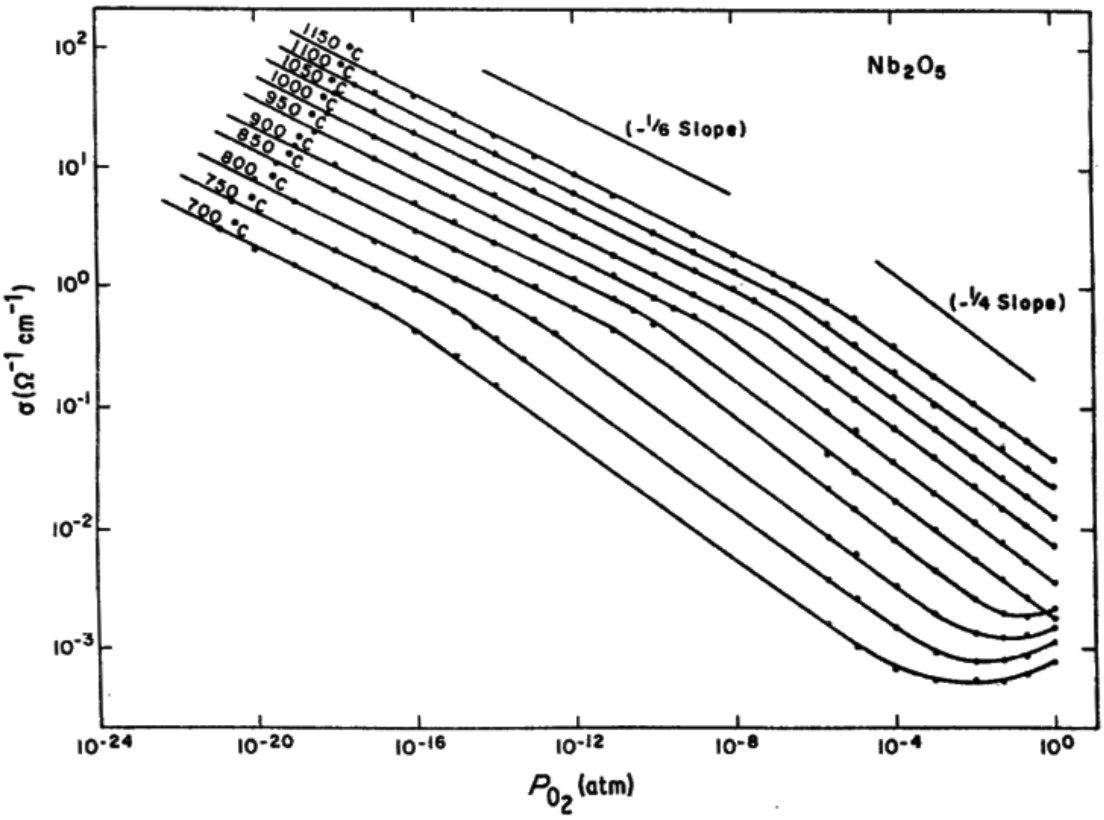

Figure 1. 11. H-Nb_2O_5 electrical conductivity as a function of partial oxygen pressure at a constant temperature - Retrieved from [46].

The curves slop at $10^{-24} < P_{O2} < 10^{-9}$ (region I) are different from $P_{O2} > 10^{-9}$ (region II), showing two defects formation phenomena. Region I present an extensive linearity region optimal for determining the defects in the n-type electrical conductivity. The presence of doubly charged oxygen vacancies is predominant in Nb_2O_5 materials in this region.

He shows in region II that there are several types of defects, like edge dislocations, impurity segregation effects, single and double ionized oxygen vacancies ([Vo], [V$\dot{o}$], [V$\ddot{o}$]) concentrations of electrons [n] and holes [p], and Frenkel disorder. Figure 1.12 shows the variation of defects as a function of the oxygen partial pressure, illustrating the described atomic defects. In low P_{O2} values, the concentration of single and double charged oxygen vacancies is high, as is the number of electron holes. The increment in the oxygen partial pressure decreases the oxygen vacancy concentration, occupying the sites with oxygen atoms; however, even at higher P_{O2}, there are some single and double charged oxygen vacancies [46].

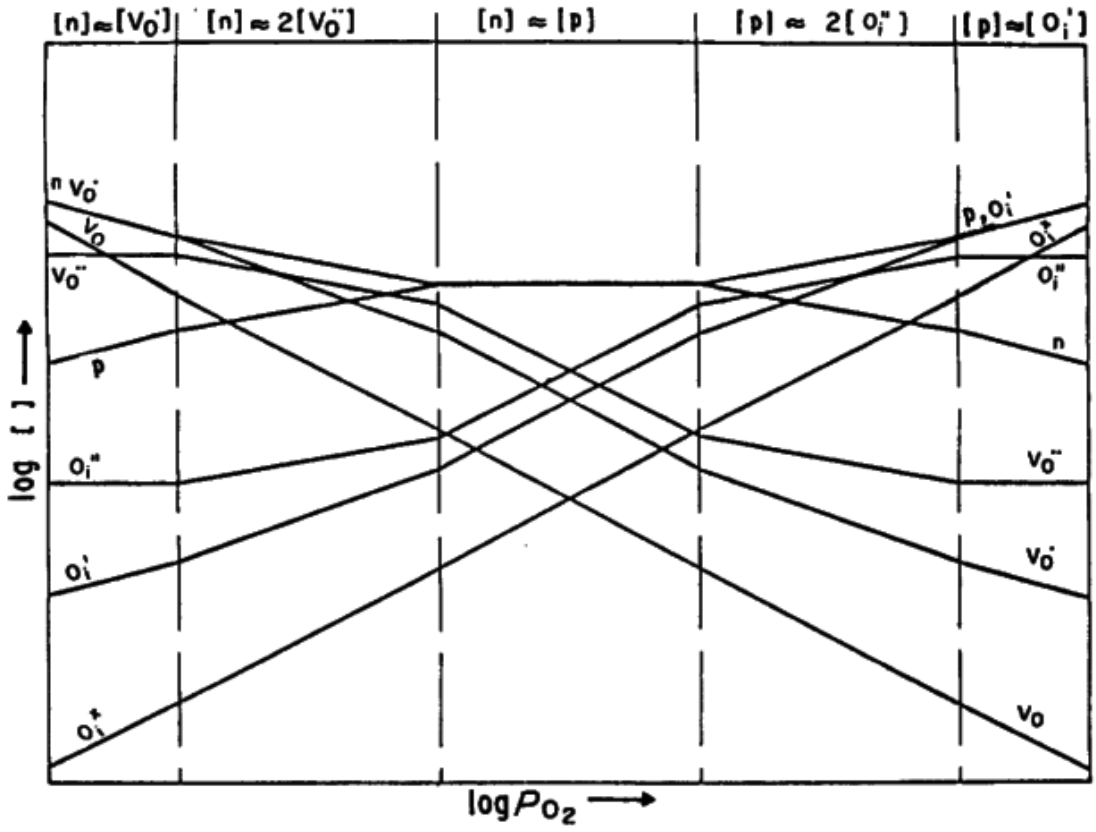

Figure 1. 12. The concentration of defects as a function of the partial oxygen pressure, accounting for Frenkel disorder - Retrieved from [46].

In the later '80s, Weissman et al. published the first complete work on structure resolution and image simulation through HRTEM micrographs [47]. They examined the stability of three crystalline phases, TT-, T-, and H-Nb_2O_5. Weissman et al. discussed the similarity between the TT- and T- phases, indicating that the two polymorphs have identical or very similar atomic structures. The work concluded that the TT-Nb_2O_5 is not a less crystalline form of T-Nb_2O_5, where the HRTEM micrographs showed a well-ordered structure. Based on past findings, Weissman proposed that the TT-phase has an analogous structure compared with the T-phase. Since the HRTEM image simulation of Figure 1.13(a) shows the same atomic positions in the structure between TT- and T-Nb_2O_5, they could propose a crystal structure in Figure 1.13(b) compared with T-Nb_2O_5.

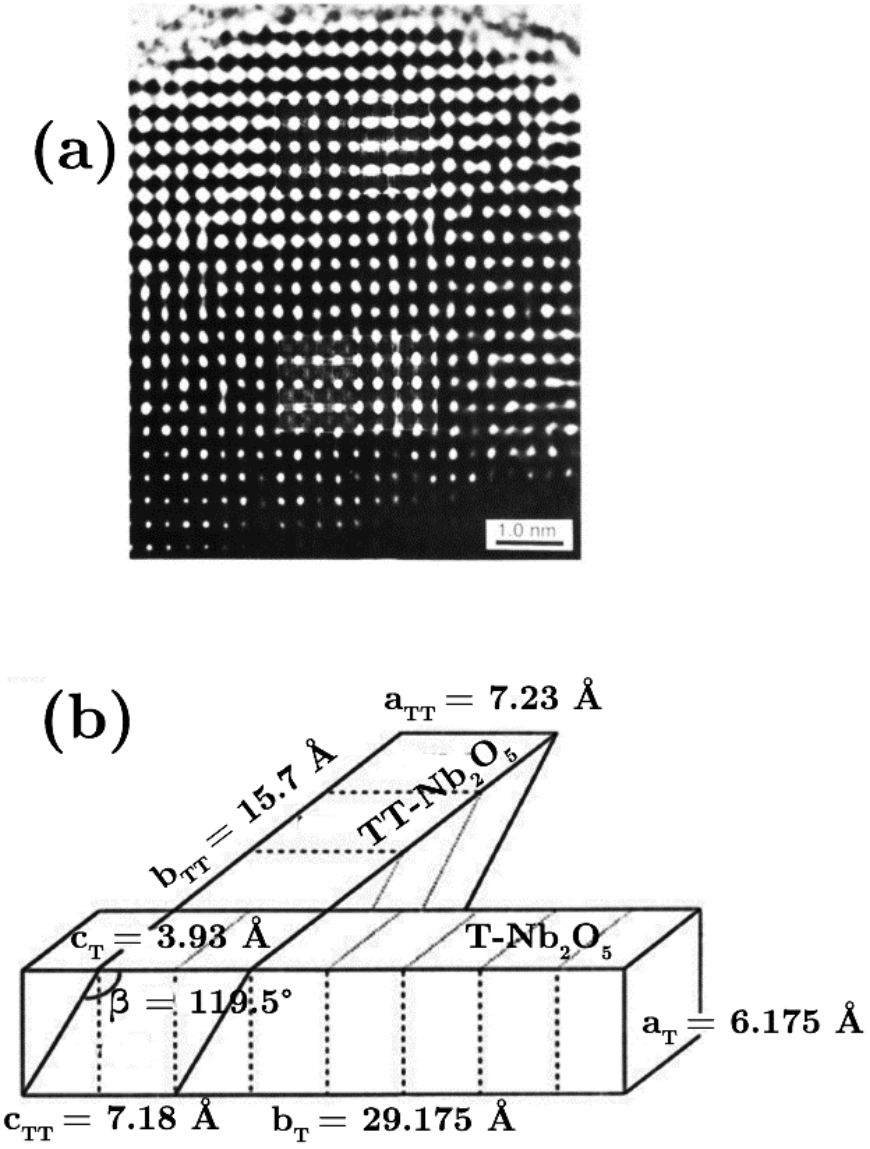

Figure 1. 13. (a) HRTEM micrograph and image simulation of (001) TT-Nb_2O_5, and (b) Geometrical relation between the unit cells of TT- and T-Nb_2O_5 with correspondents lattice parameters - Adapted from [47].

Weissman et al. discussed the principal differences between the two structures. The T-Nb_2O_5 contains 16.8 Nb atoms, where the 16 significant atomic positions are in the 8i Wyckoff sites, totalizing 32 Nb positions with 0.5 of occupancy. The remaining 0.8 Nb atoms are distributed in 4g Wyckoff sites, lying in the a-b plane at z = 0. However, the presence of broad peaks and no peak splitting in the TT- Nb_2O_5 indicates that niobium atoms are in more symmetric Wyckoff positions, 4h instead of 8i, reducing the number of Nb atoms and the number of possible weak reflections in X-ray diffraction data.

Those statements accounted for Nb atoms in the exact coordinates at the T- and TT- Nb_2O_5. However, a more symmetric atomic site can produce an open unit cell with a more evenly spaced position and increase the capability to accommodate impurities and defects, also showing that the TT- Nb_2O_5 has a non-stoichiometric unit ($Nb_{16}O_{42}$) compared with the T- Nb_2O_5, due to oxygen vacancies and the presence of OH groups.

Weissman et al. argued that their model suggests that the monoclinic TT-Nb_2O_5 could be indexed based on the orthorhombic T- Nb_2O_5. While the distortions in the TT-Nb_2O_5 could lead to a monoclinic crystallization, the structure consists of subcells domains within a superlattice, where the subcell symmetry is monoclinic, and the superlattice presents orthorhombic symmetry like T-Nb_2O_5. Figure 1.14 shows the unit cell of the T-Nb_2O_5 and the superlattice structure of TT-Nb_2O_5, evidencing the open unit cell of TT- Nb_2O_5, with more spaces between atoms.

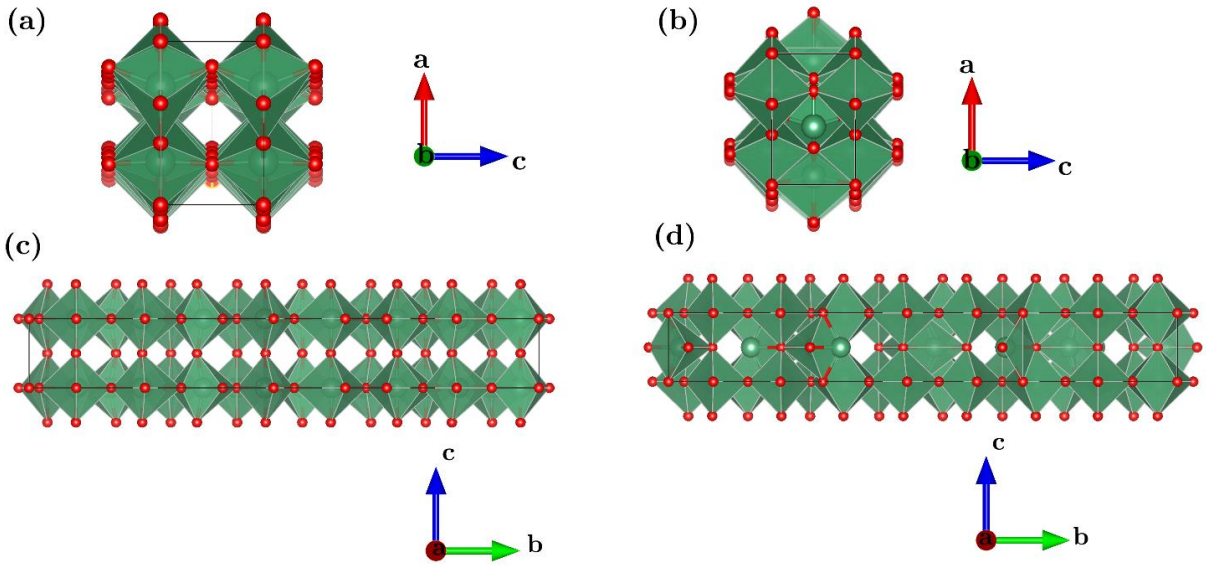

Figure 1. 14. Unit cell view along the b-axis of (a) TT- Nb_2O_5 and (b) T- Nb_2O_5. Unit cell view along the a-axis of (c) TT- Nb_2O_5 and (d) T- Nb_2O_5.

. As discussed in this chapters' section, the structural characteristics of Nb_2O_5 materials raised the scientific community's curiosity, with several published in-depth studies about Nb_2O_5 crystalline phases. Leading to a vast number of possible structures with different crystalline systems, defects, and impurities. Appendix A

presents complementary information of the known niobium pentoxide crystal structures.

3. Niobium oxide first applications

While the discoveries of the niobium pentoxide structure and elucidation occur, the beginning of the '90s is characteristic for the grown interest in understanding Nb_2O_5 properties and how it can affect their applications. The first published works report niobium pentoxide in catalysis, photocatalysis [48, 49], and lithium insertion [50].

3.1. Nb_2O_5 in the catalytic applications

The early studies reported using niobium oxide as a catalyst or support for metal particles. Maeda et al. produced Rh/TiO_2 and Rh/Nb_2O_5 when the scientific community correlated TiO_2 wide band-gap semiconductor properties with the Nb_2O_5 [51]. They discussed the role of the Nb_2O_5 as a supported and promoter catalyst, where they improved the NH_3 decomposition using niobium pentoxide; however, there is no further information about the phases and crystal structure.

Zhang et al. reported using Nb_2O_5 for aldol addition of acetone, a base-catalyzed reaction. They found that the Nb_2O_5 was the worst oxide in the aldol conversion, stating that the oxides with basic sites effectively promote the reaction [52]. Inoue et al. studied CO and CO_2's hydrogenation using an Rh-supported catalyst, showing that the Rh/Nb_2O_5 had the best performance among all metal oxides, concluding that Nb_2O_5 acts as an electron donor in acidic reactions [53].

These findings showed that Nb_2O_5 could be a suitable catalyst and photocatalyst in acidic reactions, with high selectivity and conversion. Okazaki and Kurosaki reported acid treatment on niobium pentoxide, showing that phosphoric acid suppresses crystallization and increases surface acidity, improving catalytic activity in acid reactions [54].

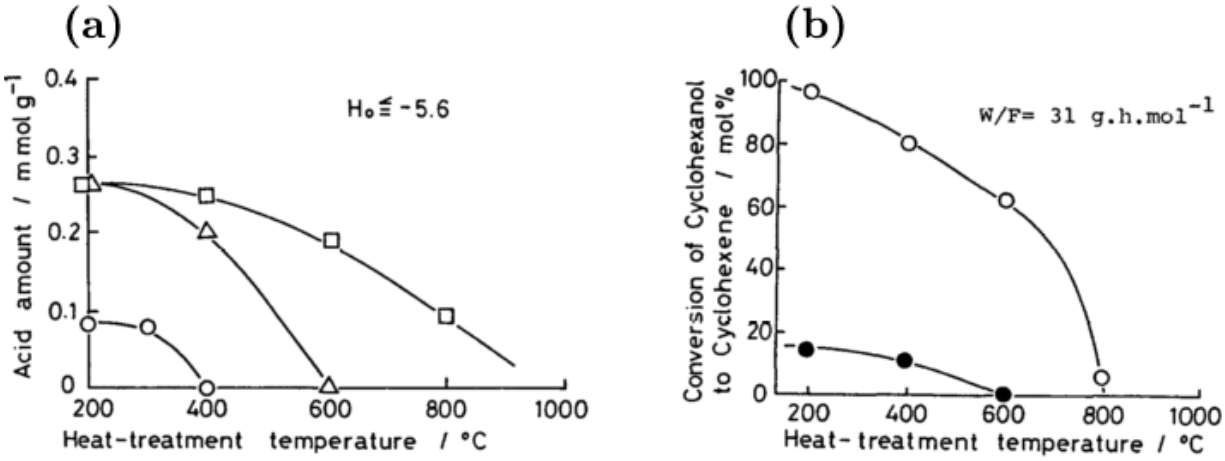

Figure 1. 15. (a) Acid amount of niobium pentoxide with no treatment (O), treated with phosphoric acid (Δ) and sulfuric acid (❑). (b) Cyclohexanol conversion using the untreated (•) and H_3PO_4 treated (o) Nb_2O_5 - Adapted from [54].

Figure 1.15(a) shows the acid concentration in the niobium pentoxide. With no acid treatment, after 400 °C, no acid species are present, but treating with phosphoric or sulfuric acid increases the surface acidity on the material. Okazaki and Kurosaki proposed that the amorphous niobium oxide, called niobic acid, could perform better-catalyzed reactions due to the higher acidity. Figure 1.15(b) shows the conversion of cyclohexanol to cyclohexene. The untreated sample performed poorly compared with the H_3PO_4 treated, showing that the niobium pentoxide's acidic sites play an essential role in catalyzed reactions.

Tanabe published the first review of niobium oxides as a catalyst, supported, and unique acid catalyst for several reactions [55]. He showed the $V_2O_5/Nb_2O_5.H_2O$ composite's improved efficiency compared with the pure vanadium pentoxide, where the Nb_2O_5 helps stabilize the catalyst and improves its mechanical properties—showing that Nb_2O_5 produces a promoter effect that is good for oxidation reactions.

The use of Nb_2O_5 as a single catalyst depends on the heat treatment. In temperatures above 500 °C, the niobium pentoxide shows an almost neutral characteristic, decreasing its acid strength. Tanabe showed niobic acid ($Nb_2O_5.nH_2O$) in several strategic reactions, like hydration reactions of alkenes. The niobic acid presented higher activity than the solid phosphoric acid (catalyst used in the industry) and higher selectivity. Niobic acid also shows excellent activity and selectivity for

esterification reactions using ethyl alcohol. Table 1.3. summarize important reactions performed using Nb_2O_5, compiled by Tanabe [55].

Table 1. 3. Catalytic activities and selectivity for Nb_2O_5 in several reactions - Adapted from [55].

Catalyst	Reaction	Conversion	Selectivity
$Nb_2O_5.nH_2O$	Cyclopentanol $\xrightarrow{250\,°C}$ Cyclopentene	99%	99%
$Nb_2O_5.nH_2O$	Benzene + NO_2 $\xrightarrow{125\,°C}$ Nitrobenzene	12.7%	100%
MoO_3-WO_3		12.7%	98%
$Nb_2O_5.nH_2O$	Isobutene + Formaldehyde $\xrightarrow{350\,°C}$ Isoprene	61%	92%
$Nb_2O_5.nH_2O$	Butyraldehyde $\xrightarrow{160\,°C}$ 2-Ethyl hexanal	92%	96%
$Nb_2O_5.nH_2O$	Metyl-t-butyl ether $\xrightarrow{250\,°C}$ Isobutene	99%	100%
γ-Al_2O_3		100%	96%
$Nb_2O_5.nH_2O$	Isobutene + Isobutyraldehyde $\xrightarrow{200\,°C}$ 2,5-Dimethyl-2,4-hexadine	97%	82%
H_2SO_4 (16 wt%)		99%	21%
(10%)Nb_2O_5/SiO_2	Methyl hemiformal + Methyl propionate $\xrightarrow{370\,°C}$ Methyl metacrylate + water	34%	91%
(10%)Ta_2O_5/SiO_2		30%	49%
(10%)WO_3/SiO_2		22%	25%

The work by Tanabe settled the importance of understanding how Nb_2O_5 could perform as a catalyst in several reactions. Ko and Weissman [56] discussed the many structures of niobium pentoxide, with various polymorphs, and how it implicates the Nb_2O_5 chemical behavior. Using niobium ethoxide as the precursor, they prepared bulk Nb_2O_5 in four modifications, TT, T, M, and H. They correlate the crystal structure with the performance in catalysis, showing a decrease in the surface acidity for high-temperature crystalline forms. However, they could obtain improved performance for TT and T-Nb_2O_5, which can be related to the interaction between molecules and the presence of trace impurities. Florentino et al. obtained niobium pentoxide in temperatures ranging from 373 to 773 K, showing lower surface acidity with increased

temperature. However, the catalytic behavior changed, where samples in higher temperatures presented different selectivity [57].

Morikawa and Togashi showed the performance of Nb_2O_5 in reductive media, performing better than Ta, Si, Al, or Ti oxides, with higher selectivity for the desired product [58]. Ross et al. show the use of niobia as a catalyst for oxidative reactions, such as oxidative dehydrogenation of methanol, ethane, and propane, and oxidative coupling of methane. They produced mixed oxides, using pure Nb_2O_5 and coupled with V, Ti, P, Cr, Mo oxides. The pure niobium pentoxide performed better in all catalytic tests, with higher selectivity (over 80%) and conversion. They studied the niobia crystalline phase influence on the dehydrogenation reaction. Showing better conversion and selectivity for the TT-Nb_2O_5, T-Nb_2O_5, and a mix of these phases, even those samples presented lower acidity than amorphous niobia [59].

Wada and Morikawa published important work on how Nb^{4+} cations in the structure could affect the catalytic properties. They reduced the Nb_2O_5 under H_2O/H_2 atmosphere, all samples crystallized in the orthorhombic T-Nb_2O_5, obtaining oxides with composition between $2.50 < x < 2.48$ (NbO_x), increasing the concentration of Nb^{4+} atoms [60]. They performed electron spin resonance (ESR) of the materials, quantifying the spin concentration of Nb^{4+}, showing that there is more nitric oxide with increased spin concentration (indicative of more paramagnetic Nb^{4+} species) adsorbed on the niobium pentoxide.

The discovery of the water-splitting employing TiO_2 by Fujishima in 1972 attracted the attention of metal oxides in photocatalysis [61]. The electronic properties of the niobium pentoxide showed to be suitable for the photocatalytic process since it absorbs light in the UV region and has a chemical similarity with the TiO_2. Yoshida et al. showed the properties of Nb_2O_5 for propene photo-oxidation, attributing the good activity to low electron density at oxygen sites as an indication of defects in the structure [48]. Hasegawa et al. showed that under photo-irradiation, the activity of niobium oxide supported on titanium dioxide decreases due to the introduction of oxygen in the system [62]. Some works investigated photocatalytic and catalytic behavior, correlating with the structure, employing vibration modes spectroscopy

techniques such as Raman [63-65] and infrared spectroscopy [66]. However, the correlation between the obtained phase and the catalytic/photocatalytic activity was not discussed, and the applications draw more attention to the use of Nb_2O_5 in catalysis and photocatalysis, increasing the number of publications [62, 67, 68].

The interest in the photocatalytic process increased during the 90s, primarily because of the studies on the TiO_2 properties. The TiO_2 is a wide band-gap photocatalyst (Bulk TiO_2 Eg = 3.2 eV), with suitable properties for photocatalysis. However, scientists were facing an impasse. They conclude that TiO_2 is inadequate for energy acquisition or vast amounts of water treatment because the light energy density is primarily low, and the TiO_2 can use only the portion of UV light from the sun. They proposed that adding metallic particles or mixed oxides could increase the absorbed light and the visible light range, improving the photocatalytic properties [69].

The studies in producing Nb_2O_5/TiO_2 started, for example, Cui et al. produced TiO_2 loaded with Nb_2O_5, and the composite had a performance 100% better than the pure titanium dioxide in the degradation of 1,4-dichlorobenzene, and enhanced adsorption of n-butylamine, correlating the acid sites strength [70]. The developments in the photocatalysts grow, as the interest in applying the niobium pentoxide in several heterogeneous catalyzed reactions [71].

The use of niobium pentoxide as a wide band-gap semiconductor started to disseminate. Its modifications vary from only Nb_2O_5, doped-Nb_2O_5, or composites, such as TiO_2/Nb_2O_5. It has been showing the excellent performance of niobium pentoxide at the beginning of the 2000s, at the use in dye-sensitized solar cells along with TiO_2 [72], TT-Nb_2O_5 photocatalytic activity in aqueous suspensions [73], Nb_2O_5/WO_3 composites presenting improved photocatalytic performance against Rhodamine B with higher niobia content [74], Nb_2O_5 and Ag/Nb_2O_5 for textile industry wastewater treatment and dye removal [75], niobium pentoxide as a powerful oxidant agent of emergent organic contaminants [76], as an efficient photocatalyst for methylene blue degradation using solar light [77], as an excellent photo oxidant for alcohols [78], and among several others applications and process [79, 80].

3.2. Nb_2O_5 uses in the energy field

The electronic properties of the niobium pentoxide dragged attention to its possible applications in the energy field. The discoveries in the 80s showed that niobium pentoxide could present different electrical properties between crystallographic phases. Some phases often presented an atomic site with cation reduction to Nb^{4+}, which explains some phases' lower resistance, such as TT, T, and H [81].

During the late 80s and the beginning of the 90s, the first applications of niobium pentoxide in rechargeable lithium batteries and lithium insertion started [50, 82]. The use of niobium pentoxide as an anodic film for impedance study, showing the usefulness of the material, which the high density of defects shrinks the band-gap and makes it a satisfying material to act as counter electrode [83]. Studies on amorphous niobium pentoxide's electrochromic properties show good Li^+ diffusion, indicating the long durability of the films without loss of their properties, like time response [84, 85]. Rüscher published a work reporting the effect on the electrical properties of niobium pentoxide with oxygen vacancies ($NbO_{2.5-x}$, $0.0 \leq x \leq 0.083$), studying the H-phase and some non-stoichiometric phases. He shows the polarized electric field along the b-axis, and the $NbO_{2.5-x}$ system shows remarkable electric properties associated with oxygen vacancies and Nb^{4+} cations [86].

During the 90s, the applications in Li insertion grew, and several studies sustained the excellent properties of niobium pentoxide, indicating that the key to obtaining better properties is to control the defect density, the obtained crystallographic phase, and the mixture of phases [87-89]. The construction of devices to convert photon-to-electron, like dye-sensitized solar cells, has been studied in the past few years [90]. The niobium pentoxide figures as one of the promising metal oxides in these fields, with studies focusing on the morphological and textural properties and the implication on efficiency [91]. The synthesis of heterojunctions of Nb_2O_5/TiO_2 to act as nanoporous electrodes in dye-sensitized solar cells [92]. Theoretical studies to understand the transport mechanism of Li^+ ions, along with the structure and the dependence of lithium concentration, show significant changes in diffusion rate in

interphases regions [93]. The Density functional theory calculations also proved the intrinsic defect stability in $LiNbO_3$ materials [94].

At the end of the 2000s, the niobium pentoxide was being tested for dye-sensitized solar cells and had proven its capability to perform great in electronic tests, being one of the metal oxides in ascension [95]. Ou et al. published a work showing the substantial photoconversion efficiency of niobium pentoxide, suggesting that the orthorhombic (T) Nb_2O_5 can perform better than the TiO_2 on dye-sensitized solar cells because it has a large unit cell dimension. However, the challenges are obtaining the correct crystalline phase and with the proper orientation. They show that the material performs better than standard TiO_2 used in these devices [96].

Augustyn et al. demonstrated the intercalation pseudocapacitance behavior of orthorhombic Nb_2O_5 (T-phase) with lithium ions insertion. They quantified the kinetics of the charge store and concluded that the T-Nb_2O_5 presents no diffusion limitations, with high-rate capability due to fast diffusion [97]. Lubimtsev et al. studied the origin of the high-rate intercalation pseudocapacitance in T-Nb_2O_5. They performed theoretical simulations using Monte Carlo and Density functional theory, showing the Li-ion migration path inside the crystal structure, which localized redox sites lead to high energy density area and produce capacitive charge storage. The presence of open channels in the crystal structure reduces the diffusion barrier for lithium, contributing to the high-rate intercalation [98].

Several studies have been reported since then, studying different shapes for Nb_2O_5 and their implications on their properties, such as microspheres [99], nanotubes [100], nanowires [101], nanorods [102], and nanoplates [103]. Despite all the efforts and the tremendous scientific production employing niobium pentoxide, there is still space for discoveries and studies, mainly focusing on the defect production, transportation mechanisms, metal doping of Nb_2O_5, composites, and several others.

The next chapter will discuss the growth in niobium pentoxide's scientific and industrial production since 1960, employing a widely used mathematical model. The state of the art of niobium pentoxide will be presented, focusing mainly on the catalytic and electronic applications, from 2015 until nowadays.

References

[1] C. Nico, T. Monteiro, M.P.F. Graça, Niobium oxides and niobates physical properties: Review and prospects, Progress in Materials Science 80 (2016) 1-37.
[2] W.P. Griffith, P.J.T. Morris, Charles Hatchett FRS (1765-1847), chemist and discoverer of niobium, The Royal Society Journal of the History of Science 57(3) (2003) 299-316.
[3] H.I. Mineralogy, Columbite-Tantalite, 2020. https://www.mindat.org/min-10303.html. (Accessed 24/08 2020).
[4] A. Ekeberg, Of the Properties of the Earth Yttria, compared with those of Glucine; of Fossils, in which the first of these Earths in contained; and of the Discovery of a metallic Nature (Tantalium), Journal of Natural Philosophy, Chemistry, and the Arts 3 (1802) 251–255.
[5] W.H. Wollaston, On the Identity of Columbium and Tantalum, Philosophical Transactions of the Royal Society 99(246-252) (1809).
[6] H. Rose, Ueber die Zusammensetzung der Tantalite und ein im Tantalite von Baiern enthaltenes neues Metall, Annalen der Physik 139(10) (1844) 317-341.
[7] G.B. Kauffman, Christian Wilhelm Blomstrand (1826–1897) Swedish chemist and mineralogist, Annals of Science 32(1) (1975) 13-37.
[8] M.C. Marignac, Recherches sur les combinaisons du niobium, Annales de chimie et de physique 4(8) (1866) 7-75.
[9] G.Z. Rayner-Canham, Zheng, Naming elements after scientists: an account of a controversy, Foundations of Chemistry 10(1) (2008) 13-18.
[10] C.K. Gupta, A.K. Suri, Extractive Metallurgy of Niobium, CRC Press (1994) 1-16.
[11] P. Aladar, Manufacture or Steel, in: U.S.P. Office (Ed.) General Electric Co, United States, 1917.
[12] B. T. Matthias, T. H. Geballe, S. Geller, E. Corenzwit, Superconductivity of Nb3Sn, American Physical Society 95(1435) (1954).
[13] C. Courier, Superconductivity and the LHC: the early days, 2011. https://cerncourier.com/a/superconductivity-and-the-lhc-the-early-days-2/. (Accessed 25/08 2020).
[14] C.H. Award, About Niobium, 2019. https://www.charles-hatchett.com/about-niobium. (Accessed 25/08 2020).
[15] CBMM, Conheça a história da CBMM e sua relação com o desenvolvimento do Nióbio, 2019. https://cbmm.com/pt/our-company/our-history. (Accessed 26/08 2020).
[16] B. Keown, Thirty Five Years of the Charles Hatchett Award, https://www.charles-hatchett.com/, 2013, p. 13.
[17] G. Brauer, Über die Oxyde des Niobs, Naturwissenschaften 28(2) (1940) 30-30.
[18] V.G. Brauer, Die Oxyde des Niobs, Zeitschrift für anorganische und allgemeine Chemie 248(1) (1941) 1-31.
[19] R.B. Hahn, Phosphates of Niobium and Tantalum1, Journal of the American Chemical Society 73(11) (1951) 5091-5093.

[20] L.K. Frevel, H.W. Rinn, Powder Diffraction Standards for Niobium Pentoxide and Tantalum Pentoxide, Analytical Chemistry 27(8) (1955) 1329-1330.
[21] F. Holtzberg, A. Reisman, M. Berry, M. Berkenblit, Chemistry of the Group VB Pentoxides. VI. The Polymorphism of Nb_2O_5, Journal of the American Chemical Society 79(9) (1957) 2039-2043.
[22] M.W. Shafer, R. Roy, The Polymorphism of Nb_2O_5, Zeitschrift für Kristallographie - Crystalline Materials 110(1-6) (1958) 241-248.
[23] A. Reisman, F. Holtzberg, Further Comments on the Polymorphism of Nb_2O_5. The High Temperature Metastable Phaseε, J. Am. Chem. Soc 81(13) (1959) 3182-3184.
[24] N. Terao, Structures des Oxydes de Niobium, Japanese Journal of Applied Physics 2(3) (1963) 156-174.
[25] H. Schäfer, R. Gruehn, F. Schulte, The Modifications of Niobium Pentoxide, Angewandte Chemie International Edition in English 5(1) (1966) 40-52.
[26] W.K. Chen, R.A. Swalin, Studies on the defect structure of α-Nb_2O_5, Journal of Physics and Chemistry of Solids 27(1) (1966) 57-64.
[27] J.A.R.R.A. Rapp, Electrical properties of NbO and NbO_2, J. Phys. Chem. Solids 30 (1969) 1119-1124.
[28] K. Sakata, Electrical and Magnetic Properties of NbO_2, Journal of the Physical Society of Japan 26(3) (1969) 867-867.
[29] T. Sakata, K. Sakata, I. Nishida, Study of Phase Transition in NbO_2, physica status solidi (b) 20(2) (1967) K155-K157.
[30] J.S. Anderson, J.L. Hutchison, F.J. Lincoln, Dislocations and Related Defects in Niobium Oxide Structures, Proceedings of the Royal Society of London. Series A, Mathematical and Physical Sciences 352(1670) (1977) 303-323.
[31] J.S. Anderson, J.M. Browne, A.K. Cheetham, R.V. Dreele, J.L. Hutchison, F.J. Lincoln, D.J.M. Bevan, J. Straehle, Point Defects and Extended Defects in Niobium Oxides, Nature 243(5402) (1973) 81-83.
[32] J.S. Anderson, J.M. Browne, J.L. Hutchison, Segregation of Impurity Atoms in Niobium Oxide, Nature 237(5351) (1972) 151-153.
[33] J.S. Anderson, J.M. Browne, J.L. Hutchison, Electron microscopy of the niobium oxides. I. Twinning and defects in H-Nb_2O_5, Journal of Solid state Chemistry 5(3) (1972) 419-431.
[34] K.M. Nimmo, J.S. Anderson, Reduction and non-stoicheiometry of niobium pentoxide, Journal of the Chemical Society, Dalton Transactions (21) (1972) 2328-2337.
[35] S. Tamura, High-pressure phase research on Nb_2O_5, Journal of Materials Science 7(3) (1972) 298-302.
[36] S. Kimura, Phase equilibria in the system NbO_2-Nb_2O_5: Phase relations at 1300 and 1400° C and related thermodynamic treatment, Journal of Solid state Chemistry 6(3) (1973) 438-449.
[37] J.F. Marucco, Electrical resistance and defect structure of stable and metastable phases of the system $Nb_{12}O_{29}$-Nb_2O_5 between 800 and 1100°C, The Journal of Chemical Physics 70(2) (1979) 649-654.

[38] J.F. Marucco, Thermodynamic study of the system NbO_2-Nb_2O_5 at high temperature J. Solid State Chem 10 (1974) 211-218.
[39] T. Matsui, K. Naito, Thermodynamic study of niobium oxides with O Nb ratios from 2.47 to 2.50 using a high-temperature galvanic cell, Journal of Solid state Chemistry 59(2) (1985) 228-236.
[40] K. Naito, T. Matsui, Review on phase equilibra and defect structures in the niobium-oxygen system, Solid State Ionics 12 (1984) 125-134.
[41] T. Matsui, K. Naito, Vaporization study on the niobium-oxygen solid solution by mass-spectrometric method, Journal of Nuclear Materials 115 (1983) 178-186.
[42] T. Matsui, K. Naito, Vaporization study on nonstoichiometric NbO_{2-x} by mass-spectrometric method, Journal of Nuclear Materials 102 (1981) 227-234.
[43] K. Naito, N. Kamegashira, N. Sasaki, Phase Equilibria in the System between NbO_2 and Nb_2O_5 at High Temperature, Journal of Solid state Chemistry 35 (1980) 305-311.
[44] A. International, Binary Alloy Phase Diagrams, American Society for Metals, 1990.
[45] U. Balachandran, N.G. Eror, On the defect structure of acceptor-doped α-Nb_2O_5, Journal of The Less-Common Metals 84(C) (1982) 215-223.
[46] U. Balachandran, N.G. Eror, Non-stoichiometric disorder in α-Nb_2O_5 at elevated temperatures, Journal of Materials Science 17(5) (1982) 1286-1296.
[47] J.G. Weissman, E.I. Ko, P. Wynblatt, J.M. Howe, High-Resolution Electron Microscopy and Image Simulation of TT-, T-, and H-Niobia and Model Silica-Supported Niobium Surface Oxides, Chemistry of Materials 1(2) (1989) 187-193.
[48] S. Yoshida, Y. Nishimura, T. Tanaka, H. Kanai, T. Funabiki, The local structures and photo-catalytic activity of supported niobium oxide catalysts, Catalysis Today 8(1) (1990) 67-75.
[49] C. Nakaoka, Y. Wada, A. Morikawa, Catalytic Activity Induced by Partial Sulfiding of Niobium Oxide for Hydrogenation of 1,3-Butadiene and Hydrodesulfurization of Thiophene, Journal of The Japan Petroleum Institute 31(2) (1988) 176-179.
[50] C.A.C. Sequeira, F.D.S. Marques, Lithium insertion in niobium pentoxide, Chemtronics 3(4) (1988) 236-239.
[51] A. Maeda, Z. Hu, K. Kunimori, T. Uchijima, Effect of high-temperature reduction on ammonia decomposition over niobia-supported and niobia-promoted rhodium catalysts, Catalysis Letters 1(5) (1988) 155-157.
[52] G. Zhang, H. Hattori, K. Tanabe, Aldol Addition of Acetone, Catalyzed by Solid Base Catalysts: Magnesium Oxide, Calcium Oxide, Strontium Oxide, Barium Oxide, Lanthanum (III) Oxide and Zirconium Oxide, Applied Catalysis 36(C) (1988) 189-197.
[53] T. Inoue, T. Iizuka, K. Tanabe, Hydrogenation of carbon dioxide and carbon monoxide over supported rhodium catalysts under 10 bar pressure, Applied Catalysis 46(1) (1989) 1-9.
[54] S. Okazaki, A. Kurosaki, Acidic properties and catalytic activities of niobic acid treated with phosphoric acid, Catalysis Today 8(1) (1990) 113-122.
[55] K. Tanabe, Application of Niobium Oxides as catalysts, Catalysis Today 8 (1990) 1-11.

[56] E.I. Ko, J.G. Weissman, Structures of niobium pentoxide and their implications on chemical behavior, Catalysis Today 8(1) (1990) 27-36.
[57] A. Florentino, P. Cartraud, P. Magnoux, M. Guisnet, Textural, acidic and catalytic properties of niobium phosphate and of niobium oxide: Influence of the pretreatment temperature, Applied Catalysis A: General 89(2) (1992) 143-153.
[58] A. Morikawa, A. Togashi, Stability of niobium oxide catalyst activity emerging in reductive medium, Catalysis Today 16(3) (1993) 333-339.
[59] J.R.H. Ross, R.H.H. Smits, K. Seshan, The use of niobia in oxidation catalysis, Catalysis Today 16(3) (1993) 503-511.
[60] Y. Wada, A. Morikawa, Catalysis by niobium oxides in their reduced states, Catalysis Today 8(1) (1990) 13-25.
[61] K. Nakata, A. Fujishima, TiO_2 photocatalysis: Design and applications, Journal of Photochemistry and Photobiology C: Photochemistry Reviews 13(3) (2012) 169-189.
[62] S. Hasegawa, H. Aritani, M. Kudo, Structures and catalytic behavior of some niobium oxides, Catalysis Today 16(3) (1993) 371-377.
[63] J.-M. Jehng, A.M. Turek, I.E. Wachs, Surface modified niobium oxide catalyst: synthesis, characterization, and catalysis, Applied Catalysis A: General 83(2) (1992) 179-200.
[64] J.-M. Jehng, I.E. Wachs, Molecular structures of supported niobium oxide catalysts under ambient conditions, Journal of Molecular Catalysis 67(3) (1991) 369-387.
[65] J.M. Jehng, I.E. Wachs, Structural chemistry and Raman spectra of niobium oxides, Chemistry of Materials 3(1) (1991) 100-107.
[66] J. Datka, A.M. Turek, J.M. Jehng, I.E. Wachs, Acidic properties of supported niobium oxide catalysts: An infrared spectroscopy investigation, Journal of Catalysis 135(1) (1992) 186-199.
[67] I. Matsuura, H. Oda, K. Oshida, Partial oxidation and ammoxidation of isobutane over Bi-Mo-based composite oxide with Nb_2O_5, Catalysis Today 16(3) (1993) 547-554.
[68] T. Ushikubo, T. Iizuka, H. Hattori, K. Tanabe, Preparation of highly acidic hydrated niobium oxide, Catalysis Today 16(3) (1993) 291-295.
[69] K. Hashimoto, H. Irie, A. Fujishima, TiO_2 Photocatalysis: A historical overview and future prospects, Japanese Journal of Applied Physics 44(12) (2005) 8269-8285.
[70] H. Cui, K. Dwight, S. Soled, A. Wold, Surface Acidity and Photocatalytic Activity of Nb_2O_5/TiO_2 Photocatalysts, Journal of Solid state Chemistry 115(1) (1995) 187-191.
[71] R.F. Howe, Recent Developments in Photocatalysis, Dev. Chem. Eng. Mineral Process 6(1) (1998) 55-84.
[72] K. EGUCHI, H. KOGA, Koshi SEKIZAWA, K. SASAKI, Nb_2O_5-Based Composite Electrodes for Dye-Sensitized Solar Cells, Journal of the Ceramic Society of Japan 108(1264) (2000) 1067-1071.
[73] H. Kominami, K. Oki, M. Kohno, S.-i. Onoue, Y. Kera, B. Ohtani, Novel solvothermal synthesis of niobium(v) oxide powders and their photocatalytic activity in aqueous suspensions, Journal of Materials Chemistry 11(2) (2001) 604-609.
[74] H. Wang, P. Xu, T. Wang, Doping of Nb_2O_5 in photocatalytic nanocrystalline/nanoporous WO_3 films, Thin Solid Films 388(1) (2001) 68-72.

[75] M.K. Silva, R.G. Marques, N.R.C.F. Machado, O.A.A. Santos, Evaluation of Nb_2O_5 and Ag/Nb_2O_5 in the photocatalytic degradation of dyes from textile industries, Brazilian Journal of Chemical Engineering 19 (2002) 359-363.
[76] A. Esteves, L.C.A. Oliveira, T.C. Ramalho, M. Goncalves, A.S. Anastacio, H.W.P. Carvalho, New materials based on modified synthetic Nb_2O_5 as photocatalyst for oxidation of organic contaminants, Catalysis Communications 10(3) (2008) 330-332.
[77] J. Gandhi, R. Dangi, S. Bhardwaj, Nb_2O_5 used as photocatalyst for degradation of methylene blue using solar energy, Rasayan J. Chem 1(3) (2008) 567-571.
[78] T. Shishido, T. Miyatake, K. Teramura, Y. Hitomi, H. Yamashita, T. Tanaka, Mechanism of Photooxidation of Alcohol over Nb_2O_5, The Journal of Physical Chemistry C 113(43) (2009) 18713-18718.
[79] Q. Sun, L. Liu, X. Xing, A. Auroux, J. Shen, Catalysis of Niobium, Petrochemical Technology 36(4) (2007) 319-327.
[80] K. Tanabe, Catalytic application of niobium compounds, Catalysis Today 78(1) (2003) 65-77.
[81] G.C. Vezzoli, Electrical properties of NbO_2 and Nb_2O_5 at elevated temperature in air and flowing argon, Physical Review B 26(7) (1982) 3954-3957.
[82] N. Kumagai, I. Ishiyama, K. Tanno, Electrochemical and structural characteristics of niobium(V) oxide in a rechargeable lithium battery, Journal of Power Sources 20(3) (1987) 193-198.
[83] F. Di Quarto, S. Piazza, C. Sunseri, Amorphous semiconductor—electrolyte junction. Impedance study on the a-Nb_2 O_5—electrolyte junction, Electrochimica Acta 35(1) (1990) 99-107.
[84] G.R. Lee, J.A. Crayston, Electrochromic Nb_2O_5 and Nb_2O_5/silicone composite thin films prepared by sol–gel processing, Journal of Materials Chemistry 1(3) (1991) 381-386.
[85] M.A.B. Gomes, L.O.d.S. Bulhões, S.C. de Castro, A.J. Damião, The Electrochromic Process at Nb_2O_5 Electrodes Prepared by Thermal Oxidation of Niobium, Journal of The Electrochemical Society 137(10) (1990) 3067-3070.
[86] C.H. Rüscher, The structural effect on the electrical properties of $NbO_{2.5-x}$ block-type compounds, Physica C: Superconductivity 200(1) (1992) 129-139.
[87] H. Yamada, M. Hibino, T. Kudo, Li-intercalated ReO_3-type solid solutions in the Nb_2O_5–WO_3 system, Materials Research Bulletin 34(6) (1999) 955-962.
[88] N. Özer, T. Barreto, T. Büyüklimanli, C.M. Lampert, Characterization of sol-gel deposited niobium pentoxide films for electrochromic devices, Solar Energy Materials and Solar Cells 36(4) (1995) 433-443.
[89] J. Blümel, E. Born, T. Metzger, Solid state NMR study supporting the lithium vacancy defect model in congruent lithium niobate, Journal of Physics and Chemistry of Solids 55(7) (1994) 589-593.
[90] K. Tennakone, J. Bandara, Multiphoton semiconductor photocatalysis, Solar Energy Materials and Solar Cells 60(4) (2000) 361-365.
[91] K. Hara, T. Horiguchi, T. Kinoshita, K. Sayama, H. Sugihara, H. Arakawa, Highly efficient photon-to-electron conversion with mercurochrome-sensitized nanoporous

oxide semiconductor solar cells, Solar Energy Materials and Solar Cells 64(2) (2000) 115-134.
[92] S.G. Chen, S. Chappel, Y. Diamant, A. Zaban, Preparation of Nb_2O_5 Coated TiO_2 Nanoporous Electrodes and Their Application in Dye-Sensitized Solar Cells, Chemistry of Materials 13(12) (2001) 4629-4634.
[93] F. Lantelme, H. Groult, N. Kumagai, Study of the concentration-dependent diffusion in lithium batteries, Electrochimica Acta 45(19) (2000) 3171-3180.
[94] H. Xu, D. Lee, J. He, S.B. Sinnott, V. Gopalan, V. Dierolf, S.R. Phillpot, Stability of intrinsic defects and defect clusters in $LiNbO_3$ from density functional theory calculations, Physical Review B 78(17) (2008) 174103.
[95] R. Jose, V. Thavasi, S. Ramakrishna, Metal Oxides for Dye-Sensitized Solar Cells, Journal of the American Ceramic Society 92(2) (2009) 289-301.
[96] J.Z. Ou, R.A. Rani, M.-H. Ham, M.R. Field, Y. Zhang, H. Zheng, P. Reece, S. Zhuiykov, S. Sriram, M. Bhaskaran, R.B. Kaner, K. Kalantar-zadeh, Elevated Temperature Anodized Nb_2O_5: A Photoanode Material with Exceptionally Large Photoconversion Efficiencies, ACS Nano 6(5) (2012) 4045-4053.
[97] V. Augustyn, J. Come, M.A. Lowe, J.W. Kim, P.-L. Taberna, S.H. Tolbert, H.D. Abruña, P. Simon, B. Dunn, High-rate electrochemical energy storage through Li^+ intercalation pseudocapacitance, Nature Materials 12(6) (2013) 518-522.
[98] A.A. Lubimtsev, P.R.C. Kent, B.G. Sumpter, P. Ganesh, Understanding the origin of high-rate intercalation pseudocapacitance in Nb_2O_5 crystals, Journal of Materials Chemistry A 1(47) (2013) 14951-14956.
[99] S.-q. Guo, X. Zhang, Z. Zhou, G.-d. Gao, L. Liu, Facile preparation of hierarchical Nb_2O_5 microspheres with photocatalytic activities and electrochemical properties, Journal of Materials Chemistry A 2(24) (2014) 9236-9243.
[100] S. Suzuki, K. Teshima, T. Ishizaki, S. Lee, K. Yubuta, T. Shishido, S. Oishi, Unique three-dimensional nano-/micro-textured surfaces consisting of highly crystalline Nb_2O_5 nanotubes, Journal of Crystal Growth 318(1) (2011) 1095-1100.
[101] X. Wang, C. Yan, J. Yan, A. Sumboja, P.S. Lee, Orthorhombic niobium oxide nanowires for next generation hybrid supercapacitor device, Nano Energy 11 (2015) 765-772.
[102] S.-M. Lam, J.-C. Sin, I. Satoshi, A.Z. Abdullah, A.R. Mohamed, Enhanced sunlight photocatalytic performance over Nb_2O_5/ZnO nanorod composites and the mechanism study, Applied Catalysis A: General 471 (2014) 126-135.
[103] H. Liu, N. Gao, M. Liao, X. Fang, Hexagonal-like Nb2O5 Nanoplates-Based Photodetectors and Photocatalyst with High Performances, Scientific Reports 5(1) (2015) 7716.

Chapter 2 – State of the Art

INTRODUCTION

The niobium pentoxide state-of-the-art applications and studies stand in this chapter. The first discussion concerns the number of publications regarding the niobium oxide materials since 1960 and how the scientific community's interest grows. The study will employ a simple mathematical model to understand the relevance of niobium oxide over the years and prospective for the number of publications. The main applications employed will also be situated, focusing on the niobium pentoxide catalytic and energy field applications.

1. Prospective of Niobium Oxide Materials

1.1. The mathematical theory of species

The scientific desire to investigate how different species changes their population over the years started at the beginning of 1900, based on a competitional ecological model, developed among the years by Volterra, in his famous work "*La theorie mathématique de la lute pour la vie*" [1], and Lotka [2]. The model translates the Darwinist theory of species into a simple mathematical model, including competition between prey and predator. Marchetti et al. [3] created the hypothesis that different primary energy sources could behave in the global market like living species, competing between them (oil, gas, solar energy, and others). They propose a mathematical approach to represent the life cycle of technologies and the applications in the energy market of the USA, and they concluded that the statistical data followed the logistic equation. Later, they could approach the evolution of innovation and inventions along the years, showing the periodicity of 55 years between the cycles of innovation and inventions in the world. Fisher and Pry [4] also noted the energy market periodicity, in which they developed the "Logistic Model" for market prediction and usage of different energy sources. The model proposed by Marchetti, Fisher, and Pry had been extended and employed in more than 3000 different applications, with several levels of

abstraction. Some of these works were published by Dr. José Israel Vargas, like the deforestation of the Amazon rainforest [5], the occurrence of Dengue in the Rio de Janeiro state [6], and the technological perspective of the world [7]. In the following sub-section, the logistic equation is going to be defined.

1.2. The Logistic Equation

Several studies used the logistic equation, presenting reliable data about some occurrences in the world, as described before. With the correct indicator, the logistic equation could obtain a consistent model so that the formal description will be identical to the studies involving the species competition. To understand the growth of scientific publications in one subject, we need to understand the world's rate of publications per year.

Chung and Park [8] proposed forecasting the number of academic papers on entrepreneurship, employing the logistic equation. The question of how long the publication process would continue is essential for those involved in researching the subject. Like the model proposed by Marchetti, Fisher, and Pry, Chung proposed that since one subject is of great interest to the world, the rate of publications will grow year after year, in other words, more scientists publishing research papers about the subject, more new researches will work into the research field.

The indicator used in the study is the:

I) The total sum of publications (N) of the studied topic across the time. The bigger the number of publications, the more significant is the probability of new researchers starting to work on that.

II) The estimated total number of publications (N*) and the number of publications will occur over the years (N* - N).

The logistic equation is

$$\boldsymbol{dN(t) = a * N(N^* - N)dt} \quad (1)$$

dN(t)/dt is the publication rate over the years, N is the sum of publications on a year (t), N* is the estimated total of publications on the subject, and 'a' constant that describes the subject publication speed.

Solving the differential equation (1) to obtain the rate of publications over the year, we obtain its integrated formula

$$N(t) = \frac{N^*}{(1 + e^{-(at+b)})} \tag{2}$$

Where b is a constant of integration, figure 2.1 shows a graphical representation of equation (1), showing that at the beginning of a topic study, the publication rate is low (dN/dt) because N is small; however, with the interest growth in the subject, the publication rate grows, and reach the maximum number of publications at N = 0.5 N*.

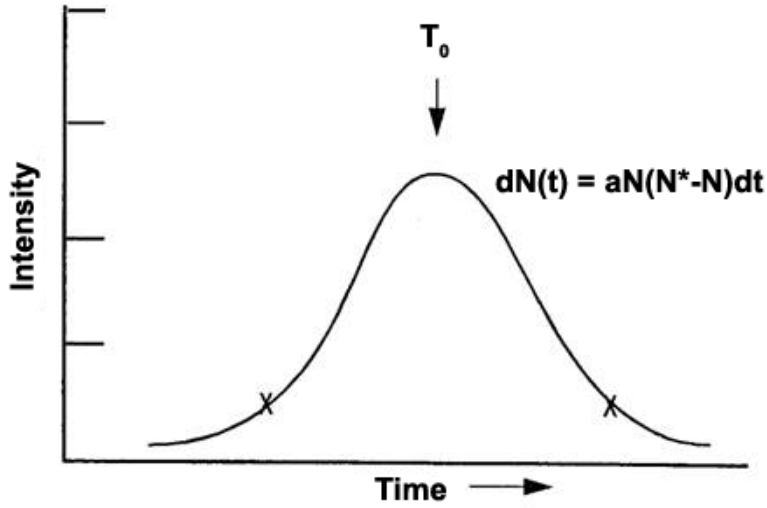

Figure 2. 1. Graphical representation of the differential form of the logistic equation – Adapted from [7]

Equation (2) is called a logistic or epidemiological equation. An S-shaped curve graphically represents it. When adopting a comparative approach for this equation, the fraction of publications is F = N/N*. Further proceeding with simple mathematical operations, the logistic equation (2) is

$$\frac{F}{(1 - F)} = e^{(at+b)} \tag{3}$$

After obtaining the natural logarithm on both sides, the equation assumes its linear form, called Fisher-Pry representation [4].

$$\ln\left[\frac{F}{(1-F)}\right] = at + b \tag{4}$$

The graphical representation of equations (3) and (4) are in Figure 2.2. The marked points represent the initial point of 10% and 90% of publications fraction (F = N/N*), indicating a time-lapse Δt which the publication process evolves from F = 0.1 to F = 0.9 (10 to 90% expected publications). It represents 80% of the completion of the entire publication process, where Δt is related to the 'a' constant as Δt = 4.39/a. At half of the process, the time is T_0, described as T_0 = b/a.

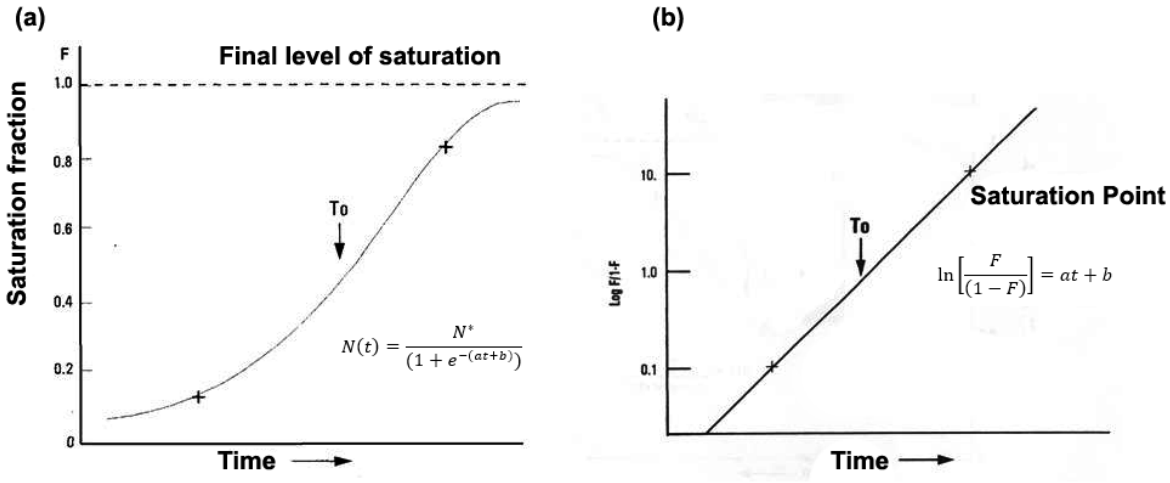

Figure 2. 2. Example plot of the (a) saturation fractions (F) against time and its (b) linearized form – Adapted from [7].

1.3. The Niobium Oxide Prospective

As discussed in Chapter 1, niobium oxide is a material with a very complex crystalline system, and it possesses applications in several fields of science. However, the uncertainty about the crystalline phase obtainment, the electronic properties, and the presence of non-stoichiometric oxides leads the scientific community to expand and improve their studies on structural characterization and state-of-the-art applications.

First, to apply the logistic equation on the niobium oxide subject, the total number of publications was evaluated from 1940 until 2016, collecting published papers in scientific journals. The above time was selected because the first report by Brauer was in 1940 [9], about the niobium oxide crystal structure, and very few articles on the

subject were available by the time. The Scopus database platform acted as a scientific catalog, and all the search parameters were in the abstract, keywords, or title.

The following search code was employed: TITLE-ABS-KEY ("óxido de nióbio" OR "Niobium pentoxide" OR "Niobium dioxide" OR "Niobium Oxide" OR "oxide niobium" OR "Nb_2O" OR "Nb_2O_3" OR "NbO" OR "NbO_2" OR "Nb_2O_5" OR "Niobs oxyde" OR "oxyde des niobs"). Figure 2.3 shows the publications for each year and the total number of publications over the years.

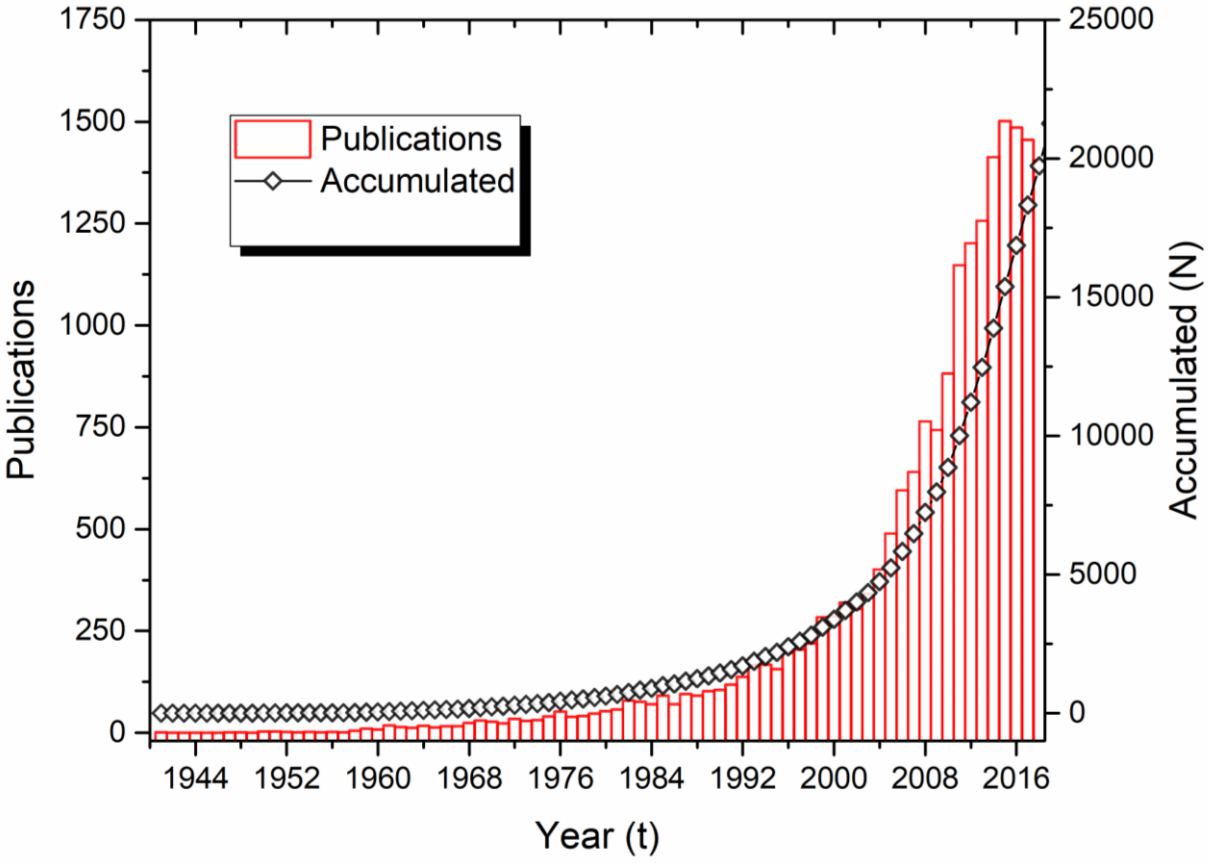

Figure 2. 3. Publications and accumulated number of publications per year.

It is evident by the presented curve that the growth in the publications number exponentially, showing an increase, especially during the 90s and 2000s. To estimate the total number of publications possible (N*), the equation (2) reorganizes in the form of a 2° degree polynomial function:

$$\frac{dN(t)}{dt} = aN^{*}N - aN^{2} \tag{5}$$

When plotting the dN/dT x N, estimating the second-order polynomial function by performing regression is presented in Figure 2.4. Fig 2.4(a) shows the obtained data. Fig 2.4(b) shows the fitted regression curve for the second-order polynomial function, where the constant 'a' is equal to the term multiplying the x^2 (N^2), and the expected total of publications (N*) is equal to 'a' divided by the constant term of 'x.' The estimated number of publications, N*, is equal to 52,511 scientific articles during the publication cycle of niobium oxides.

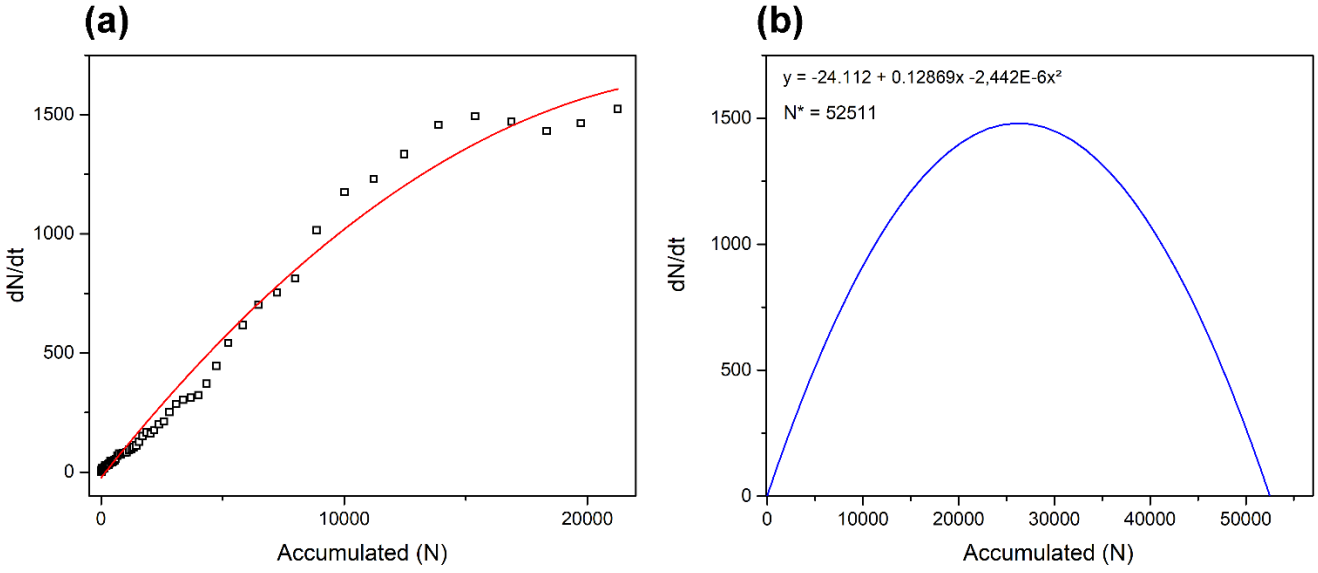

Figure 2. 4. (a) dN/dt x N plot evidence second-order behavior and (b) regression.

The accumulated number of publications over the years (N) can be estimated using the obtained N*. The total number of publications can be obtained, as the number of publications in a particular year in the future. The Fisher-Pry linear representation is the F (N/N*) plot against the time (t), and the results can extend for several years of publications on the niobium oxide subject. Figure 2.5 shows the logistic curve representation (S-shaped curve) and the linear curve known as Fisher-Pry representation. The logistic curve shows a slight increase in publications in the early years (1960-1990). In the 90s, the publications rate increased, pointing to 10% in 2002, achieving T_0 at 2023, showing interest in the scientific community.

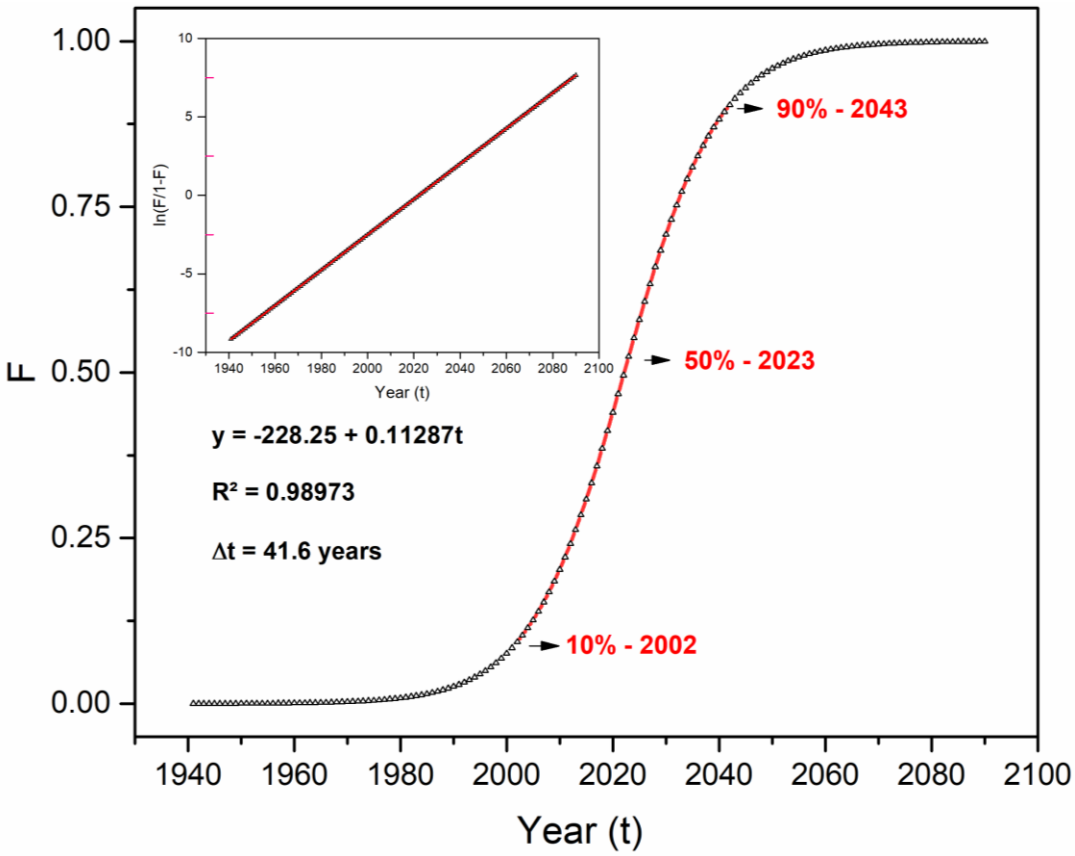

Figure 2. 5. Logistic equation of the niobium oxides publication and its respective Fisher-Pry representation.

The logistic study of niobium oxide materials shows a saturation point around 2043, where the subject will reach 90% of publications occupation in scientific journals. The time interval Δt is necessary for the publication process to evolve from $F = 0.1$ to 0.9 (10 to 90%), representing 80% of the publication cycle. The niobium oxide shows an approximated 42 years to complete the publication process of the subject, showing that there is still enough space for new publications and discoveries on the niobium oxide materials.

The logistic mathematical model shows good coherence with the subject, but as discussed in chapter 1, there is still several contradictions and misinformation regarding the niobium oxides [10], and plenty of room for new exciting scientific discoveries involving those materials. The main discoveries on niobium oxides show a particular interest in correlating its structural and electronic properties to its good performance in several applications in this chapter. Figure 2.6 shows the changes in the publication rate (dN/dt) over the years, showing changes around 1989 and 2003, and the

discoveries of niobium oxide can explain it as a suitable acid catalyst at the beginning of the 90s [11-13], and its applications in electronic devices like solar cells, Li-ion batteries, among other during the 2000s [14-17].

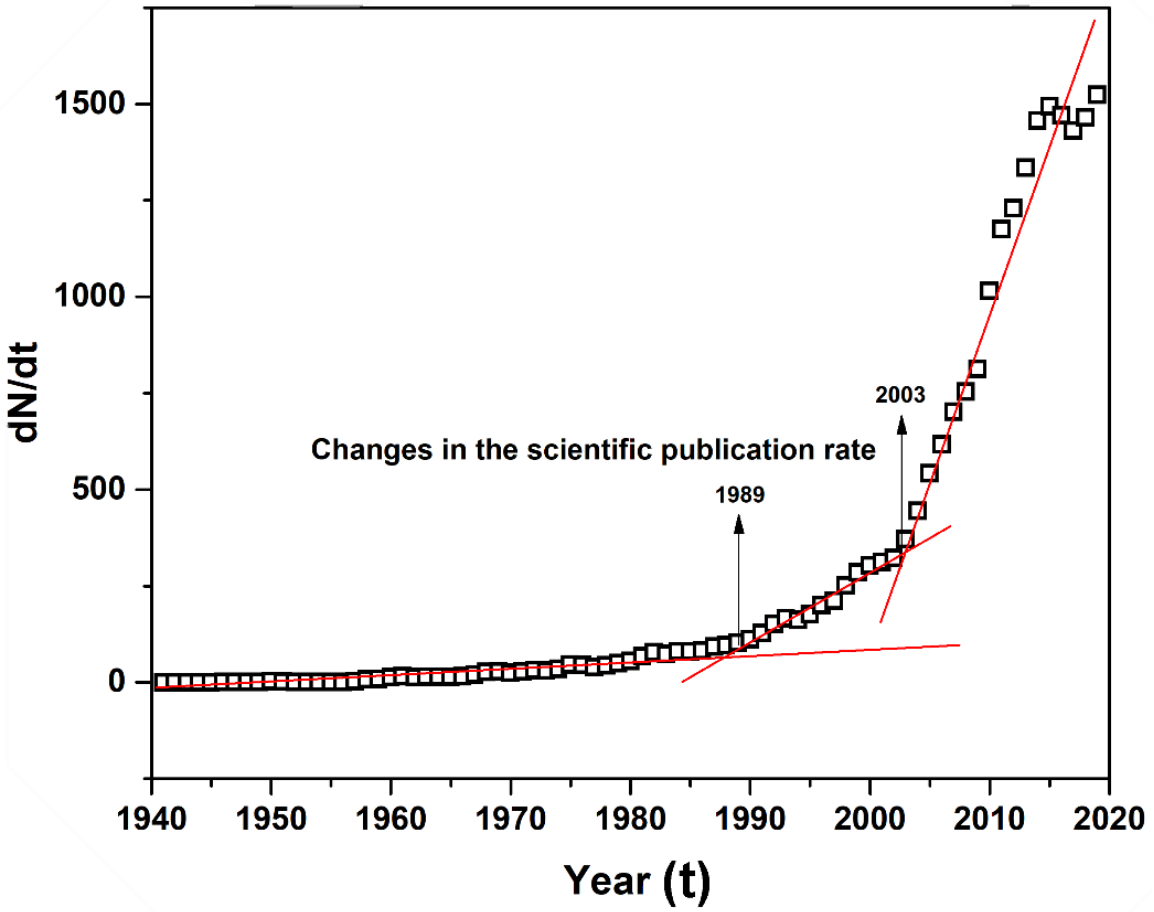

Figure 2. 6. A plot of the changes in publication rate of niobium oxide over the years.

Figure 2.7 shows the number of publications and their projection in the last ten years, showing a good correlation between the actual publication number and the logistic model. The discrepancy between the values occurs due to fluctuations in the scientific interest, for example, the publication number increase in solar cell energy after TiO_2 discoveries for water splitting [18], or, as a recent and prominent example, the growth in publications about SARS-Covid19, biological protection, and hazard during the pandemics.

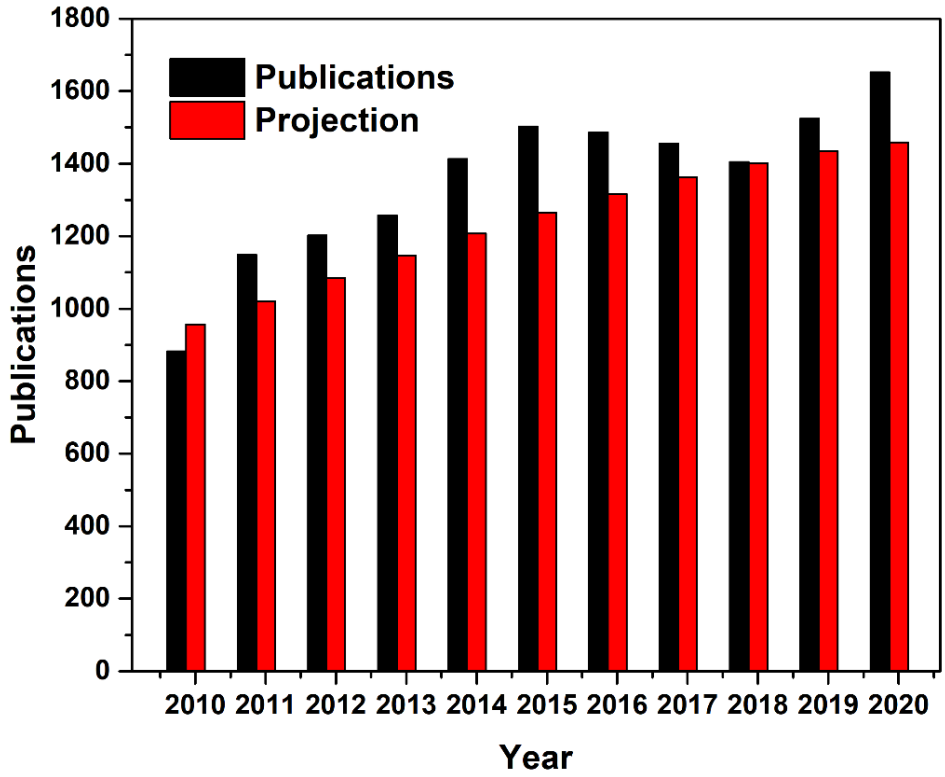

Figure 2. 7. Comparison between the number of published scientific articles and their projection over the last ten years.

The niobium oxide materials' projection can also suffer changes over the years. The discovery of a new characterization technique or new synthetic ways to obtain the non-stoichiometric materials can boost the publications at niobium oxide subject, also their uses at new applications.

Also, worth mentioning that this study employed only niobium oxide as the subject; however, in the past few years, there has been a significant increase in publications regarding niobium oxide composites synthesis, doping in the niobium pentoxide structure, synthesis of heterojunctions, and solar cells employing Nb_2O_5, among several others applications that will address in the next chapter.

2. Niobium Pentoxide applications

The last chapters showed the considerable potential for niobium pentoxide applications. The scientific community's efforts could still provoke breakthrough research about niobium pentoxide's crystal structure and applications. In the past few years, publications are still rising, demonstrating plenty of space for discoveries employing Nb_2O_5. As discussed by Alves and Coutinho in 2015 [19], the worldwide

niobium demand grows 10% each year for the past decade, increasing the production of Nb_2O_5 as the demand rises.

Those applications are in the state-of-the-art baseline, employing fine chemistry and physics to obtain the desired properties. One example is the synthesis of nanostructured black-Nb_2O_5, where Cui et al. produced in 2015 for the first time highly ordered oxygen-deficient Nb_2O_5, which presented a black color due to the presence of Nb^{4+} in the structure. The obtained material crystallized in the TT- and T- phases and improved solar energy absorption by 75.5% compared with pristine Nb_2O_5. They also stated that the presence of Nb^{4+} in the structure makes, for the first time, the Nb_2O_5 suitable for a photoelectrochemical cell application, showing a relatively large photocurrent [20]. In addition, Herval et al. produced the TT- and T-phases employing Pechini synthesis and demonstrated the Nb_2O_5 paramagnetic behavior caused by oxygen vacancies, which are responsible for the niobia magnetic moments [21]. Those results corroborate the past discussion about the importance of controlling the number of defects in the niobium pentoxide structure.

The possibility of obtaining defects in the niobium pentoxide structure through several synthetical methods raised the discussions, and the Nb_2O_5 applications started to understand its electronic properties. The electronic properties of niobium pentoxide have a crucial role in several applications, such as photocatalytic process, supercapacitors, photodetector, resistive memory applications, and electrochemical energy storage.

For example, Kong et al. synthesized T-Nb_2O_5 and graphene oxide (GO) composites, showing an ultrahigh gravimetric/volumetric capacitance for Li-ion intercalation. The orthorhombic niobia synthesized through polyol-mediated reaction led to a material with mesoporous channels and high capacitance and conductivity [22, 23]. Qamar et al. also synthesized Nb_2O_5/rGO composites, showing high efficiency as a photoelectrochemical agent for the water-splitting process under UV and visible light [24]. Liu et al. synthesized hexagonal nanoplates of Nb_2O_5, obtaining the TT, T, and H phases and their mixture. They showed that the obtained materials are suitable for photodetectors and photocatalysis, with remarkable sensitivity and high external

quantum efficiency (EQE of 9617%), making a suitable material for high-performance UV-A photodetector and photocatalyst [25]. Raba et al. studied the effect of the preparation method on the photocatalytic activity of Nb_2O_5 materials. They reported different methods like Pechini [26] and sol-gel [27], employing two niobium precursors, the niobium ethoxide and niobium chloride. They showed that the synthetic method led to a different crystalline phase formation, and the material's structure strongly depends on the raw materials and synthetic route. They also reported changes in the band-gap values and differences in the particle homogeneity between the two methods, where the Pechini yields particles with smaller crystallite size, and sol-gel is more uniformed [27, 28].

In the past few years, the niobium pentoxide materials have emerged as one of the most prominent materials for batteries, supercapacitors, anode material in Li-ion batteries, as an electrode for supercapacitors, where the crystal structure strongly influences its performance [29]. For example, preferential orientation in niobium pentoxide material strongly correlates with electrochemical characteristics. Wang et al. [30] synthesized the TT- and T-Nb_2O_5 employing the hydrothermal method, obtaining the material with preferential orientation along the [001] direction. The TT-Nb_2O_5 nanowires showed small crystallite and preferential orientation and transition at 600 °C to a highly crystalline orthorhombic Nb_2O_5. The material exhibited high rate pseudocapacitive Li^+ storage performance with high cycling stability. However, there is no experimental description of the TT-modification performance.

Li et al. produced self-assembled Nb_2O_5 nanosheets for high energy sodium-ion capacitors, showing that the use of niobium pentoxide as an anode material delivers an exceptionally high-energy density and high-power density, with long and stable life after cycles [31]. They produced TT and T-phases with preferential orientation along the [001] direction, showing the crystal orientation's importance. Another feature of Nb_2O_5 materials is the good redox potential of the Nb^{5+}/Nb^{4+} pair, which occurs during the charge and discharge process in Li-ion batteries.

In 2017, Chen et al. won the Charles Hatchett award for being the first to propose and describe a mechanism for the fast energy storage of T-Nb_2O_5 [32]. They

approached the problem employing experimental and computational methods, using in-situ Raman spectroscopy during the insertion and discharge of Li ions. They proposed that the structure plays a crucial role in the process. The spaced unit cell between two atomic layers works as a channel to accommodate the Li-ions inside the structure. Figure 2.8 shows the proposed mechanism, in which the Li-ions enter along the b-axis between two atomic lines in a tunnel-like structure with a height of approximately 4 Å. The oxygen between sites helps stabilize the Li-ion and promotes a clear path through the crystal structure, where there is a favored transport along the [010] direction. However, as a criticism of their findings, as shown in Figure 1.14 of Chapter 1, the discussion around a spaced and open unit cell is on the TT-Nb_2O_5 structure, not the T-modification, leading to believe that they used a mixed phase material to perform the tests.

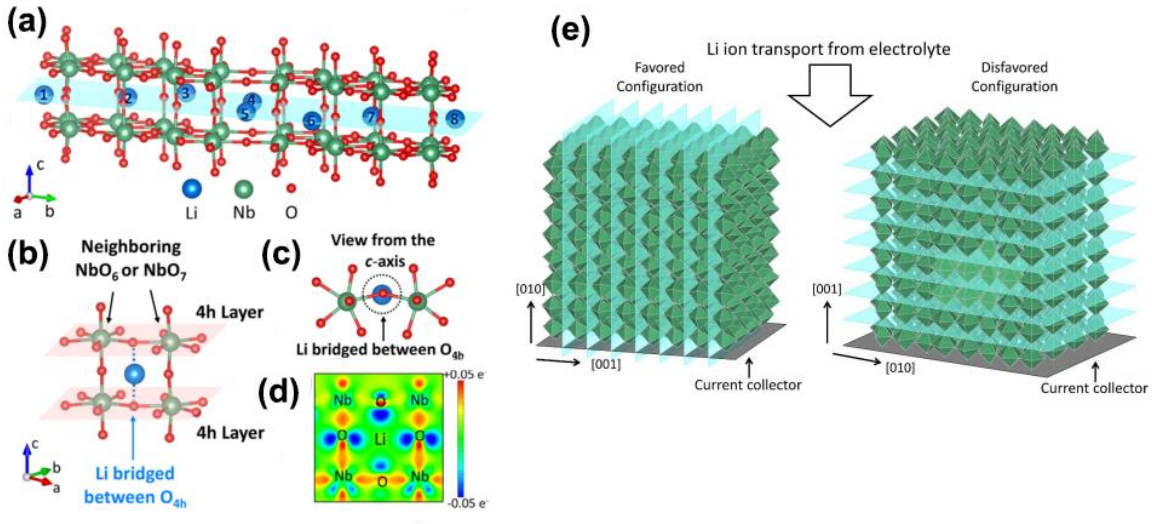

Figure 2.8. (a) The crystal structure of lithiated Nb_2O_5. (b) The local bonding structure of an incorporated Li-ion. (c) Local bonding structure view along the c-axis, and the (d) distribution of charge difference of neighboring Nb and O due to Li-ion coordination. (e) Schematic representation of favored configuration for Li-ion transport – Adapted from [32]

The proposed mechanism by Chen et al. raised the publications about obtainment of the TT and T- phases, along with an extensive study of their photochemical properties relating to their crystal structure. Another important finding was the favored configuration for Li-ion transportation, where the goal of several scientific groups was to obtain the Nb_2O_5 with the proper crystallographic orientation, phase, and stoichiometry. Liao et al. demonstrated how simple changes in the synthetic

route could affect the materials' size, shape, crystalline phase, and electrochemical efficiency. They obtained TT- and T-Nb_2O_5 nanoparticles, and TT-Nb_2O_5 nanosheets, where the nanosheets showed a capacity five times higher than the simple nanoparticles [33]. Deng et al. reported the synthesis of Nb_2O_5 nanorods and their use in flexible organic hybrid supercapacitors on carbon cloth by hydrothermal process. The T-Nb_2O_5 electrode exhibited outstanding rate capability and pseudocapacitive behavior for Li-ion intercalation. The excellent performance is due to the preferential orientation and to present a short-range ion diffusion pathway, demonstrating high gravimetric and volumetric energy/power densities and good flexibility [34].

Despite the excellent performance of niobium pentoxide in energy storage applications, some challenges are still unraveling. While the TT- and T-Nb_2O_5 are some of the most promising materials for energy storage with rapid Li-ion intercalation, there are still challenges to achieving high-rate charge transfer when applied on thick electrodes. Zhang et al. report a facile method to create intrinsic defects in the niobium pentoxide crystalline system, which effectively overcome the material limitations [35]. They performed a reduction pre-treatment using molecular hydrogen (H_2) to introduce oxygen vacancies in the structure. The obtained materials showed improved electrochemical properties, presenting paramagnetic behavior due to oxygen vacancies and a color change. The introduction of oxygen vacancies enhanced the specific capacity of the materials due to an increased donor density and conductivity, promoting improved charge transfer kinetics.

The studies about the electronic properties of the niobium pentoxide include applications regarding photoactivation of the material. So, in the past few years, some effort has been dedicated to understanding and producing niobium pentoxide for photochemical processes. Since the discoveries of the remarkable properties of the Nb_2O_5 photocatalytic behavior, the studies addressed the attention to obtaining the material controlling the oxygen vacancies and the Nb^{5+}/Nb^{4+} ratio. Shishido et al. [36] reported that the Nb_2O_5 shows remarkable properties on the photooxidation of alcohols at mild temperatures, showing high selectivity and conversion. They argued that

niobium pentoxide has a different mechanism of photooxidation in comparison with other metal oxides, where Fig 2.9 represents the proposed mechanism.

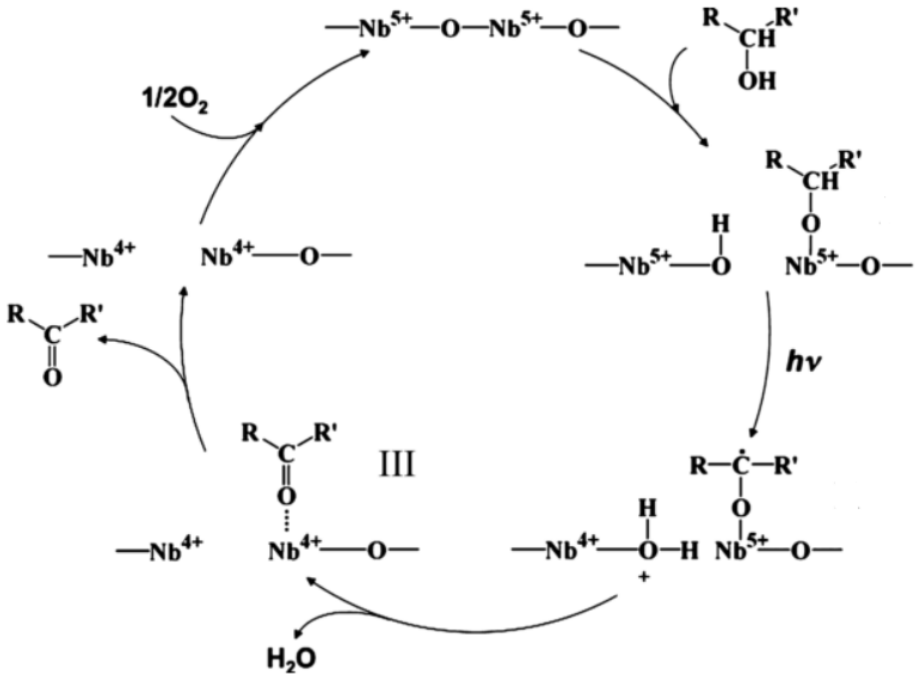

Figure 2. 9. Mechanism of alcohol photooxidation over Nb_2O_5 photocatalyst - Adapted from [36].

They could conclude that niobium pentoxide has outstanding properties due to oxygen vacancies and the possibility of using the Nb^{5+}/Nb^{4+} redox pair to oxidize the alcohol, creating a unique chemical environment for the obtainment of target molecules. Molinari et al. examined the effect of the electron's photo accumulation on TiO_2, showing that intra-bandgap states mediate photoconversion and selectivity for molecule transformations. It sets the importance of controlling the defects in the metal oxides, extending to the use of Nb_2O_5 [37].

Those properties combined could enhance the niobium pentoxide performance, which has driven studies in the past few years. For example, Chen et al. synthesized niobium pentoxide nanospheres that crystallized at the TT-, and T-modifications and tested the material for the photodegradation of Rhodamine B, showing a high degradation ratio under visible light for TT- and T- phases, presenting the mechanism in which the niobium pentoxide receives an electron from the dye valence band, producing superoxide radicals [38]. Zhou et al. synthesized pure H-Nb_2O_5 nanorods employing the hydrothermal method. The materials presented an H_2

evolution rate 151 times higher than the commercial Nb_2O_5 powder, which justifies the improved spatial separation of the photogenerated charge carriers, which correlates to oxygen vacancies in the structure [39].

Kumari et al. discussed the dependence of the crystal structure and the photoactivity of niobium pentoxide. They synthesized several samples, obtaining the TT-, T-, H- and a mixture of the phases. The materials showed a small specific surface area and enlarged crystallite size. However, all samples presented good photodegradation of methylene blue under UV light regarding oxygen vacancies in the structure. The oxygen vacancies can trap the generated electrons, hindering the electron/hole recombination. This phenomenon creates an electron accumulation on the valence band, and the holes on the conduction band interact with H_2O molecules or the OH^- group to form hydroxyl radicals. Based on the results, they inferred that oxygen vacancy plays a dominant role in enhancing the niobium pentoxide photoactivity, and the increase in crystallite size does not harm the activity of the material [14].

Yun et al. synthesized TT-Nb_2O_5, monoclinic NbO_2, and a mixture of them. The materials exhibited excellent photocatalytic activity and performance in dye-sensitized solar cells. The theoretical part of the research proved that the activity significantly influences the intrinsic electronic structure of the Nb_2O_5, where the unpaired electron of Nb^{4+} enhances the interaction and promotes efficient electron transfer from the monoclinic NbO_2 to the electrolyte [40]. Ücker et al. show the influence of niobium pentoxide crystal structure on photocatalytic efficiency in the Rhodamine B degradation. They performed the photocatalytic essay showing 100%, 96%, and 57% Rhodamine B degradation for the amorphous, TT-, and T-Nb_2O_5 phases. They stated that materials owing a higher degree of the long-range disorder in the crystal structure perform better, suggesting that an appropriate synthetic method could improve the niobium pentoxide performance [41].

In 2021, Su et al. published a comprehensive paper regarding photocatalysts based on Nb_2O_5. They point to the good properties of the niobium pentoxide, as a typically nontoxic metal oxide, eco-friendly, with strong oxidation ability and unique

Lewis (LAS) and Brønsted (BAS) acid sites. They showed the influence of the structure size on photocatalytic behavior (0D, 1D, 2D, or 3D), showing that several applications could rely on the obtainment of nanorods, nanospheres, and other structures. The use of dopant and heterostructures with Nb_2O_5 can improve its photocatalytic behavior. Several applications benefit from its behavior, such as photodegradation of pollutants, the evolution of H_2 and O_2, photoreduction of CO_2, and the selective transformation and oxidation of organic molecules. They presented an extensive discussion about the electronic properties and how the crystalline phase, unsaturated niobium sites, oxygen vacancies, and surface acidity influence its activity. They concluded that understanding the niobium pentoxide photocatalyst greatly relies on studies about its local structure. The niobium pentoxide is a strong candidate for converting waste plastics and biomass into organic molecules with great importance due to the suitable photoredox potential under light irradiation. However, they stated that there are still challenges and issues still a concern. The roles of NbO_4 and NbO_6 polyhedrons in the structure, controlling the obtainment of crystal phases and defects (such as oxygen vacancy) and understanding the process on the photocatalyst active sites [42].

The use of niobium pentoxide does not limit to photocatalysis. There is a constant growth of the subject and a new class of applications, such as memristors [43]. The application and development of these devices showed to be outstanding employing NbO_2 and Nb_2O_5, where one of the most different applications of niobium pentoxide, which could be the best description for "state of the art" is the production of artificial neurons based on Nb_2O_5 threshold switching memristor [44].

The niobium pentoxide clearly shown to be a promising material for next-generation applications in science and technology. To summarize, and quoting Nico et al. [10], "...future studies on niobium oxides focused in understanding and controlling the phase transformations, oxidations and oxygen vacancies are crucial to take advantage of the broad range of properties. Not only fundamental characterization is necessary, but also the synthesis and fabrication of micro and nanostructure are worth to be further explored.", we can have a glimpse of the nearby future of the niobium pentoxide as an emergent material.

References

[1] V. Volterra, Leçon sur la Theorie Mathematique de la Lute pour la Vie, Paris, Gauthier – Vilars (1931).
[2] A.J. Lotka, ELEMENTS OF PHYSICAL BIOLOGY, Science Progress in the Twentieth Century (1919-1933) 21(82) (1926) 341-343.
[3] C. Marchetti, Rinaldi, C., and Schneiders, A.,, Gas: The Great Energy Asset,, Scientific and Technical Review of the European Communities, Euro Spectra , XII (4):107--130. (1973).
[4] J.C. Fisher, and Pry, R. H., A Simple Substitution Model of Technological Change, Technological Forecasting and Social Change 3(1) (1971) 75-88.
[5] R.G.e.C.F.A. José Israel Vargas, ACOMPANHAMENTO DA EVOLUÇÃO DO DESFLORESTAMENTO DA AMAZÔNIA USANDO MODELAGEM MATEMÁTICA SIMPLES, Economia e Energia – Economy and Energy 95 (2017).
[6] C.F.A. José Israel Vargas, Omar Campos Ferreira, Pedro Maciel Corgozinho, Tratamento Logístico das Ocorrências Anuais de Dengue no Rio de Janeiro (1985 - 2008), Economia & Energia 71 (2008).
[7] J.I. Vargas, A PROSPECTIVA TECNOLÓGICA: PREVISÃO COM UM SIMPLES MODELO MATEMÁTICO, Economia & Energia 45 (2004).
[8] W.S. Chung, C.Y. Park, FORECASTING THE NUMBER OF PUBLICATIONS OF PAPERS ON ENTREPRENEURSHIP IN ACADEMIC JOURNALS, Research In Higher Education Journal 4(1) (2009) 1-12.
[9] G. Brauer, Über die Oxyde des Niobs, Naturwissenschaften 28(2) (1940) 30-30.
[10] C. Nico, T. Monteiro, M.P.F. Graça, Niobium oxides and niobates physical properties: Review and prospects, Progress in Materials Science 80 (2016) 1-37.
[11] K. Tanabe, Application of Niobium Oxides as catalysts, Catalysis Today 8 (1990) 1-11.
[12] J.-M. Jehng, I.E. Wachs, The molecular structures and reactivity of supported niobium oxide catalysts, Catalysis Today 8(1) (1990) 37-55.
[13] S. Yoshida, Y. Nishimura, T. Tanaka, H. Kanai, T. Funabiki, The local structures and photo-catalytic activity of supported niobium oxide catalysts, Catalysis Today 8(1) (1990) 67-75.
[14] N. Kumari, K. Gaurav, S.K. Samdarshi, A.S. Bhattacharyya, S. Paul, B. Rajbongshi, K. Mohanty, Dependence of photoactivity of niobium pentoxide (Nb_2O_5) on crystalline phase and electrokinetic potential of the hydrocolloid, Solar Energy Materials and Solar Cells 208 (2020) 110408.
[15] K. EGUCHI, H. KOGA, Koshi SEKIZAWA, K. SASAKI, Nb_2O_5-Based Composite Electrodes for Dye-Sensitized Solar Cells, Journal of the Ceramic Society of Japan 108(1264) (2000) 1067-1071.
[16] S.G. Chen, S. Chappel, Y. Diamant, A. Zaban, Preparation of Nb_2O_5 Coated TiO_2 Nanoporous Electrodes and Their Application in Dye-Sensitized Solar Cells, Chemistry of Materials 13(12) (2001) 4629-4634.
[17] F. Lantelme, H. Groult, N. Kumagai, Study of the concentration-dependent diffusion in lithium batteries, Electrochimica Acta 45(19) (2000) 3171-3180.

[18] K. Hashimoto, H. Irie, A. Fujishima, TiO_2 Photocatalysis: A historical overview and future prospects, Japanese Journal of Applied Physics 44(12) (2005) 8269-8285.
[19] A.R. Alves, A.d.R. Coutinho, The Evolution of the Niobium Production in Brazil, Materials Research 18(1) (2015) 106-112.
[20] H. Cui, G. Zhu, Y. Xie, W. Zhao, C. Yang, T. Lin, H. Gu, F. Huang, Black nanostructured Nb2O5 with improved solar absorption and enhanced photoelectrochemical water splitting, Journal of Materials Chemistry A 3(22) (2015) 11830-11837.
[21] L.K.S. Herval, D. von Dreifus, A.C. Rabelo, A.D. Rodrigues, E.C. Pereira, Y.G. Gobato, A.J.A. de Oliveira, M.P.F. de Godoy, The role of defects on the structural and magnetic properties of Nb_2O_5, Journal of Alloys and compounds 653 (2015) 358-362.
[22] L. Kong, C. Zhang, J. Wang, W. Qiao, L. Ling, D. Long, Free-Standing T-Nb2O5/Graphene Composite Papers with Ultrahigh Gravimetric/Volumetric Capacitance for Li-Ion Intercalation Pseudocapacitor, ACS Nano 9(11) (2015) 11200-11208.
[23] L. Kong, C. Zhang, S. Zhang, J. Wang, R. Cai, C. Lv, W. Qiao, L. Ling, D. Long, High-power and high-energy asymmetric supercapacitors based on Li+-intercalation into a T-Nb_2O_5/graphene pseudocapacitive electrode, Journal of Materials Chemistry A 2(42) (2014) 17962-17970.
[24] M. Qamar, M. Abdalwadoud, M.I. Ahmed, A.M. Azad, B. Merzougui, S. Bukola, Z.H. Yamani, M.N. Siddiqui, Single-Pot Synthesis of ⟨001⟩-Faceted N-Doped Nb_2O_5/Reduced Graphene Oxide Nanocomposite for Efficient Photoelectrochemical Water Splitting, ACS Applied Materials & Interfaces 7(32) (2015) 17954-17962.
[25] H. Liu, N. Gao, M. Liao, X. Fang, Hexagonal-like Nb_2O_5 Nanoplates-Based Photodetectors and Photocatalyst with High Performances, Scientific Reports 5(1) (2015) 7716.
[26] A.M. Raba, J. Barba-Ortega, M.R. Joya, The effect of the preparation method of Nb_2O_5 oxide influences the performance of the photocatalytic activity, Applied Physics A 119(3) (2015) 923-928.
[27] A.M. Raba, J. Bautista-Ruíz, M.R. Joya, Synthesis and Structural Properties of Niobium Pentoxide Powders: A Comparative Study of the Growth Process, Materials Research 19(6) (2016) 1381-1387.
[28] A.M. Raba, J. Bautista, E. Murillo, Synthesis and characterization of the oxide nanoparticles obtained by the polymeric precursor method, Journal of Physics: Conference Series 687 (2016) 012084.
[29] L. Yan, X. Rui, G. Chen, W. Xu, G. Zou, H. Luo, Recent advances in nanostructured Nb-based oxides for electrochemical energy storage, Nanoscale 8(16) (2016) 8443-8465.
[30] X. Wang, C. Yan, J. Yan, A. Sumboja, P.S. Lee, Orthorhombic niobium oxide nanowires for next generation hybrid supercapacitor device, Nano Energy 11 (2015) 765-772.
[31] H. Li, Y. Zhu, S. Dong, L. Shen, Z. Chen, X. Zhang, G. Yu, Self-Assembled Nb_2O_5 Nanosheets for High Energy–High Power Sodium Ion Capacitors, Chemistry of Materials 28(16) (2016) 5753-5760.

[32] D. Chen, J.H. Wang, T.F. Chou, B. Zhao, M.A. El-Sayed, M. Liu, Unraveling the Nature of Anomalously Fast Energy Storage in T-Nb_2O_5, J Am Chem Soc 139(20) (2017) 7071-7081.
[33] J. Liao, R. Tan, Z. Kuang, C. Cui, Z. Wei, X. Deng, Z. Yan, Y. Feng, F. Li, C. Wang, J. Ma, Controlling the morphology, size and phase of Nb_2O_5 crystals for high electrochemical performance, Chinese Chemical Letters 29(12) (2018) 1785-1790.
[34] B. Deng, T. Lei, W. Zhu, L. Xiao, J. Liu, In-Plane Assembled Orthorhombic Nb_2O_5 Nanorod Films with High-Rate Li+ Intercalation for High-Performance Flexible Li-Ion Capacitors, Advanced Functional Materials 28(1) (2018) 1704330.
[35] S. Zhang, G. Liu, W. Qiao, J. Wang, L. Ling, Oxygen vacancies enhance the lithium ion intercalation pseudocapacitive properties of orthorhombic niobium pentoxide, J Colloid Interface Sci 562 (2020) 193-203.
[36] T. Shishido, T. Miyatake, K. Teramura, Y. Hitomi, H. Yamashita, T. Tanaka, Mechanism of Photooxidation of Alcohol over Nb_2O_5, The Journal of Physical Chemistry C 113(43) (2009) 18713-18718.
[37] A. Molinari, A. Maldotti, R. Amadelli, Probing the role of surface energetics of electrons and their accumulation in photoreduction processes on TiO_2, Chemistry - A European Journal 20(25) (2014) 7759-7765.
[38] J. Chen, H. Wang, G. Huang, Z. Zhang, L. Han, W. Song, M. Li, Y. Zhang, Facile synthesis of urchin-like hierarchical Nb_2O_5 nanospheres with enhanced visible light photocatalytic activity, Journal of Alloys and compounds 728 (2017) 19-28.
[39] C. Zhou, R. Shi, G. Yang, X. Meng, L.Z. Wu, C.H. Tung, T. Zhang, Spatial separation of charge carriers in Nb_2O_5 nanorod superstructures for enhanced photocatalytic H2 production activity, Materials Today Chemistry 10 (2018) 259-263.
[40] S. Yun, Y. Si, J. Shi, T. Zhang, Y. Hou, H. Liu, S. Meng, A. Hagfeldt, Electronic Structures and Catalytic Activities of Niobium Oxides as Electrocatalysts in Liquid-Junction Photovoltaic Devices, Solar RRL 4(3) (2020).
[41] C.L. Ücker, F.C. Riemke, N.F. de Andrade Neto, A.d.A.G. Santiago, T.J. Siebeneichler, N.L.V. Carreño, M.L. Moreira, C.W. Raubach, S. Cava, Influence of Nb_2O_5 crystal structure on photocatalytic efficiency, Chemical Physics Letters 764 (2021) 138271.
[42] K. Su, H. Liu, Z. Gao, P. Fornasiero, F. Wang, Nb_2O_5-Based Photocatalysts, Advanced Science n/a(n/a) (2021) 2003156.
[43] J. Radhakrishnan, S. Slesazeck, H. Wylezich, T. Mikolajick, A. Ascoli, R. Tetzlaff, A physics-based Spice model for the Nb_2O_5 threshold switching memristor, 15th International Workshop on Cellular Nanoscale Networks and their Applications, CNNA 2016, Desden, Alemanha, 2016.
[44] X. Zhang, W. Wang, Q. Liu, X. Zhao, J. Wei, R. Cao, Z. Yao, X. Zhu, F. Zhang, H. Lv, S. Long, M. Liu, An Artificial Neuron Based on a Threshold Switching Memristor, IEEE Electron Device Letters 39(2) (2018) 308-311.

Chapter 3 – Aims and Objectives

Aim of the Research

This work aims to synthesize Nb_2O_5 nanomaterials, evaluate their crystal structure, the presence defects, and correlate with their electronic properties and employ the materials in the meaningful photocatalytic process.

Specific Objectives

The specific objectives of this work are:

- The production of niobium pentoxide nanoparticles through simple synthetic methods employing the ammonium niobate (V) oxalate hydrate ($NH_4[NbO(H_2O)_2(C_2O_4)_2].xH_2O$) as Nb^{5+} source.
- Obtainment of the TT, T, H, $Nb_{12}O_{29}$ crystalline phases with dislocation defects, and oxygen vacancies.
- Perform an in-depth study of the crystalline behavior of the TT-Nb_2O_5.
- Structural studies of the obtained crystallographic phases employing X-ray diffraction (XRD), Rietveld refinement, Peak distribution function (PDF), and High-resolution transmission electron microscopy (HRTEM).
- Strain studies using geometric phase analysis (GPA) in HRTEM micrographs of TT and T-Nb_2O_5.
- Studies of the electronic properties of niobium pentoxide using X-ray photoelectron spectroscopy (XPS), Electron paramagnetic resonance (EPR), and Diffuse reflectance spectroscopy (DRS).
- Study the correlation between the niobium pentoxide crystallographic phase and the adsorption and photodegradation capability against crystal violet dye.
- Study the influence of defects and oxygen vacancies in niobium pentoxide crystal structure and the selective alcohol photooxidation for solketal production.

Chapter 4 – Synthesis of niobium pentoxide

INTRODUCTION

Synthesis of niobium pentoxide nanoparticles can be challenging since diverse synthetic methods lead to different properties, such as particle size, specific surface area, porosity, crystalline phase, presence of defects, and others [1, 2].

The niobium precursor employed in this thesis is the ammonium niobate (V) oxalate hydrate (NbOX - $NH_4[NbO(H_2O)_2(C_2O_4)_2].xH_2O$), produced by the CBMM in Araxá, and it will be called NbOX for summarizing purposes. The choice for the NbOX is due to the excellent stability, high solubility in water (325 $g.L^{-1}$ at 20 °C), price, and availability, since we could obtain the reagents free of charge from the CBMM. The NbOX also presents crystalline form at standard conditions, which Figure 4.1. shows the molecular structure, the experimental diffractogram for the precursor, and the ICSD #200043 standard.

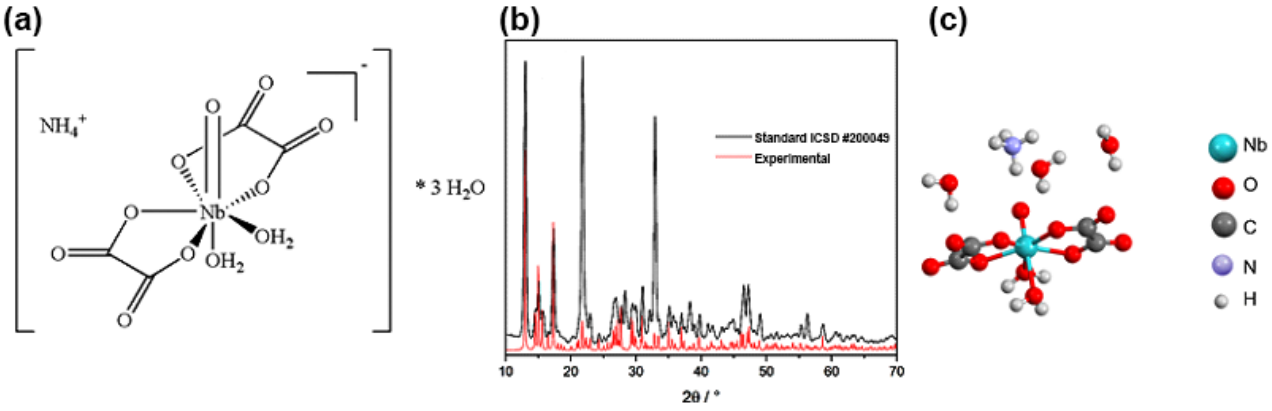

Figure 4. 1. (a) NbOX molecular structure, and its respective (b) XRD experiment and (c) crystal structure.

To fulfill the objectives of the present thesis, we carefully chose the synthetical methods, considering the high water solubility of NbOX, thermal stability, and its chemical properties.

The Pechini method of synthesis contemplates all the desired properties, as it is a water-based synthesis with low cost and the possibility to produce nanomaterials associated with crystalline defects due to present a reductive media, as previously reported [3, 4]. The Pechini method employed in the thesis assembles past studies retired from published scientific papers. The study by Brayner and Bozon-Verduraz in 2003 settled the capability to produce niobium pentoxide nanoparticles using the NbOX precursor from CBMM. They produced Nb_2O_5 nanoparticles and obtained several polymorphs, like the TT, T, and H modifications. They obtained the nanoparticles with crystalline defects, assessed with HRTEM and EPR, in which samples produced in reductive media presented singly ionized oxygen vacancies (SETOVs) [4].

A series of works published by Raba et al. presented the synthesis of Nb_2O_5 through the sol-gel and Pechini methods, employing niobium (V) chloride ($NbCl_5$) and ethoxide ($Nb(OC_2H_5)_5$). They found that TT and T-Nb_2O_5 are the best crystalline phases for pollutant photodegradation, and they obtained them through both synthetic methods [5]. They performed diffuse reflectance spectroscopy (DRS) measurements of the samples and found that samples synthesized using Pechini absorb light in the visible region, indicating the presence of structural defects. However, the sol-gel samples did not exhibit the same behavior, absorbing only at the UV region [2, 6]. Recent works reported the synthesis of niobium pentoxide using the NbOX as a niobium source, arguing about the good electronic properties of Nb_2O_5 nanoparticles for solar cell applications and the consequences of the synthetical method [7, 8]. Those conclusions of the Nb_2O_5 synthesis accounted for the choice of the Pechini synthesis in the present thesis.

Another synthesis of Nb_2O_5 nanomaterial employed in this thesis is the simple precursor burnt of the NbOX at several temperatures. Figure 4.2. shows the thermogravimetric analysis of the NbOX, as reported in our previously published work [9]. There is a consistent mass loss (around 70%) associated with exothermic events at the range of 50-300 °C, which are attributed to the loss of hydration water at 190 °C (.nH_2O), the release of ammonia (NH_3), and carbon dioxide (CO_2) release through oxalate decomposition at 300 °C. An endothermic event at 500 °C corresponds to the

transition between amorphous→TT-Nb_2O_5, which converts to T-Nb_2O_5 at 600 °C, with a slight mass loss. Those events relate to the crystalline transition and late CO_2 desorption from the Nb_2O_5 lattice, confirmed by Su et al. [10]. The slight changes in the mass around 700-900 °C occur due to oxygen stoichiometry changes during crystalline transitions of niobium pentoxide.

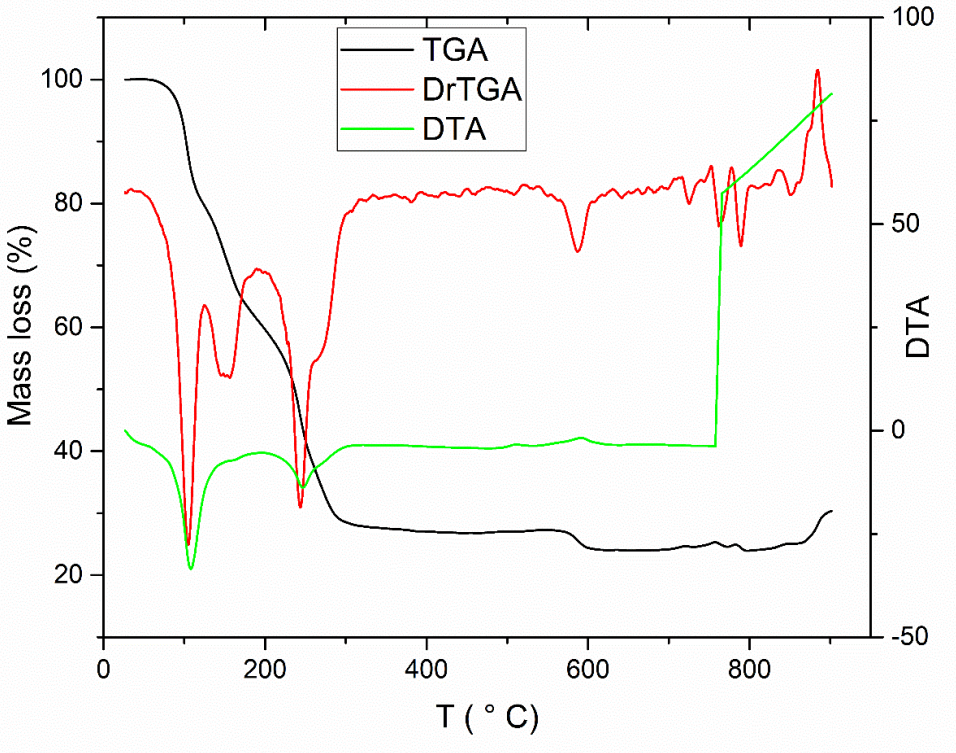

Figure 4. 2. Thermal analysis of the NbOX precursor.

Under the presented arguments in this chapter's introduction, the calcination temperature of the materials sets to 500, 700, and 900 °C. The present temperature choice is due to the phase transitions that occur around those temperatures to obtain the most specific number of crystalline phases to perform the present study.

1. Synthetical procedures of Nb_2O_5 nanoparticles

1.1. Pechini synthesis

The Pechini method takes the name of its creator, Maggio P. Pechini, where he developed the methodology in 1963 and patented the synthetical route in 1967 on the synthesis of niobates [11]. The method occurs in three steps, represented in Figure 4.3.

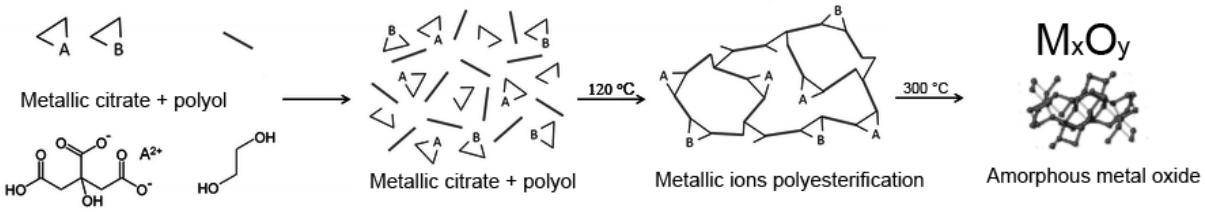

Figure 4. 3. Pechini synthesis scheme

The first step involves mixing the citric acid (CA) at low pH with the metallic salt to form a metallic citrate complex. Then, the polyol, commonly the ethyleneglycol (EG), is mixed in the solution, and the temperature is raised to 120 °C to form the polymeric network with trapped metallic cations. After the reaction, the final Pechini resin is burnt in an oven at 300 °C to eliminate all the organic content and obtain the desired amorphous metal oxide structure.

The employed Pechini method presents the proportion of 1:3:3 of Nb^{5+}:CitricAcid:Polyol, similar to some reported works previously presented in the thesis, changing the polyol and niobium source. First, the ammonium niobium oxalate was dissolved in water at pH = 4, controlled by adding HNO_3 and kept at constant stirring for 30 minutes to ensure the complete solubilization of Nb^{5+} cations in the aqueous solution. Then the citric acid (CA) was added to form the metallic citrate, and the temperature was raised and kept at 60 °C for one hour for complete complexation of the CA and Nb^{5+} cations. The desired polyol, ethyleneglycol (EG) or polyethylene glycol 400 (PEG 400), was added to the solution, the temperature was raised to 100 °C and kept stirring for one hour until the polymerization process is complete. Pechini resins were set in the oven at 300 °C for two hours to remove residual water and organic content and then calcined at 500, 700, and 900 °C for 2 hours. The name of the samples corresponds to a code: XXYYY, where XX corresponds to the employed polyol (EG or PEG) and YYY for the calcination temperature (500, 700, or 900), yielding six samples: EG500, EG700, EG900, PEG500, PEG700, PEG900.

1.2. NbOX burnt

The precursor burnt employed the NbOX, and it is the simple thermal treatment of the ammonium niobate (V) oxalate hydrate at 500, 700, and 900 °C for 2 hours, yielding three samples: NbOX500, NbOX700, and NbOX900.

References

[1] K. Su, H. Liu, Z. Gao, P. Fornasiero, F. Wang, Nb_2O_5-Based Photocatalysts, Advanced Science n/a(n/a) (2021) 2003156.
[2] A.M. Raba, J. Bautista-Ruíz, M.R. Joya, Synthesis and Structural Properties of Niobium Pentoxide Powders: A Comparative Study of the Growth Process, Materials Research 19(6) (2016) 1381-1387.
[3] X. Yu, W. Li, Z. Li, J. Liu, P. Hu, Defect engineered Ta_2O_5 nanorod: One-pot synthesis, visible-light driven hydrogen generation and mechanism, Applied Catalysis B: Environmental 217 (2017) 48-56.
[4] R. Brayner, F. Bozon-Verduraz, Niobium pentoxide prepared by soft chemical routes: morphology, structure, defects and quantum size effect, Physical Chemistry Chemical Physics 5(7) (2003) 1457-1466.
[5] A.M. Raba, J. Barba-Ortega, M.R. Joya, The effect of the preparation method of Nb_2O_5 oxide influences the performance of the photocatalytic activity, Applied Physics A 119(3) (2015) 923-928.
[6] A.M. Raba, J. Bautista, E. Murillo, Synthesis and characterization of the oxide nanoparticles obtained by the polymeric precursor method, Journal of Physics: Conference Series 687 (2016) 012084.
[7] G. Taques Tractz, F. Staciaki da Luz, S. Regina Masetto Antunes, E. do Prado Banczek, M. Taras da Cunha, P. Rogério Pinto Rodrigues, Nb_2O_5 synthesis and characterization by Pechini method to the application as electron transport material in a solar device, Solar Energy 216 (2021) 1-6.
[8] T.L. Valerio, G. Tractz, G.A. Rodrigues Maia, E.d.P. Banczek, P.R. Pinto Rodrigues, Minimizing of charge recombination by Nb_2O_5 addition in dye-sensitized solar cells, Optical Materials 109 (2020) 110310.
[9] L.F.d.S. Lima, C.R. Coelho, G.H.M. Gomes, N.D.S. Mohallem, Nb_2O_5/SiO_2 mesoporous monoliths synthetized by sol–gel process using ammonium niobate oxalate hydrate as porogenic agent, Journal of Sol-Gel Science and Technology 93(1) (2019) 168-174.
[10] T.T. Su, Y.C. Zhai, H. Jiang, H. Gong, Studies on the thermal decomposition kinetics and mechanism of ammonium niobium oxalate, Journal of Thermal Analysis and Calorimetry 98(2) (2009) 449.
[11] M.P. Pechini, Method of preparing lead and alkaline earth titanates and niobates and coating method using the same to form a capacitor, in: U. Patent (Ed.) Estados Unidos, 1967.

Chapter 5 – Niobium pentoxide structure and morphology

INTRODUCTION

The present chapter is going to elucidate the niobium pentoxide crystalline phase transitions. X-ray diffraction (XRD) with Rietveld refinement proved to be a robust tool to obtain reliable data about the crystal structure of the materials, allied with High-Resolution Transmission Electron Microscopy (HRTEM) and the use of mathematical computational software. Possessing this systematic data, we could elaborate on the very complex niobium-oxygen system of the niobium pentoxide and move further in this subject.

1. Methodology

1.1. X-ray diffraction (XRD) and Rietveld refinement

The XRD analysis was performed using a SHIMADZU XRD-7000 of the Chemistry Department at UFMG, with Cu tube (Kα = 1.5406 Å), 30.0 kV of voltage, and 30.0 mA current. Divergence and scatter slit of 1.000 degrees and receiving slit of 0.15000 mm. Scanning procedure in a Theta-2Theta configuration, with a step size of 0.02°, collection time of 2s and 2ϑ range of 15.00° – 80.00°.

The Rietveld refinement process of TT-Nb_2O_5 is in subsection 5.3. Unraveling the TT-Nb2O5 crystal structure, along with the crystal data, data collection, and structure refinement details. TT-Nb_2O_5 has a similar structure to T-Nb_2O_5 in an orthorhombic system; space group Pmba, and a super-lattice structure, with niobium cations set in four atomic positions, with 4h Wyckoff symmetry, fixed z = 0.500 and occupancy of 1.0. The Rietveld method with F_{obs} extraction, general Marquardt dumping of 1.00, and convergence criteria of 0.01. The first refined parameter was the equipment zero and the scale factor. The fitted background is a shifted Chebyshev function of the first kind, with 20 parameters. The profile function is the

EXPGUI/GSAS [1] type 5, a variation of a pseudo-Voigt function, with a good description of reflection asymmetry, strain effects, and a peak shape function. For example, all the refined parameters were kept with physical meaning (GV <0 and GW > 0). Spherical Harmonic (ODF) Preferential orientation was refined. After those procedures, the unit cell was refined—the lattice parameters, the atomic coordinates, and a five-damping coefficient. The U_{iso} parameter was refined for all atoms separated, respecting values > 0 (constrain included), and the total occupancy was settled at 1.0 for all atoms in the unit cell. All the crystal structures visualization and images were drawn using the VESTA free software [2].

The refinement of the other Nb_2O_5 samples used the same method employed for the TT-Nb_2O_5 refinement, using the specific standard crystallographic information file (CIF) for each crystalline phase.

1.2. Pair Distribution Function (PDF)

The atomic pair distribution function (PDF) analysis was performed using the collected XRD data. The analysis consists of a statistical chance of finding an atom at a certain distance (r), where the first intensity peaks correspond to the shorter interatomic bonding distance in the crystal. The atomic PDF can be obtained experimentally by a simple setup and through a powder diffraction experiment. The software employed for XRD PDF analysis was a Python-based library called Diffpy.PdfgetX, which converts X-ray diffraction data into atomic PDF readable data [3]. The software PDFgui was employed as a graphical interface for PDF analysis, data plot, and fitting, suitable for nanoparticles analysis [4]. The G(r) x r plot used the calculation for Cu X-ray source (λ = 1.5406 Å), rpoly = 1.3236, qmaxinst = 4.67855, qmin = 0, qmax = 4.67855, rmin = 0, rmax = 30, and rstep = 0.01. Further information about equations and mathematical steps can be seen in past work by Korsunskiy et al. [5].

1.3. High-resolution Transmission Electron Microscopy (HRTEM) and Geometric Phase Analysis (GPA)

An HRTEM-Tecnai/G2-20-SuperTwin-FEI – 200 kV, located at the UFMG Microscopy Center, LaB_6 filament, Cs = 2mm, point resolution of 0.27 nm, line resolution of 0.144 nm, exposure time of 1s, double tilt holder, coma-free alignment for high-resolution objective lens centering, produced the images and SAED patterns. All qualitative and quantitative image analyses employed Gatan DigitalMicrograph® software, with DiffTools script, containing SAED filtering and calculation analysis [6]. The GPA analysis adopted the FRWRtools plugin (https://www.physics.hu-berlin.de/en/sem/software/software_frwrtools) for DigitalMicrograph®.

The Geometric Phase Analysis (GPA) was described by Hÿtch *et al.* 1988 [7] and worked reconstructing the displacement fields by two selected Fourier spots of the HRTEM micrograph power spectrum. The spots are related to the crystalline planes in the studied material, and they should have two different orientations to measure the displacement of deformed lattice fringes, which uses lattice interference fringes as a reference. The crystallographic plane and its Fourier components, or called geometric phase $P_g(r)$, are related to the displacement field, u(r), in the direction of the reciprocal lattice vector, g, given the following equation:

$$\boldsymbol{P_g(r) = -2\pi g.u(r)} \quad (1)$$

The displacement field of the geometric phases of two diffracted spots in the Fourier component is:

$$\boldsymbol{u(r) = -\frac{1}{2\pi}[P_{g1}(r)a_1 + P_{g2}(r).a_2]} \quad (2)$$

The a_1 and a_2 are the basis vector from the real space lattice, which corresponds to the g_1 and g_2 vector of the reciprocal space lattice, related by $a_i g_j = \delta_{ij}$.

The displacement field mathematically separates into two-dimensional factors, $u_x(g)$ and $u_y(g)$, and the equation (2) in a matrix form is:

$$\begin{pmatrix} u_x \\ u_y \end{pmatrix} = -\frac{1}{2\pi}\begin{pmatrix} a_{1x} & a_{2x} \\ a_{1y} & a_{2y} \end{pmatrix}\begin{pmatrix} P_{g1} \\ P_{g2} \end{pmatrix} \quad (3)$$

The plane strain (ε_{xx} and ε_{yy}) is the ratio of the displacement field in the desired direction:

$$\boldsymbol{\varepsilon_{xx}} = \frac{\partial u_x}{\partial x} \; ; \boldsymbol{\varepsilon_{yy}} = \frac{\partial u_y}{\partial y} \qquad (4)$$

1.4. Gas adsorption analysis

Gas physisorption analyses were performed in a QuantaChrome Autosorb-1 located in our laboratory, with 44 analysis points in the range of 0.05 to 0.99 P/P°, using N_2 as adsorbent and a 6 mm sample cell. The degasification process was carried out at 250 °C until the process was complete, determined by the equipment. The specific surface area (SSA) calculation employed the BET method in the pressure range of 0.05-0.30 P/P°. The adsorbed gas volume at the saturation point of 0.99 P/P° determined the total pore volume, and the Barrett-Joyner-Halenda (BJH) method calculated the pore size distribution, employing the desorption curve, ignoring points below P/P° < 0.35. All calculations and data analysis employed the QuantaChrome Autosorb AS1 software.

2. The Nb_2O_5 phase transformations

2.1. Qualitative analysis

The niobium pentoxide, known as Niobia (Nb_2O_5), presents several crystalline modifications, changing to amorphous-Nb_2O_5 to H-Nb_2O_5 (monoclinic, P 2/m, a = 21.153 Å, b = 3.8233 Å, c = 19.556 Å, β = 119.80°) [8] which is the most thermodynamically stable form under standard conditions [9]. As previously discussed in Chapter 1 the phase transformation path depends on several factors [10],. However, for summarizing purposes, it follows the subsequent path:

$$\text{Amorphous } Nb_2O_5 \xrightarrow[300-500\,°C]{} \text{TT-}Nb_2O_5 \xrightarrow[500-900\,°C]{} \text{T-}Nb_2O_5 \xrightarrow[>800\,°C]{} \text{H-}Nb_2O_5$$

The phase obtainment strongly depends [11] on the presence of impurities and defects [12, 13], particle size [14], and synthesis method [15-17]. The phases also could show non-stoichiometric behavior and crystallization in several structures at temperatures between 600 and 900 °C.

Figures 5.1, 5.2, and 5.3 show the XRD analysis of EG, PEG, and the NbOX niobium pentoxide series, respectively. The samples obtained through the Pechini synthesis crystallized at 500 °C into TT-Nb_2O_5, characterized by broad peaks, no weak reflections, and no peak asymmetry at 29° (2ϑ), as discussed by some previous works [11, 18]. The NbOX500 hardly shows broad peaks, with some intensity around the TT-Nb_2O_5 crystalline planes, indicating the amorphous transition to TT-Nb_2O_5. Since the TT and T-phases present very similar crystal structures [18] (orthorhombic, Pbam, a = 6.175 Å, b = 29.175 Å, c = 3.930 Å) [19], it is hard to determine the transition between TT→T phases, and we probably have a mixture of them. Some authors argued that the phase transformation is characterized by a decomposition of the single peak into two at 59° [11, 20], correlated to crystal symmetry changes between the TT and T phases, which some works argued that the TT phase has niobium atoms in a more symmetric Wyckoff position (4h instead of 8i) in the unit cell [18].

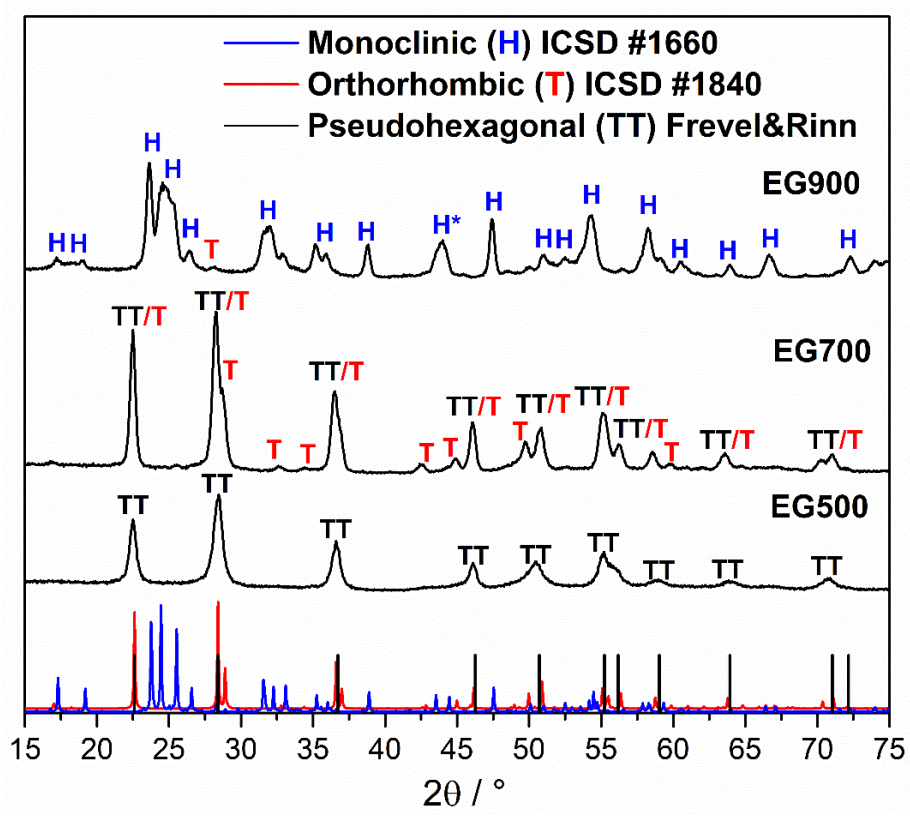

Figure 5. 1. X-ray diffraction of the EG's series of niobium pentoxide nanoparticles.

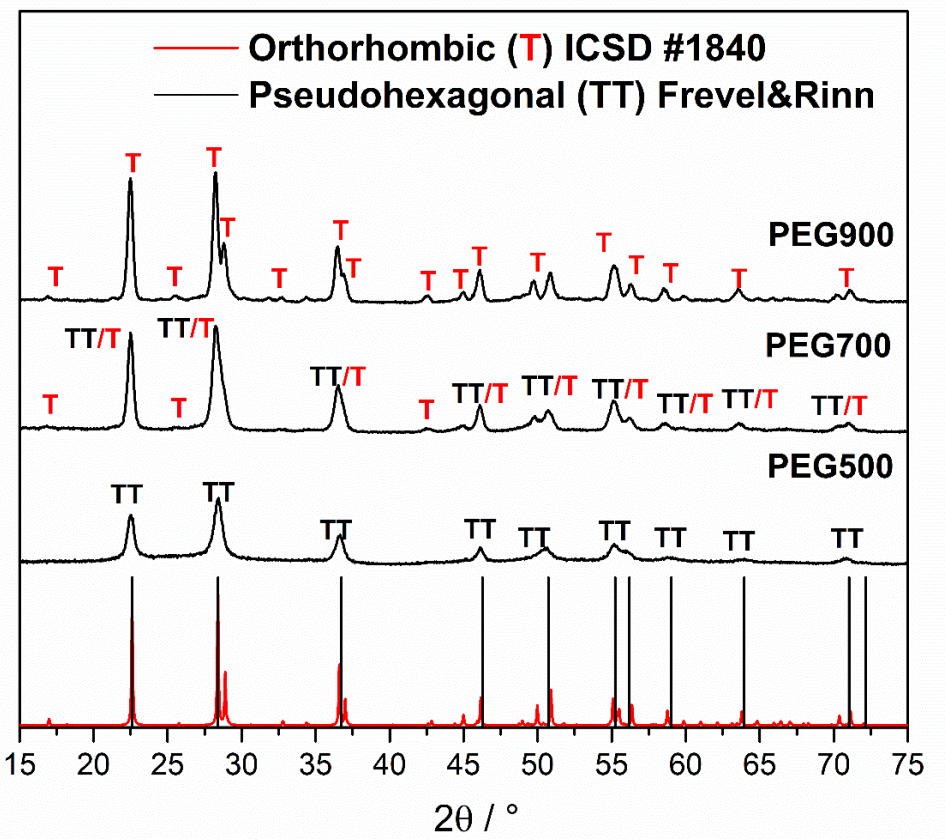

Figure 5. 2. X-ray diffraction of the PEG's series of niobium pentoxide nanoparticles.

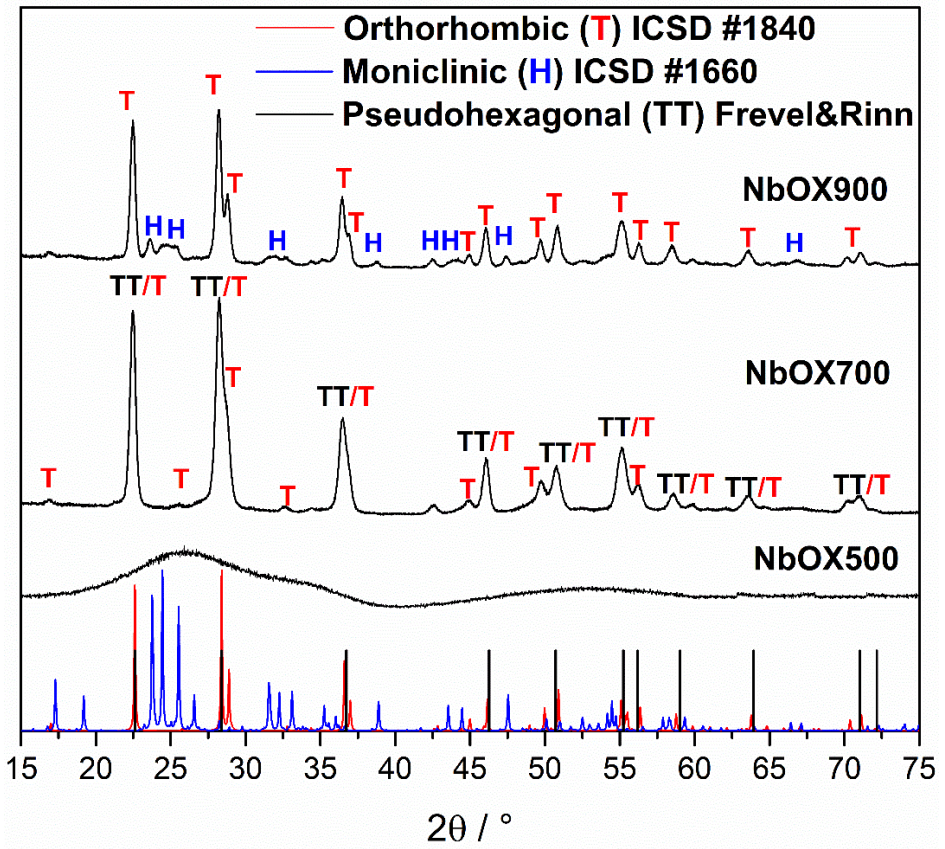

Figure 5. 3. X-ray diffraction of the NbOX's series of niobium pentoxide nanoparticles.

All samples treated at 700 °C (EG700, PEG700, NbOX700) showed the transition to the T-Nb_2O_5, where small intensity reflections appear around 17°, indicating the presence of exclusive (130) crystalline plane from the orthorhombic lattice presented by the T-modification. However, it is worth mentioning that all samples at 700 °C presented a mixture of the TT and T phases, and the materials obtained through Pechini synthesis showed broader peaks, indicating smaller crystallite size and strain effects in the structure.

The samples treated at 900 °C demonstrated distinct behavior. The NbOX900 presented a complete transition between TT→T phases and the formation of the H-phase, presenting a mixture of T and H, with higher content of the orthorhombic phase. The PEG900 sample presented complete crystallization at the T-modification, with no evidence of the H-phase formation.

The EG900 sample presented the transition to the H-Nb_2O_5 and a minimum intensity related to the (180) crystallographic plane correspondent to the T-phase presence. The peak around 44° (2ϑ) has a blue * on it, representing an odd crystalline plane, not expected from the H-phase. Figure 5.4 shows a closer look at the EG900 XRD with the H-Nb_2O_5, $Nb_{12}O_{29}$, and $Nb_{22}O_{59}$ standard diffraction data. To further evaluate the presence of non-stoichiometric phases, we prepared the EG1100 samples by calcinating the EG900 at 1100 °C for two hours for comparison purposes. All H-Nb_2O_5 peaks are present in the diffractogram, with the presence of high-intensity peaks, represented with grey dashed lines, at 32.2°, 44,5°, 47.5°, 54.2°, 58.3°, and 67°, which correlates the $Nb_{12}O_{29}$ phase presence, indicating that the non-stoichiometric phase is an intermediate between the T→H phase transition in the presence of defects and impurities. The increase in the temperature to 1100 °C provoked two peak splitting, around 44°, and 67°, that correlates to low content of the $Nb_{12}O_{29}$ and higher amount of H-Nb_2O_5, showing that at 900 °C, we could stabilize the presence of the non-stoichiometric phase with the H-modification.

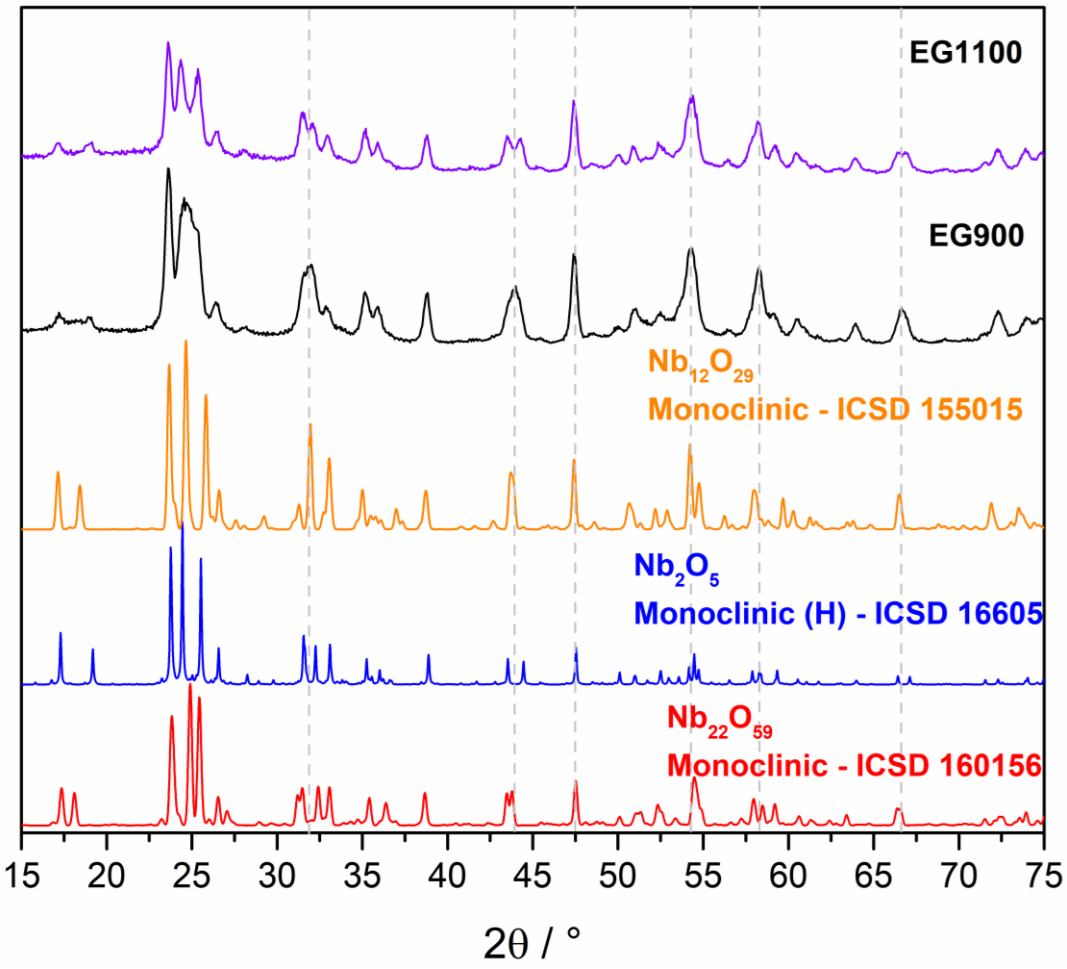

Figure 5. 4. X-ray diffraction of EG900 compared with niobium oxides standard data.

Figure 5.5 (a), (b), (c), and (d) shows the crystal structure of TT-, T-, H-, and $Nb_{12}O_{29}$ modifications, respectively. The TT-phase having more symmetric niobium positions creates a more open and less dense unit cell, consisting of fewer niobium atoms with a higher occupancy in the unit cell, which occurs due to defects and disordered NbO_6 and NbO_7 polyhedral in the structure [18, 21]. The packed unit cell of H-Nb_2O_5 and $Nb_{12}O_{29}$ illustrates the similarity between the two phases, where the H-Nb_2O_5 shows a well-ordered ReO_3-like block structure, with NbO_6 octahedrons sharing edges along the [010] zone axis. The presence of tetrahedral NbO_5 species occurs between octahedron collum to accommodate block-dislocations in the unit cell [22]. However, when higher dislocation effects take place in the unit cell, due to impurities or defects in the structure, the phase segregation of the non-stoichiometry $Nb_{12}O_{29}$ occurs, with more tetrahedral groups to accommodate different oxidation

states along with the crystal structure, creating a $NbO_{2.42}$ formula with a similar monoclinic structure, and a more comprehensive disorder in the unit cell [23].

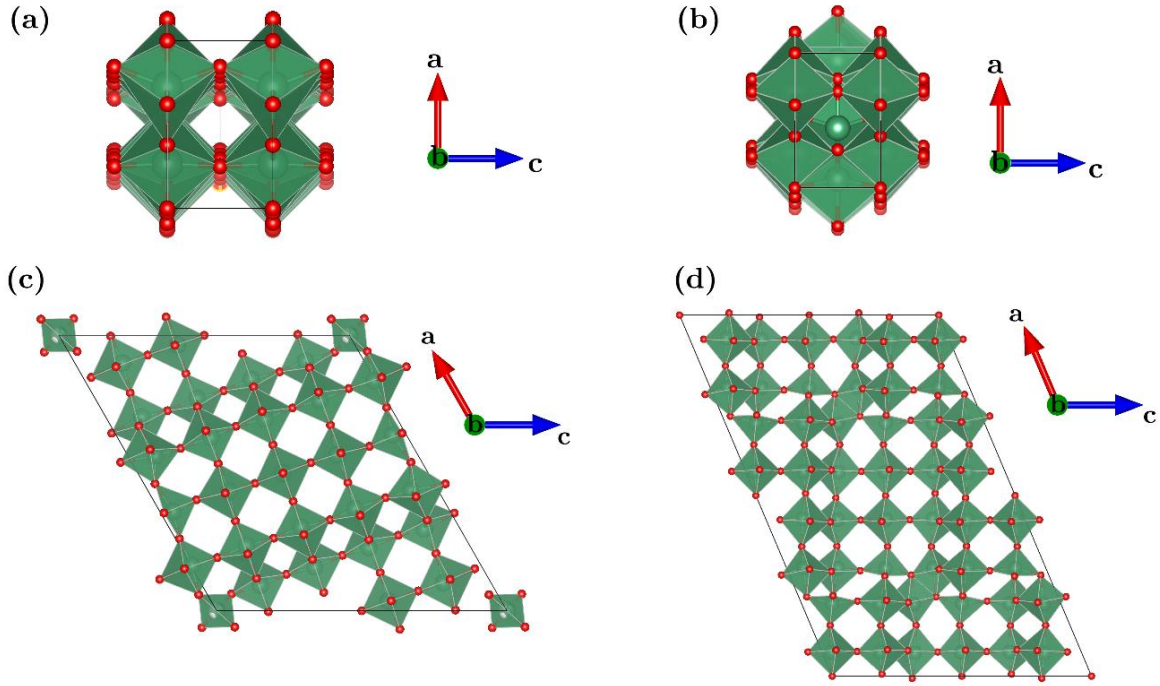

Figure 5. 5. The crystal structure of a packed unit cell representing the (a) TT-, (b) T-, (c) H-, and (d) $Nb_{12}O_{29}$ modifications along the b-axis.

2.2. Crystal structure elucidation

All the samples presented high peak intensity, except for the NbOX500. The samples that showed a reasonable degree of crystallinity could be refined employing the Rietveld method described in the methodology subsection. Table 5.1 shows the statistical data from the Rietveld refinement analysis. All samples presented reliable values, where the reduced chi-square (χ^2) values are lower than five, which indicates a good analysis. Another essential factor for good analysis is observing the difference curve between the experimental and calculated data, as shown in Figure 5.6. All difference curves from the refined samples appear almost flat on their entire domain, indicating good coherence between the crystal structure of the samples and the employed method [24].

Table 5. 1. Statistical data of all refined samples.

Sample	R_p / %	R_{wp} / %	χ^2
EG500	4.61	5.59	2.876
EG700	4.91	6.44	3.250
EG900	5.70	7.32	2.929
PEG500	4.59	5.87	2.417
PEG700	4.97	6.27	3.513
PEG900	5.74	7.05	4.854
NbOX700	4.26	5.18	2.480
NbOX900	5.35	6.80	2.708

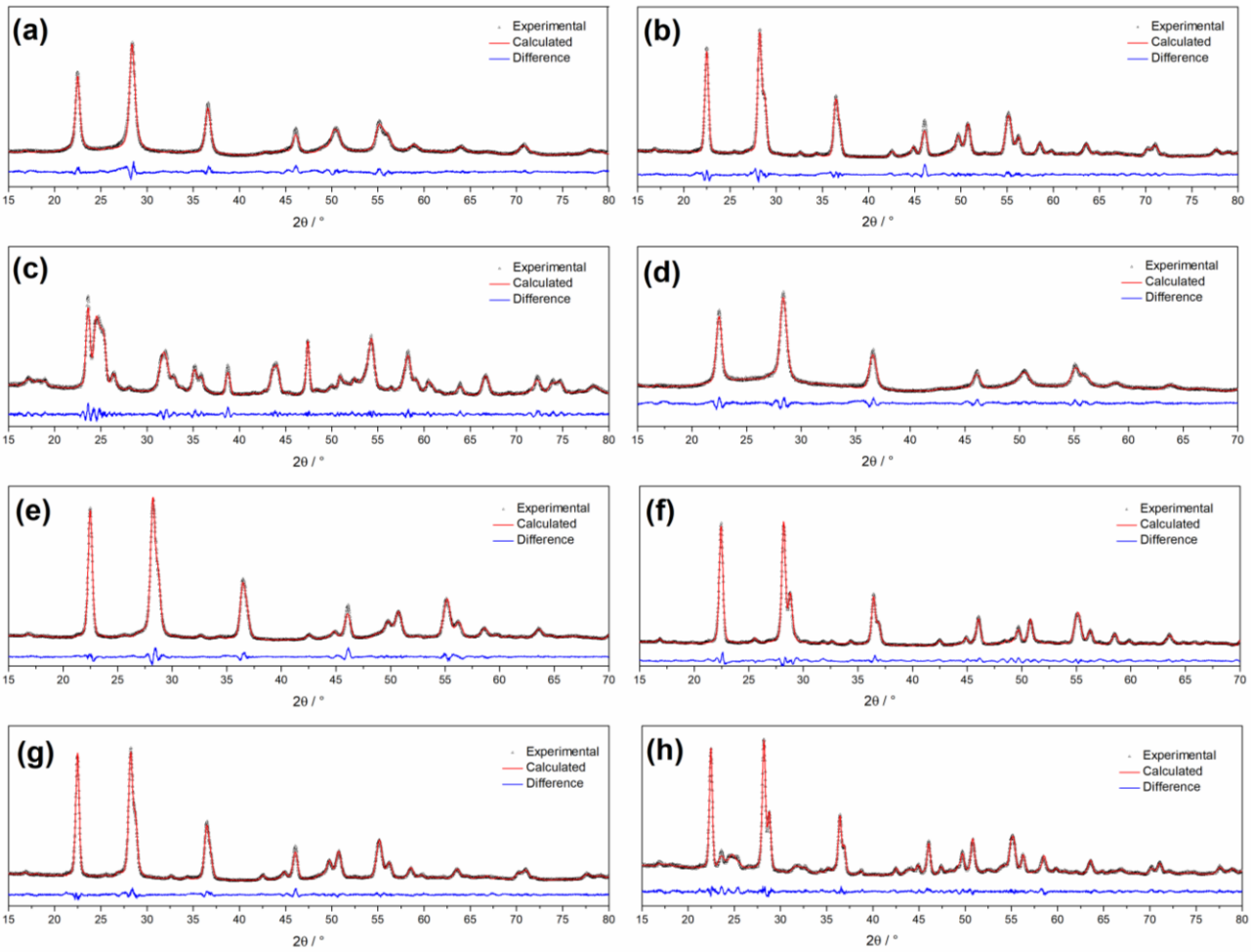

Figure 5.6. Extracted rietveld refinement graphs of the (a) EG500, (b) EG700, (c) EG900, (d) PEG500, (e) PEG700, (f) PEG900, (g) NbOX700, and (h) NbOX900.

Table 5.2. shows the refinement data for the EG samples. The phase transition behavior is explicit, where the EG500 and EG700 crystallized at the TT- and T-phases, respectively, and presented a non-stoichiometric unit cell with an excess of oxygen (Nb_2O_{5+x}). It is also evident that the EG500 has high strain and density dislocation values, indicating defects in the crystal structure. However, the EG700 also showed significant strain and density dislocation values, lower than the EG500. The TT-Nb_2O_5 shows to be more efficient to accommodate defects in the crystal structure, and with the transition to T-phase, the number of defects decreases since there is also an increase in the crystallite size. This behavior accounts for the transition between T $\rightarrow$ H phases with the appearance of the $Nb_{12}O_{29}$ non-stoichiometric phase. Since the H-Nb_2O_5 is the most stable thermodynamic form of niobium pentoxide at high temperatures, it shows a well-organized crystal structure with very few defects, as evidenced by the low strain and density dislocation values of the EG900. However, to compensate for defects in the EG500 and EG700 crystal structure, the EG900 produced two distinct crystalline phases. The EG900 shows the H-Nb_2O_5 and $Nb_{12}O_{29}$, at the proportion of 72% and 28%. The $Nb_{12}O_{29}$ appears due to the number of crystalline defects. For being a non-stoichiometric phase, it can better accommodate the defects in the structure [23].

The changes in the polymeric chain in the Pechini synthesis lead to odd behavior of the samples. The poly(ethylene glycol) 400 has a large and disordered polymeric chain, so its hydroxyls are not as available to carry out the esterification (resin production process) with NbOx than those of ethylene glycol. As a result, the EG500 polymer resin is more viscous and denser, which reduces the permeability of atmospheric O_2 in the system during heating of this sample. This lower amount of molecular oxygen to burn the resin favors its oxidation at the expense of the structural oxygen of Nb_2O_5, yielding a greater amount of defects in EG500 than in PEG500, increasing the strain and density dislocation values.

Table 5.2. also shows the lattice parameters for all EG samples and the standard employed for the Rietveld refinement. For the EG500 sample, the refinement

of the TT-modification will be in subsection three of chapter five. All samples presented slight differences compared with the standard. However, those minor differences account for changes in the bond length, angle, and local geometry, contributing to point and line defects in the structure.

Table 5.2. EG-Nb_2O_5 crystallographic data extracted from the Rietveld refinement procedure.

Sample	Phase	Lattice Parameters / Å	Strain / %	Crystallite Size / nm	Dislocation Density / m^{-2}	Fraction / %
EG500	TT ($Nb_2O_{5.09}$)	a = 6.225(8) b = 29.05(8) c = 3.927(5)	0.370	8	$1.56x10^{16}$	100
EG700	T ($Nb_2O_{5.14}$)	a = 6.165(1) b = 29.15(2) c = 3.917(9)	0.107	33	$9.18x10^{14}$	90
EG900	H (Nb_2O_5)	a = 21.287(2) b = 3.8435(2) c = 19.3994(1) β = 119.85°	0.008	86	$1.35x10^{14}$	72
	$Nb_{12}O_{29}$	a = 31.373(4) b = 3.8297(1) c = 20.703(7) β = 113.77°	0.017	61	$2.69x10^{14}$	28
Standard	T (Orthorombic)	a = 6.175(1) b = 29.175(4) c = 3.930(1)	ICSD #1840			
	H (Monoclinic)	a = 21.153(7) b = 3.8233(5) c = 19.3560(5) β = 119.80°	ICSD #29			
	$Nb_{12}O_{29}$ (Monoclinic)	a = 31.3200 b = 3.8320 c = 20.7200 β = 112.93°	ICSD# 24111			

Table 5.3. shows the refinement data of the PEG samples. The PEG500, similar to the EG500, crystallized in the TT phase and presented the transition to T-phase at 700 °C. However, the PEG900 showed the complete transition to the T-Nb_2O_5, with no evidence of the H-phase. The rise at the temperature treatment caused an increase in the crystallite size and reduced strain and density dislocation values, similar to the EG sample. The odd behavior of the PEG900 sample occurs due to changes in the polymeric chain. The polyethylene glycol 400 presents more oxygen in the structure and a longer organic chain length, which directly affects the crystalline behavior of the samples. Despite the EG and PEG differences, the samples calcined at 500 and 700 °C showed similar behavior and a significant difference in the crystallization path at higher temperatures.

Table 5. 3. PEG-Nb_2O_5 crystallographic data extracted from the Rietveld refinement procedure

Sample	Phase	Lattice Parameters / Å	Strain / %	Crystallite Size / nm	Dislocation Density / m^{-2}	Fraction / %
PEG500	TT ($Nb_2O_{5.12}$)	a = 6.21974(1) b = 28.8530(9) c = 3.91681(3)	0.276	10	$1.00x10^{16}$	89
PEG700	T ($Nb_2O_{5.14}$)	a = 6.12328(0) b = 28.9247(5) c = 3.88858(8)	0.120	48	$4.34x10^{14}$	99
PEG900	T (Nb_2O_5)	a = 6.14995(9) b = 29.1785(2) c = 3.91763(8)	0.068	66	$2.29x10^{14}$	100
Standard	T (Orthorombic)	a = 6.175(1) b = 29.175(4) c = 3.930(1)	ICSD #1840			

Table 5.4. shows the refinement data of the NbOX samples. The NbOX700 showed complete crystallization at the T-Nb_2O_5, presenting low strain and dislocation density values than the Pechini samples (EG and PEG), corroborating that the Pechini method could yield metal oxide with defects [11]. The NbOX900 showed the beginning

of a transition between the T → H modifications, with a phase proportion of 83% and 17%, respectively.

Table 5. 4. NbOX-Nb_2O_5 crystallographic data extracted from the Rietveld refinement procedure.

Sample	Phase	Lattice Parameters / Å	Strain / %	Crystallite Size / nm	Dislocation Density / m^{-2}	Fraction / %
NbOX700	T ($Nb_2O_{5.09}$)	a = 6.16515(3) b = 29.1534(1) c = 3.91799(5)	0.033	38	$2.97x10^{14}$	100
NbOX900	T (Nb_2O_5)	a = 6.16506(3) b = 29.2530(9) c = 3.92810(4)	0.000	52	$3.70x10^{14}$	83
	H (Nb_2O_5)	a = 21.287(2) b = 3.8435(2) c = 19.399(1) β = 119.85°	0.000	47	$4.52x10^{14}$	17
Standard	T (Orthorombic)	a = 6.175(1) b = 29.175(4) c = 3.930(1)	ICSD #1840			
	H (Monoclinic)	a = 21.153(7) b = 3.8233(5) c = 19.356(5) β = 119.80°	ICSD #29			

The NbOX900 also presents zero average strain for both crystalline phases, showing that the precursor burnt technique is an excellent fit to produce pure T-Nb_2O_5 and a mixture of T- and H- phases. However, we could not obtain the TT-modification employing this method, at least not with good crystallinity. This different behavior of the NbOX sample compared with the Pechini samples presents insight into defects in the Nb_2O_5 crystal structure. The materials synthesized employing the Pechini method lead to high strain and dislocation density values and the obtainment of four distinct crystalline phases, the TT, T, H, and $Nb_{12}O_{29}$. All those findings elucidate defects in the crystal structure, which is crucial for the TT-phase obtainment.

The PDF analysis can provide the mean bond length using the XRD experiment. The first peaks with intensity > 0 represent the short-length atomic bonds in the crystal structure. All samples presented similar behavior, except for the NbOX500, as shown in Figure 5.7. The shorter interatomic bonding appears with maximum intensity around 2.10 Å, corresponding to the mean distance of the Nb—O bond in the crystal structure. The average length values for the Nb—O bond vary from 1.95, 2.05, and 2.15 Å, depending on the oxygen position in the crystal structure [19]. The NbOX500 presents a maximum at 1.62 Å, indicating a lower Nb—O bond value due to the sample's low crystallinity and amorphous Nb_2O_5, which presents a smaller interatomic distance. Another important finding is the lack of long-range crystallinity order for the NbOX500. This fact shows that the material has tiny crystalline nanoparticles forming in an amorphous-Nb_2O_5 matrix, an odd behavior compared with the Pechini samples.

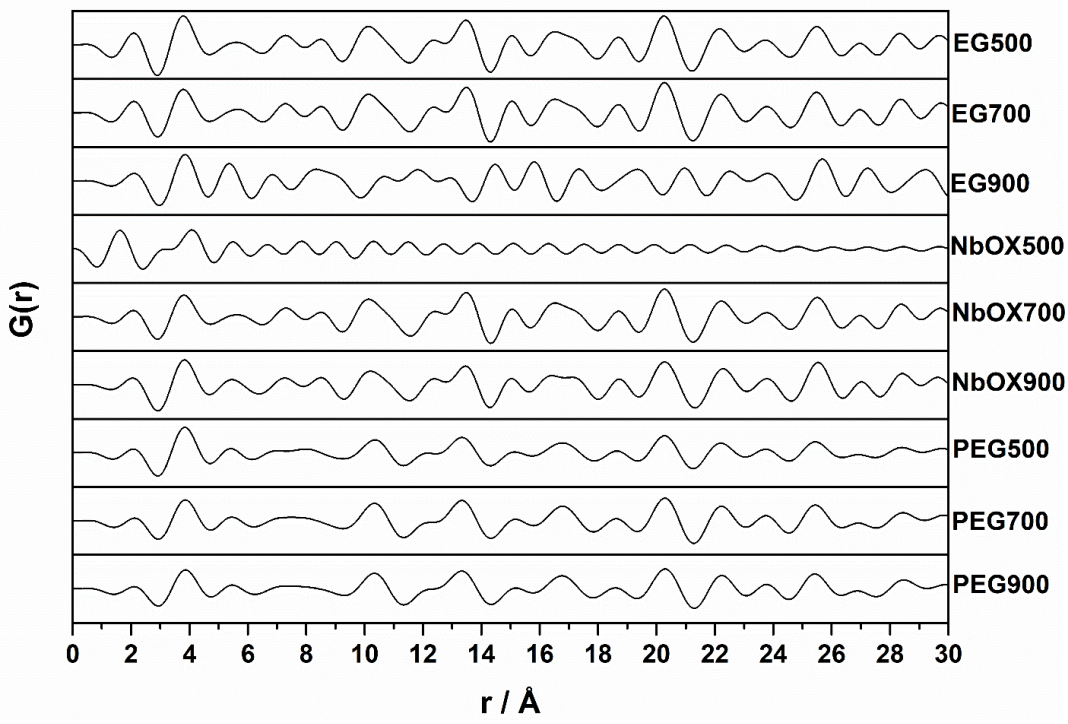

Figure 5. 7. PDF analysis of all obtained niobium pentoxide samples.

The second high-intensity value for the G(r) appears around 3.70 Å, corresponding to the neighbor Nb—Nb atomic interaction, which has an average length of 3.38 Å, 3.62 Å, and 3.72 Å. The third high-intensity value appears around 5.80 Å, corresponding to the long-range bond between Nb———Nb atoms [19].

Different intensities with values higher than 6.00 Å correspond to the crystal structure repetition of the samples and some complex Nb—O—Nb bonds. Despite the similarity between the crystalline samples, the number of local disorders can slightly change the PDF analysis, corresponding to the different bond length, angle, and lattice parameters.

3. Unraveling the TT-Nb_2O_5 crystal structure

As previously discussed, one of the main challenges in the structure elucidation of niobium pentoxide is the presence of TT-modification and the vigorous debate held around it. An initial built CIF employed past findings published in the literature to provide reliable information about its crystal structure. First, we approximate the TT-Nb_2O_5 crystal structure as a superlattice structure analogous to the T-Nb_2O_5. However, several essential constraints should apply, like using the atomic coordinates and Wyckoff positions proposed by Weissman et al. for the TT-modification and the reliable and published T-Nb_2O_5 crystal data (ICSD #1840) from Kato and Tamura. The initial crystallographic information file (CIF) has the exact coordinates for oxygen atoms and the same isotropic displacement (U_{iso}) for all atoms in the T-Nb_2O_5 phase [18, 19].

The TT-Nb_2O_5 from the EG500 sample is suitable for XRD refinement since the sample showed crystallization at the TT-modification, with a good crystallinity degree. Figure 5.8. shows the experimental diffractogram and the extracted Rietveld graph. The lack of sharp peaks, low-intensity reflections, and no peak splitting at 59° corroborates the presence of TT-Nb_2O_5, as previously discussed. The calculated refinement shows good coherence with the experimental data, as the difference curve is almost flat, and all the R (R_p, R_{wp}, and $R_{(F^2)}$) factors and goodness of fit ($\chi 2$) presents low values shown in Table 5.5.

The reduced chemical formula of the TT-Nb_2O_5 is Nb_8O_{21}, like previously proposed by Weissman et al. The TT-phase presents 16 niobium atoms, not 16.4, like the T-modification, proposing a chemical formula of $Nb_{16}O_{42}$ [18]. The statistical parameters of the refinement are R_p = 5.3%, R_{wp} = 6.80%, R_{exp} = 3.80%, $R_{(F^2)}$ = 6.99%, $\chi 2$ = 3.168, S = 1.78, and $(\Delta/\sigma)_{max} < 0.001$, indicating an excellent refinement

process since the values are substantial low considering that the initial built CIF is theoretical.

Table 5. 5. Rietveld refinement data analysis of the TT-Nb_2O_5 sample.

Chemical formula	Nb_8O_{21}
M_r	1079.23
Crystal system, space group	Orthorhombic, *Pbam*
Temperature (K)	298
a, *b*, *c* (Å)	6.2083 (5), 29.004 (3), 3.9227 (2)
V (Å^3)	706.32 (6)
Z	2
Radiation type	Cu $K\alpha_1$, λ = 1.540500 Å
Specimen shape, Size (mm)	Flat sheet, 15 × 15 × 5
Density (g.cm^{-3})	5.074
	Data collection
Diffractometer	Shimadzu XRD-7000
Specimen mounting	Packed powder pellet
Data collection mode	Reflection
Scan method	Continuous
2ϑ values (°)	$2\vartheta_{min}$ = 15.03 $2\vartheta_{max}$ = 80.01 $2\vartheta_{step}$ = 0.02
	Refinement
R factors and goodness of fit	R_p = 0.0530., R_{wp} = 0.068, R_{exp} = 0.038, $R_{(F2)}$ = 0.06985, χ^2 = 3.168
S = 1.78	$(\Delta/\sigma)_{max} < 0.001$
No. of parameters	24

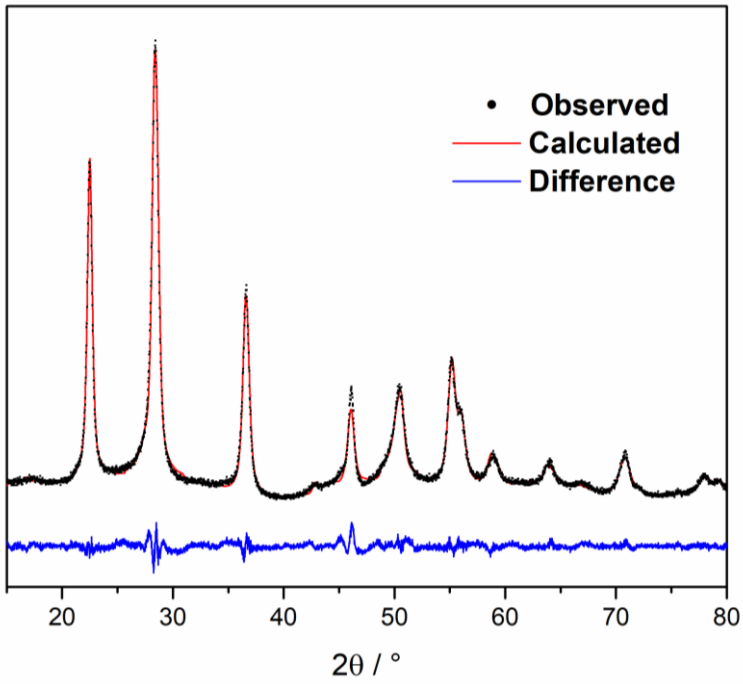

Figure 5. 8. The plot of measured intensity (•) and intensity versus measured 2ϑ (°), with the difference plot below, from the studied EG500 - TT-Nb_2O_5 sample.

Table 5.6. shows the results for the initial four niobium atom positions and the theoretical density compared with the past works employed for the CIF construction.

Table 5. 6. Atomic coordinates of the first four niobium atoms in the orthorhombic lattice.

	T-Nb_2O_5 (Kato and Tamura) [19]			TT-Nb_2O_5 (Weissman et al.) [18]			This work		
Atom	x	y	z	x	y	z	x	y	z
Nb1	0.2807	0.03551	0.5445	0.25	0.03126	0.5	0.27470	0.03695	0.5
Nb2	0.1857	0.15370	0.5477	0.25	0.15626	0.5	0.23382	0.15762	0.5
Nb3	0.2522	0.27586	0.5470	0.25	0.28126	0.5	0.25434	0.27897	0.5
Nb4	0.2376	0.40702	0.5543	0.25	0.40626	0.5	0.23475	0.40643	0.5
Density ($g.cm^{-1}$)	5.236			4.930			5.074 (Calculated)		

It is also worth mentioning the change in the density value for the TT-modification compared with the T-modification. The refinement yields a theoretical density of 5.074 g.cm^{-3}, which is lower than the theoretical density of the T-modification. The density of our obtained TT-modification is closer to the proposed density of Weissman et al., another indicator of the excellent coherence between the theoretical and experimental crystal structure. The obtained atomic positions of the niobium atoms are closer to the findings by Weissman et al., showing that the TT-Nb_2O_5 is a superlattice structure similar to the T-Nb_2O_5.

Figure 5.9. shows an ellipsoid plot of the TT-Nb_2O_5 super-lattice along the a-axis, with a 50% displacement probability. Atomic displacements occur mainly in the oxygen atoms along the a-b and b-c planes due to the disordered subcell structure and changes in bond lengths and angles, creating a disordered linkage between NbO_6 NbO_7 polyhedrons.

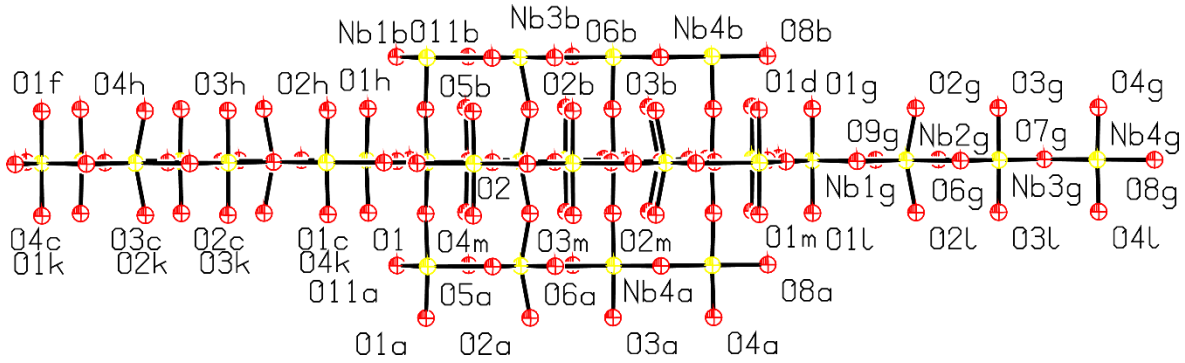

Figure 5. 9. A view of the structure of TT-Nb_2O_5, showing the atom-labeling scheme. Displacement ellipsoids are at the 50% probability level.

Figure 5.10. shows the TT super-lattice structure in several orientations. The results show a different structure than T-Nb_2O_5, presented in Figure 1.14(c,d) (ICSD #1840). It is possible to observe a less packed structure, with fewer atoms and polyhedra in the unit cell, which corroborates the lower density values for the TT-modification, closer to the proposed density proposed by Weissman et al., shown in Table 2. Past works discussed the high rate of Li-ion exchange in the T-modification, in which the ion could pass through along the b-axis [15, 16]. However, Figure 5.5(b) shows a packed structure for the T-Nb_2O_5 along the b-axis, which does not correspond to the reports of the transport path reports for ion-exchange, leading to the belief that

the energy storage process is more efficient in the TT-modification since it has a less packed structure, like as proposed in Figure 5.10(b).

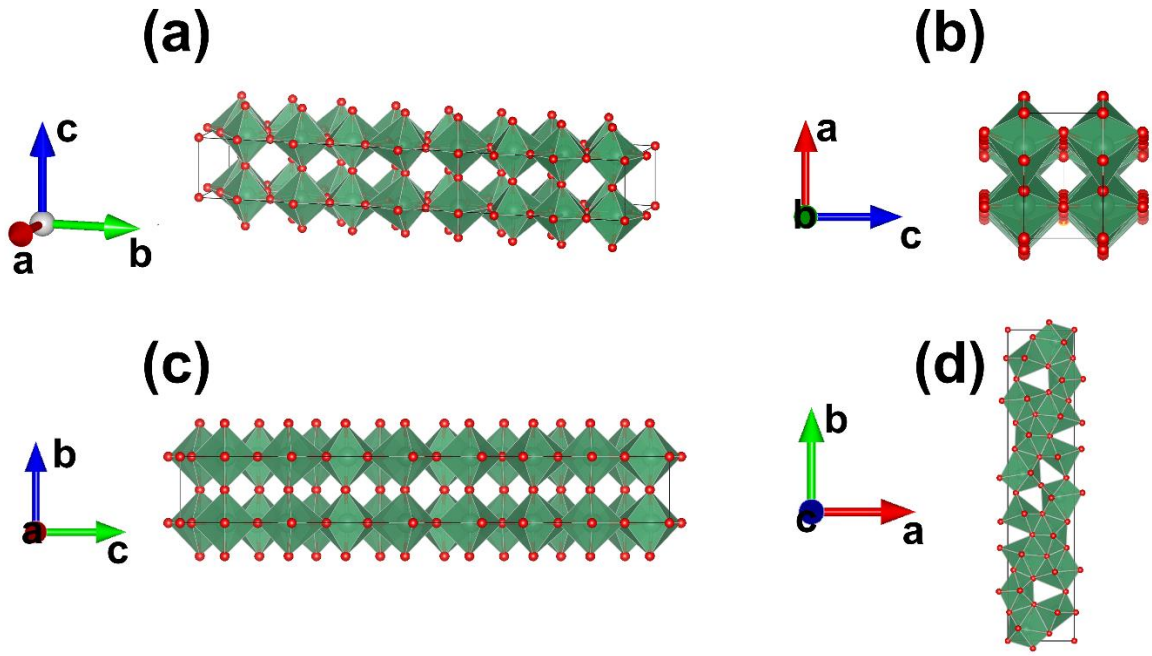

Figure 5. 10. Super-lattice structure of TT-Nb_2O_5 from (a) normalized position, (b) b-axis, (c) a-axis, and (d) c-axis.

Table 5.7. shows the atomic coordinates for the TT-modification super-lattice, consisting of a less dense unit cell with Nb atoms in 4h Wyckoff positions. The refinement process showed suitable using X-ray diffraction, which provides reliable information about the atomic position, lattice parameters, and structural behavior. Since the crystal structure of the niobium pentoxide plays a crucial role in its applications and properties, it is of most importance to instigate this subject.

The construction and refinement of the CIF could be possible due to essential tools, like checkCIF/Platon and pubICIF for data programming and curation. The refined structure in the thesis is currently available in the Inorganic Crystal Structure Database (ICSD), published as an ICSD Communication [25], under the Cambridge Crystallographic Data Centre (CCDC) code 2103847, and its DOI is https://dx.doi.org/10.25505/fiz.icsd.cc28m716. The Dataset citation is: "*Gomes, Gustavo H. M., D. S.; Mohallem, Nelcy, CCDC 2103847: Experimental Crystal Structure Determination, DOI: 10.25505/fiz.icsd.cc28m716*"

Table 5. 7. Atomic parameters of the TT-Nb_2O_5 super-lattice.

Atom	Site label	x	y	z	Occupancy	U_{iso}	Wyckoff position
Nb^{5+}	Nb1	0.27470	0.03695	0.5	1.0	0.00032	4h
Nb^{5+}	Nb2	0.23382	0.15762	0.5	1.0	0.00032	4h
Nb^{5+}	Nb3	0.25434	0.27897	0.5	1.0	0.00032	4h
Nb^{5+}	Nb4	0.23475	0.40643	0.5	1.0	0.00032	4h
O^{2-}	O1	0.15496	0.04019	0.0	1.0	0.00532	4g
O^{2-}	O2	0.18418	0.16191	0.0	1.0	0.01355	4g
O^{2-}	O3	0.20894	0.27832	0.0	1.0	0.02305	4g
O^{2-}	O4	0.24803	0.40894	0.0	1.0	0.01089	4g
O^{2-}	O5	0.02331	0.09142	0.5	1.0	0.01571	4h
O^{2-}	O6	0.08833	0.22796	0.5	1.0	0.01001	4h
O^{2-}	O7	0.36949	0.34161	0.5	1.0	0.01026	4h
O^{2-}	O8	0.12204	0.47602	0.5	1.0	0.01583	4h
O^{2-}	O9	0.39316	0.11671	0.5	1.0	0.00912	4h
O^{2-}	O10	0.38101	0.20098	0.5	1.0	0.00428	4h
O^{2-}	O11	0.0	0.0	0.5	1.0	0.03002	2b

To show the correlation between the obtained CIF and the obtained nanoparticle, Figure 5.11. shows the sample SAED pattern at the zone-axis and the respective SAED simulation using JEMS software. It is possible to observe the particle orientation at the [101] zone axis of the crystal, presenting coherence with the obtained sample's crystallographic planes, with a 76° orientation shift. The JEMS simulations were performed, showing only one Laue zone and an approximated crystal thickness of 42 nm. The SAED results corroborate the orthorhombic super-lattice structure of the TT-Nb_2O_5, which could be indexed employing the produced CIF as a standard for the Laue Zone simulation, with brighter spots than the simulation due to sample tilt in the microscopy.

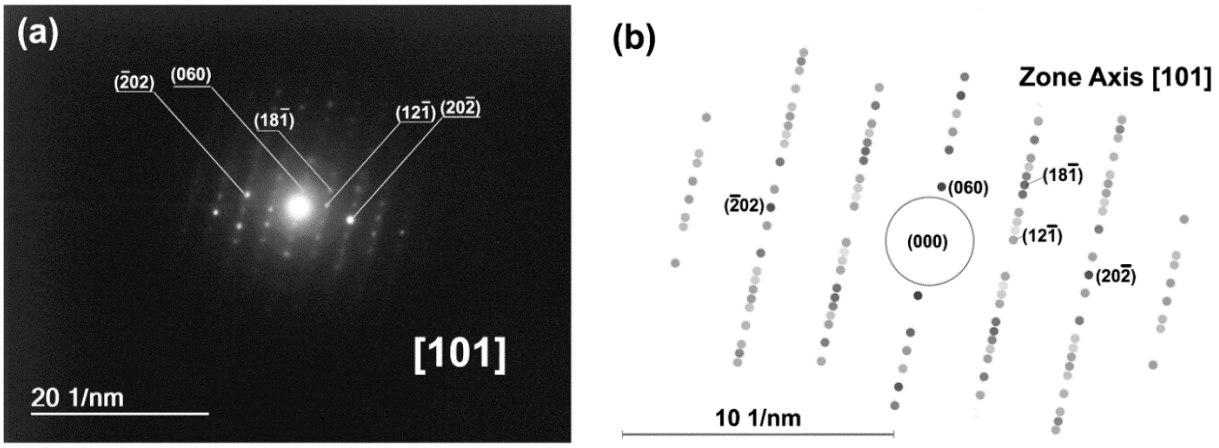

Figure 5. 11. (a) SAED pattern experimentally obtained from TT-Nb_2O_5 nanoparticle and (b) respective [101] zone axis SAED simulation using the produced CIF of this work as a standard.

3.1. Computer programs

Structure and cell refinement: GSAS/EXPGUI. CIF programming: pubICIF, Notepad. Structure Visualization: VESTA, platonPLOT, plotCIF. Data reduction: VESTA, pubICIF. 3D packed crystal structure models: VESTA. SAED analysis software: DigitalMicrograph®. SAED simulation: JEMS. Image Processing Softwares: Photoshop, DigitalMicrograph®. Software used to prepare material: Microsoft Word, printCIF, pubICIF. CIF validation: checkCIF/PLATON, pubICIF.

4. Influence of defects on the TT → T-Nb_2O_5 phase transition

The presence of defects in the TT-phase crystal structure is a fact. An essential tool for crystal structure characterization is the HRTEM analysis, where it is possible to see crystallinity, preferential orientation, particle size and have a deeper understanding of the local degree of defects in the nanoparticles. In this sense, the HRTEM allied with the GPA and other image analysis tools are crucial for defects determination. For this purpose, the EG sample series showed to be the best object of study since it presented crystallization at four distinct crystalline phases (TT, T, H, and $Nb_{12}O_{29}$) and showed the high strain and dislocation density values, which is suitable for strain mapping employing the GPA method.

TEM images of the EG500 (Figure 5.12) show an aggregation of nanoparticles (NP), with an interconnected mesoporous network, formed by nanoparticles of (24 ± 8) nm, which is considered small for Nb_2O_5 materials. Figures 5.12(c,d) shows a

polycrystalline material, with agglomerated particles, showing d-spacing of 0.314 nm, representing the (100) crystalline plane of the TT-Nb_2O_5. The analysis shows the presence of mesoporous, ranging between 3—6 nm, and a polycrystalline material showing nanoparticles oriented along the (100) planes, with rotation and interaction between crystallographic orientations, producing different levels of contrast in the image. Figure 5.13(a) shows the SAED pattern from Fig. 5.12(d), with an applied, reveal a weak reflection filter (Figure 5.13(b)), where no weak reflections from the T-Nb_2O_5 are present, corroborating the formation of only the TT-Nb_2O_5. The indexed pattern in Figure 5.13(b) shows the principal crystalline planes, (001), (100), (101), (110), (002), (102), (201), and (112), with a preferable orientation at the (001), (100), and (101) direction.

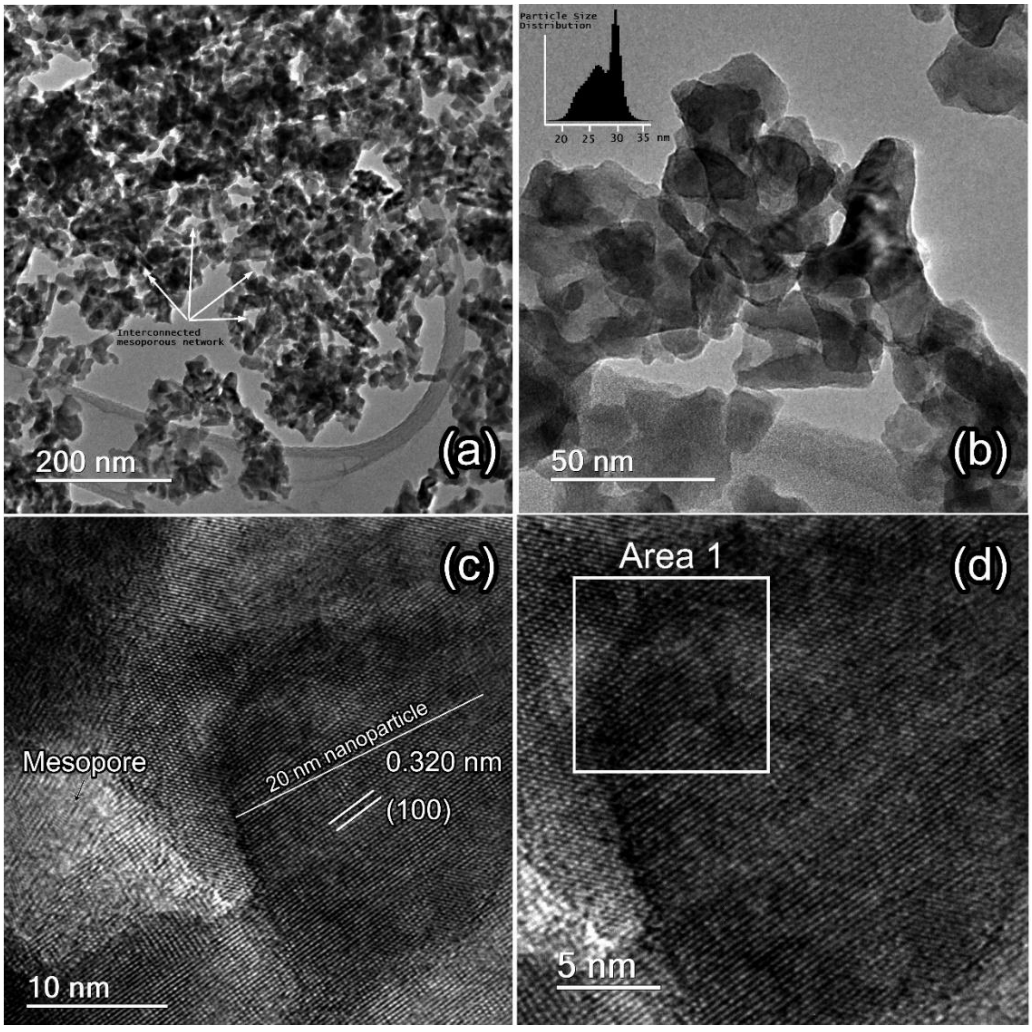

Figure 5. 12. HRTEM images of EG500 show an (a) mesoporous network, (b) the particle size distribution, (c) a nanoparticle oriented in the (100) plane, and (d) magnification of the observed region showing the analysis Area 1.

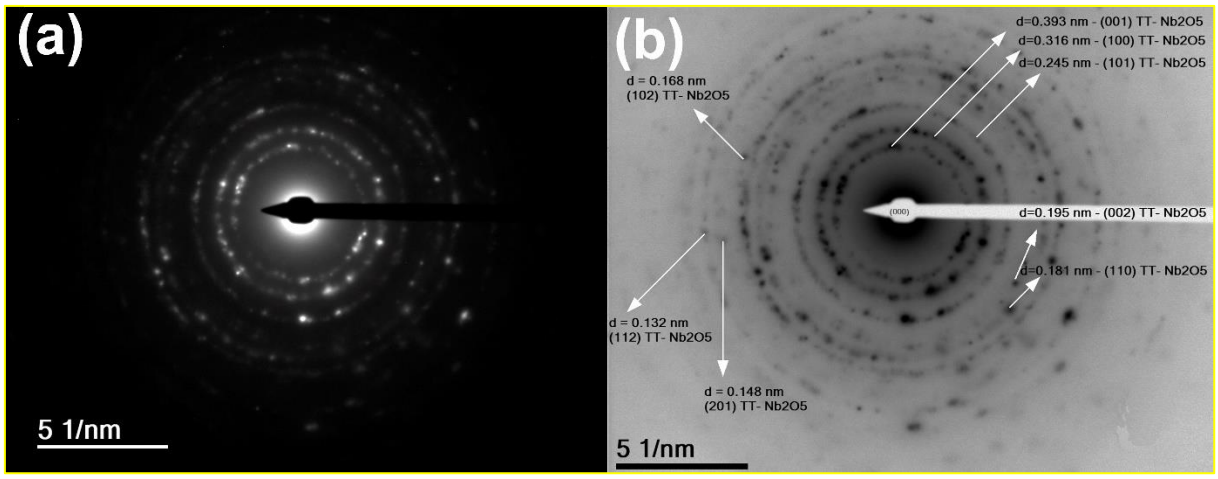

Figure 5. 13. (a) SAED analysis of EG500 and the (b) reveal weak reflection filter.

The GPA is a powerful tool in HRTEM image analysis to study the strain distribution. However, several factors contribute to errors in the analysis, like defocus values, spot resolution size, smoothing, strain matrix values, profile width, reference region, and source image resolution [26, 27]. The analysis counted all these factors that interfere during the GPA analysis, and the presented results were carefully analyzed.

Figure 5.14(a) shows the selected area from Figure 5.12(d), with its respective FFT and the Bragg filtered images obtained from spots g_1 and g_2. Fig 5.14(a) shows a clear indication of different orientations of the (100) crystallographic plane as an indicator of a polycrystalline material. The obtained FFT presents [100] orientation along the vectors of g_1 and g_2 spots, shown in Fig 5.14(c) and (d), respectively. Despite the low degree of defects inside the nanoparticles, the boundaries between crystallographic planes present a column dislocation, as shown in Fig 5.14(d), which corroborates the higher value of density dislocation and small crystallite size obtained through Rietveld refinement analysis presented in the subsection 2.2. Crystal structure elucidation.

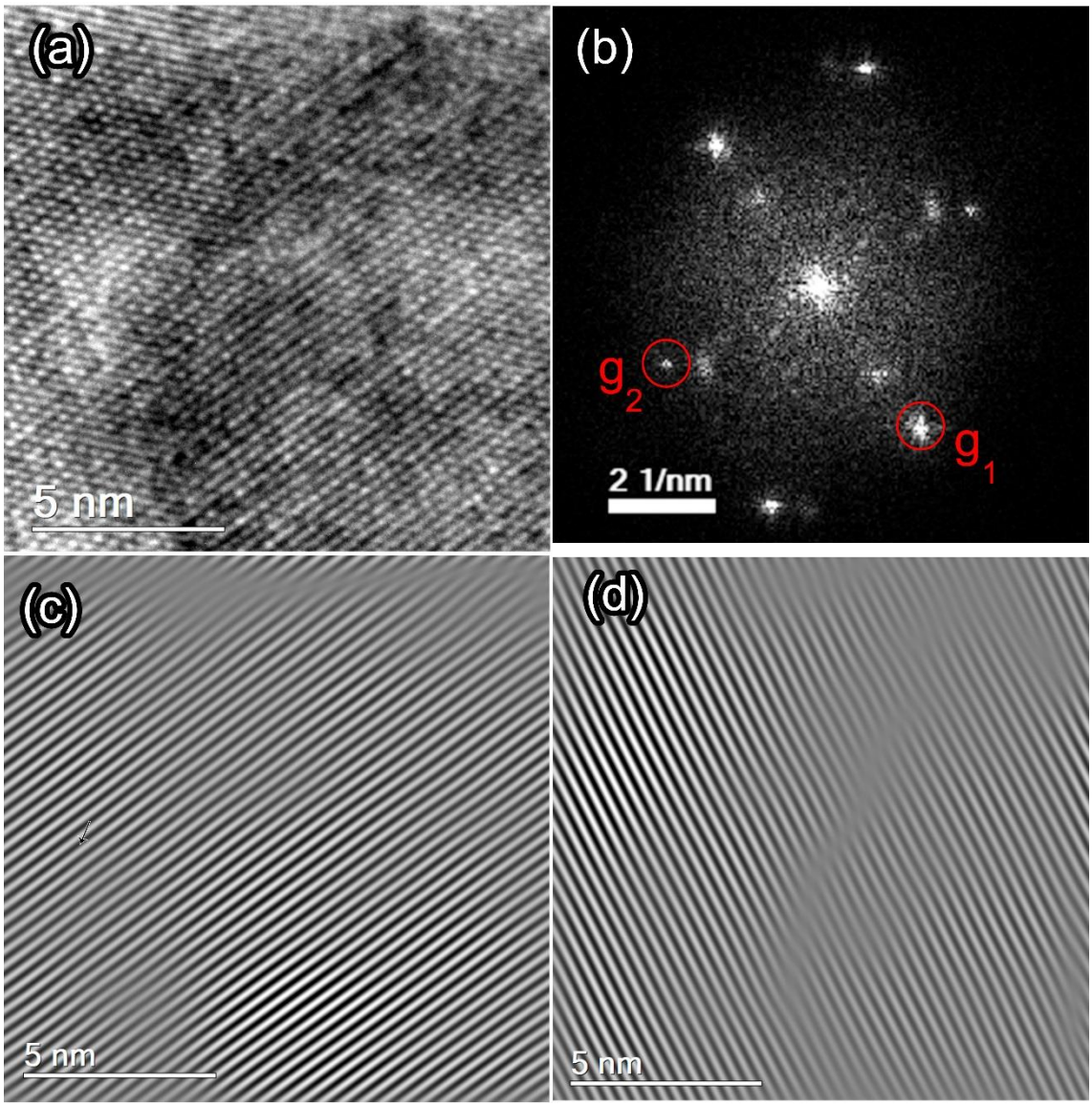

Figure 5. 14. (a) The studied region of EG500 with its respective (b) FFT with the correspondent excited Bragg spots (g_1 and g_2). The filtered inverse FFT from the (c) g_1 and (d) g_2 spots.

Figure 5.15 shows the GPA analysis of strain values in the x-direction (ε_{xx}), y-direction (ε_{yy}), the shear strain (ε_{xy}), and rotation (ω), and the vertically measured strain line profile in the center of the image. The strain distribution on the x and y direction shows a low strain effect inside the nanoparticle, with strain values between -0.2 and +0.2%, which is non-significative for the strain analysis employing GPA due to limitations of the experimental setup. However, the increase in strain values between crystallographic boundaries and superposed nanoparticles is apparent, where strain values of 1.5% are observable in the x-direction. Despite not showing significant strain values in the y-direction, the shear strain and rotation indicate dislocation effects in

the boundaries between particles, shown from the g_2 [100] direction in Fig 5.14(d), showing values up to -2.0% and +2.8°, respectively. This result contributes to producing a polycrystalline material with high values of density dislocation.

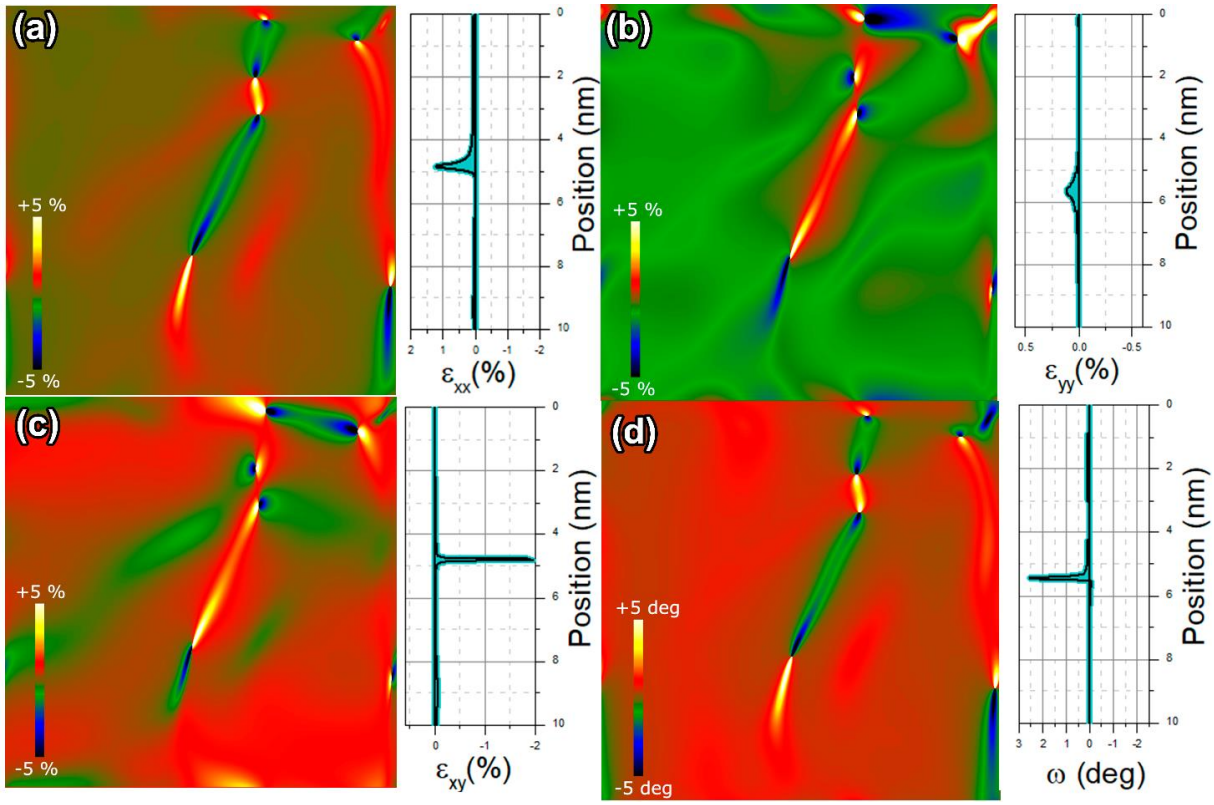

Figure 5. 15. The EG500 strain map distribution and its vertical line profile (a) ε_{xx} direction, (b) ε_{yy} direction. The (c) shear strain (ε_{xy}) and (d) the (δ) rotation map.

Fig. 5.16 shows the TEM images and analysis of the EG700. The increase in the temperature provoked an increase in the particle size to (155 ± 40) nm and the beginning of coalescence between the particles, evidencing several diffractions contrasts with different packing densities. The presence of several diffraction contrasts and Moiré fringes are due to the overlap of several crystalline planes and variations in particle density, crystallographic orientation, or structure. Fig. 5.16(c) exhibits a single round-shaped Nb_2O_5 nanoparticle with approximately 75 nm diameter, oriented along the [100] zone axis for the GPA analysis, evidenced by the selected areas. The isolated particle analysis brings more confidence to the obtained results than a particle agglomeration analysis, as the images can genuinely reflect the material's crystal structure. To further investigate the crystal structure of these regions, the selected areas are on the interface between the contrast variations in the nanoparticle, which

indicates a region of high disorder and crystalline phase mixture. Fig. 5.16(d) shows the SAED pattern with a weak reflection filter, with evidence of the T- Nb_2O_5 formation due to the presence of exclusive crystalline planes, such as (130), (180), (200), and (181). However, TT- Nb_2O_5 is present in the sample, where small crystalline domains overlap between (001) and (100) crystallographic planes.

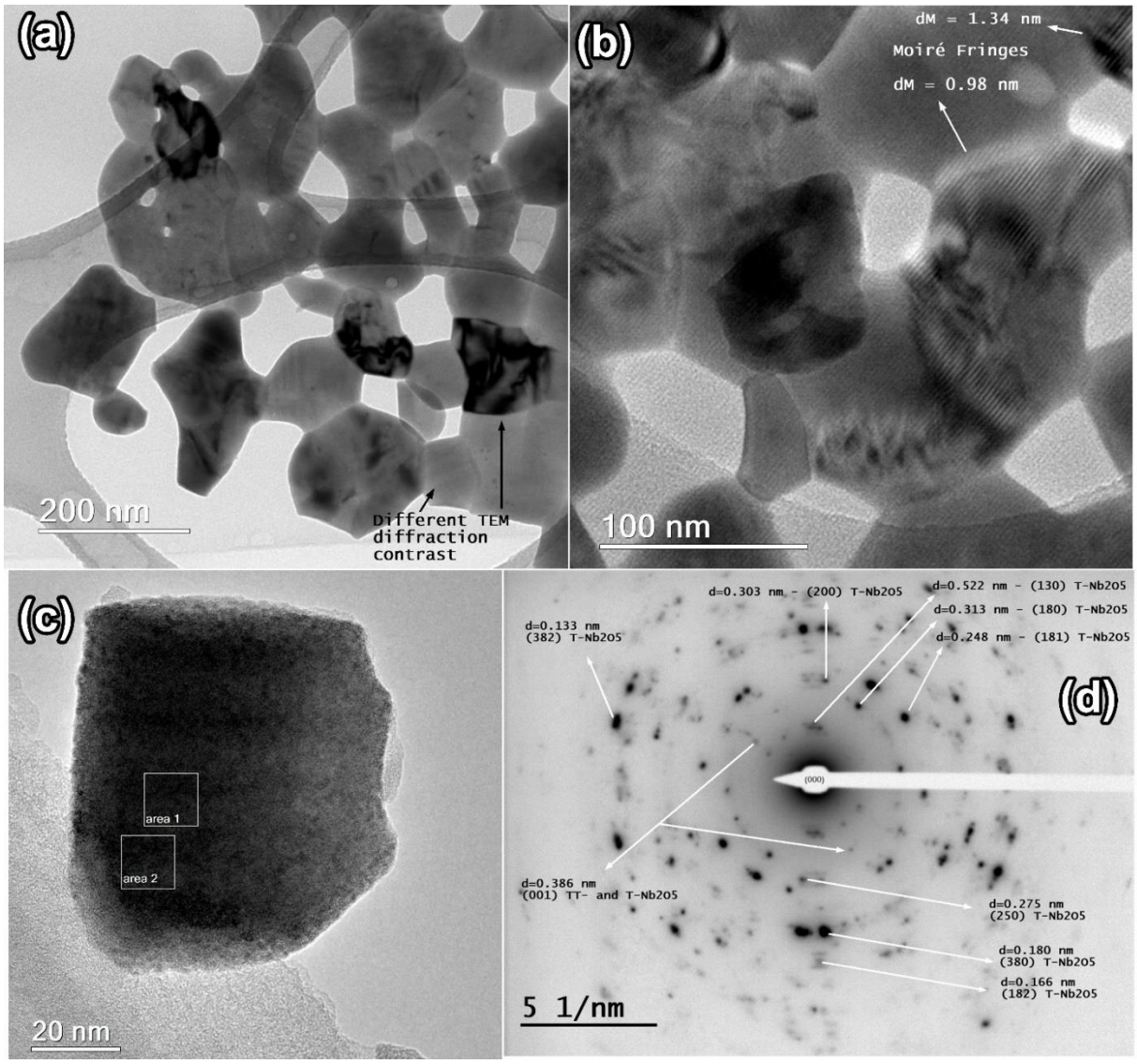

Figure 5. 16. HRTEM images of EG700 showing (a) nanoparticle agglomerate with different diffraction contrasts. (b) Particle coalescence and presence of Moiré fringes. (c) Studied nanoparticles from the EG700 with two selected areas of study and (d) The SAED pattern

Fig. 5.17 shows the HRTEM image of area 1 from Figure 5.16(c) and the respective FFT of this region with the selected g_1, g_2 spots, and the IFFT of the filtered Bragg spots. Fig 5.17(a) shows a clear indication of curvature of the interference fringes on the bottom side of the image, presenting a distortion of ~ 4.8° between vertical and

inclined fringes. Fig 5.17(b) evidenced this phenomenon, in which the g_1 [130] vector has a broadening effect along with its respective Bragg spot. The g_1 and g_2 orientations are orthogonal on the FFT for GPA analysis, in which the red circles represent the mask spot diameter. Fig 5.17(c) and (d) show the filtered IFFT images from the g_1 and g_2 spots, respectively. The analysis suggests that the interference fringes from the g_1 direction, corresponding to T-Nb_2O_5 [130], do not show a variation in the spacing between crystallographic planes, indicating no defects. However, the g_2 direction, Nb_2O_5 [100], presents an atomic spacing variation in several image points, indicative of point defects that produce strain along the b-c axis [100]. The area 2 analysis in Fig 5.19(c) presents the same discussion and results, corresponding to Figure S1 on the supplementary information.

The GPA analysis of Figure 5.17 shows the strain on the x-direction (ε_{xx}), y-direction (ε_{yy}), the shear strain (ε_{xy}), and rotation (ω), shown in Figure 5.18, and their respective vertically measured line profile. The analysis of only the strain distribution along the ε_{xx} and ε_{yy} direction is uncertain about observing any different characteristics between the top and bottom regions of the image. Instead, the strain maps reveal only variations along the interference fringes in the filtered g_1 and g_2 spots, as seen in Figure 5.17(c) and (d), respectively. The vertically measured line profile in the center of the image reveals small average values for the ε_{xx} component, varying between +0.3% and -0.3%, like the average values for the ε_{yy} component on the top and bottom part of the image. Despite the low average strain value for the ε_{yy}, some regions show strain values up to +2.5%, which could be associated with the displacements observed in the filtered g_2 spot of Figure 5.17(d).

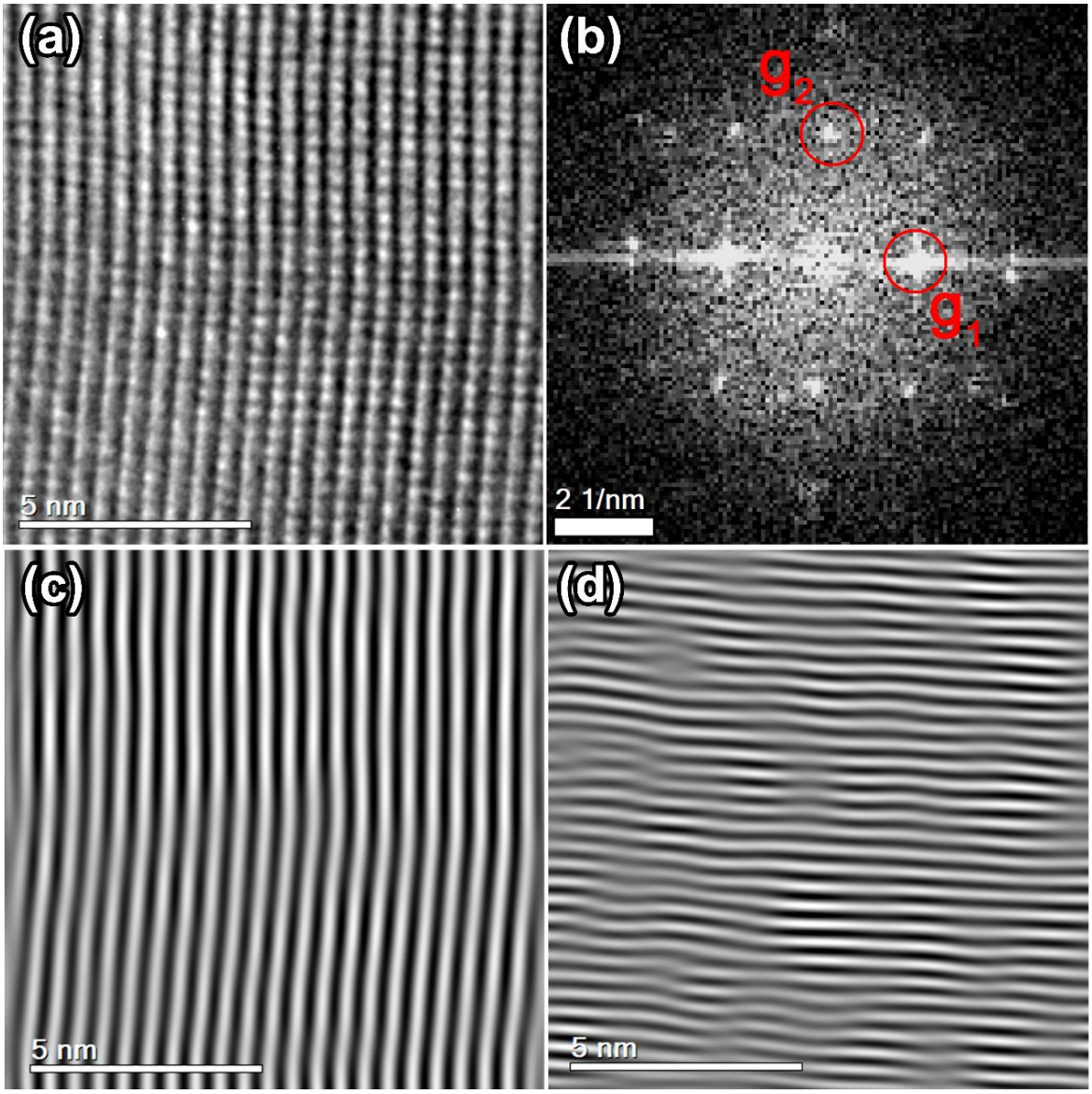

Figure 5. 17. (a) The area 1 region of EG700 from Fig 5.16(c) with its respective (b) FFT with the correspondent excited Bragg spots (g_1 and g_2). The filtered inverse FFT from the (c) g_1 and (d) g_2 spots.

Regardless of the strain maps, the ε_{xx} and ε_{yy} directions did not reveal variations on the lattice parameter from the top and bottom region of Fig 5.17(a). The shear strain and the rotation showed a significant difference between the two regions (top and bottom). Analyzing the strain map along the ε_{xy} direction, the strain on the bottom region is more significant than the top region, showing average values of +4.0% and 0%, respectively. The rotation map shows an average value of 4.8° on the bottom region, which corroborates the measured value (~5°) in the HRTEM image of Fig. 5.17(a). Although the GPA analysis of EG700 showed the lack of defects in the interface of these two distinct regions, the atomic planes show significant shear strain

and rotation. The variations of contrast intensity inside the nanoparticle suggest that the two regions are distinct crystal structures with similar zone axis, atomic planes, and interplanar distance. However, it shows a rotation of 5° between them, which indicates the mixture of TT- and T- modifications in the EG700 sample. The GPA analysis of area 2 reveals the exact behavior of area 1, as presented in Figure 5.20, increasing the reliability of the analysis.

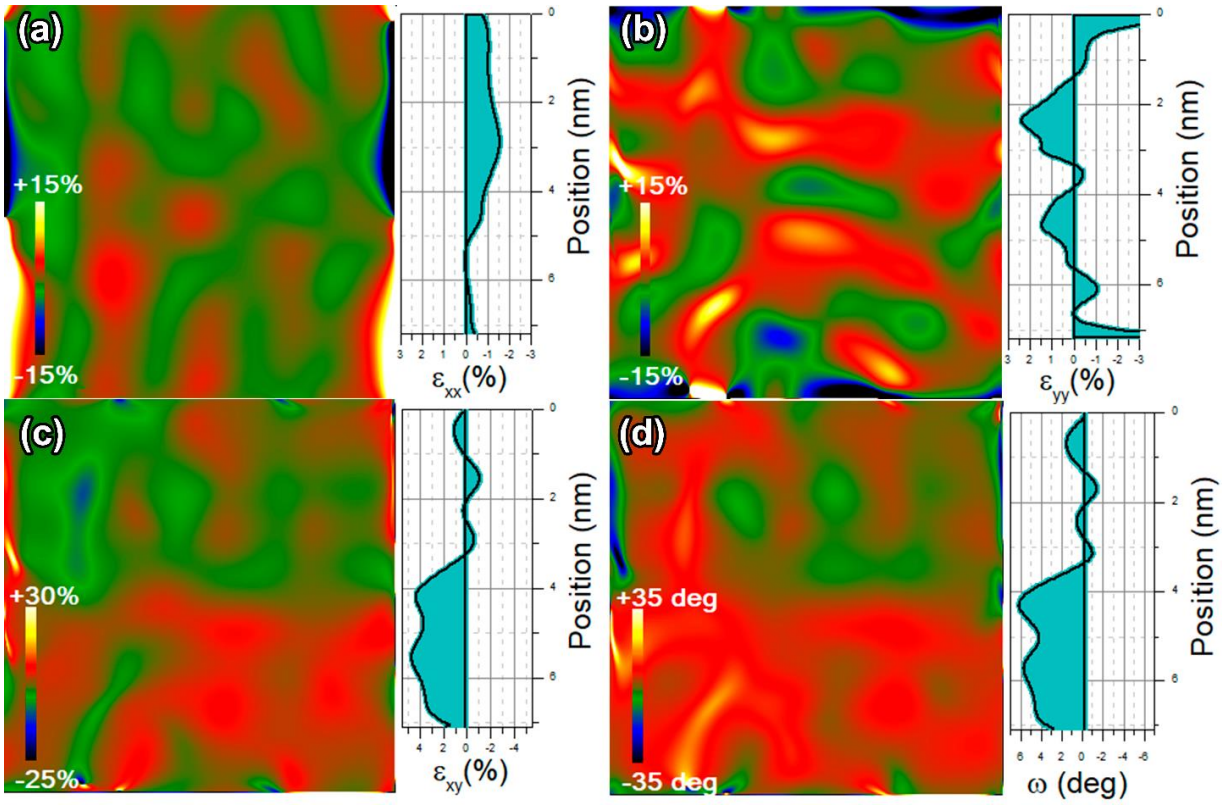

Figure 5. 18. The EG700 strain map distribution and its vertical line profile along the (a) ε_{xx} direction, (b) ε_{yy} direction. The (c) shear strain (ε_{xy}) and (d) the (δ) rotation map.

The present study discussed in this chapter is currently available in the Micron Journal [28], which is an interdisciplinary forum for all work that involves new applications of microscopy, published under the title "*Investigation of phase transition employing strain mapping in TT- and T-Nb_2O_5 obtained by HRTEM micrographs.*" and DOI: 10.1016/j.micron.2021.103112.

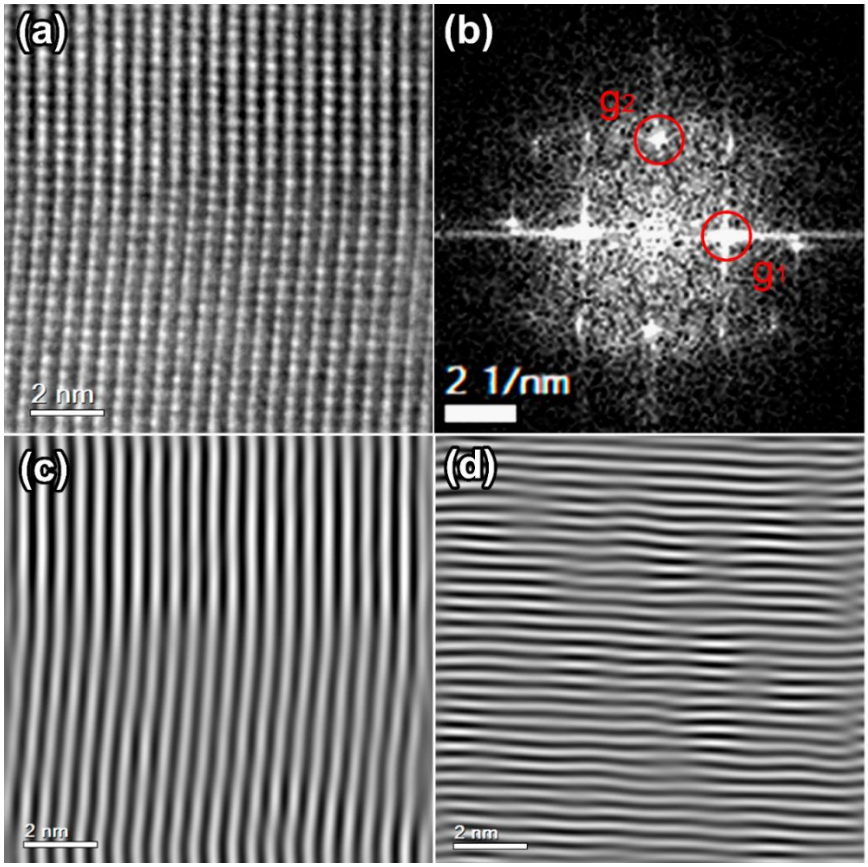

Figure 5. 19. (a) The area 2 region of EG700 from Fig 5.16(c) with its respective (b) FFT with the correspondent excited Bragg spots (g_1 and g_2). The filtered inverse FFT from the (c) g_1 and (d) g_2 spots.

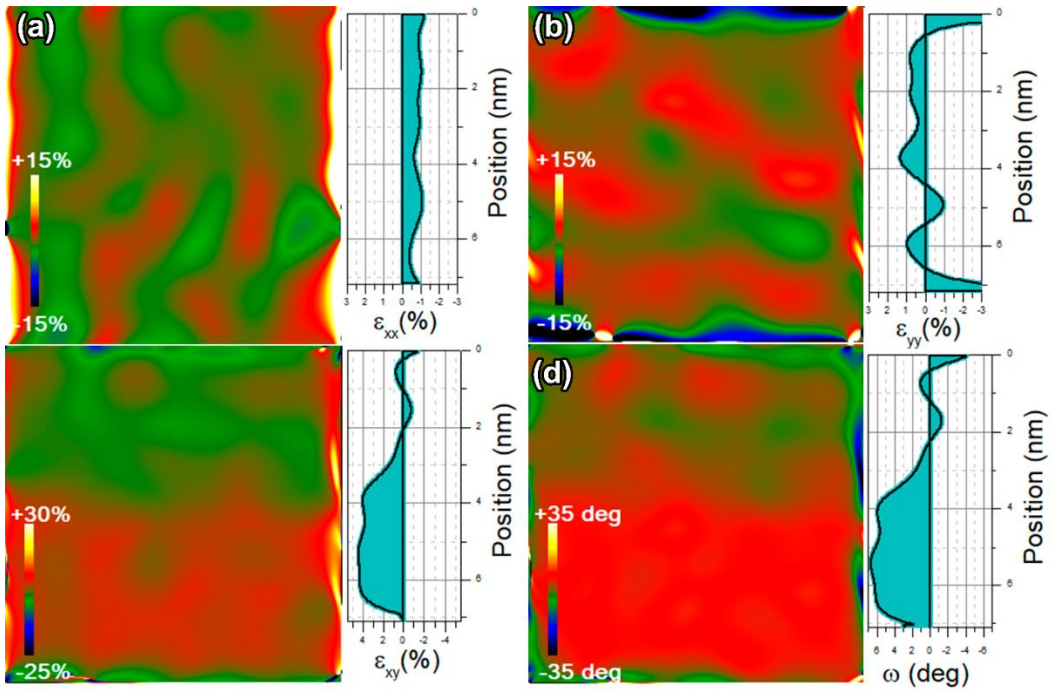

Figure 5. 20. The EG700 area 2 strain map distribution and its vertical line profile along the (a) ε_{xx} direction, (b) ε_{yy} direction. The (c) shear strain (ε_{xy}) and (d) the (δ) rotation map.

5. Textural analysis of niobium pentoxide

Figure 5.21(a-c) shows the N_2 physisorption analysis of all prepared samples and (d) the pore size distribution of EG500, PEG500, and NbOX500. Table 5.8 shows the textural properties of the different Nb_2O_5 samples. In all applied methods, the increase in the crystallite size and the phase transition between TT → T phases decreased the adsorbed gas volume. The low calcination temperature materials presented the higher specific surface area (SSA), corroborating some previous works in the literature. All samples calcined at 500 °C presents a similar surface specific area (SSA - 57~63 $m^2.g^{-1}$) and total pore volume (0.18 ~ 0.21 $cm^3.g^{-1}$). However, there are changes in the isotherm shape and type, indicating a different pore formation in the samples

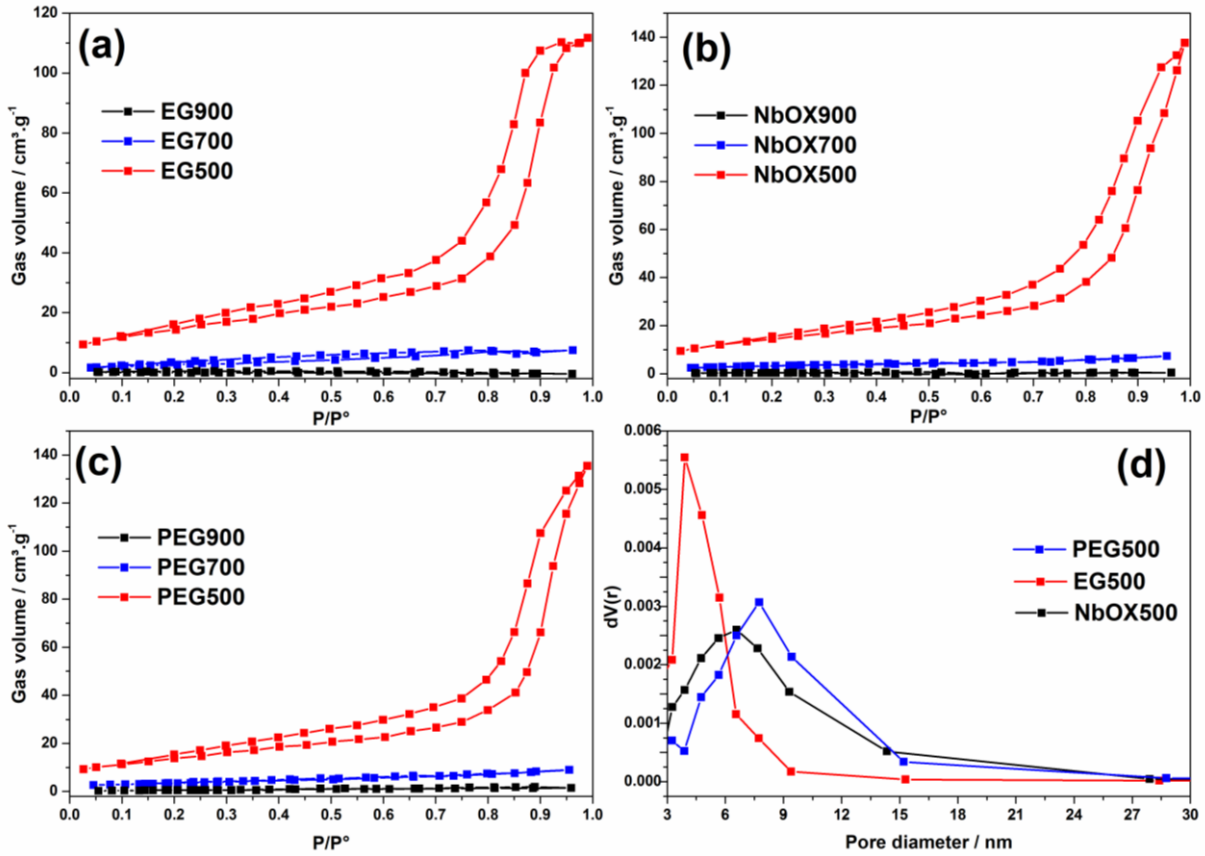

Figure 5. 21. N_2 adsorption isotherms of (a) EG, (b) NbOX, and (c) PEG. (d) Pore size distribution of EG500, PEG500, and NbOX500.

All the hysteresis are a combination of type II and type IV, indicating the presence of macropores (> 50 nm) and mesopores (2—50 nm) in the samples calcined at 500 °C, corroborating HRTEM and STEM analysis. The EG500 shows a well-defined plateau

in high-pressure values, and it can be described as a mixture of H1 and H2 hysteresis loops, indicating the presence of a narrow distribution of uniform pores, with a more likely cylindric or spherical shape.

Table 5. 8. Textural properties of Nb2O5 from gas adsorption analysis with different synthesis methods.

Sample	SSA / $m^2.g^{-1}$	C	R^2	Average Pore Diameter / nm	Total Pore Volume† / $cm^3.g^{-1}$
NbOX500	57	91	0.999830	8.1	0.20
EG500	63	84	0.999468	5.5	0.18
PEG500	58	77	0.999476	8.4	0.21
NbOX700	12	< 0*	0.998966	-	-
EG700	10	56	0.990896	-	-
PEG700	13	132	0.999431	-	-
NbOX900	1	< 0*	0.949746	-	-
EG900	1	< 0*	0.901488	-	-
PEG900	2	13	0.921488	-	-

*C < 0 has no physical meaning. †Measured at the saturation point ($P/P^\circ = 0.99$)

The PEG500 and NbOX500 presented a similar pore structure, described as a combination of H1, H2, and H3 hysteresis. Both present a mesoporous and macroporous structure, but the increase in the adsorbed gas volume in high P/P° (0.995) shows that both samples have disordered pores in their structure, which occurs due to the large organic groups leaving the material's structure during the pore formation, such as PEG500 which presents more extensive chain length than ethylene glycol. Those differences lead to different pore size distribution, illustrated in Figure 5.21(d), where the EG500 shows a uniform pore distribution with an average size of 5.5 nm, and the PEG500 and NbOX500 presents a more varied pore size, due to disordered pore shape, with an average diameter between 8-8.5 nm. It is worth mentioning that all analysis was carried with the respective constraints to obtain an excellent textural

analysis. The pore size distribution was measured employing the desorption curves and the total pore volume at the high-pressure saturation point. The positive C constant, with values around 80, is an indicator of a good BET analysis, performed in the range of 0.05-0.30 P/P°. The samples calcined at 700 and 900 °C presented no significant SSA and adsorbed gas volume, and some of them presented $C < 0$, as shown in Table 5.8, which has no physical meaning, showing that there is no physisorption phenomenon occurring in those samples.

The HRTEM imaging and analysis is a powerful technique to confirm the texture and morphology of the nanoparticles. When employing the correct sample preparation and imaging setup, it is possible to confirm some aspects found in the gas adsorption analysis and defects in the crystal structure. Since the EG500, PEG500, and NbOX500 presented higher SSA and interesting textural aspects, the HRTEM analysis focused on those samples.

Figures 5.22(a, b) show the transmission electron microscopy (TEM) of the EG500 and PEG500, respectively. Both samples present a similar morphology, e.g., agglomeration of round nanoparticles within an interconnected mesoporous network with an average pore size of (3 ± 1) nm. Despite the long-range porous network (—700 nm), it is small and presents a more likely random growth, which can be a characteristic of the Pechini synthesis. Fig. 5.22(c) shows the NbOX500, presenting a very dense agglomeration of nanoparticles with no interconnected porous network, corroborating the differences observed in the gas adsorption analysis. STEM image of EG500 (Figure 5.22 (d)) reveals with more detail the surface morphology of the sample, evidencing the mesoporous and the particle agglomeration, showing different contrasts due to particle overlap and crystalline orientation. Figure 5.22(e) presents the STEM line profile, showing a porous surface with a different distribution, ranging from 2.6 to 19.6 nm in diameter, and showing the presence of smaller pores within bigger pores.

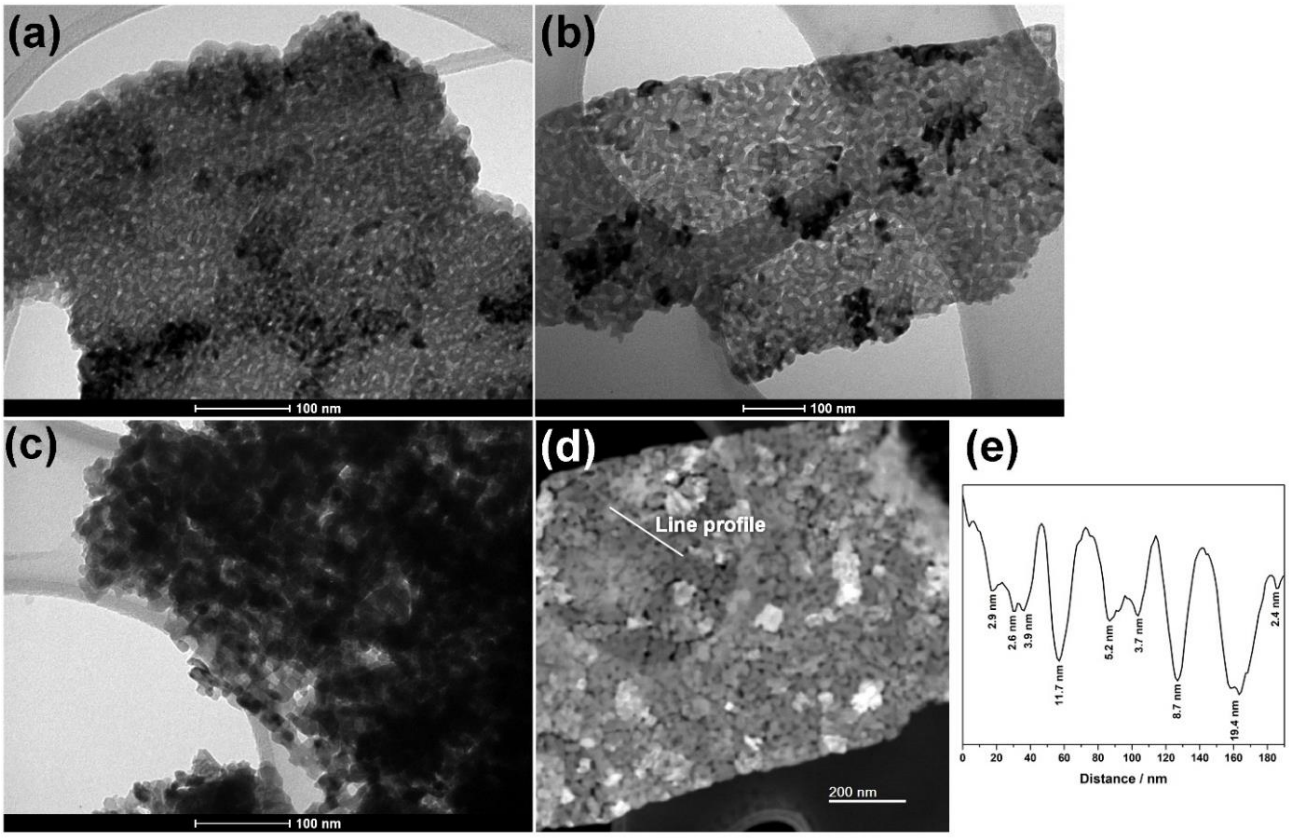

Figure 5. 22. Transmission Electron Microscopy images of (a) EG500, (b) PEG500, (c) NbOx500, and (d) STEM image from EG500 and its respective (e) surface line profile.

Figure 5.23 shows the different morphology of niobium pentoxide nanoparticles calcinated at 500 °C. Fig 5.23(a) shows the EG500 interconnected mesoporous network, composed by an agglomerate of nanoparticles at several diffraction contrasts, evidencing a polycrystalline material. Figure 5.23(c) and (e) show the PEG500 and NbOX500, respectively. Both samples present similar morphology with a nanoparticle agglomerate and superposition. The differences in particle morphology correlate to the synthesis method. The ethylene glycol is a smaller molecule than PEG400, therefore provokes a minor steric effect and can be easily eliminated in the calcination process. The NbOX500 is a crystalline complex of one niobium(v) bonding with two water molecules, two oxalate groups, and one oxygen atom. Its thermal behavior has been reported in the literature, and it has three thermal events until 500 °C, which release a significant amount of water and ammonia, and can itself be a porogenic agent for Nb_2O_5 materials [29].

Those observations corroborate the N_2 adsorption analysis, in which the EG500 shows a cylinder pore network along the nanoparticles agglomerated (Fig 5.23(a)), and the PEG500 and NbOX500 show pore along the nanoparticle's intersection. Figure 5.23(b) shows the polycrystalline behavior of EG500. The nanoparticles are oriented at the (100) and (101) directions, presenting a round shape ranging between 5-15 nm, with a 3.5 nm mesopore, corroborating the pore size distribution. Figure 5.23(d) shows the PEG500, with the (100) and (101) planes, and overlap between them. Figure 5.23(f) shows the NbOX500, with two crystallites in a different orientation, corroborates the formation of the TT-Nb_2O_5, which did not occur in the XRD experiment. There is an intersection between the (100) and (001) crystalline planes and a 5.8 nm mesopore. Pechini synthesis directly influences the obtained crystal phase, as the EG500 and PEG500 present an XRD signal for TT-Nb_2O_5. The NbOX500 shows particles oriented in the (100) and (001) direction, while the EG500 and PEG500 show orientation in the (100) and (101) planes, evidencing the different crystallographic behavior of the synthesis methods.

HRTEM images in Figure 5.24(a,c,e) reveal a clear presence of lattice fringes caused by interference with the diffracted beam on the sample. All samples show nanoparticle agglomeration, but the EG500 and PEG500 samples showed no clear distinction on nanoparticle separation, where the interference fringes go along with the material growth, corroborating the nanoparticle agglomeration presence. Both samples consist of small nanoparticles with sizes ranging from (11 $\pm$ 3) nm and the presence of some mesopores with an average size of 3 nm. On the other hand, NbOX500 shows stacked nanoparticles with no long-range interference fringes, corroborating the PDF analysis, showing the formation of some crystalline sites, but most of the sample is amorphous.

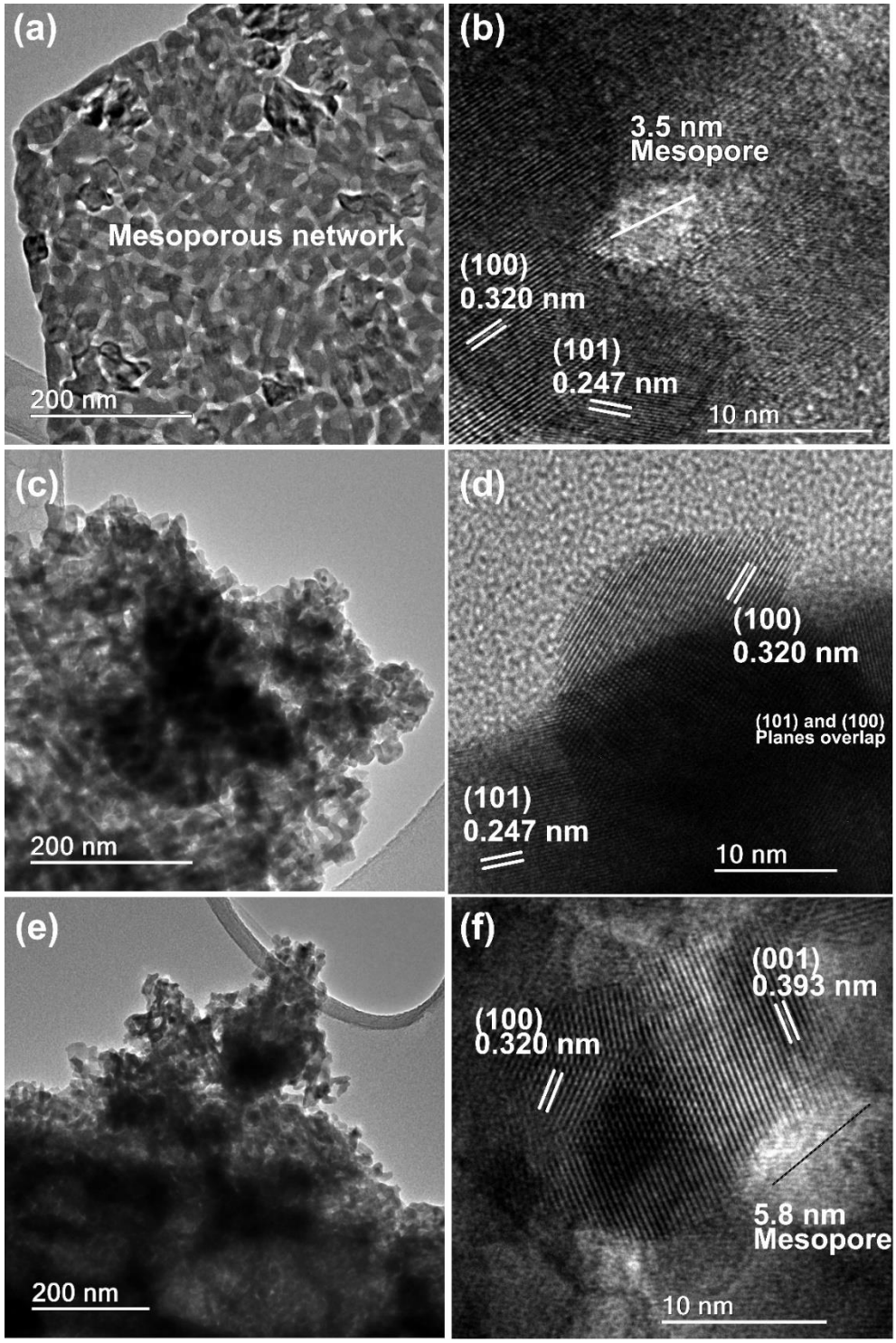

Figure 5. 23. HRTEM micrographs of (a,b) EG500, (c,d), PEG500 and (e,f) NbOX500.

Figure 5.24(b,d,f) shows the inverse fast Fourier transform (IFFT) of the selected region of interest (ROI), which were obtained by applying an FFT on the HRTEM images, filtering the diffracted spots with an applied mask, and performing the IFFT calculation. Figure 5.23(b) shows the IFFT of the EG500, evidencing the orientation along the [101] direction, with an interplanar spacing of 0.247 nm. Another

important finding is the presence of atomic column displacement all over the sample, showing long-range line defects, such as edge and screw dislocations, which occur due to oxygen vacancies or cation substitutions in the crystal structure, corroborating higher strain values. PEG500 (Fig. 5.23(d)) also presented orientation at [101] direction and interplanar spacing of 0.247 nm. However, there is no significant observation of long-range line defects, indicating that ethylene glycol induces more defects in the crystal structure due to oxygen capture from the lattice during the crystallization process. Figure 5.23(f) shows the IFFT of NbOX500, with a different orientation along the [100] direction, with an interplanar spacing of 0.321 nm. There is no evidence of atomic displacement, only at the crystalline plane's interface.

Figure 5.25 shows the TEM images of the (a,b) EG700, (c) PEG700, and (d) NbOX700. The increase in the temperature treatment provoked the increase of the particle size and coalescence between them. The long-range porous network presented by the EG500 and PEG500 collapsed with the temperature increase, leading to an agglomeration of nanoparticles of varied sizes and shapes, as shown in Figure 5.25(a,c). However, a further investigation on the EG700 showed two distinct nanoparticles morphology, shown in Figure 5.25(a) and (b), which corresponds to the T and TT-Nb_2O_5 mixture in the sample. The region presented in Figure 5.25(b) resembles the morphological structure of the EG500 sample, corresponding to the TT-modification, while Fig. 5.25(a) shows distinct nanoparticles with coalescence between them, which is characteristic of the T-modification, as shown in Figure 5.25(c), where the PEG700 presented the same characteristics of the T-modification of EG700.

Figure 5.25(d) shows the TEM image of the NbOX700. The NbOX700 nanoparticles have a more significant length than the EG700 and PEG700, showing that the synthetical route influences the morphology of the nanoparticle agglomerated. All samples presented different TEM contrasts in the image, which occurs due to several crystalline orientations and superpositions, and the presence of distinct crystalline phases. TEM images of Figure 5.25 also corroborate the gas adsorption

analysis, where all samples presented low specific surface area (SSA), attributed to the bigger particle size and the extinction of the long-range mesoporous network.

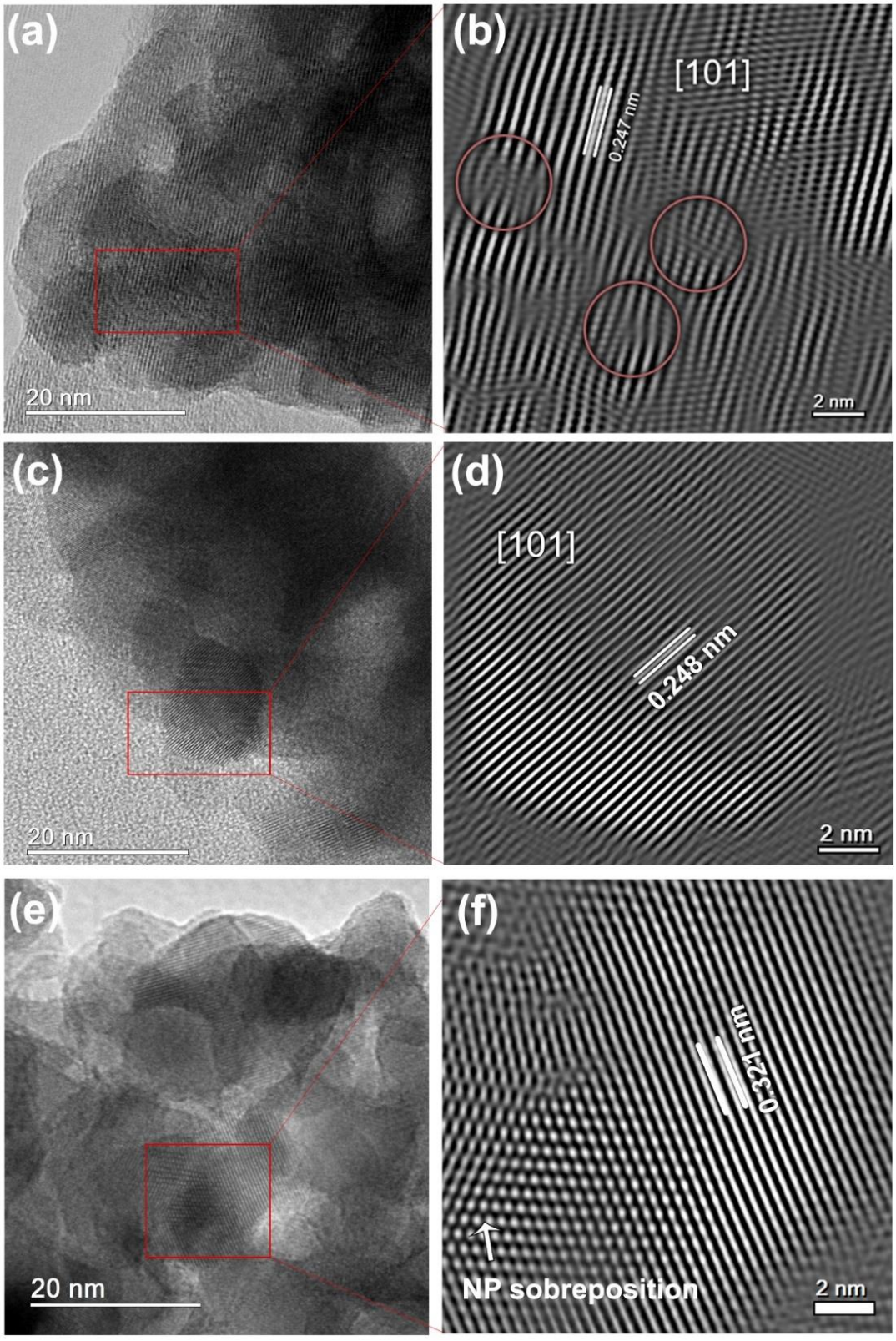

Figure 5. 24. HRTEM images and the respective Bragg spots filtered inverse FFT evidencing the atomic columns of (a,b) EG500, (c,d) PEG500, and (e,f) NbOX500.

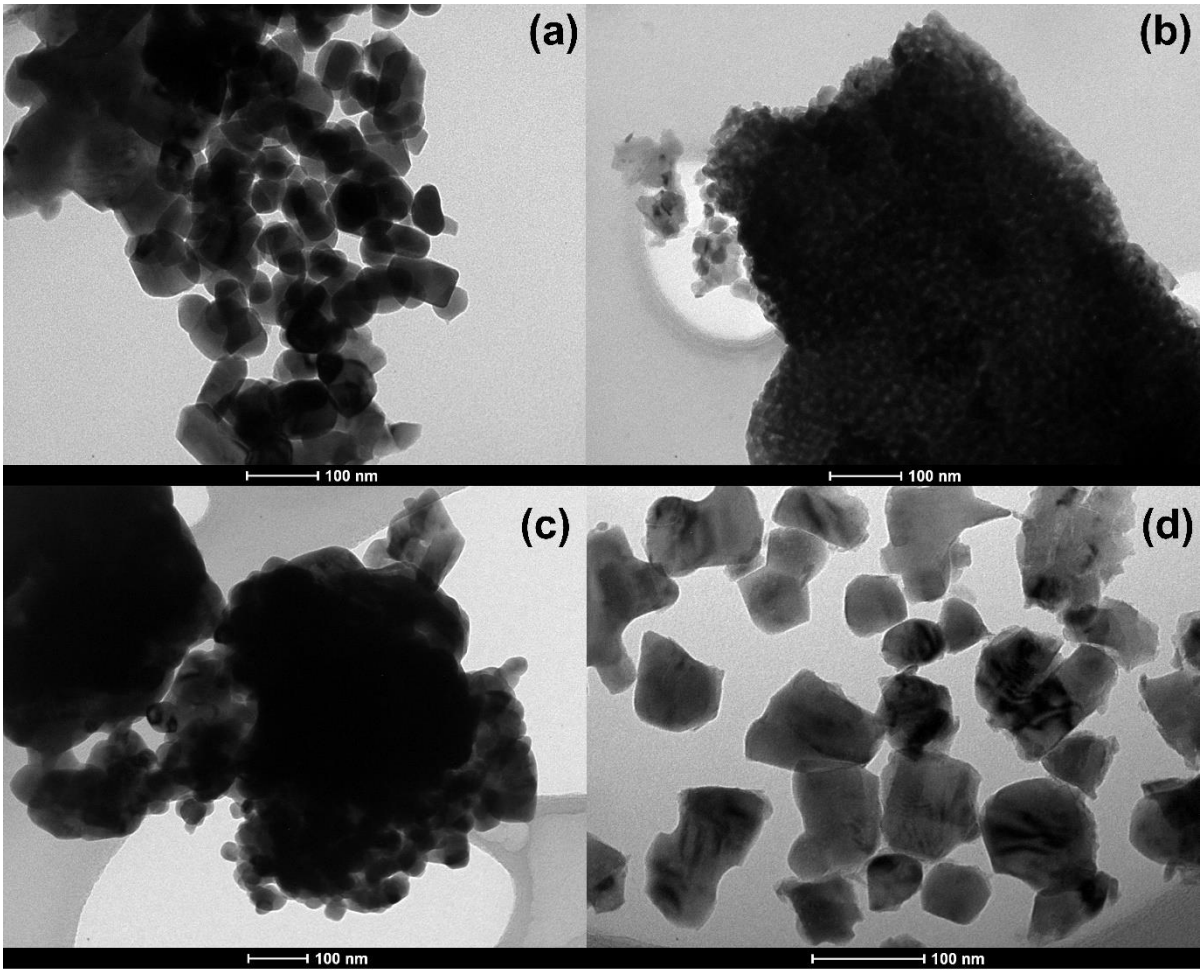

Figure 5. 25. TEM images from the (a,b) EG700, (c) PEG700, and (d) NbOX700.

The odd characteristic and phase mixture of the EG700 instigated further investigation about its morphology and structure. Figure 5.26 shows the obtained HRTEM images and analysis for the EG700. The particle size has an average size of (155 ± 40) nm, and the coalescence between particles evidencing several diffraction contrasts, as seen in Fig. 5.26(a). As observed in Fig. 5.26(a,b), the presence of several diffraction contrasts is due to the overlap of several crystalline planes, which presents Moiré fringes as well, indicating the presence of defects in the material. Fig. 5.26(c) presents a magnification in the boundary between grown particles, showing the presence of TT and T phase, which the characteristic (130) – d = 0.521 nm – of T-Nb_2O_5 is in the image, and the presence of (001) – d = 0.396 nm - crystalline plane in the interface between the two particles, and the (100) – d = 0.320 nm - from the TT-Nb_2O_5. Fig. 5.26(d) shows a magnification on the particles interface, the separation between crystalline phases is an indication of phase transformation TT → T, where the

(130) do not exist in the TT phase, however, the presence of (001), which are present in both phases, are evidenced, which leads to the evidence that this crystalline plane plays an essential role on the phase transition.

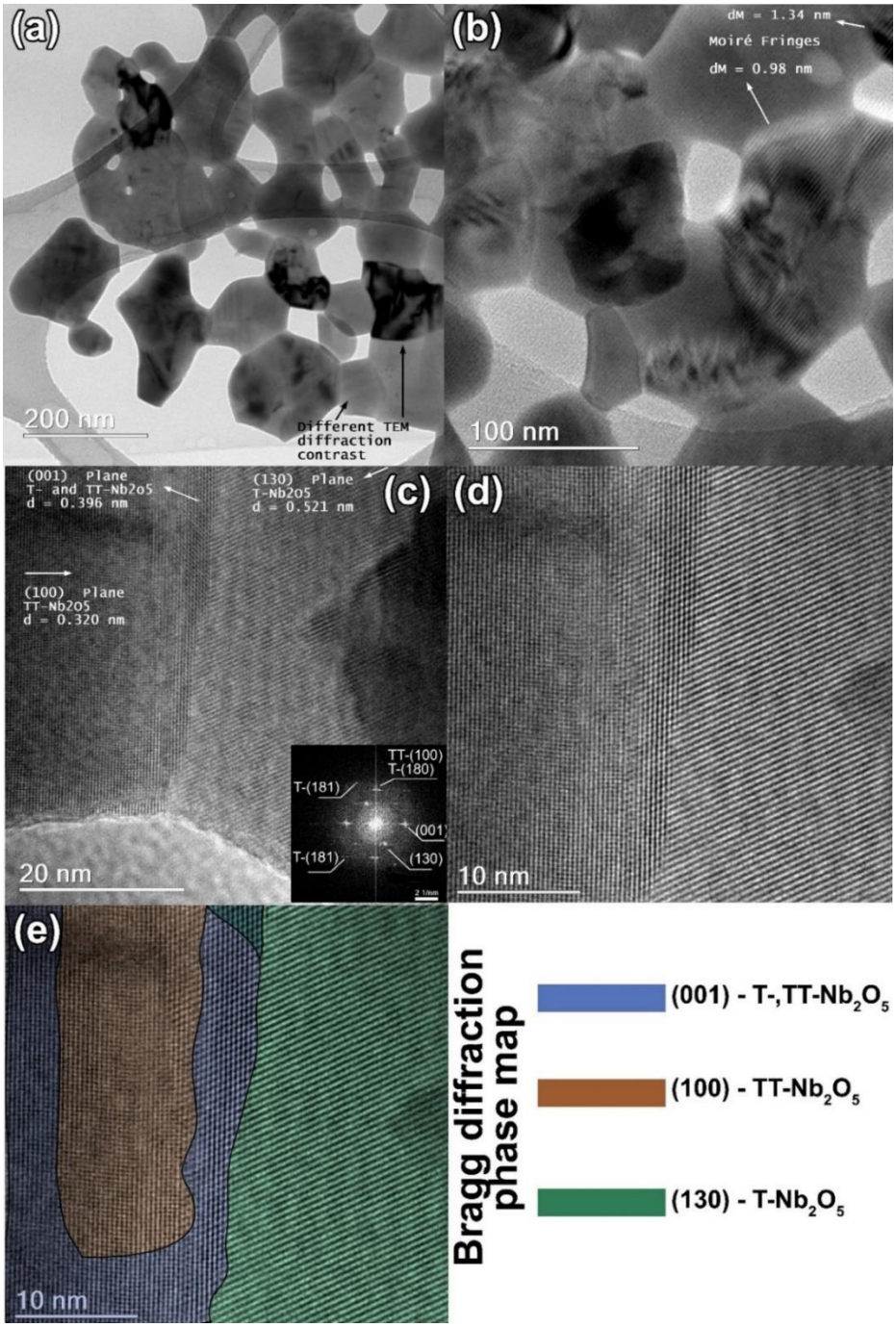

Figure 5. 26. TEM images of EG700, evidencing the (a) different diffraction contrasts, (b) presence of Moiré fringes, (c) interface between different crystalline orientations and phases, the extracted FFT, and (d) interface magnification of region on the (c). The (e) colored diffraction phase map of (d).

Figure 5.26(e) shows a Bragg diffraction filtered map, separating the crystallographic planes by colors represented on the right side of the image. The color

map indicates the T-modification on the right side, where the (130) crystallographic plane occurs. In the boundaries between the crystallographic domains, the existence of (001) phase, a shared crystallographic plane between the T and TT modification, indicates that during the TT → T transition, the segregation of planes occurs, leading to a mixture and superposition of crystalline planes. Those findings corroborate the GPA analysis presented in subsection 4 of this chapter.

Figure 5.27 shows the indexed SAED pattern obtained from the region presented in Fig. 5.26(c). As discussed, the pattern presents a polycrystalline behavior, forming diffraction circles, indicating multiple orientations of the crystallographic planes. The presence of the (130) plane occurs as a faded spot near the (000) center, which indicates a higher d value for this plane (d = 0.522 nm). That analysis indicated the phase mixture and performed above expectation to determine crystallographic planes in the sample.

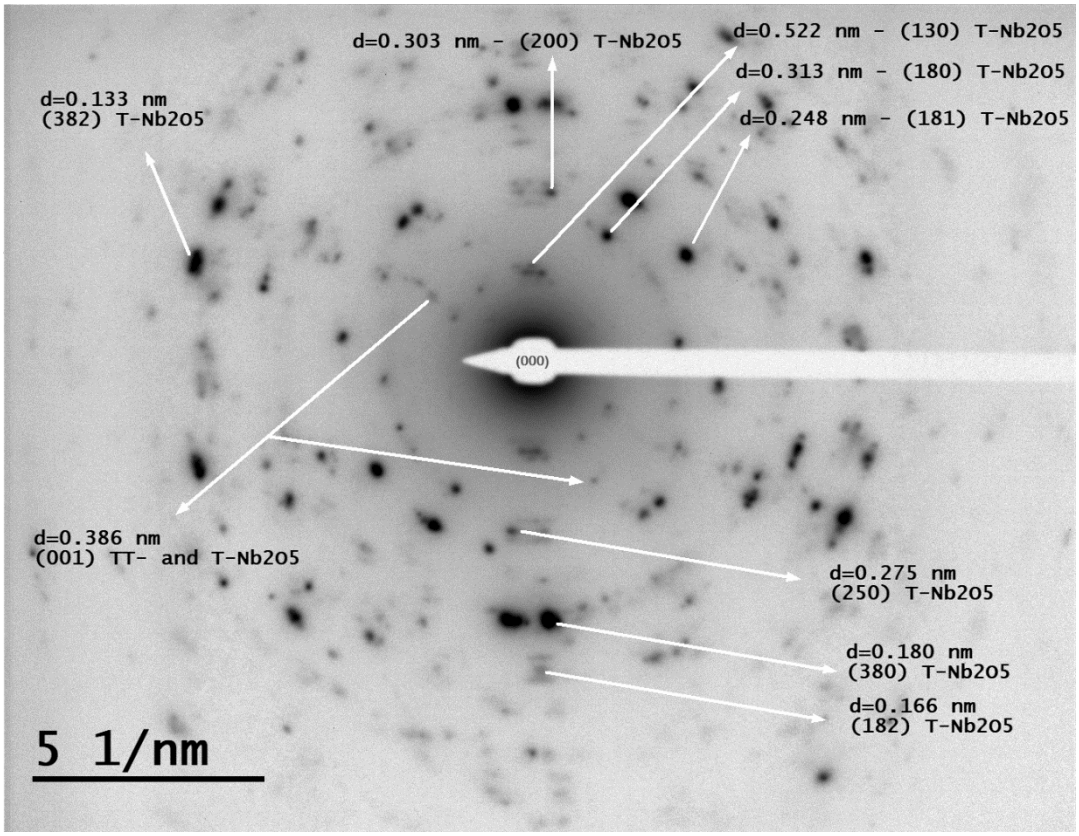

Figure 5. 27. Selected area electron diffraction (SAED) with applied reveal weak reflection filter from Fig. 5.26(c).

Figure 5.28 shows the TEM images from the samples calcined at 900 °C. The EG900 sample presented two distinct particle morphologies composing the sample,

shown in Figures 5.28(a.b), indicating H-Nb_2O_5 and the $Nb_{12}O_{29}$, where the non-stoichiometric phase shows smaller nanoparticles than H-modification, corroborating this the XRD analysis, where the crystallite size of the $Nb_{12}O_{29}$ is also smaller than H-Nb_2O_5. It is worth mention the phase mixture has a content of 72% H-Nb_2O_5 and 28% $Nb_{12}O_{29}$ calculated by Rietveld refinement, and the TEM analysis corroborates this finding, where most of the sample's investigation led to dense agglomeration of big nanoparticles, characteristic of the H-Nb_2O_5 in our investigation.

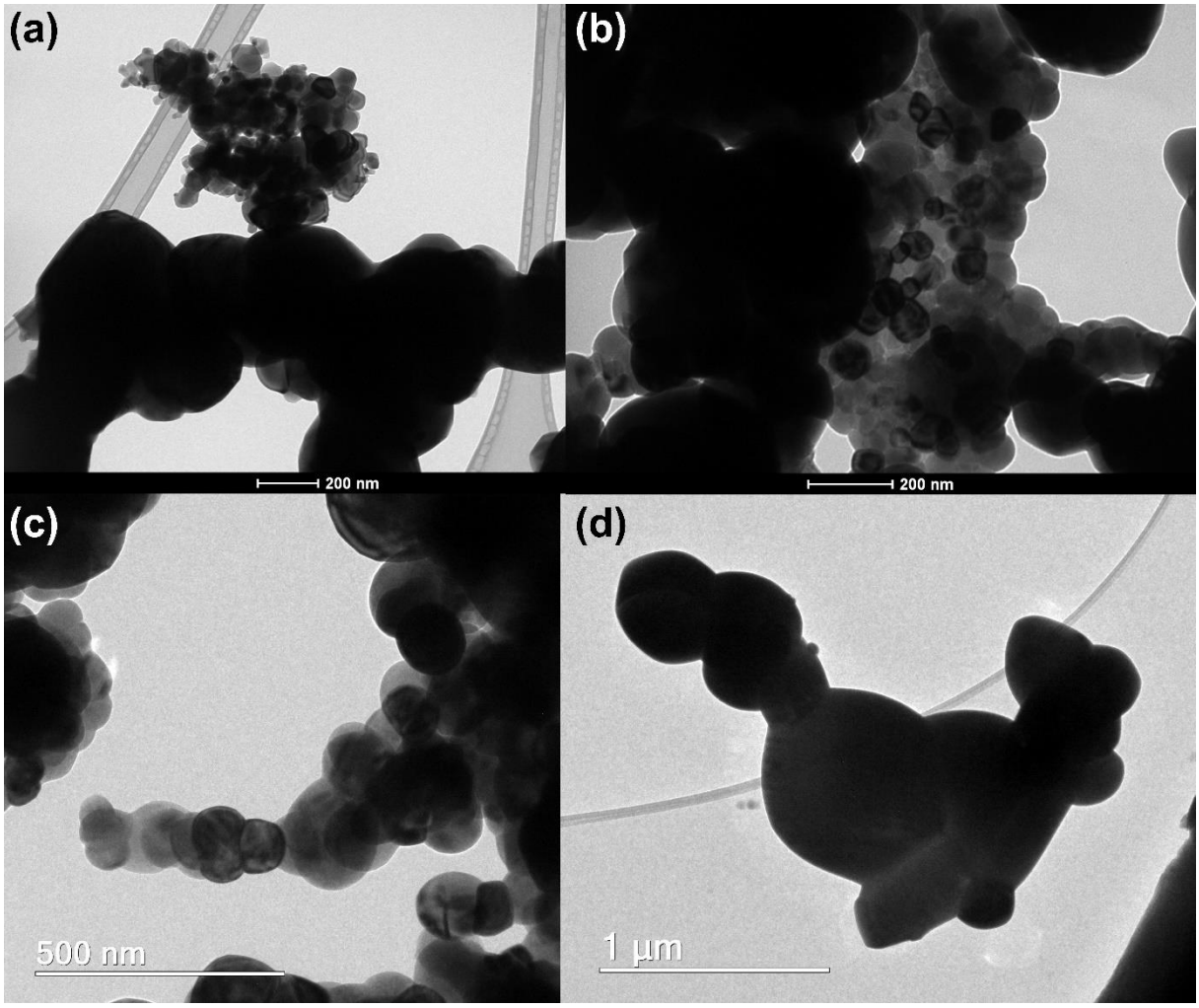

Figure 5. 28. TEM images from the (a,b) EG900, (c) PEG900, and (d) NbOX900.

Figure 5.28(c) shows the PEG900 sample, with large nanoparticles in a uniform distribution in all the investigated parts of the sample. This behavior corroborates the presence of only the T-Nb_2O_5 with large crystallite and nanoparticle size. The nanoparticles showed coalescence and densification, with the full release of all organic content in the Pechini synthesis. The temperature rise caused the collapse of

the porous network for EG900 and PEG900, leading to a dense agglomeration of nanoparticles at several contrasts. Figure 5.28(d) shows the NbOX900 sample, as a dense particle agglomeration, with a size ranging between 200 – 900 nm. The lack of a polymeric chain in the synthetical route leads to different materials at high temperatures, where the EG900 and PEG900 kept some porous structure in all the samples and presented smaller nanoparticle sizes compared with NbOX900. Despite the presence of H and T phase mixture in the NbOX900, there was no clear distinction between particle morphology in the TEM analysis, showing the beginning of the sintering process for the NbOX900 particles. Those finds about the NbOX900 prove another feature for the Pechini synthesis, where the polymeric template inhibits the crystallite growth at higher temperatures, which makes possible by the presence of defects in the crystalline system and the presence of a long-range porous network.

References

[1] B. Toby, EXPGUI, a graphical user interface for GSAS, Journal of Applied Crystallography 34(2) (2001) 210-213.
[2] K.M.a.F. Izumi, VESTA 3 for three-dimensional visualization of crystal, volumetric and morphology data, J. Appl. Crystallogr. 44 (2011) 1272-1276.
[3] P. Juhás, T. Davis, C.L. Farrow, S.J.L. Billinge, PDFgetX3: A rapid and highly automatable program for processing powder diffraction data into total scattering pair distribution functions, pdfJ. Appl. Crystallogr. 46 (2013) 560-566.
[4] C.L. Farrow, P. Juhas, J.W. Liu, D. Bryndin, E.S. Božin, J. Bloch, T. Proffen, S.J.L. Billinge, PDFfit2 and PDFgui: computer programs for studying nanostructure in crystals, Journal of Physics: Condensed Matter 19(33) (2007) 335219.
[5] V. I. Korsunskiy, R.B. Neder, A. Hofmann, S. Dembski, C. Graf, E. Rühl, Aspects of the modelling of the radial distribution function for small nanoparticles, Journal of Applied Crystallography 40(6) (2007) 975-985.
[6] D.R.G. Mitchell, DiffTools: Electron diffraction software tools for DigitalMicrograph™, Microscopy Research and Technique 71(8) (2008) 588-593.
[7] M.J. Hÿtch, E. Snoeck, R. Kilaas, Quantitative measurement of displacement and strain fields from HREM micrographs, Ultramicroscopy 74 (1998) 131—146.
[8] K. KATO, Structure Refinement of H-Nb_2O_5, Acta Cryst 1976(B32) (1975) 764.
[9] C. Nico, T. Monteiro, M.P.F. Graça, Niobium oxides and niobates physical properties: Review and prospects, Progress in Materials Science 80 (2016) 1-37.
[10] H. Schäfer, R. Gruehn, F. Schulte, The Modifications of Niobium Pentoxide, Angewandte Chemie International Edition in English 5(1) (1966) 40-52.

[11] R. Brayner, F. Bozon-Verduraz, Niobium pentoxide prepared by soft chemical routes: morphology, structure, defects and quantum size effect, Physical Chemistry Chemical Physics 5(7) (2003) 1457-1466.
[12] L.I. Skatkov, V.P. Gomozov, B.I. Bayrachnyi, Effect of impurities in niobium on the concentration of defects in Nb_2O_5 anode oxide films, Physics and chemistry of materials treatment 24(2) (1990) 169-171.
[13] L.K.S. Herval, D. von Dreifus, A.C. Rabelo, A.D. Rodrigues, E.C. Pereira, Y.G. Gobato, A.J.A. de Oliveira, M.P.F. de Godoy, The role of defects on the structural and magnetic properties of Nb_2O_5, Journal of Alloys and compounds 653 (2015) 358-362.
[14] N. Kumari, K. Gaurav, S.K. Samdarshi, A.S. Bhattacharyya, S. Paul, B. Rajbongshi, K. Mohanty, Dependence of photoactivity of niobium pentoxide (Nb_2O_5) on crystalline phase and electrokinetic potential of the hydrocolloid, Solar Energy Materials and Solar Cells 208 (2020) 110408.
[15] Z. Liu, W. Dong, J. Wang, C. Dong, Y. Lin, I.W. Chen, F. Huang, Orthorhombic Nb_2O_{5-x} for Durable High-Rate Anode of Li-Ion Batteries, iScience 23(1) (2020) 100767.
[16] J. Chen, H. Wang, G. Huang, Z. Zhang, L. Han, W. Song, M. Li, Y. Zhang, Facile synthesis of urchin-like hierarchical Nb_2O_5 nanospheres with enhanced visible light photocatalytic activity, Journal of Alloys and compounds 728 (2017) 19-28.
[17] M. Joya, J. Barba Ortega, A. Raba Paez, J. da Silva Filho, P. Cavalcante Freire, Synthesis and Characterization of Nano-Particles of Niobium Pentoxide with Orthorhombic Symmetry, Metals 7(4) (2017) 142.
[18] J.G. Weissman, E.I. Ko, P. Wynblatt, J.M. Howe, High-Resolution Electron Microscopy and Image Simulation of TT-, T-, and H-Niobia and Model Silica-Supported Niobium Surface Oxides, Chemistry of Materials 1(2) (1989) 187-193.
[19] K. Kato, S. Tamura, Die Kristallstruktur von T-Nb_2O_5, Acta Crystallographica Section B 31(3) (1975) 673-677.
[20] A.M. Raba, J. Bautista-Ruíz, M.R. Joya, Synthesis and Structural Properties of Niobium Pentoxide Powders: A Comparative Study of the Growth Process, Materials Research 19(6) (2016) 1381-1387.
[21] C.L. Ücker, F.C. Riemke, N.F. de Andrade Neto, A.d.A.G. Santiago, T.J. Siebeneichler, N.L.V. Carreño, M.L. Moreira, C.W. Raubach, S. Cava, Influence of Nb_2O_5 crystal structure on photocatalytic efficiency, Chemical Physics Letters 764 (2021) 138271.
[22] J.S. Anderson, J.M. Browne, J.L. Hutchison, Electron microscopy of the niobium oxides. I. Twinning and defects in H-Nb_2O_5, Journal of Solid state Chemistry 5(3) (1972) 419-431.
[23] J.S. Anderson, J.L. Hutchison, F.J. Lincoln, Dislocations and Related Defects in Niobium Oxide Structures, Proceedings of the Royal Society of London. Series A, Mathematical and Physical Sciences 352(1670) (1977) 303-323.
[24] B.H. Toby, R factors in Rietveld analysis: How good is good enough?, Powder Diffraction 21(1) (2006) 67-70.
[25] G.H.M. Gomes, N.D.S. Mohallem, CCDC 2103847: Experimental Crystal Structure Determination, ICSD Communication, 2021.

[26] Y. Wang, W. Zhang, Mapping the strain distribution within embedded nanoparticles via geometrical phase analysis, Micron 125 (2019) 102715.
[27] Y. Wang, J. Yu, X. Zhang, A geometric phase analysis method dedicated to nanomaterials orienting along high-index zone axis, Micron 113 (2018) 20-23.
[28] G.H. de M. Gomes, R.R. de Andrade, N.D.S. Mohallem, Investigation of phase transition employing strain mapping in TT- and T-Nb_2O_5 obtained by HRTEM micrographs, Micron (2021) 103112.
[29] L.F.d.S. Lima, C.R. Coelho, G.H.M. Gomes, N.D.S. Mohallem, Nb_2O_5/SiO_2 mesoporous monoliths synthetized by sol–gel process using ammonium niobate oxalate hydrate as porogenic agent, Journal of Sol-Gel Science and Technology 93(1) (2019) 168-174.

Chapter 6 – Electronic properties of niobium pentoxide

INTRODUCTION

This chapter presents a comprehensive study of the electronic properties of synthesized niobium pentoxide materials. The discussion is based on studying quantitatively and qualitatively the presence of defects in the crystal structure and phase mixture and how it affects the niobium oxidation state, the absorption in the UV-visible region, and the magnetic properties through spin resonance.

1. Methodology

1.1. Diffuse reflectance spectroscopy (DRS)

The Diffuse Reflectance Spectroscopy (DRS) was performed on a Shimadzu 3550 diffuse reflectance spectrophotometer located at the Chemistry Department of UFMG, with an analysis range from 200 to 1400 nm, using $BaSO_4$ as reference material. The analysis used 10 mg of each material to obtain the DRS spectra.

1.2. X-ray photoelectron spectroscopy (XPS)

The X-ray photoelectron spectroscopy (XPS) employed Thermo Scientific K-Alpha equipment located at the Plasma Laboratory (LPFS) at UDESC-Joinville. All spectra used an Al Kα source gun, a spot size of 400 μm, and standard lens mode. All the survey spectra used the constant analyzer energy (CAE) mode, with a pass energy of 200.00 eV and energy step size of 1.000 eV. The Nb 3d and O 1s spectra were recorded using CAE analyzer mode, pass energy of 50.00 eV, and an energy step size of 0.100 eV. The deconvolution analysis of all spectra was employed using the OriginLab and PeakFit software.

1.3. Electron paramagnetic resonance (EPR)

EPR measurements employed a MiniScope MS400 spectrometer (Magnettech, Germany) operating at X-band (~9.40 GHz) located at the Physics Department of

UFMG. The experimental parameters used were: microwave power 10 mW, 100 kHz field modulation amplitude 0.2 mT, central field 337 mT, and scan time 60 s. To acquire powdered niobium pentoxides spectra, they were weighed and placed in an ultra-pure quartz tube (Wilmad Labglass, USA). The quantification of paramagnetic species (with a 10% error) was performed by double integration of the paramagnetic signals, and the concentration values were obtained using dry vanadyl sulfate standard ($VOSO_4$).

2. The influence of defects in the Nb_2O_5 electronic properties

Figure 6.1(a,b,c) shows the UV-visible range diffuse reflectance spectra (DRS) and their respective band-gap plot for all synthesized samples. There is a step absorption around the band-gap values for all samples, indicating the electronic transition valence band-conduction band (VB → CB). The band-gap values were calculated using the Kubelka-Munk (K—M) method to approximate the extinction coefficient and the traditional Tauc method to calculate the in direct band-gap. The K—M method is suitable for photocatalytic materials and based on the following equation

$$\alpha \sim F(R) = \frac{(1-R)^2}{2R}$$

F(R) is proportional to the extinction coefficient (α), and R is the reflectance value. The traditional Tauc method [1] consists in approximate the absorption at the edge of the VB → CB transition, described by

$$\alpha(hv) \approx B(hv - E_g)^n$$

E_g is the optical band-gap, hv is the photon energy, B is a constant, and α is the extinction coefficient, proportional to F(R). The n corresponds to the electronic transition, in which n = 2 is for an indirect allowed transition and n = ½ for a direct allowed transition. The band-gap value is obtained by plotting the $(F(R)hv)^{\wedge 1/n}$ versus the photon energy (hv), then a linear curve is obtained, extrapolating the slop to α = 0.

The obtained band-gap values agree with the literature values, as shown in Figure 6.1(d), where the synthesis method can change the band-gap of Nb_2O_5 nanoparticles. The samples EG500, EG700, PEG500, EG700, and NbOX500, show an additional absorption in the visible region (400 – 700 nm). The absorption in the visible region is

associated with defects in the crystal structure. Those defects create energy levels between the VB and CB, and these intervalence transition occurs at lower photon energy than the optical E_g. The defects intrinsically correlate with the studied crystal phase, which is known that the TT-Nb_2O_5 is stabilized in the presence of defects and trace impurities.

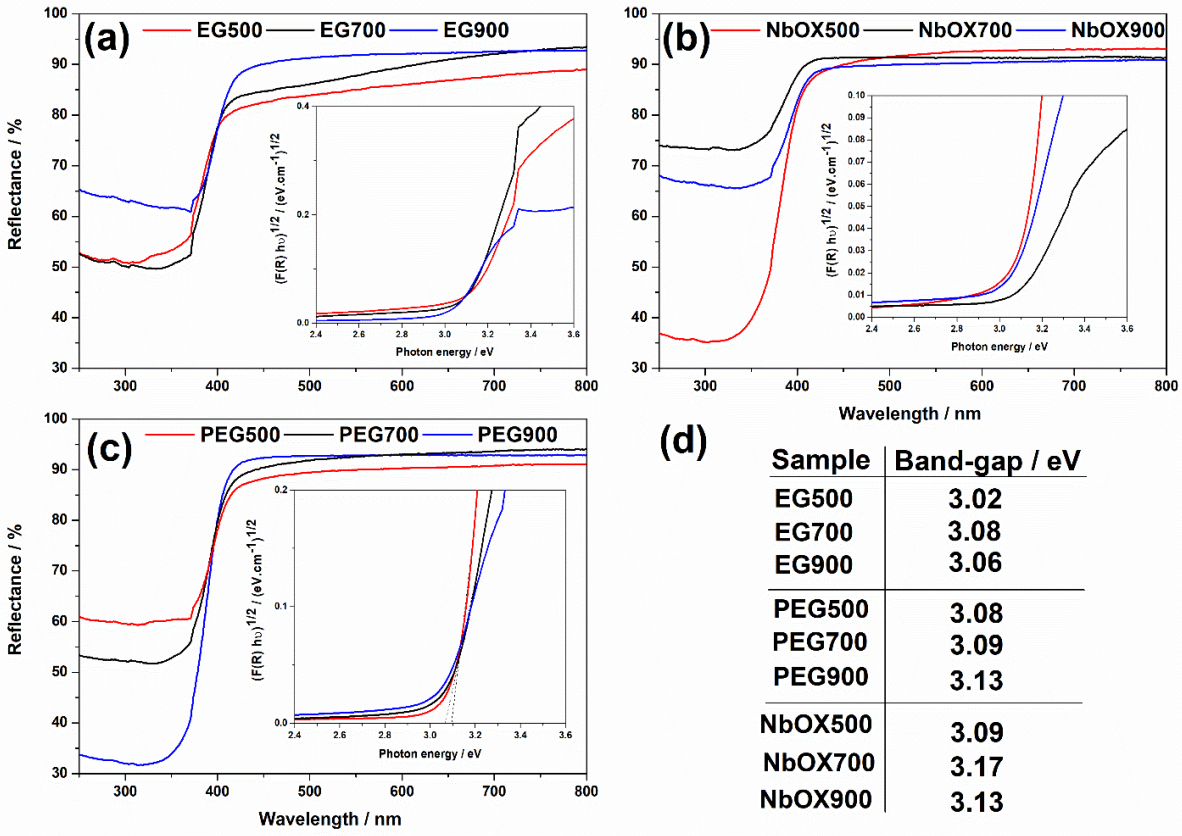

Figure 6. 1. Diffuse reflectance spectra of niobium pentoxide materials on (a) EG series, (b) NbOx, and (c) PEG. The table contains the (d) calculated optical band-gap for all samples.

The defects occur due to oxygen vacancies (described as neutral (V_o), singly (V_o^+) or doubly charged (V_o^{2+}) oxygen vacancies), and formation of Nb^{4+} species, which can be ascribed according to Kröger-Vink notation

$$O_o^x \rightleftarrows \frac{1}{2}O_{2(g)} + V_o$$

$$V_o \rightleftarrows V_o^+ + e^-$$

$$V_o^+ \rightleftarrows V_o^{2+} + e^-$$

$$2Nb^{5+} + V_o \rightleftarrows 2Nb^{4+} + V_o^{2+}$$

Those defects generate energy levels in the semiconductor forbidden energy band, as qualitatively represented in Figure 6.2. Nb^{4+} species generated by oxygen vacancies promote electrons populating intermediate energy levels, absorbing lower energy values (E'_g). Isolated Nb^{4+} species are paramagnetic with one unpaired electron (S = 1/2), and Nb^{5+} is diamagnetic (S =0). The Nb^{4+} species serve as electron donors since the electron can promote the conduction band, favoring the material's photocatalytic processes. These phenomena may explain the greyish color of the EG 500 after degasification, as shown in Figure 6.3, evidencing the presence of absorption levels in the visible range, like reported in some previous works [2-4].

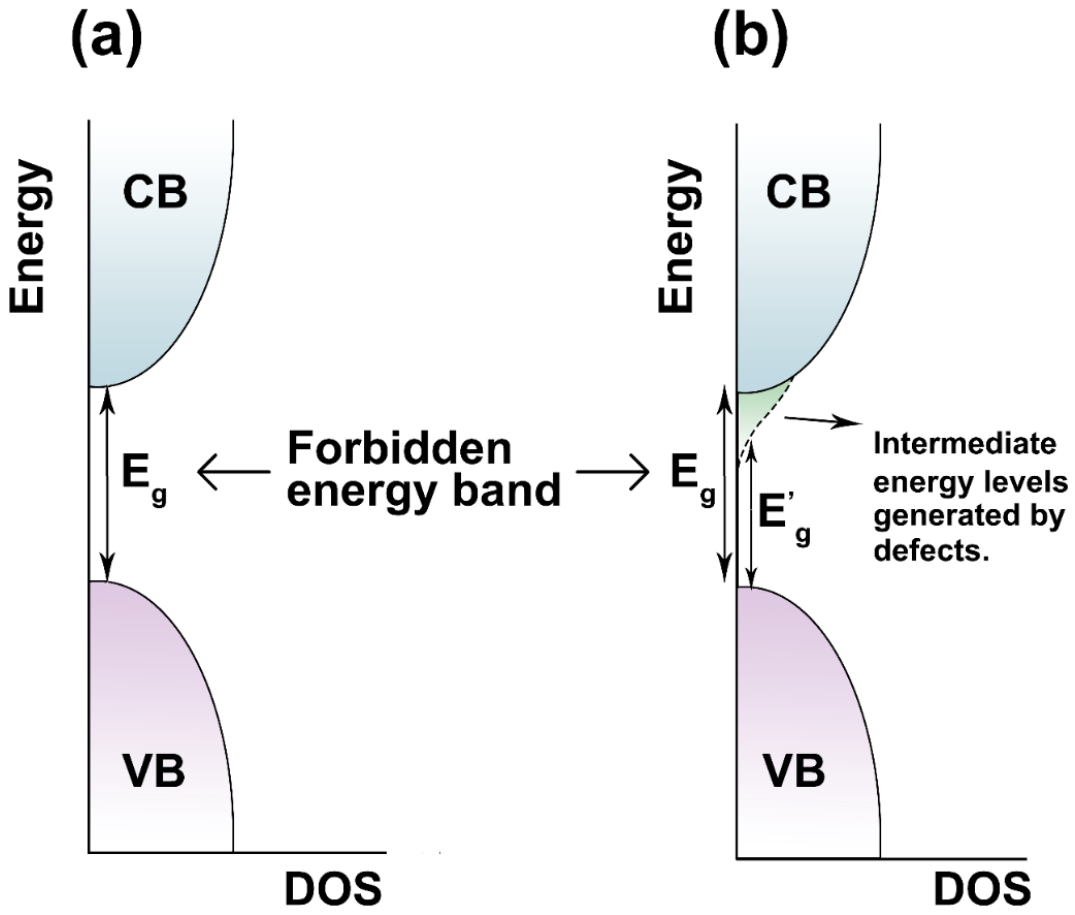

Figure 6. 2. Qualitative representation of the conduction band (CB) and valence band (VB) diagram of Nb_2O_5 - Evidencing intermediate levels at the forbidden levels.

X-ray photoelectron spectroscopy (XPS) investigated all sample composition and oxidation states. The XPS survey spectra of the samples calcined at 500 °C are in Figure 6.4. The recorded spectra show the presence of Nb and O for all samples, with no signal of trace impurities on the surface. Figure 6.5(a,c,e) shows the Nb 3d XPS spectra for the

EG500, PEG500, and NbOX500 samples, respectively. All samples presented two prominent bands with higher intensity, centered around 206.5 and 209.3 eV, which correspond to the spin-orbit splitting of the Nb^{5+} 3d orbital, into the $3d_{5/2}$ and $3d_{3/2}$, respectively. The EG500 and PEG500 samples show an Nb 3d binding energy redshift compared with NbOX500, indicating Nb^{4+} or Nb^{5+} - V_o species. The deconvolution of Nb 3d XPS spectra showed that the EG 500 and PEG 500 presented the peaks corresponding to the Nb^{4+} species, centered at 206.00 and 207.45 eV, previous corroborating works in the literature [5-7].

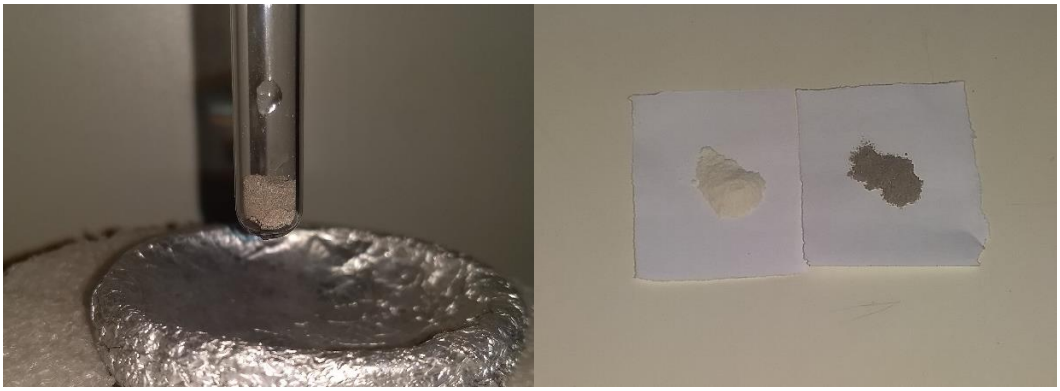

Figure 6. 3. EG500 samples during, before, and after the degasification process for gas adsorption analysis.

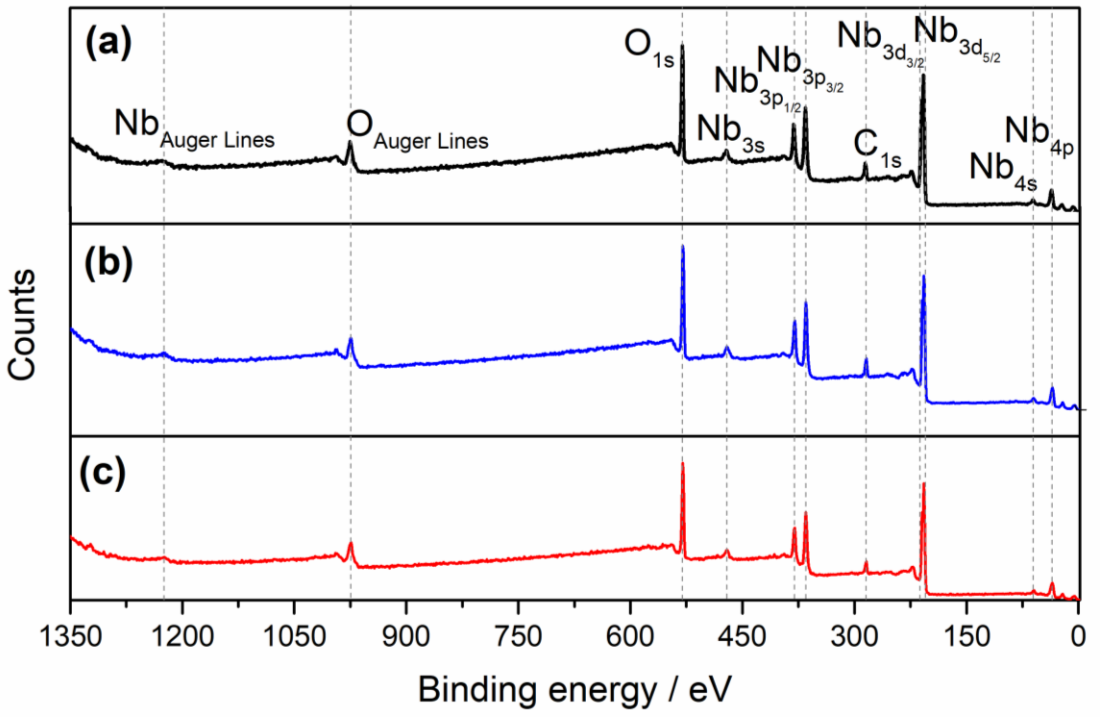

Figure 6. 4. XPS survey spectra from the (a) EG500, (b) PEG500, and (c) NbOX500.

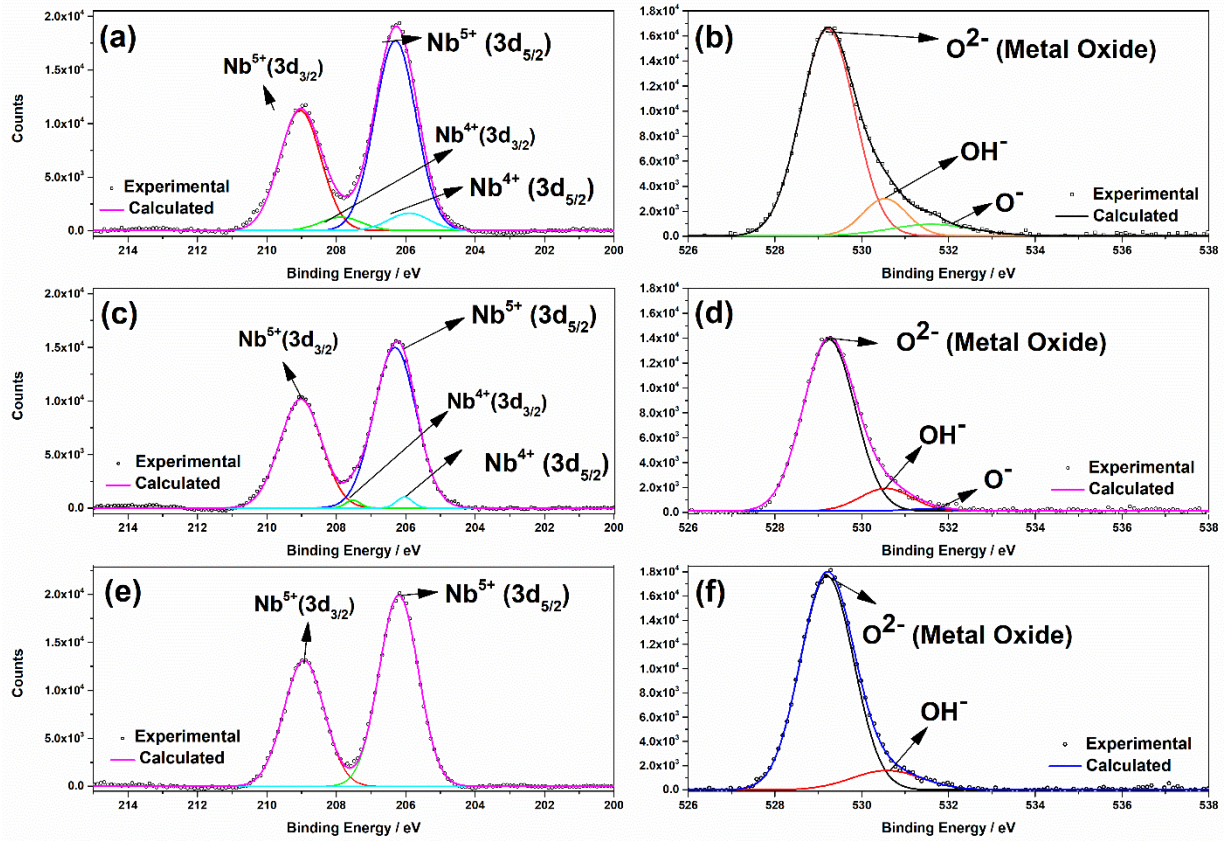

Figure 6. 5. Respective XPS spectra of Nb 3d and O 1s of (a,b) EG500, (c,d) PEG500, and (e,f) NbOX500.

The quantitative analysis of EG 500, PEG 500, and NbOX500 showed 8.33, 2.46, and 0.00% atomic weight of Nb^{4+}, respectively. These values corroborate the DRS analysis, where the EG500 shows stronger absorption in the visible region. It is worth mentioning that all deconvolution and quantitative performed calculations respected some constraints, such as the same FWHM for all peaks, the Nb 3d area ratio (3:2), constant spin-orbit splitting energy (2.7 eV), and the correct sensitivity factor [7, 8].

The XPS spectra of the oxygen species are presented in Figure 6.5(b,d,f) for EG500, PEG500, and NbOX500, respectively. All samples show a high-intensity band centered around 529.20 eV, corresponding to the O^{2-} species in the metal oxide crystal structure [9, 10]. The deconvolution of the O 1s spectra shows two species for NbOX500 and three for EG500 and PEG500. The binding energy centered around 530.55 eV attributed to hydroxyl groups on the material's surface present in all samples [9]. The EG500 and PEG500 present a low-intensity peak centered around 531.6 eV, corresponding to a less negative oxygen species (O^-). The O^- species could be described as having a higher covalence of Nb—O bonding, which presents lower electron density than the lattice O^{2-}

ions. The presence of O^- species occurs due to the presence of Nb^{4+} species in the material generated by oxygen vacancies, as the formation of O^- occurs to allow some charge and deficiencies compensation in the metal oxide subsurface [9].

The calculated atomic weight of the oxygen species and the O^- species are present only in the EG500 and PEG500 samples with a concentration of 8.14% and 2.18%, respectively, corroborating the Nb^{4+} atomic fractions. Table 6.1 summarizes the XPS data from the EG500, PEG500, and NbOX500 samples.

Table 6. 1. Quantitative XPS data of the niobium pentoxide samples calcinated at 500 °C.

Sample	EG500	PEG500	NbOX500	Reference
Binding Energy / eV ± 0.05				
Nb^{5+} ($3d_{5/2}$)	206.30	206.31	206.91	207.5—206.9
Nb^{5+} ($3d_{3/2}$)	209.04	209.03	209.53	210.2—209.2
ΔE (Nb^{5+} 3d)	2.74	2.72	2.72	2.7
Nb^{4+} ($3d_{5/2}$)	205.90	206.00	-	207.60—205.20
Nb^{4+} ($3d_{3/2}$)	207.43	207.52	-	-
Nb^{5+} Area ratio ($3d_{5/2}/3d_{3/2}$)	1.55	1.48	1.47	1.50
Nb^{4+} Area ratio ($3d_{5/2}/3d_{3/2}$)	1.44	1.53	-	1.50
O 1s (O^{2-})	529.21	529.24	529.20	530.5—527.7
O 1s (OH^-)	530.53	530.55	530.57	530.5—531.0
O 1s (O^-)	531.61	531.59	-	531.0—532.0
Atomic Weight (%)				
Nb^{5+}	91.67	97.54	100.00	-
Nb^{4+}	8.33	2.46	0.00	-
O^{2-}	80.12	87.39	89.54	-
OH^-	11.74	10.43	10.46	-
O^-	8.14	2.18	0.00	-

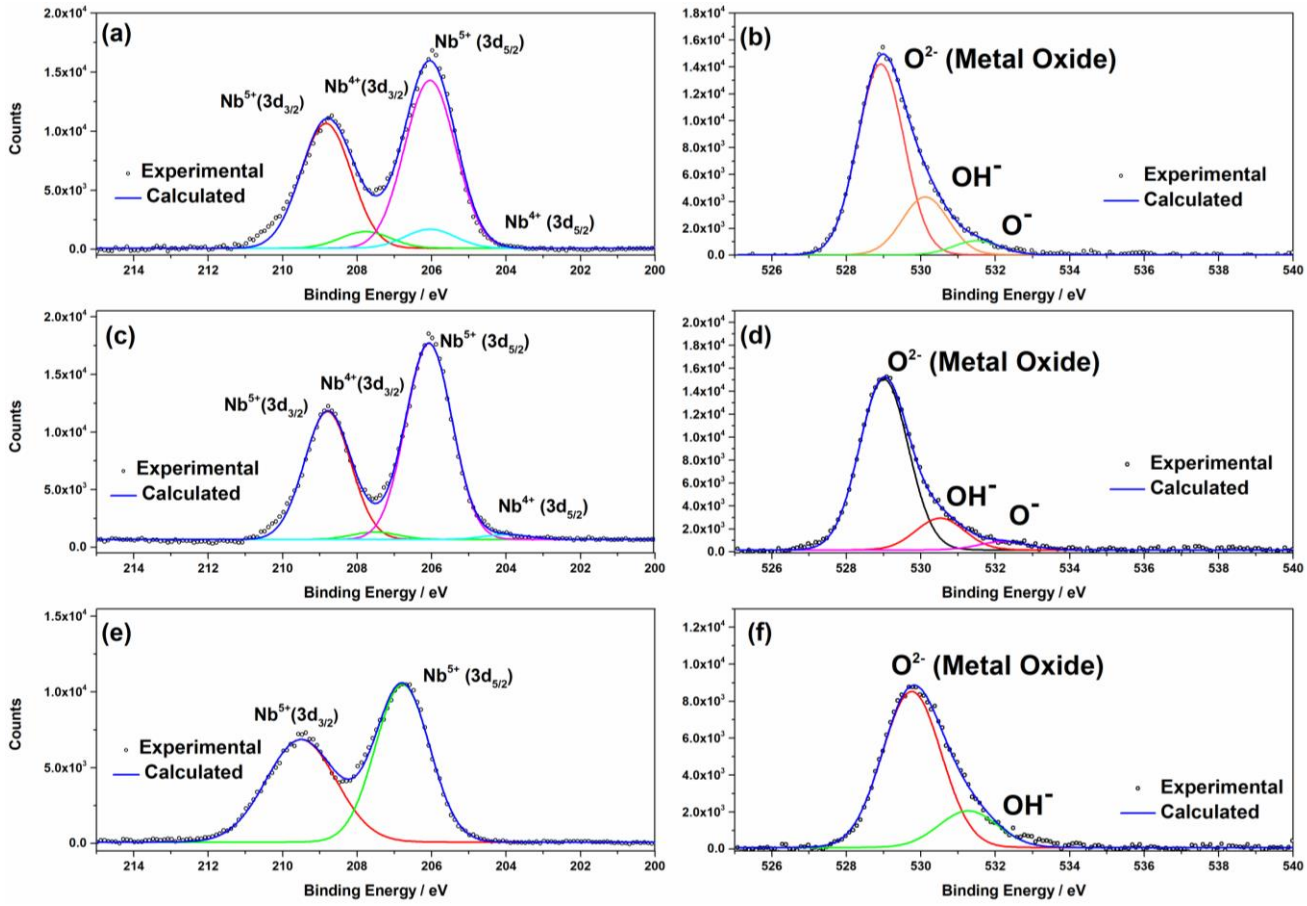

Figure 6. 6. Respective XPS spectra of Nb 3d and O 1s of (a,b) EG700, (c,d) PEG700, and (e,f) NbOX700.

Figure 6.6(a,c,e) shows the Nb 3d XPS, and Figure 6.6(b,d,f) the O 1s XPS spectra for the EG700, PEG700, and NbOX700 samples, respectively. The same behavior presented by the samples calcinated at 500 °C occurred in the EG700, PEG700, and NbOX700. The Pechini samples presented a low amount of Nb^{4+} cations and less negative oxygen species (O-), which indicates defects in the crystal structure, as previously stated. The NbOX700 presented 0.00% of Nb^{4+} cations, and hydroxyl groups decreased on the material's surface due to the increase at the calcination temperature that lowered the number of acid sites on the material [11, 12]. The same behavior for the hydroxyl species occurs for the EG700 and PEG700.

Table 6.2 summarizes all the quantitative data obtained from the XPS spectra of the samples calcinated at 700 °C. There is a decrease in the number of Nb^{4+} in the EG700 sample, expected by the rise at the calcination temperature. The obtained values

for the O^- species agree with the Nb^{4+}, showing that the Pechini resin leads to defects in the crystalline system.

Table 6. 2. Quantitative XPS data of the niobium pentoxide samples calcinated at 700 °C.

Sample	EG700	PEG700	NbOX700	Reference
Binding Energy / eV ± 0.05				
Nb^{5+} ($3d_{5/2}$)	206.09	206.07	206.78	207.5—206.9
Nb^{5+} ($3d_{3/2}$)	208.83	208.79	209.51	210.2—209.2
ΔE (Nb^{5+} 3d)	2.74	2.72	2.73	2.7
Nb^{4+} ($3d_{5/2}$)	206.04	205.01	-	207.60—205.20
Nb^{4+} ($3d_{3/2}$)	207.77	207.51	-	-
Nb^{5+} Area ratio ($3d_{5/2}/3d_{3/2}$)	1.43	1.53	1.39	1.50
Nb^{4+} Area ratio ($3d_{5/2}/3d_{3/2}$)	1.29	1.54	-	1.50
O 1s (O^{2-})	528.92	529.01	529.76	530.5—527.7
O 1s (OH^-)	530.52	530.52	531.05	530.5—531.0
O 1s (O^-)	531.49	532.02	-	531.0—532.0
Atomic Weight (%)				
Nb^{5+}	92.62	96.37	100	-
Nb^{4+}	7.38	3.63	0.00	-
O^{2-}	84.70	86.74	93.88	-
OH^-	10.04	9.87	6.12	-
O^-	5.26	3.39	0.00	-

Figure 6.7(a,c,e) shows the Nb 3d XPS, and Figure 6.7(b,d,f) the O 1s XPS spectra for the EG900, PEG900, and NbOX900 samples, respectively. Except for the EG900, all the samples did not present the Nb^{4+} and O^- signal, indicating no defects in the crystal structure. However, the EG900 presented a small concentration of Nb^{4+} cation, which corresponds to the presence of the $Nb_{12}O_{29}$ phase in the sample. All samples

presented a lower concentration of the surface hydroxyl groups, characteristic of niobium pentoxide calcined at high temperatures.

Table 6.3. summarizes the XPS data from the samples calcined at 900 °C. All samples presented good analysis results, with energy differences around 2.7, $3d_{5/2,}$ and $3d_{3/2}$ ratio of 1.5, and right binding energy center. There is a strong redshift in the Nb^{5+} ($3d_{5/2}$) orbital energy in the EG900 sample, indicating the presence of niobium atoms in a lower oxidation state. The PEG900 and NbOX900 did not show this redshift, corroborating the XRD quantitative analysis and the presence of phase mixture in the EG900. The calculated Nb^{4+} for the EG900 is 3.55%, agreeing with the 2.29% atomic fraction of O^- species in the crystal sublattice.

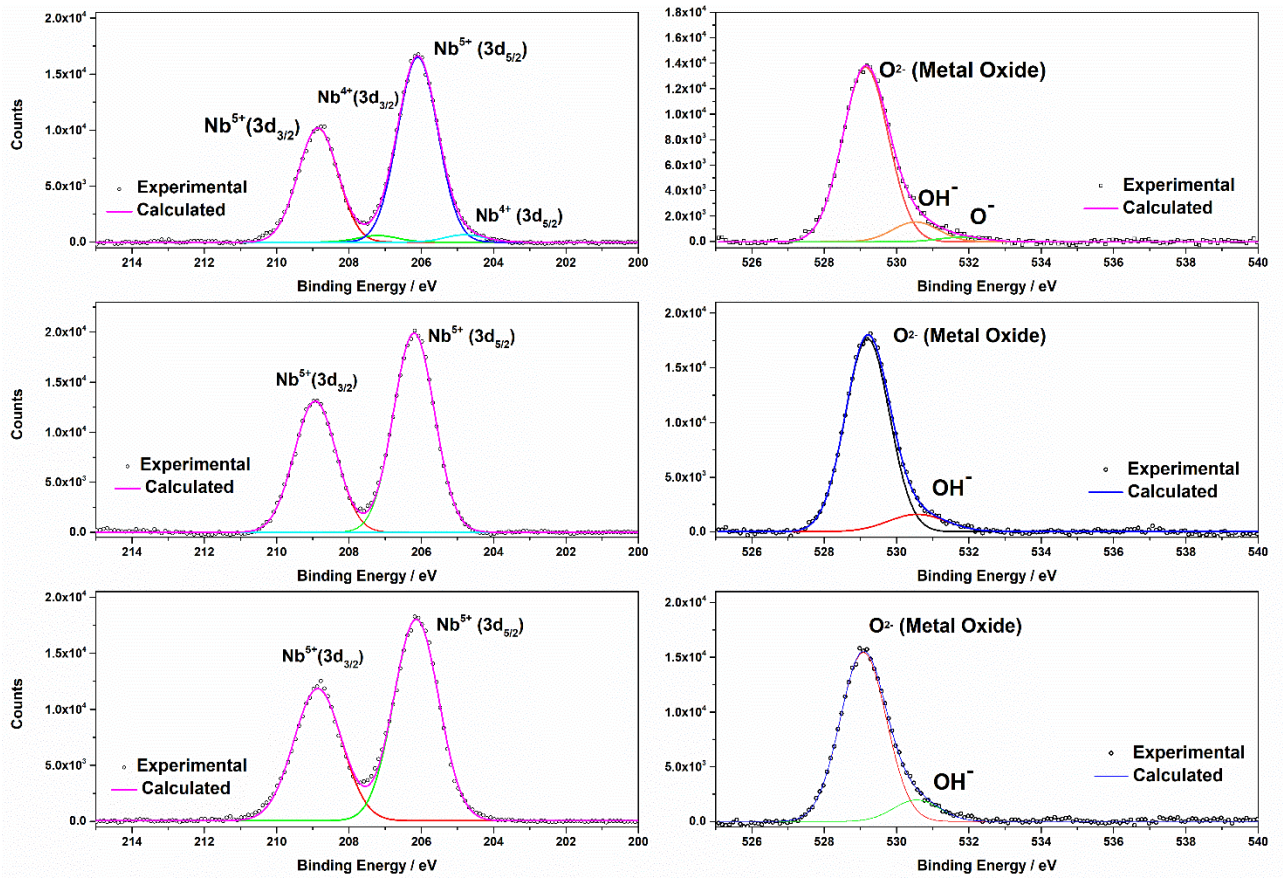

Figure 6. 7. Respective XPS spectra of Nb 3d and O 1s of (a,b) EG900, (c,d) PEG900, and (e,f) NbOX900.

Table 6. 3. Quantitative XPS data of the niobium pentoxide samples calcinated at 900 °C.

Sample	EG900	PEG900	NbOX900	Reference
Binding Energy / eV ± 0.05				
Nb^{5+} ($3d_{5/2}$)	206.10	207.14	207.11	207.5—206.9
Nb^{5+} ($3d_{3/2}$)	208.86	208.90	209.72	210.2—209.2
ΔE (Nb^{5+} 3d)	2.76	2.76	2.71	2.7
Nb^{4+} ($3d_{5/2}$)	204.80	-	-	207.60—205.20
Nb^{4+} ($3d_{3/2}$)	207.21	-	-	-
Nb^{5+} Area ratio ($3d_{5/2}/3d_{3/2}$)	1.61	1.44	1.48	1.50
Nb^{4+} Area ratio ($3d_{5/2}/3d_{3/2}$)	1.35	-	-	1.50
O 1s (O^{2-})	529.15	529.08	529.10	530.5—527.7
O 1s (OH^-)	530.52	530.55	530.51	530.5—531.0
O 1s (O^-)	531.79	-	-	531.0—532.0
Atomic Weight (%)				
Nb^{5+}	96.45	100	100	-
Nb^{4+}	3.55	0	-	-
O^{2-}	87.74	90.70	92.56	-
OH^-	9.97	9.30	7.44	-
O^-	2.29	0	0	-

It is known that XPS analysis could lead to misinformation. To show the excellent fit for all our analyses, Table 6.4 shows the adjusted R^2 for all the deconvoluted samples, proving the best fit since all samples presented $R^2 > 0.99000$.

Table 6. 4. Coefficient of Determination and Adjusted R^2 for all XPS samples.

Sample	R^2 (COD)	Adjusted R^2
NbOX500 (O)	0.99781	0.99775
NbOX500 (Nb)	0.99870	0.99876
EG500 (O)	0.99834	0.99823
EG500 (Nb)	0.99871	0.99862
PEG500 (O)	0.99723	0.99717
PEG500 (Nb)	0.99867	0.99867
NbOX700 (O)	0.99489	0.99512
NbOX700 (Nb)	0.99646	0.99651
EG700 (O)	0.99642	0.99631
EG700 (Nb)	0.99375	0.99352
PEG700 (O)	0.99625	0.99609
PEG700 (Nb)	0.99793	0.99785
NbOX900 (O)	0.99612	0.99607
NbOX900 (Nb)	0.99746	0.99771
EG900 (O)	0.99721	0.99711
EG900 (Nb)	0.99873	0.99865
PEG900 (O)	0.99566	0.99555
PEG900 (Nb)	0.99762	0.99755

The powder EPR spectra (Figure 6.8) show that the EG500 and PEG500 have paramagnetic centers in their structure. Nevertheless, NbOX500 is diamagnetic. The EPR signal, shared by EG500 and PEG500, is characterized by an unresolved symmetric line. The EPR spectra analysis reveals that the electronic g-factor is equal to 2.005(1) with Lorentzian line shape and a full width at half maximum (FWHM) of ΔB_{pp} of 0.36 and 1.05 mT for the EG500 and PEG500 samples, respectively. Such a signal is related to single electron trapped oxygen vacancies, V_o^+ (SETOVs) generated during calcination in the presence of reducing agents [13, 14], in this case, ethylene glycol for

EG500 and polyethylene glycol for PEG500. The broader line width for the PEG500 sample may indicate a higher disorder in the vacancy neighborhood. The SETOVs concentration in the EG500 structure is approximately double that found for PEG500 with values of 20 nmol/g and 9 nmol/g, respectively. This result indicates that the substitution of alcohol in the synthesis modifies the degree of defects in the structure of the niobium oxides, enabling fine adjustments in their electronic properties.

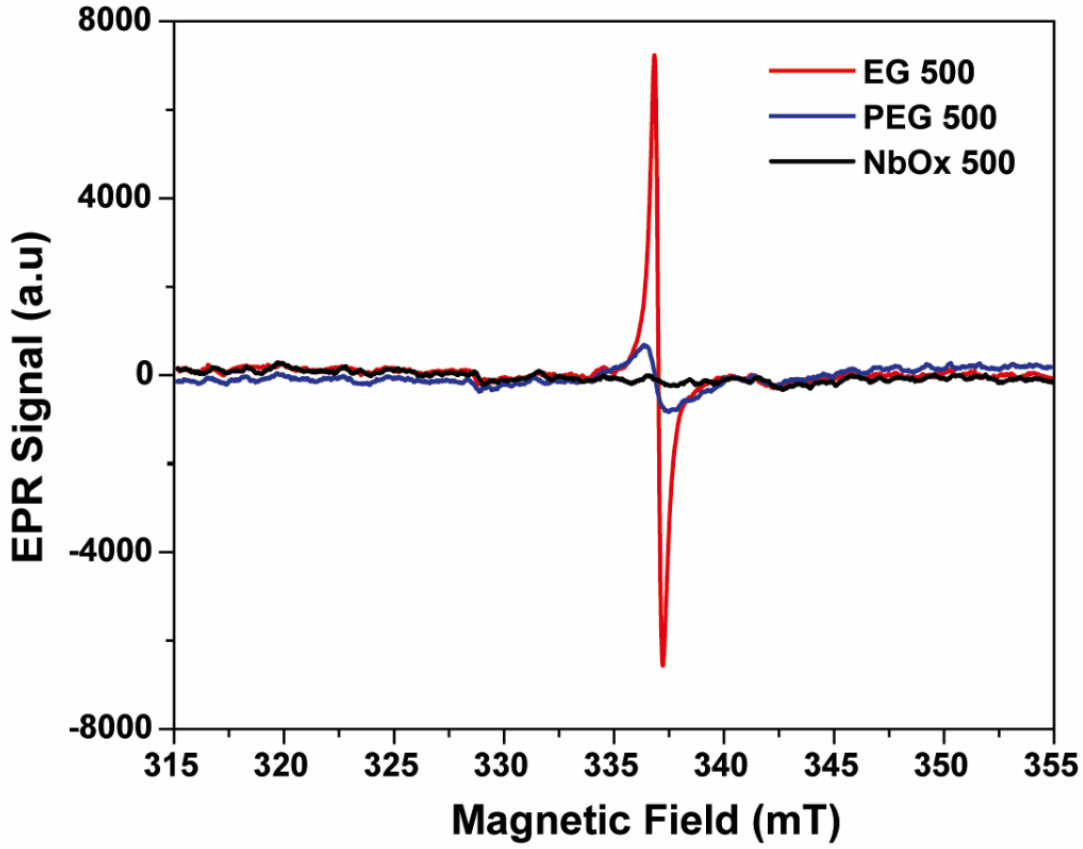

Figure 6. 8. Electron paramagnetic resonance powder spectra of niobium pentoxides obtained at room temperature and microwave frequency of ~9.40 GHz.

REFERENCES

[1] J. Tauc, R. Grigorovici, A. Vancu, Optical Properties and Electronic Structure of Amorphous Germanium, physica status solidi (b) 15(2) (1966) 627-637.
[2] B.T. da Fonseca, E. D'Elia, J.M. Siqueira Junior, S.M. de Oliveira, K.L. Dos Santos Castro, E.S. Ribeiro, Study of the characteristics and properties of the $SiO_2/TiO_2/Nb_2O_5$ material obtained by the sol-gel process, Sci Rep 11(1) (2021) 1106.
[3] J. Chen, H. Wang, G. Huang, Z. Zhang, L. Han, W. Song, M. Li, Y. Zhang, Facile synthesis of urchin-like hierarchical Nb_2O_5 nanospheres with enhanced visible light photocatalytic activity, Journal of Alloys and compounds 728 (2017) 19-28.

[4] A.V. Rosario, E.C. Pereira, The effect of composition variables on precursor degradation and their consequence on Nb_2O_5 film properties prepared by the Pecchini Method, Journal of Sol-Gel Science and Technology 38(3) (2006) 233-240.
[5] G. Taques Tractz, F. Staciaki da Luz, S. Regina Masetto Antunes, E. do Prado Banczek, M. Taras da Cunha, P. Rogério Pinto Rodrigues, Nb_2O_5 synthesis and characterization by Pechini method to the application as electron transport material in a solar device, Solar Energy 216 (2021) 1-6.
[6] Z. Liu, W. Dong, J. Wang, C. Dong, Y. Lin, I.W. Chen, F. Huang, Orthorhombic Nb_2O_{5-x} for Durable High-Rate Anode of Li-Ion Batteries, iScience 23(1) (2020) 100767.
[7] Z. Weibin, W. Weidong, W. Xueming, C. Xinlu, Y. Dawei, S. Changle, P. Liping, W. Yuying, B. Li, The investigation of $NbO_2$and Nb_2O_5electronic structure by XPS, UPS and first principles methods, Surface and Interface Analysis 45(8) (2013) 1206-1210.
[8] D.R. Baer, K. Artyushkova, C.R. Brundle, J.E. Castle, M.H. Engelhard, K.J. Gaskell, J.T. Grant, R.T. Haasch, M.R. Linford, C.J. Powell, A.G. Shard, P.M.A. Sherwood, V.S. Smentkowski, Practical Guides for X-Ray Photoelectron Spectroscopy (XPS): First Steps in planning, conducting and reporting XPS measurements, J Vac Sci Technol A 37 (2019).
[9] J.-C. Dupin, D. Gonbeau, P. Vinatier, A. Levasseur, Systematic XPS studies of metal oxides, hydroxides and peroxides, Physical Chemistry Chemical Physics 2(6) (2000) 1319-1324.
[10] A.I. Boronin, S.V. Koscheev, G.M. Zhidomirov, XPS and UPS study of oxygen states on silver, Journal of Electron Spectroscopy and Related Phenomena 96(1) (1998) 43-51.
[11] K. Tanabe, Catalytic application of niobium compounds, Catalysis Today 78(1) (2003) 65-77.
[12] H. Cui, K. Dwight, S. Soled, A. Wold, Surface Acidity and Photocatalytic Activity of Nb_2O_5/TiO_2 Photocatalysts, Journal of Solid state Chemistry 115(1) (1995) 187-191.
[13] K. Su, H. Liu, Z. Gao, P. Fornasiero, F. Wang, Nb_2O_5-Based Photocatalysts, Advanced Science n/a(n/a) (2021) 2003156.
[14] Y. Wada, A. Morikawa, Catalysis by niobium oxides in their reduced states, Catalysis Today 8(1) (1990) 13-25.

Chapter 7 - Niobium pentoxide applications

INTRODUCTION

1. Methodology

1.1. Crystal Violet adsorption and photocatalytic tests

The adsorption study was carried out under different conditions: solution pH of crystal violet (CV), concentration, effects of ionic strength, and reusability. For pH variations, 15 mL of 100 mg L^{-1} crystal violet solution was added to 50 mL beaker capacity containing 20 mg of each Nb_{OX500}, $Nb_{EG500,}$ and Nb_{PEG500}. The pH was adjusted to pH 2, 4, 6, 8, and 10 using dilute HCl and NaOH solution under constant stirring. The adsorption process was left for 24 h, after which the unabsorbed CV in the solution was measured using a UV-Vis spectrophotometer (U-2010, Hitachi) at λmax 585 nm. The amount (q) adsorbed (mg g^{-1}) was calculated using equation 1.

$$q = \frac{(C_o - C_e)V}{m} \qquad 1$$

C_o and C_e in the equation stand for initial and final concentration (mg L^{-1}) of CV, respectively, m is the mass of each adsorbent (g), and V is the solution volume.

The pH at which the maximum amount of each CV was adsorbed was taken as optimum pH and used for further studies. A concentration study was carried out within the range of 20 – 200 mg L^{-1} of CV, 15 mL solution, and 20 mg adsorbent. The results obtained were used to plot the isotherms. The effect of ionic strength was done by using 0.02, 0.04, 0.06, 0.08, and 0.1 mol L^{-1} of $NaNO_3$. The reusability of the materials was done by degrading the adsorbed CV at 500 °C for two hours and reusing the CV-desorbed material for three cycles.

The photocatalytic activity of the EG500, EG700, and EG900 was studied, employing 30 mg of each material added to a beaker containing 50 mL of 20 mg L^{-1} Crystal Violet dye solution. Before turning on the UV lamp, each photocatalyst was

suspended under magnetic stirring for 150 minutes to reach adsorption equilibrium. After this, the suspension was illuminated by a low-pressure Hg lamp (UV-C centered at 254 nm), and at different times, aliquots were extracted and analyzed in a UV-Vis Shimadzu UV-1601PC spectrophotometer.

1.2. Alcohol photooxidation for Solketal production

For the photocatalytic tests, 20 mg of EG500, PEG500, and NbOX500 were weighed and added to the quartz reactors, previously filled with 5 mL of isopropyl alcohol and one mmol of glycerol. After the addition, the sealed reactor and each system were subjected to UV or visible light radiation. The identification of the reaction products and quantification used an Agilent 7890B gas chromatography coupled to Agilent 5977B MSD mass spectrometer. The chromatograph runs were performed on HP - INNOWAX column (30 m, 0.250 mm, and 0.15 µm), and the method parameters were: helium flux of 1.2 mL/ min, 1:50 split ratio, the injection volume of 1 µL, injector set up at 270 ^{o}C, the analysis started at 40 °C and ended at 250 °C with a heating rate of 10 °C/min. The mass spectrometer detection was carried out at 150 °C ranging from 34 to 200 m/z.

The following steps were performed for the spin trap measurements using EPR spectroscopy: 10 mg of EG500 photocatalyst was dispersed into 2 mL of isopropyl alcohol containing 35 mg of the spin trap molecule N-tert-Butyl-α-phenylnitrone (better known as PBN, CAS 3376-24-7, 98% purchased from TCI America, Japan). The suspension was then illuminated with UV light under constant stirring. Aliquots of 50 µL were extracted from this system (using glass capillaries tubes) at different times to observe the radicals generated in the photocatalytic process. The spin Hamiltonian parameters were extracted from EPR spectra simulations using the Easyspin@ software [1]. The electron accumulation experiment also employed the DRS technique. We added 100 µL of glycerol over the illuminated materials by UV for 5 minutes and then recorded the reflectance spectra of the material.

2. Crystal Violet decoloration

2.1. Adsorption tests

2.1.1. Effect of solution pH and adsorbents surface charge

The pH of an adsorbate solution and the surface charge of an adsorbent are among the factors that affect the adsorption process and help understand the adsorption mechanism [2]. The results obtained from the effect of pH on the adsorption of crystal violet (CV) are shown in Figure 7.1a, while the results of the zeta potential measurement show the surface charge of NbOX500, EG500, and PEG500 are in Figure 7.1b. The adsorption of CV on the surface of the three adsorbents increases with an increase in the solution pH. The amount adsorbed at pH 2 is almost insignificant compared with pH 4, 6, 8, and 10. Relating these results with the surface charge of the adsorbents as shown in Fig 7.1b, the adsorbents (NbOX500, EG500, and PEG500) possess a positive charge at pH two and a negative charge at pH 4, 6, 8, and 10. More so, as shown in Figure 7.2, CV is a cationic dye. Therefore, the insignificant amount of CV adsorbed at pH 2 was due to the electrostatic repulsion between CV^+ and positively charged surface ($NbOX500^+$, $EG500^+$, and $PEG500^+$) of the adsorbents. Particles of similar charges move toward each other, and there is induction of potential electrical fields on their surfaces, which overcome attractive van der Waals force, resulting in electrostatic repulsion between the particles [3].

Meanwhile, when the surface of the three adsorbents became negatively charged ($NbOX500^-$, $EG500^-$, and $PEG500^-$), a significant amount of CV was adsorbed. The amount adsorbed at a pH higher than two is due to the electrostatic attraction between CV^+ and the negative surface of niobium materials. Given this, the mechanism of adsorption of CV by the three adsorbents is due to electrostatic interaction. The amount of CV that PEG500 adsorbed was rapid from pH 4 to 8 and reached equilibrium at pH 10, while the amount adsorbed by NbOX500 and EG500 increases steadily as pH increases. This behavior could be related to the total pore volume PEG500 being slightly higher than EG500. However, EG500 having the highest SSA and more defects, adsorbed more CV at pH 10 than NbOX500 and PEG500.

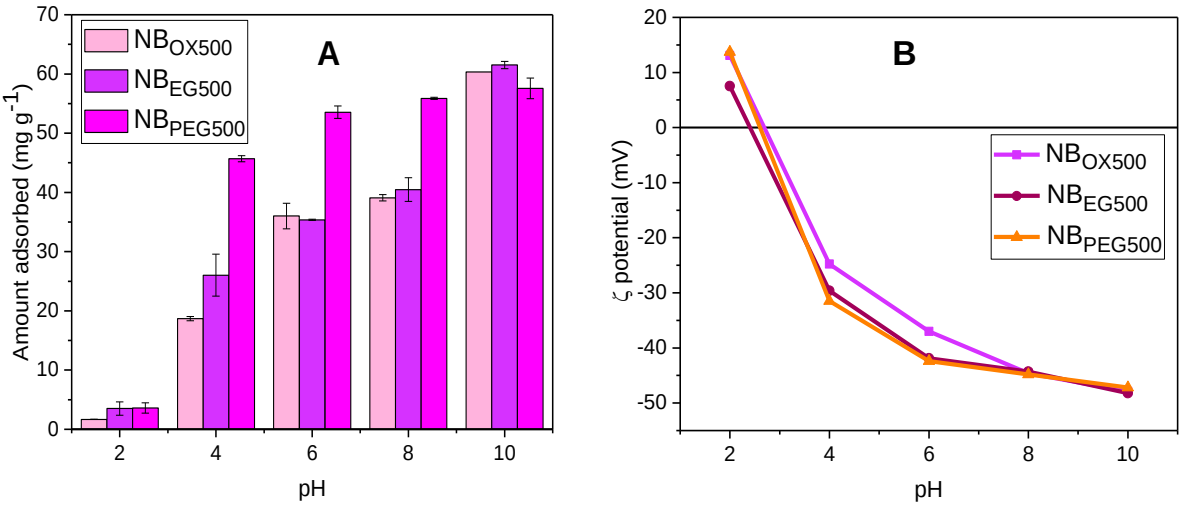

Figure 7. 1. The effect of pH (A) and surface charge (B) on the adsorption of crystal violet

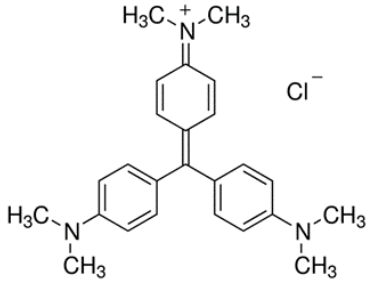

Figure 7. 2. Structure of crystal violet

2.1.2. Effect of ionic strength

In textile industries, salts are generally used when applying dyes on fabric, making effluents from these industries contain a high amount of salts, among which is sodium nitrate [4-6]. The presence of salts could, in one way or the other, interfere with the adsorption of dyes during effluents treatment. Therefore it is of great importance to study the effect of ionic strength on the adsorption of CV. Figure 7.3 shows the $NaNO_3$ effect on the adsorption of CV (at pH 10) using the three adsorbents (NbOX500, EG500, and PEG500), showing a decreasing trend in the amount removed as the concentration of $NaNO_3$ increases. More than 50% reduction of CV uptake in the presence of 0.1 mol L^{-1} of $NaNO_3$ occurred. The presence of salt on the adsorption capacity of the adsorbent influences the ionic nature, hydrophobicity, and solubility of the adsorbate [7]. It was gathered that the intense competition of electrolyte cations with the adsorbate that is cationic for the available adsorption sites has consequently led to the reduction in the adsorption capacity of the targeted adsorbate [3]. The

reduction of CV uptake with an increase in Na^+ can also be attributed to compression of the electric double layer due to increased salt concentration. Thereby driving away dye (CV) molecules from adsorbing on the adsorbent sites, showing that our photocatalyst could not show high performance when working with natural wastewater (textile, mining, paper pulp.) samples that have various cations and anions in solution [8].

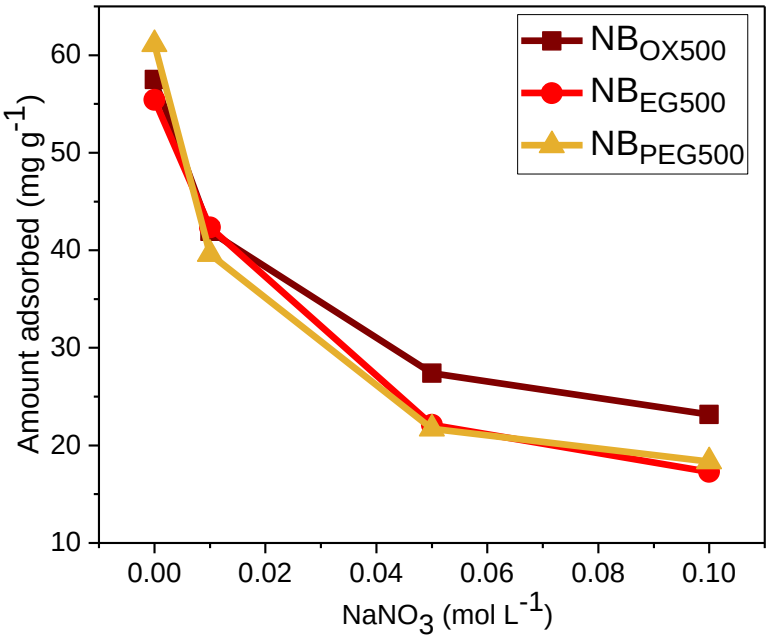

Figure 7. 3. Effect of ionic strength.

2.1.3. FTIR analysis before and after adsorption

FTIR spectra of all the three adsorbents before and after adsorption are in Figure 7.4. FTIR analysis helps to identify changes in the spectra after adsorption of CV. There is no noticeable difference between the spectra of NbOX500, EG500, and PEG500. Despite the different synthesis routes, no organic content is present in the materials. The peaks at 867 and 587 cm^{-1} are assigned to Nb-O stretching vibration [9]. The CV spectrum shows a peak at 3419 cm^{-1}, attributed to N-H stretching vibrations. While the characteristic peaks at 2905, 1591, 1370, 1168, and 1021 cm^{-1} are due to the presence of C-H stretching (CH_3 group), C=C stretching (benzene ring), C-N stretching (Aromatic tertiary amine), C-N stretching (Tertiary amine) and C-C bond respectively [10-12]. There is a slight difference in the spectra of the NbOX500, EG500, and PEG500 after the adsorption of CV. The new peaks at 1579 and 1174 cm^{-1} are due to the

adsorption of CV. The fact that the intensity of these peaks is not vigorous implies that the interaction between CV and the adsorbents is not a strong interaction, which is an outer sphere interaction.

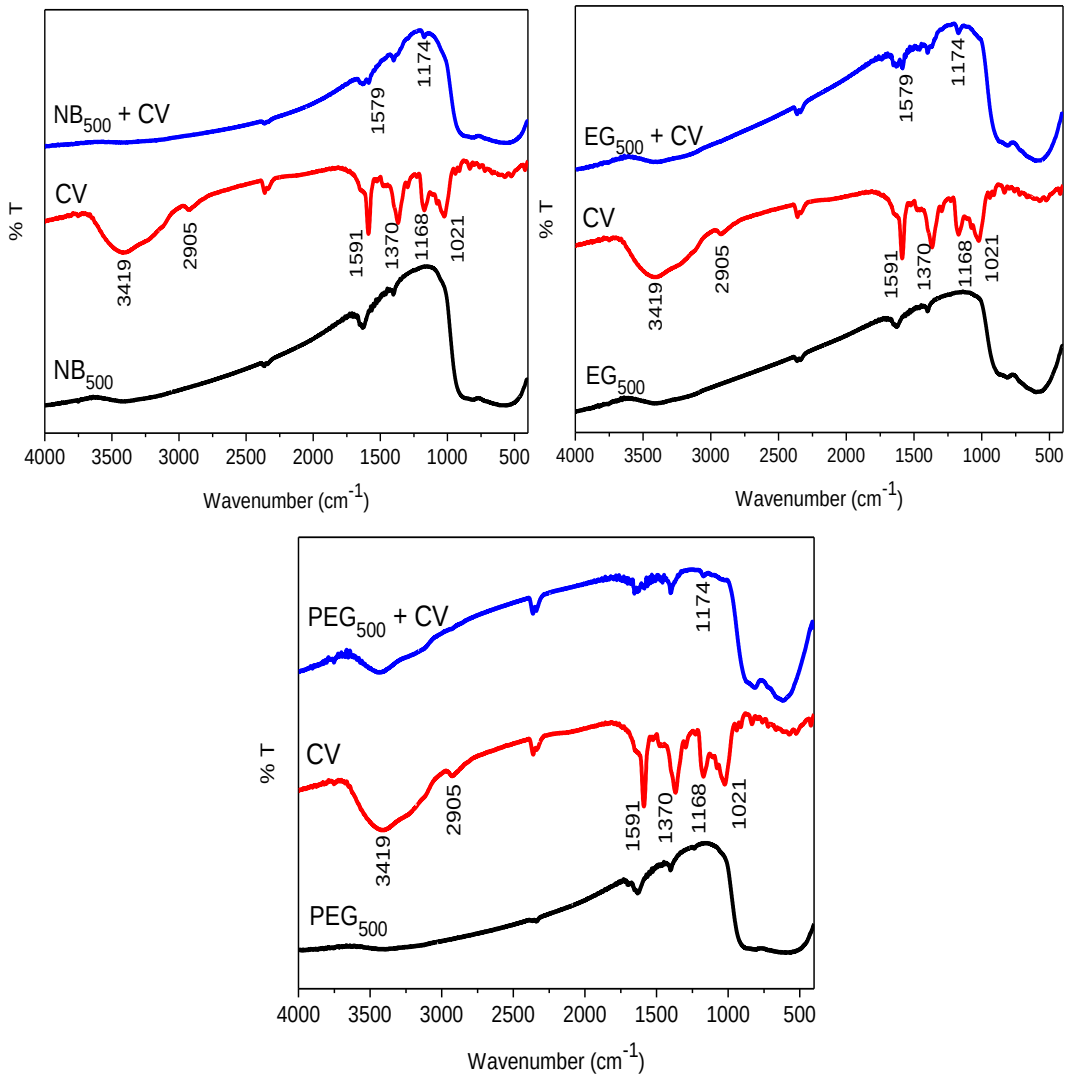

Figure 7. 4. FTIR spectra of NbOX500, EG500, and PEG500 before and after adsorption

2.1.4. Regeneration and reusability of the materials

Since the three adsorbents are thermally stable and CV degrades thermally, a thermal process was used to regenerate the used NbOX500, EG500, and PEG500. After the regeneration, the adsorbents were used again for three cycles. This method was adopted from our previous studies [13, 14].

Desorbing CV thermally rather than using chemical methods will prevent it from getting back into the environment. After each adsorption, the adsorbent was separated from the solution, dried at 100 °C in an oven, transferred to a furnace, and

calcined at 500 °C to degrade the CV. As shown in Figure 7.5, the amount adsorbed after the third cycle is almost the same as the first cycle. Showing that thermal treatment did not in any way affect the active site of the adsorbents. Therefore, regeneration and reuse of NbOX500, EG500, and PEG500 are possible.

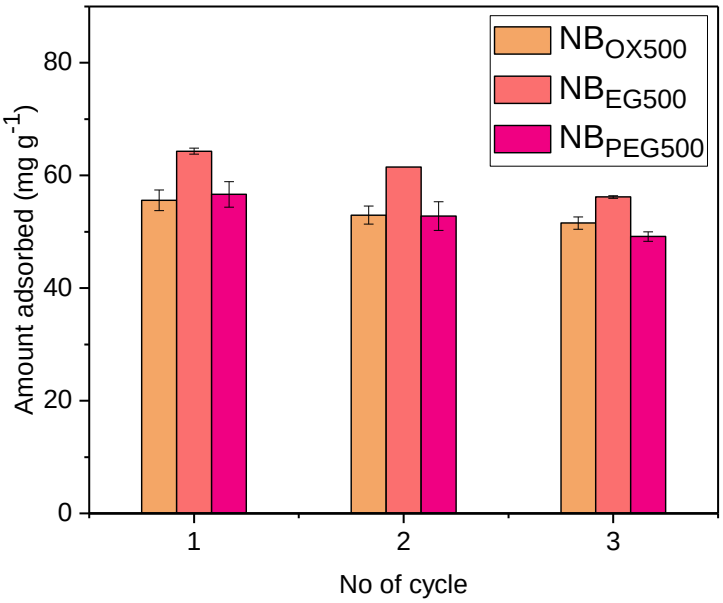

Figure 7. 5. The reusability of NbOX500, EG500, and PEG500. (CV concentration: 100 mg L-1; pH: 10)

2.1.5. Adsorption isotherm

This study used three isotherm models (Langmuir, Freundlich, and Liu) to describe and understand the equilibrium between the Nb_{OX500}, Nb_{EG500}, and Nb_{PEG500} surface CV in the aqueous phase. The nonlinear equations that describe these isotherms are in equations 1, 2, and 3 for Langmuir, Freundlich, and Liu isotherms. The nonlinear curve fits are in Figure 7.6.

$$q_e = \frac{q_{max} * Ce * K_L}{(1 + K_L * Ce)} \quad (1)$$

$$q_e = K_F C_e^{1/n_F} \quad (2)$$

$$q_e = \frac{q_{max}(C_e * K_g)^{n_L}}{(1 + (C_e * K_g))^{n_L}} \quad (3)$$

C_e is the equilibrium concentration in solution (mg L^{-1}), q_e is the amount of CV adsorbed (mg g^{-1}), q_{max} is the maximum adsorption capacity (mg g^{-1}), K_L is

Langmuir equilibrium constant (L mg^{-1}), K_F is the Freundlich constant (mg g^{-1} (mg L^{-1})$^{-1/nF}$), K_g is the Liu equilibrium constant (L mg^{-1}), n_F and n_L are the dimensionless exponent of Freundlich and Liu equations, respectively. Monolayer and multilayers adsorption processes are associated with Langmuir and Freundlich, respectively. Whereas Liu prescribes the combination of the description of Langmuir and Freundlich by assuming that the active sites on the adsorbent cannot have the same energy due to different surface energy [15-17]. As expressed in equations 1 and 3, Langmuir and Liu give information on the maximum adsorption capacity. However, the accuracy of the q_{max} that is from the two isotherms based on the values of SD and $R^2_{adjusted}$. The isotherm with the lowest SD and highest $R^2_{adjusted}$ is more applicable to relate the equilibrium data [14].

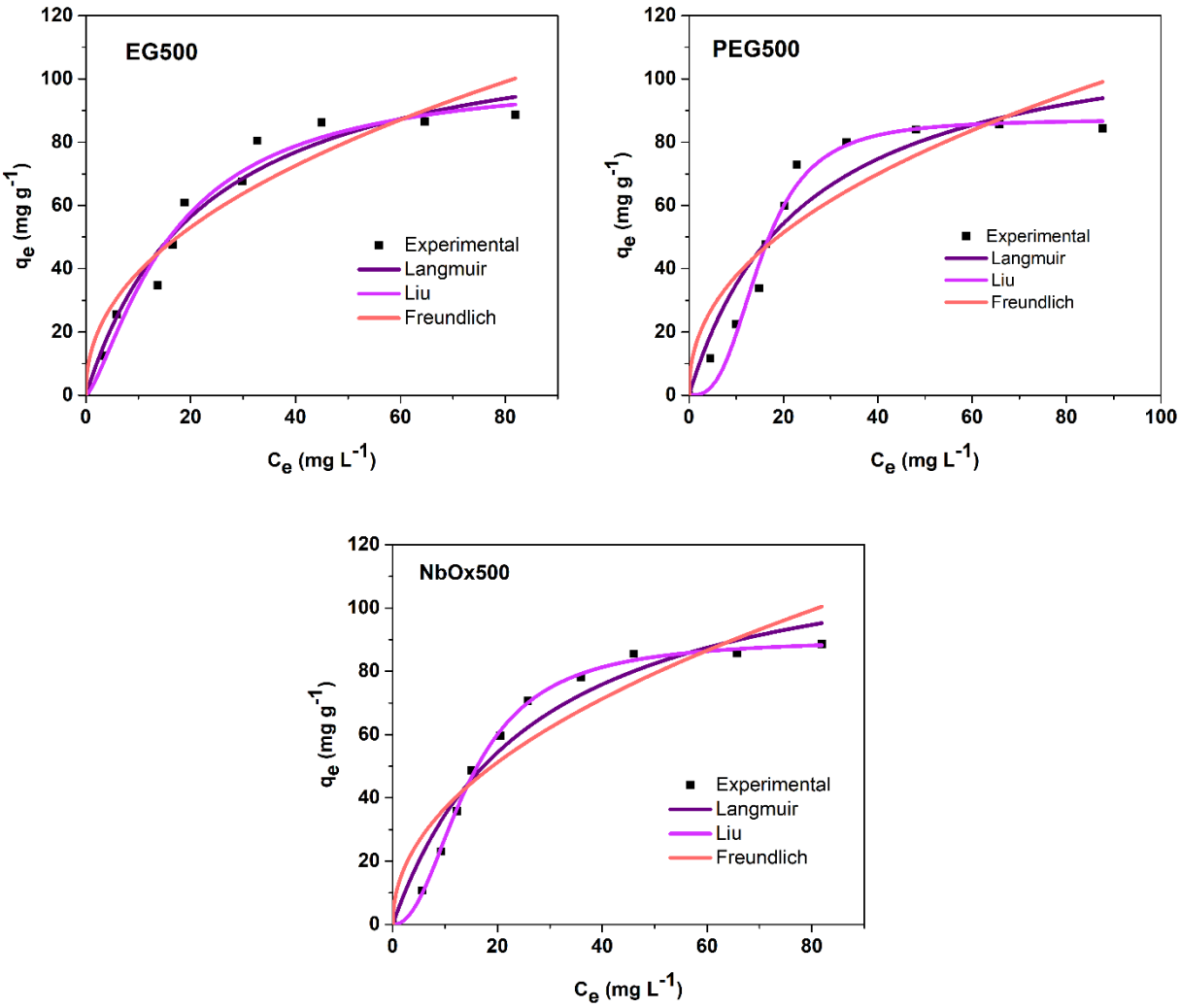

Figure 7. 6. Adsorption isotherm for the removal of CV.

Table 7. 1. Langmuir, Liu, and Freundlich isotherms parameters for the adsorption CV using NbOX500, EG500, and PEG500 at room temperature.

	NbOX500	EG500	PEG500
Langmuir			
$\mathbf{q_{max}}$ (mg g^{-1})	125	120	119
$\mathbf{K_L}$ (L mg^{-1})	0.037	0.044	0.041
$\mathbf{R^2_{adjusted}}$	0.9497	0.9627	0.9095
SD (mg g^{-1})	7.14	6.12	9.52
$\mathbf{q_{max}}$ $\boldsymbol{/SSA}$ (mg m^2)	2.19	1.76	2.05
Liu			
$\mathbf{q_{max}}$ (mg g^{-1})	90	101	87
$\mathbf{K_g}$ (L mg^{-1})	0.068	0.061	0.065
$\mathbf{n_L}$	2.19	1.37	2.92
$\mathbf{R^2_{adjusted}}$	0.9978	0.9667	0.9797
SD (mg g^{-1})	1.48	5.77	5.03
$\mathbf{q_{max}}$ $\boldsymbol{/SSA}$ (mg m^2)	1.58	1.59	1.50
Freundlich			
$\mathbf{K_F}$ (mg g^{-1} (mg L^{-1})$^{-1/nF}$	12.23	13.81	13.58
$\mathbf{n_F}$	2.09	2.22	2.25
$\mathbf{R^2_{adjusted}}$	0.8837	0.9115	0.8323
SD (mg g^{-1})	10.87	9.44	12.95

As itemized in Table 7.1, Liu isotherm best describes the equilibrium between the three adsorbents and CV remaining in the solution. Therefore, EG500 has the

highest q_{max} of 101 mg g^{-1}, while PEG500 and NbOX500 are almost identical, 87 and 90 mg g^{-1} respectively.

When comparing the samples with other adsorbents studied for CV removal, shown in Table 7.2, our adsorbents performed better than some of the high surface area adsorbents reported in the literature.

Table 7. 2. Comparison of the maximum monolayer adsorption (q_max) of different adsorbents for the removal of the CV

Adsorbents	q_{max}(mg g^{-1})	References
GA-cl-poly (AAm)NHG	90	[18]
Eucalyptus leaves	88	[19]
Eichhornia plant	58	[20]
Polymer composite	20	[21]
Calcium ferrite	10	[22]
NaOH-modified rice husk	44	[12]
ZnO-NRs-AC	81	[23]
Chitin nanowhiskers	38	[24]
Jute fiber carbon	31	[25]
AC -Oak leaves	41	[26]
NbOX500	90	This work
EG500	101	This work
PEG500	87	This work

2.2. Photocatalytic degradation of Crystal Violet

The removal of crystal violet dye by the EG500, EG700, and EG900 niobium pentoxides is in Figure 7.7. UV-C radiation purely degraded 31% of the crystal violet in the entire test, while the materials applied in this study removed more than twice that value at the end of the 150 minutes of reaction, indicating that there was indeed a photocatalytic response by them. Among the Nb oxides, the EG500 was the most efficient material for removal by both adsorption and photocatalysis, followed by EG900 and finally EG700. The best performance of the EG500 can be explained by its

significant SSA (compared to other semiconductors) since the photocatalytic activity is also dependent on this parameter.

Despite not showing micro or mesoporosity, the materials EG700 and EG900 adsorbed the dye relatively well, 26.3% and 43.2%, respectively. However, the photocatalytic activity was much more pronounced by EG900, fully discoloring crystal violet in 150 minutes (as well as EG500). It appears that the crystalline phase mixture (H and $Nb_{12}O_{29}$) of this niobium pentoxide favored this process, probably due to the reduction of lattice defects that is crucial for more severe oxidation [27]. The kinetic constants (Table 7.3) numerically corroborate the efficiency above. All values were calculated according to the pseudo-first-order model [28] and considering the initial concentration after the adsorption process., with an R^2 of fitting above 0.93.

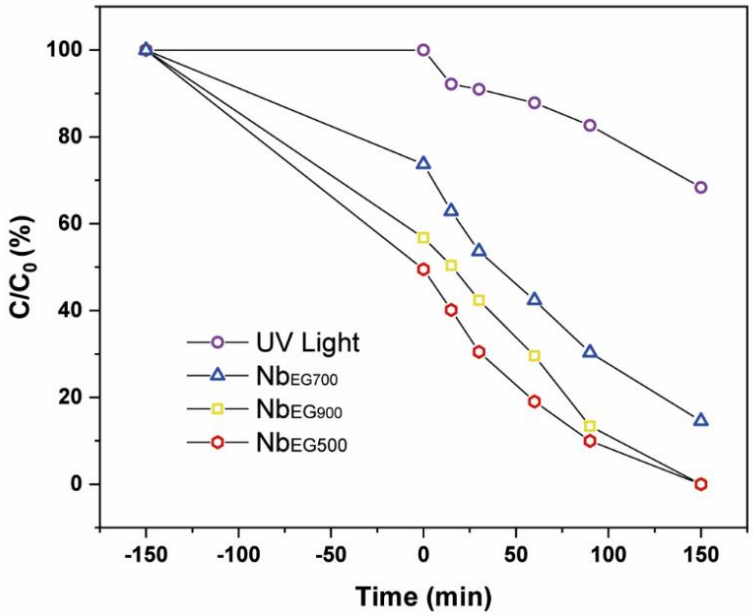

Figure 7. 7. Photocatalytic test of EG500, EG700, and EG900, 150 minutes of adsorption and 150 minutes under UV-C radiation.

Table 7. 3. Pseudo-first-order constants obtained from crystal violet degradation kinetics.

Material	Pseudo-first-order Kinect constants, k (min^{-1})
UV-C Light	0.00230
EG500	0.01771
EG700	0.01064
EG900	0.01569

There is a difficulty in comparing photocatalytic results in the literature due to different setup, light flux, and other parameters [29]. However, comparing the Crystal violet degradation by EG500, EG700, and EG900 with other niobium pentoxide materials found in the literature, as shown in Table 7.4, our materials performed better than other works.

Table 7. 4. Comparison of the properties of the samples and their photocatalytic behavior with several Nb_2O_5 employed in the literature.

Sample	Phase	Synthesis method	Bandgap / eV	SSA / $m^2.g^{-1}$	Dye removal	Catalyst Weight / g	Ref
EG500	TT	Pechini	3.02	63	100% / 2.5h †	0.030	This work
EG700	T	Pechini	3.08	10	83% / 2.5h †	0.030	This work
EG900	H and $Nb_{12}O_{29}$	Pechini	3.06	1	100% / 2.5h †	0.030	This work
TiO_2/ Nb_2O_5	Anatase/ T	Sol-gel	3.00	89	65% / 2h†	0.030	[29]
Nb_2O_5	T	Commercial	3.07	4	32% / 2h‡	0.10	[30]
Nb_2O_5	H	Commercial	2.96	2	17% / 2h‡	0.10	[30]
Nb_2O_5/C	M	Coprecipitation	3.3	13	36% / 2h‡	0.25	[31]
Nb_2O_5/C	TT	Coprecipitation	3.3	23	43% / 2h‡	0.025	[32]
Nb_2O_5	TT	Solution combustion	3.0	28	41% / 2h‡	0.050	[33]
Nb_2O_5	TT	Pechini	-	39	48% / 2h	0.050	[34]
Nb_2O_5	TT/T	Pechini	-	17	-	-	[34]
Nb_2O_5	T	Pechini	3.32	5	-	-	[35]
Nb_2O_5	T	Sol-gel	3.36	2	-	-	[35]
Nb_2O_5	Amorphous	Pechini	3.40	76	-	-	[35]
Nb_2O_5	TT	Hydrothermal	-	16	90% / 2h	0.050	[36]
Nb_2O_5	T	Hydrothermal	-	2	38% / 2h	0.050	[36]

†Degradation of Crystal Violet dye.

‡Degradation of Methylene Blue dye.

3. Selective photocatalytic conversion of glycerol into solketal

3.1. Glycerol photocatalysis

In 24 hours of UV radiation (254 nm), the most effective conversion of glycerol was obtained by EG 500 (47.8%), followed by PEG 500 (41.7%) and NbOx 500 (22.1%). Only three products derived from glycerol were found in the chromatographic analyzes, Solketal, 2,2-Dimethyl-1,3-dioxan-5-ol (here called Dioxane), and 1-Isopropoxy-2,3-propanediol (abbreviated as Alpha-ether). In addition to being the best photocatalyst in converting glycerol, the EG500 showed excellent selectivity for Solketal (69.8%), while the remaining 30.2% were represented by Alpha-ether, with no formation of Dioxane. The highest selectivity values for PEG500 and NbOX500 were represented by Dioxane, 68.1 and 59.9%, respectively. These data are in Table 7.5. No conversion occurred using visible light instead of UV or in the absence of photocatalysts.

Table 7. 5. Photocatalytic conversion of glycerol in 24 hours under UV radiation using EG500, PEG500, and NbOX500 materials.

		Selectivity of Glycerol (%)		
Photocatalyst	Conversion (%)	Solketal	Dioxane	Alpha-ether
EG500	47.8	69.8	-	30.2
PEG500	41.7	15.7	68.1	16.2
NbOX500	22.1	27.9	59.9	12.2

The better photocatalytic performance of the materials synthesized by the Pechini method was expected, as they present a well-defined crystallinity, lower band-gap energy, greater surface area, and SETOVs, which can trap and significantly reduce the recombination of photogenerated charges. Nevertheless, an interesting additional feature was observed during the reactions, the colors of both EG500 and PEG500

changed with UV light exposure, while NbOX500 remained white (Figure 7.8). This phenomenon has been reported in the literature as an electron accumulation process [37, 38]. However, it only happens when the system has a low oxygen concentration, which is not the case because these reactions were carried out in ambient conditions. Usually, oxygen vacancies are linked to the worst photocatalytic activity [39]. However, we observed the opposite. Probably these oxygen vacancies (previously evidenced by EPR as V_0^+ and XPS measurements as Nb^{4+}) were responsible for stabilizing the electron accumulation even in an aerobic environment, as well as these accumulated electrons influenced the excellent performance in the conversion of glycerol by EG500 and PEG500 compared to NbOX500.

Figure 7. 8. Coloration changes during the electron accumulation phenomenon.

3.1.2. Electron accumulation process

During the photocatalytic process of EG500 and PEG500, isopropyl alcohol (customarily used as a hole scavenger) is rapidly oxidized by the photogenerated holes, producing acetone and H^+ as a by-product and favoring the electron accumulation on the semiconductor surface. Such electrons are the driving force for proton intercalation on the surface (to guarantee the electroneutrality of the solid) [40], thus generating an induced acidity that is not governed by normal adsorption/desorption equilibrium [41]. This effect, illustrated in Figure 7.9, was crucial for the acetalization of glycerol with acetone (the latter produced here exclusively via photocatalysis), generating Solketal or Dioxane since this reaction is acid-catalyzed [41].

It is known that the accumulation of electrons in the conduction band causes an increase in the absorption in the visible and near-infrared range of metal oxides [42], so to assess the behavior of this effect in the photocatalysts in question, DRS measurements were conducted. Figure 7.10 shows a noticeable change in the reflectance profiles in both materials after UV radiation. The PEG500 spectrum (Figure 7.10(a)), shows an abrupt increase in the absorption at 400 nm, and that extends up to 1400 nm, whereas for EG500, this increase only occurs after 800 nm (Figure 7.10(b)). This difference in absorption spectra during UV exposure, along with the color change, could probably be a direct response to different SETOVs amounts in each material. As the EPR and XPS showed that the number of vacancies is higher in the EG500, it is plausible that the induced acidity was more pronounced and stabilized for this niobium oxide, reflecting a more excellent conversion of glycerol into solketal.

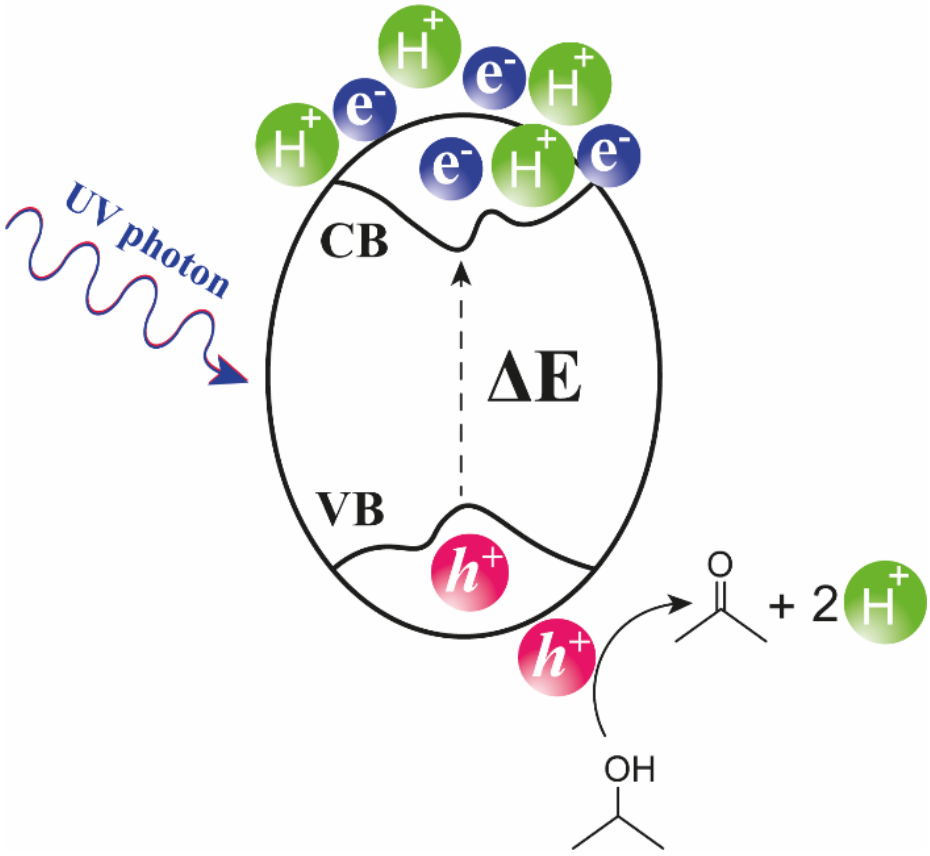

Figure 7. 9. Representation of electron accumulation and proton intercalation (induced acidity) in the semiconductor by the scavenger effect of isopropyl alcohol.

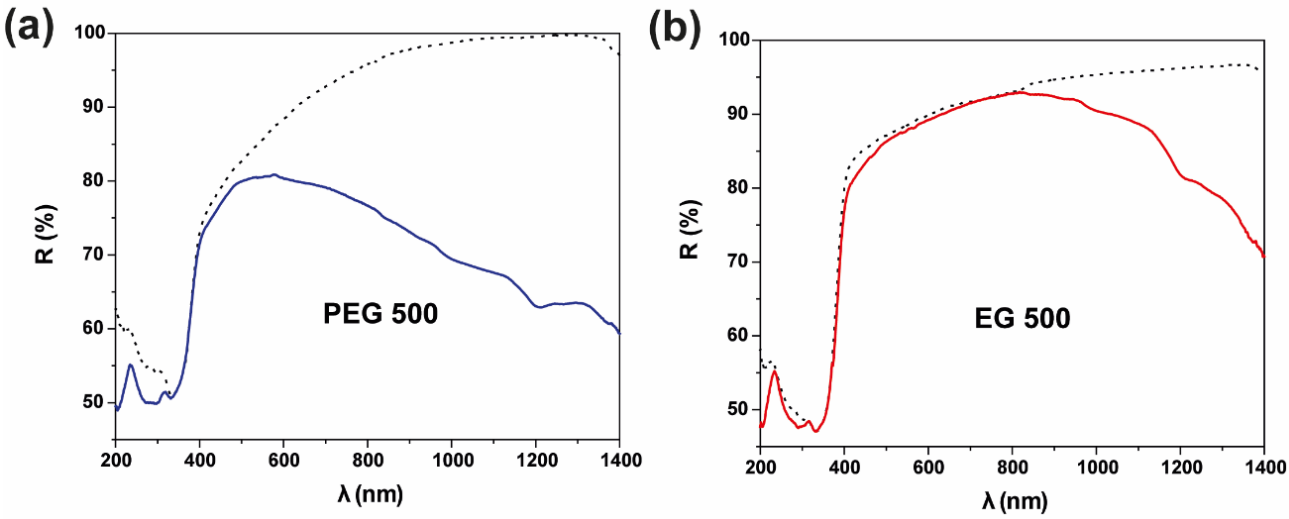

Figure 7. 10. Diffuse reflectance spectra for niobium oxides (a) PEG500 and (b) EG500. The dotted curve refers to the pure material, while the solid is the spectrum obtained from the electron accumulation experiment.

Given the better behavior of the photocatalyst EG 500 in the conversion of glycerol and a considerable selectivity for solketal, the following discussions were devoted to this photocatalyst to understand the mechanism behind this reaction.

3.2. The role of Nb_2O_5 as an acid catalyst and the solketal formation mechanism

In the first two hours of reaction, no solketal formation was observed. The expressive conversion of solketal occurred only after four hours of exposure to UV light and reached a saturation regime in 24 hours (Figure 7.11 (a)). The selectivity data, Figure 7.11(b), show that solketal was the primary product of the photocatalytic test. However, there was an inversion in the selectivity curves at 8 hours, where Alpha-ether had its highest selectivity value, 58.1%. Despite this event, the concentration of solketal increased, and this compound became the main product derived from glycerol in the subsequent times.

The anomalies observed in both the kinetic conversion (delay of 4 hours) and selectivity (inversion in 8 hours) curves can be better understood by evaluating the pH throughout the reaction, Figure 7.11(c). In the first 8 hours of reaction, the rate of change in pH was -0.249/h from that moment. The rate drastically dropped to -0.014/h. It is possible to observe that at the point where the conversion became significant when

pH is below 4. The delay could be related to the acetalization stage itself; as previously stated, it depends on acidity (mainly induced by electron accumulation). So, it does not matter if acetone is in the reaction medium. The conversion will be expressive when an adequate amount of protons are on the material's surface, a type of "surface activation". On the other hand, the inversion of the curves occurs due to the competition between acetalization and etherification. As the pH value decreased by more than two units up to that point, the etherification of isopropyl alcohol with glycerol was also favored, decreasing the selectivity of the solketal.

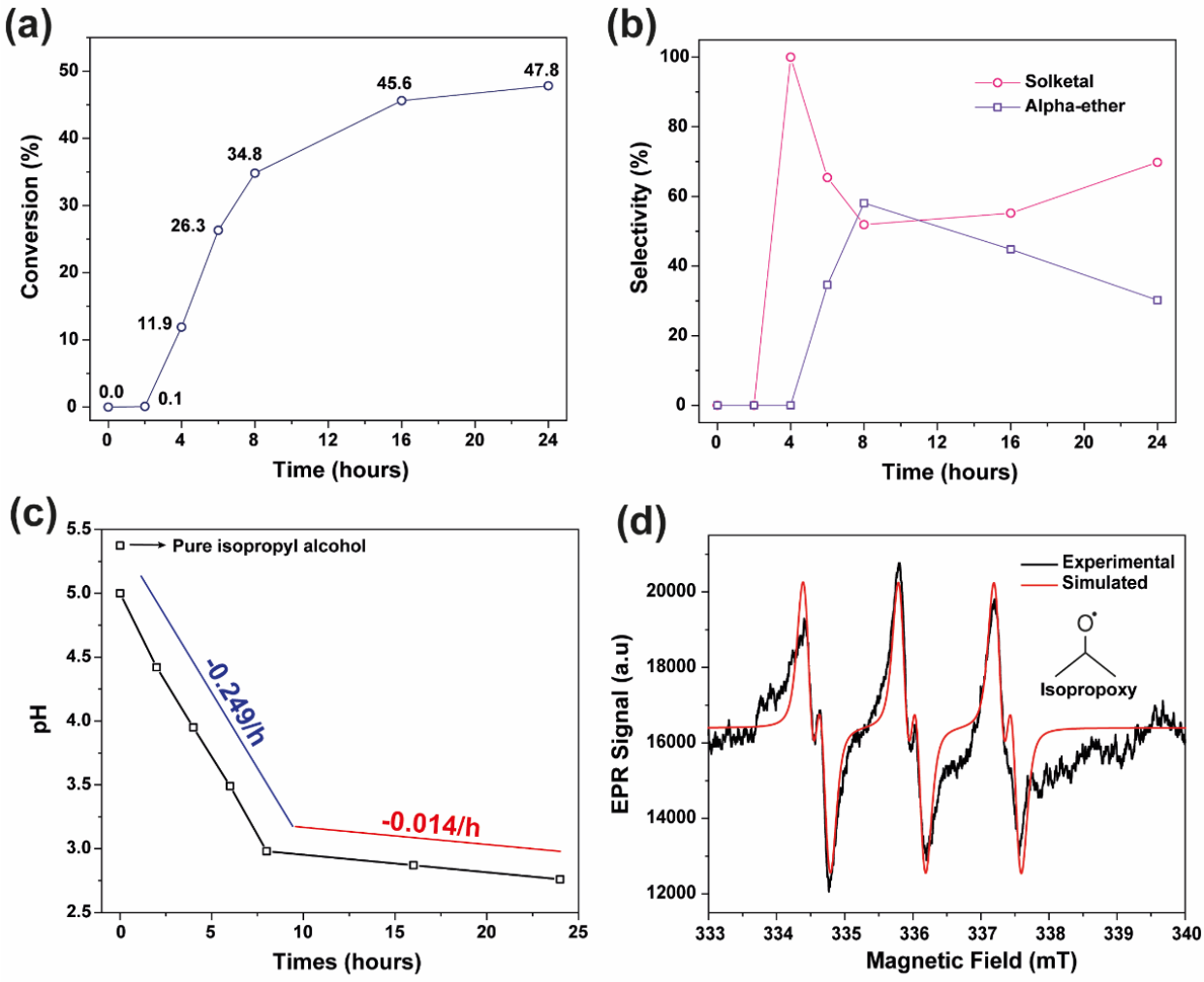

Figure 7. 11. Kinetics curves of (a) glycerol conversion and (b) solketal and alpha-ether selectivity; (c) pH curve as a function of reaction time and d) EPR spectrum of UV irradiated-suspension of EG 500, containing isopropyl alcohol, and the PBN spin trap molecule

The EPR technique allied with the spin trapping method is a powerful tool to investigate the radical species of isopropyl alcohol that are intermediates in the formation of solketal. In this experiment, the PBN spin adduct signal intensity is

sufficient after 10 minutes of UV illumination. Six transitions characterize such an adduct. The EPR spectrum simulation revealed the values of the hyperfine (hf) interaction with two different nuclear spins: a_N =1.40 mT due to $I = 1$ of ^{14}N and $a_{H(\beta)}$ = 0.22 mT due to I = 1/2 of ^{1}H. This result indicates that the EG500 exclusively produces isopropoxy radicals [43] (inset in Figure 7.11(d)) under UV radiation, which is then oxidized once again by the valence band holes to form acetone and the glycerol substrate for acetalization reaction to form solketal.

Figure 7.12 shows the proposed mechanism for alcohol photooxidation and the electron accumulation process. Figure 7.13 shows the susceptive solketal formation with the subproducts.

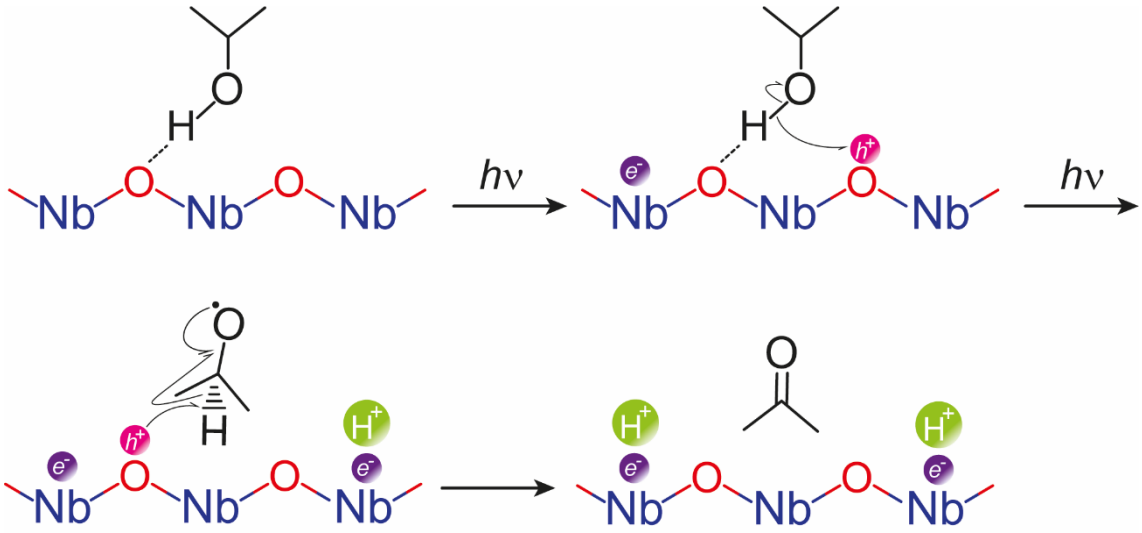

Figure 7. 12. Mechanism of isopropanol photooxidation into acetone through UV light irradiation.

The Nb^{5+} atoms on the lattice surface have induced acidity through the electron accumulation process, in which the isopropanol molecules could perform intermolecular hydrogen bonds with lattice oxygen. With the generation of the electron/hole pair, the holes in the valence band react with the linked isopropanol molecule, being stabilized by the formation of a tertiary carbocation. Another hole captures the hydrogen from the tertiary carbocation, yielding the acetone molecule and two protons (H^+). In the aerobic system (with oxygen content), the niobium pentoxide lattice captures the oxygen molecules, returning to the initial state. The presence of SETOVs stabilizes the formation of Nb^{4+} atoms in the crystal sub-lattice, which are crucial for the high selectivity for the solketal production, as shown in Figure 7.13. The three produced

chemicals form with the reaction of one glycerol molecule with one isopropanol or acetone molecule. The high selectivity of EG500 is due to the higher amount of oxygen vacancies, which induces the production of acetone through the isopropyl alcohol photooxidation process [44], leading to the production of solketal or dioxane. However, its main feature is the exclusive production of solketal when reacting with acetone, leading to 0% of dioxane in the system. Despite 30.2% of Alpha-ether production, the EG500 proved the excellent selectivity for the Solketal production, demonstrating that oxygens vacancies in the crystalline system directly affect its photocatalytic behavior.

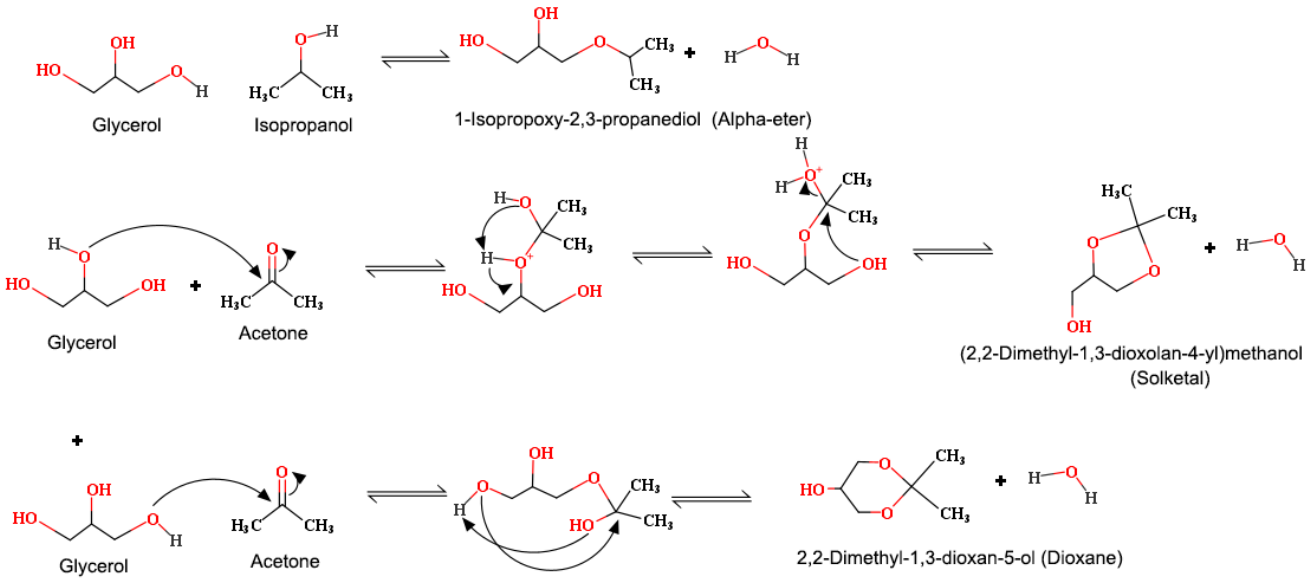

Figure 7. 13. Proposed mechanism for all products formation.

REFERENCES

[1] S. Stoll, A. Schweiger, EasySpin, a comprehensive software package for spectral simulation and analysis in EPR, Journal of Magnetic Resonance 178(1) (2006) 42-55.
[2] S.J. Olusegun, L.F. de Sousa Lima, N.D.S. Mohallem, Enhancement of adsorption capacity of clay through spray drying and surface modification process for wastewater treatment, Chemical Engineering Journal 334 (2018) 1719-1728.
[3] Y. Zhang, C. Zhu, F. Liu, Y. Yuan, H. Wu, A. Li, Effects of ionic strength on removal of toxic pollutants from aqueous media with multifarious adsorbents: A review, Science of The Total Environment 646 (2019) 265-279.
[4] D.A. Yaseen, M. Scholz, Textile dye wastewater characteristics and constituents of synthetic effluents: a critical review, International Journal of Environmental Science and Technology 16(2) (2019) 1193-1226.
[5] H. Mirbolooki, R. Amirnezhad, A.R. Pendashteh, Treatment of high saline textile wastewater by activated sludge microorganisms., J. Appl. Res. Technol. 15 (2017) 167-172.

[6] S.P. Buthelezi, A.O. Olaniran, B. Pillay, Textile Dye Removal from Wastewater Effluents Using Bioflocculants Produced by Indigenous Bacterial Isolates, Molecules 17(12) (2012).
[7] H.A. Arafat, M. Franz, N.G. Pinto, Effect of Salt on the Mechanism of Adsorption of Aromatics on Activated Carbon, Langmuir 15(18) (1999) 5997-6003.
[8] L.A. Sepulveda, C.C. Santana, Effect of solution temperature, pH and ionic strength on dye adsorption onto Magellanic peat, Environmental Technology 34(8) (2013) 967-977.
[9] M.H. Habibi, R. Mokhtari, First Observation on S-doped Nb_2O_5 Nanostructure Thin Film Coated on Carbon Fiber Paper Using Sol–Gel Dip-Coating: Fabrication, Characterization, Visible Light Sensitization, and Electrochemical Properties, Journal of Inorganic and Organometallic Polymers and Materials 22(1) (2012) 158-165.
[10] S. Shanmugam, P. Ulaganathan, S. Sivasubramanian, S. Esakkimuthu, S. Krishnaswamy, S. Subramaniam, Trichoderma asperellum laccase mediated crystal violet degradation–Optimization of experimental conditions and characterization, Journal of Environmental Chemical Engineering 5(1) (2017) 222-231.
[11] Y. Cheng, F. Zhou, S. Li, Z. Chen, Removal of mixed contaminants, crystal violet, and heavy metal ions by using immobilized stains as the functional biomaterial, RSC Advances 6(72) (2016) 67858-67865.
[12] S. Chakraborty, S. Chowdhury, P. Das Saha, Adsorption of Crystal Violet from aqueous solution onto NaOH-modified rice husk, Carbohydrate Polymers 86(4) (2011) 1533-1541.
[13] S.J. Olusegun, E.T.F. Freitas, L.R.S. Lara, N.D.S. Mohallem, Synergistic effect of a spinel ferrite on the adsorption capacity of nano bio-silica for the removal of methylene blue, Environmental Technology (2019) 1-14.
[14] S.J. Olusegun, N.D.S. Mohallem, Insight into the adsorption of doxycycline hydrochloride on different thermally treated hierarchical $CoFe_2O_4$/bio-silica nanocomposite, Journal of Environmental Chemical Engineering 7(6) (2019) 103442.
[15] H. Khallok, M. Zbair, S. Ojala, K. Ainassaari, R. Brahmi, R.L. Keiski, Z. Hatim, Ceramic hydroxyapatite foam as a new material for Bisphenol A removal from contaminated water, Environmental Science and Pollution Research 28(14) (2021) 17739-17751.
[16] S. Rovani, J.J. Santos, S.N. Guilhen, P. Corio, D.A. Fungaro, Fast, efficient and clean adsorption of bisphenol-A using renewable mesoporous silica nanoparticles from sugarcane waste ash, RSC Advances 10(46) (2020) 27706-27712.
[17] É.C. Lima, M.A. Adebayo, F.M. Machado, Kinetic and Equilibrium Models of Adsorption, in: C.P. Bergmann, F.M. Machado (Eds.), Carbon Nanomaterials as Adsorbents for Environmental and Biological Applications, Springer International Publishing, Cham, 2015, pp. 33-69.
[18] G. Sharma, A. Kumar, M. Naushad, A. García-Peñas, A.a.H. Al-Muhtaseb, A.A. Ghfar, V. Sharma, T. Ahamad, F.J. Stadler, Fabrication and characterization of Gum arabic-cl-poly(acrylamide) nanohydrogel for effective adsorption of crystal violet dye, Carbohydrate Polymers 202 (2018) 444-453.

[19] K. Ghosh, N. Bar, A.B. Biswas, S.K. Das, Elimination of crystal violet from synthetic medium by adsorption using unmodified and acid-modified eucalyptus leaves with MPR and GA application, Sustainable Chemistry and Pharmacy 19 (2021) 100370.
[20] S. Kaur, S. Rani, R.K. Mahajan, Adsorptive removal of dye crystal violet onto low-cost carbon produced from Eichhornia plant: kinetic, equilibrium, and thermodynamic studies, Desalination and Water Treatment 53(2) (2015) 543-556.
[21] M. Sulyman, J. Kucinska-Lipka, M. Sienkiewicz, A. Gierak, Development, characterization and evaluation of composite adsorbent for the adsorption of crystal violet from aqueous solution: Isotherm, kinetics, and thermodynamic studies, Arabian Journal of Chemistry 14(5) (2021) 103115.
[22] S. An, X. Liu, L. Yang, L. Zhang, Enhancement removal of crystal violet dye using magnetic calcium ferrite nanoparticle: Study in single- and binary-solute systems, Chemical Engineering Research and Design 94 (2015) 726-735.
[23] E.A. Dil, M. Ghaedi, A. Asfaram, The performance of nanorods material as adsorbent for removal of azo dyes and heavy metal ions: Application of ultrasound wave, optimization and modeling, Ultrasonics Sonochemistry 34 (2017) 792-802.
[24] S.P. Druzian, N.P. Zanatta, L.N. Côrtes, A.F.M. Streit, G.L. Dotto, Preparation of chitin nanowhiskers and its application for crystal violet dye removal from wastewaters, Environmental Science and Pollution Research 26(28) (2019) 28548-28557.
[25] K. Porkodi, K. Vasanth Kumar, Equilibrium, kinetics and mechanism modeling and simulation of basic and acid dyes sorption onto jute fiber carbon: Eosin yellow, malachite green and crystal violet single component systems, Journal of Hazardous Materials 143(1) (2007) 311-327.
[26] M. Sulyman, J. Namieśnik, A. Gierak, Utilization of New Activated Carbon Derived from Oak Leaves for Removal of Crystal Violet from Aqueous Solution, Polish Journal of Environmental Studies 23(6) (2014) 2223-2232.
[27] F. Parrino, M. Bellardita, E.I. García-López, G. Marcì, V. Loddo, L. Palmisano, Heterogeneous Photocatalysis for Selective Formation of High-Value-Added Molecules: Some Chemical and Engineering Aspects, ACS Catalysis 8(12) (2018) 11191-11225.
[28] A. Mohamed, R. El-Sayed, T.A. Osman, M.S. Toprak, M. Muhammed, A. Uheida, Composite nanofibers for highly efficient photocatalytic degradation of organic dyes from contaminated water, Environmental Research 145 (2016) 18-25.
[29] S. Zarrin, F. Heshmatpour, Facile preparation of new nanohybrids for enhancing photocatalytic activity toward removal of organic dyes under visible light irradiation, Journal of Physics and Chemistry of Solids 140 (2020) 109271.
[30] N. Kumari, K. Gaurav, S.K. Samdarshi, A.S. Bhattacharyya, S. Paul, B. Rajbongshi, K. Mohanty, Dependence of photoactivity of niobium pentoxide (Nb2O5) on crystalline phase and electrokinetic potential of the hydrocolloid, Solar Energy Materials and Solar Cells 208 (2020) 110408.
[31] N.P. de Moraes, R. Bacani, M.L.C.P. da Silva, T.M.B. Campos, G.P. Thim, L.A. Rodrigues, Effect of Nb/C ratio in the morphological, structural, optical and

photocatalytic properties of novel and inexpensive Nb_2O_5/carbon xerogel composites, Ceramics International 44(6) (2018) 6645-6652.
[32] N.P. de Moraes, R.B. Anselmo, L.O. Sartor, G.V.J. Dantas, L.A. Rodrigues, L. Chaguri e Carvalho, Spray drying as feasible processing technique to enhance the photocatalytic activity of the Nb_2O_5/carbon xerogel composite, Materials Letters 273 (2020) 127932.
[33] B. Boruah, R. Gupta, Jayant M. Modak, G. Madras, Enhanced photocatalysis and bacterial inhibition in Nb_2O_5via versatile doping with metals (Sr, Y, Zr, and Ag): a critical assessment, Nanoscale Advances 1(7) (2019) 2748-2760.
[34] A.M. Raba, J. Barba-Ortega, M.R. Joya, The effect of the preparation method of Nb_2O_5 oxide influences the performance of the photocatalytic activity, Applied Physics A 119(3) (2015) 923-928.
[35] A.M. Raba, J. Bautista-Ruíz, M.R. Joya, Synthesis and Structural Properties of Niobium Pentoxide Powders: A Comparative Study of the Growth Process, Materials Research 19(6) (2016) 1381-1387.
[36] C.L. Ücker, F.C. Riemke, N.F. de Andrade Neto, A.d.A.G. Santiago, T.J. Siebeneichler, N.L.V. Carreño, M.L. Moreira, C.W. Raubach, S. Cava, Influence of Nb_2O_5 crystal structure on photocatalytic efficiency, Chemical Physics Letters 764 (2021) 138271.
[37] J.B.G. Filho, R.D.F. Rios, C.G.O. Bruziquesi, D.C. Ferreira, H.F.V. Victória, K. Krambrock, M.C. Pereira, L.C.A. Oliveira, A promising approach to transform levulinic acid into γ-valerolactone using niobic acid photocatalyst and the accumulated electron transfer technique, Applied Catalysis B: Environmental 285(November 2020) (2021).
[38] S. Kohtani, T. Kurokawa, E. Yoshioka, H. Miyabe, Photoreductive transformation of fluorinated acetophenone derivatives on titanium dioxide: Defluorination vs. reduction of carbonyl group, Applied Catalysis A: General 521 (2016) 68-74.
[39] X. Yu, W. Li, Z. Li, J. Liu, P. Hu, Defect engineered Ta_2O_5 nanorod: One-pot synthesis, visible-light driven hydrogen generation and mechanism, Applied Catalysis B: Environmental 217 (2017) 48-56.
[40] A. Molinari, A. Maldotti, R. Amadelli, Probing the role of surface energetics of electrons and their accumulation in photoreduction processes on TiO_2, Chemistry - A European Journal 20(25) (2014) 7759-7765.
[41] B.I. Lemon, J.T. Hupp, Photochemical quartz crystal microbalance study of the nanocrystalline titanium dioxide semiconductor electrode/water interface: Simultaneous photoaccumulation of electrons and protons, The Journal of Physical Chemistry® 100(35) (1996) 14578-14580.
[42] R. Qian, H. Zong, J. Schneider, G. Zhou, T. Zhao, Y. Li, J. Yang, D.W. Bahnemann, J.H. Pan, Charge carrier trapping, recombination and transfer during TiO2 photocatalysis: An overview, Catalysis Today (October) (2018).
[43] L.A. Bivona, A. Vivian, L. Fusaro, S. Fiorilli, C. Aprile, Design and catalytic applications of 1D tubular nanostructures: Improving efficiency in glycerol conversion, Applied Catalysis B: Environmental 247(January) (2019) 182-190.

[44] T. Shishido, T. Miyatake, K. Teramura, Y. Hitomi, H. Yamashita, T. Tanaka, Mechanism of Photooxidation of Alcohol over Nb_2O_5, The Journal of Physical Chemistry C 113(43) (2009) 18713-18718.

Chapter 8 – Conclusions

The present thesis brought insights about the wonders regarding the niobium pentoxide (Nb_2O_5) materials. First, we raised the question: Is niobium pentoxide an emergent material? We scoured scientific databases to answer this question, filtering the published articles each year since the early 1900s. We found that Nb_2O_5 is a material that has contradictory information in the literature, especially regarding its crystal structure. The Nb_2O_5 presents an odd behavior due to non-stoichiometric phases and defects in the crystal structure, making it unique for several applications. Despite the findings of Nb_2O_5 crystal structure in the early 60s and 70s, nowadays, most scientific publications focus only on the applications. This lack of crystal structure information made us eager to produce quality material about the basic structure of Nb_2O_5 and how it affects its properties.

In this work, several polymorphs could be obtained, and all of them had their structure refined, showing the vast potential to obtain several crystalline forms changing small parameters in the synthetic route. We also presented one of the major subjects for the future of niobium pentoxide studies: defect engineering and its impact. One of its remarkable properties is that even simple synthetic methods employed here can produce defects in the niobium pentoxide, such as single-electron trapped oxygen vacancies, edge-dislocations, and substitutional defects at the niobium coordinates. We proved that those defects could create intermediary energy levels in the forbidden intraband, associated with light absorption on the visible region, and enhanced properties for numerous applications. We also showed that we could obtain good results by employing the correct Nb_2O_5 crystalline phase in crystal violet decoloration and glycerol conversion into solketal. Defects in the material are crucial to obtain good selectivity in photocatalytic conversions. These properties created a sufficiently promising and straightforward material to be employed in several state-of-the-art chemical transformations under UV-Vis light, whether in pollutant degradation or biomass conversion.

Overall, the results in the present thesis question the crystalline behavior of niobium pentoxide materials, stating the crucial role of defects in the system and how they impact the applications of these materials. Moreover, the findings provide a fundamental understanding of the niobium pentoxide crystal structure, which proved to be an emergent material in the metallic oxide classes. Our results encourage future work with niobium oxide to further investigate the impact of the synthetical route on the crystalline phase, the elucidation of complex niobium compounds, the presence of new dopants, and how we can perform material engineering to obtain the most suitable properties for the desired applications.

Appendix A – Future Work

Despite all findings in the present thesis, we expect to move towards a deeper understanding of the niobium pentoxide, prompting future works:

- We will work on a more detailed crystallization path, employing simple synthetic routes with a broader range of temperatures (100 to 1200 °C, varying 50-100 °C between the samples).
- We plan to advance on the microscopy analysis of niobium pentoxide, employing powerful STEM techniques at LNNano facilities to allow us to see the structural organization and defects of Nb_2O_5 and perform image simulation.
- We plan to perform an in-depth analysis of the structural and electronic properties of the niobium pentoxide, employing techniques using a synchrotron light source at Campinas / São Paulo.
- We will carry out electrochemical characterization of the materials with the best performance in photocatalysis and advance in electrochemical applications.
- We will perform physical synthesis methods to better control oxygen stoichiometry, evaluate the presence of oxygen defects, and correlate with electrochemical properties and applications.
- We expect to produce niobium pentoxide with cation substitution (with Mo, W, and others) to enhance its photocatalytic and electrochemical properties. We also expect to produce nanocomposites with several materials, including graphite and graphene oxide, to evaluate their performance in several applications.
- We will also further evaluate the complex oxides with niobium (like perovskite structure) employing suitable metallic cations to produce new materials for several applications.

Appendix B – Nb_2O_5 crystal structure data

B-Nb_2O_5

The B polymorph was first discovered in 1966, by Schäfer et al. [1], during the chemical transport synthesis of Nb_2O_5 crystals. The B-Nb_2O_5 presents a monoclinic crystal structure, indexed at the C2/c space group, and it contains four-unit formulas per unit cell. The lattice parameters are a = 5.560 Å, b = 12.740 Å, c = 4.883 Å, and γ = 105.02°. The structure is composed of 8 niobium atoms located at 8f Wyckoff position and 20 oxygen atoms placed at three Wyckoff positions: 4e and two 8f. In the B-Nb_2O_5 phase, the crystal structure is built up by blocks of distorted NbO_6 octahedra arranged in strings composed of pairs of edge-sharing octahedra linked in a zigzag of corner-sharing octahedra [2].

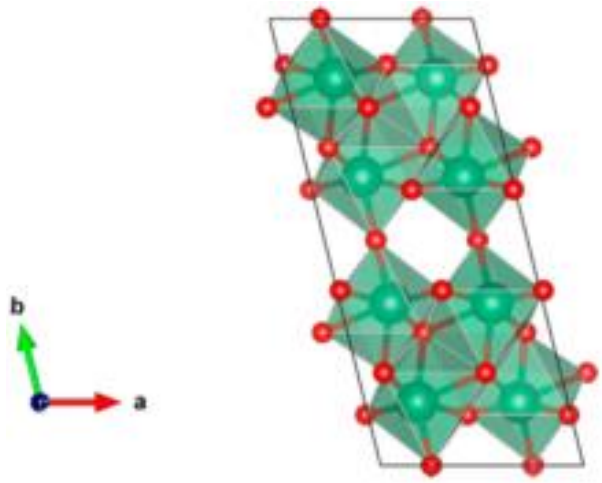

Figure A1. B-Nb_2O_5 crystal structure.

M-Nb_2O_5

Brauer first described the M polymorph in 1941 [3]. The M modification could be obtained by calcinating niobic acid at high temperatures (900 – 950 °C) with short times. It is not easy to obtain pure M-Nb_2O_5 since considerable amounts of H-Nb_2O_5 are produced together. The M phase crystallizes in a tetragonal structure, space group I4/mmm, containing 16 unit formulas in the unit cell, where the Nb atoms occupy two 8i and 8h and three 16l Wyckoff positions. The lattice parameters are a = 20.44 Å, and c = 3.830 Å. The structure is a 4x4 block of corner-sharing octahedra, with adjacent blocks linked by the octahedra edge.

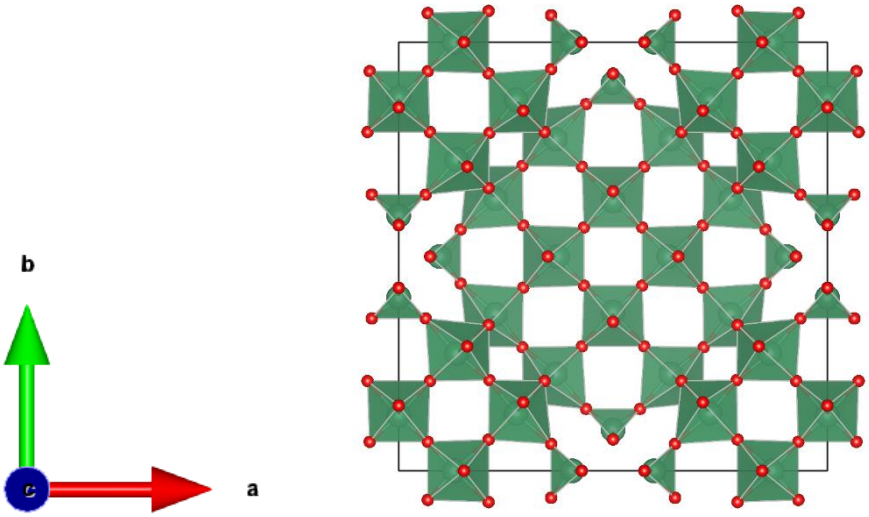

Figure A2. M-Nb_2O_5 crystal structure.

N-Nb_2O_5

The N polymorph occurs together with the M-modification, making it hard to separate and obtain the pure polymorph. This has never been done. The N-Nb_2O_5 crystallizes at the monoclinic system, space group C2/m, with lattice parameters a = 28.51 Å, b = 3.830 Å, c = 17.48 Å, and γ = 120.8°. Past works discuss that the N-phase could be obtained in the presence of F^- and OH^-, employing chemical transport

or hydrothermal synthesis. Its monoclinic structure is described as a 4x4 block structure of corner-sharing octahedra, where the blocks are linked by edge-sharing. There are 8 Nb and 20 O atoms occupying 4i Wyckoff positions [2].

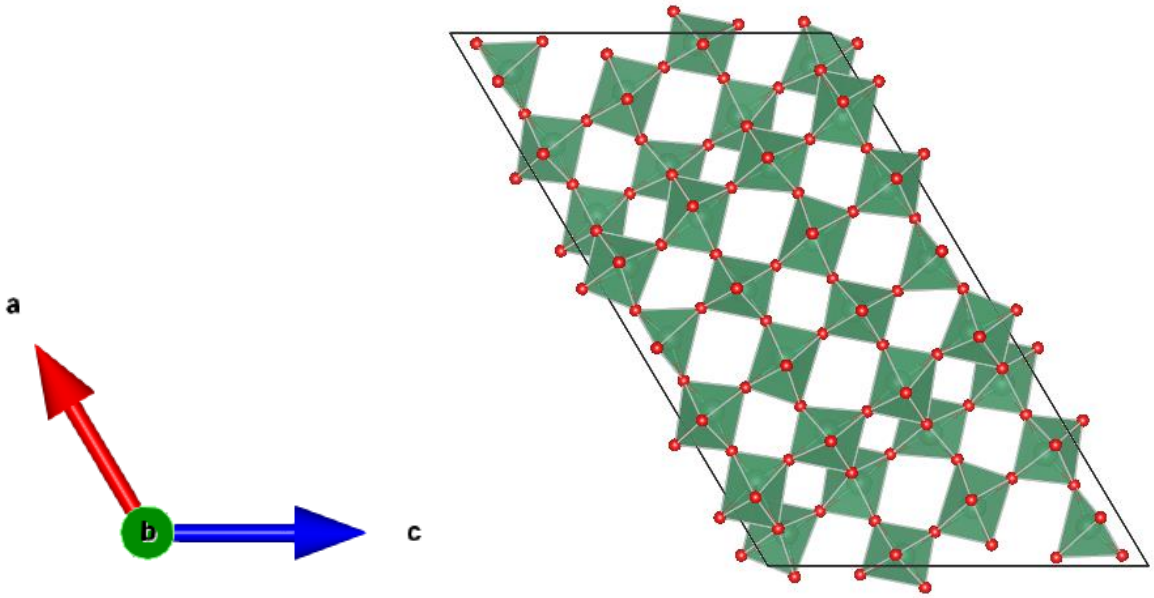

Figure A3. N-Nb_2O_5 crystal structure.

P-Nb_2O_5

The P polymorph is obtained employing chemical transport synthesis of Nb_2O_5 crystals in the presence of halide anions. The difficulty of obtaining the pure P phase made it impossible to have a reliable experimental diffractogram. The structure of P-Nb_2O_5 is an idealization by Professor Osório-Guillén [4]. The P-modification crystallizes in the tetragonal system, with lattice parameters a = 3.876 Å and c = 25.43 Å, and space group $I4_122$. The P-Nb_2O_5 has four formula units per unit cell, where the Nb atoms occupy the 8c, the O atoms a 4i, and two 8c Wyckoff positions. The structure has distorted octahedra in blocks of two edge-sharing positions, and the blocks are linked by corner-sharing.

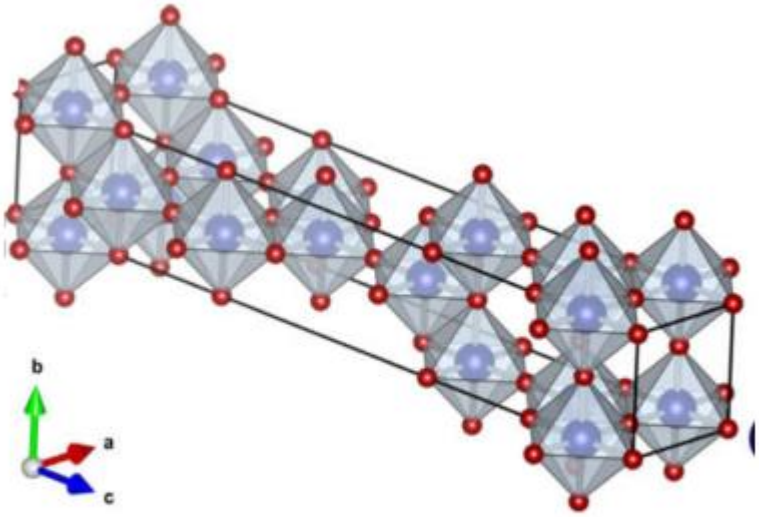

Figure A4. P-Nb_2O_5 crystal structure [2].

R-Nb_2O_5

The R polymorph was first described in 1966 by Gruehn [5]. It is not common to find information about this polymorph in the literature. However, Gruehn could obtain the material by the chemical transport synthesis of Nb_2O_5 crystals at 700 °C. He stated that he could not obtain the pure material but a mixture of P or TT. It is considered one of the simplest forms of niobium pentoxide. It crystallizes in the monoclinic system, with two formula units per unit cell, Nb atoms occupying the 4i Wyckoff positions, and the O atoms the 2a and 4i positions along the b-axis, linked by corner-sharing. The lattice parameters are a = 12.79 Å, b = 3.826 Å, c = 3.983 Å, and γ = 90.02°. The angle distortion near 90° approximates the structure to an orthorhombic unit cell related to the TT and T phases.

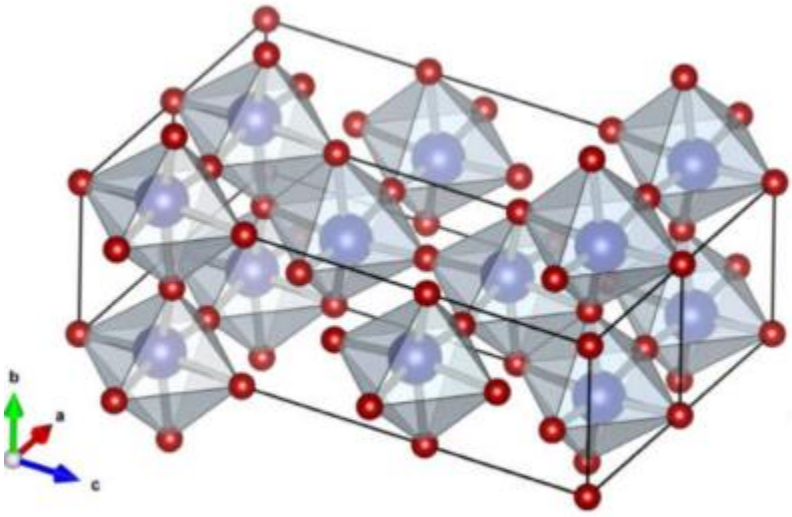

Figure A5. R-Nb_2O_5 crystal structure [2].

Z-Nb_2O_5

The Z polymorph was first discovered in 1998 by Zibrov et al. [6]. They reported the occurrence of Z modification during the synthesis of B-phase in a high-pressure synthesis (8 GPa) at 800 °C. They could determine the structure employing X-ray diffraction allied with Rietveld refinement. The Z-Nb_2O_5 crystallizes in the monoclinic system, indexed at the C 2 space group. The lattice parameters are a = 5.219 Å, b = 4.699 Å, c = 5.928 Å, and γ = 108.56°. The Z modification presents an odd behavior, is one of the few niobium pentoxide structures without octahedra coordination (six-fold). It presents trigonal prisms with sevenfold coordination, with Nb atoms occupying 4c, and O atoms a 2b and two 4c Wyckoff positions.

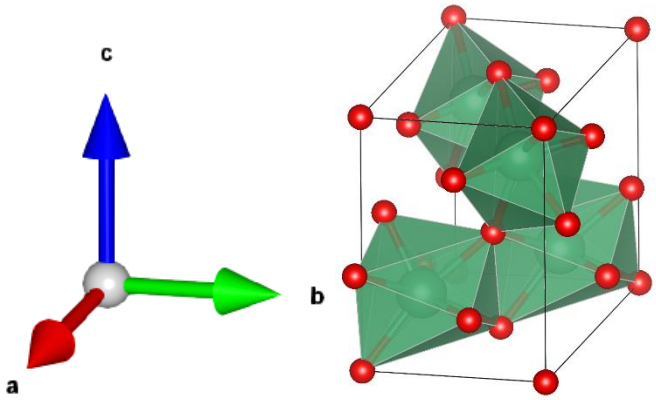

Figure A 6. Z-Nb_2O_5 crystal structure

References

[1] Schäfer, H., Gruehn, R., Schulte, F., 1966. The Modifications of Niobium Pentoxide. Angewandte Chemie International Edition in English 5, 40-52.

[2] Nico, C., Monteiro, T., Graça, M.P.F., 2016. Niobium oxides and niobates physical properties: Review and prospects. Progress in Materials Science 80, 1-37.

[3] Brauer, G., 1941. Die Oxyde des Niobs. Zeitshrift fiir anorganische und allgemeine Chemie 248, 1-31.

[4] Valencia-Balvin, C., Perez-Walton, S., Dalpian, G.M., Osório-Guillén, J.M., 2014. First-principles equation of state and phase stability of niobium pentoxide. Computational Materials Science 81, 133-140.

[5] Gruehn, R., 1966. Eine weitere neue Modifikation des niobpentoxids. Journal of the Less Common Metals 11, 119-126.

[6] Zibrov, I.P., Filonenko, V.P., Werner, P.E., Marinder, B.O., Sundberg, M., 1998. A New High-Pressure Modification of Nb_2O_5. Journal of Solid State Chemistry 141, 205-211.

Appendix C – TT-Nb_2O_5 crystallographic information file

data_TTNb2O5_publ

start Validation Reply Form
_vrf_DENSD01_TTNb2O5_publ
;
PROBLEM: The ratio of the submitted crystal density and that
RESPONSE: Given density was retrieved from past works in the literature.
;
_vrf_PLAT021_TTNb2O5_publ
;
PROBLEM: Ratio Unique / Expected Reflections too High ... 2.008
RESPONSE: This is due to the TT-Nb2O5 superlattice structure.
;
_vrf_PLAT044_TTNb2O5_publ
;
PROBLEM: Calculated and Reported Density Dx Differ by .. 0.1454 Check
RESPONSE: Given density was retrieved from past works in the literature.
;
_vrf_PLAT046_TTNb2O5_publ
;
PROBLEM: Reported Z, MW and D(calc) are Inconsistent .... 5.075 Check
RESPONSE: Given density was retrieved from past works in the literature.
;
_vrf_PLAT701_TTNb2O5_publ
;
PROBLEM: Bond Calc 1.76660(10), Rep 1.76647(13), Dev.. 1.30 Sigma
RESPONSE: TT-Nb2O5 presents a distorted structure compared with T- Nb2O5.
;
_vrf_PLAT742_TTNb2O5_publ
;
PROBLEM: Angle Calc 179.71(1), Rep 180.00 ..... Missing s.u.
RESPONSE: TT-Nb2O5 presents a distorted structure compared with T- Nb2O
;
_vrf_PLAT769_ttnb2o5_pub
;
PROBLEM: CIF Embedded explicitly supplied scattering data
RESPONSE: The use of charged atoms in the refinement
;
end Validation Reply Form
_publcif_datablock.id '{b0119e8f-70c2-4d36-93be-efa11c8fd139}'

publcif _publ_body_element loop end

_pd_block_id
2021-02-22T14:10|TESTE2|e_de_Magalh?es_Gomes|Shimadzu_XRD-7000

_audit_creation_method "from EXP file using GSAS2CIF"
_audit_creation_date 2021-02-22T14:10

```
_audit_author_name                    "Gustavo
Henrique de Magalh?es Gomes"
_audit_update_record
;
2021-02-22T14:10    Initial    CIF    as    created    by
GSAS2CIF

2021-02-22 # Formatted by publCIF
;

#==============================
==============================
====================
# this information describes the project, paper etc.
for the CIF            #
# Acta Cryst. Section C papers and editorial
correspondence is generated    #
#   from   the   information   in   this   section
#
#                                                #
#    (from)    CIF submission form for Rietveld
refinements (Acta Cryst. C)    #
#                                  Version 14
December 1998  #
#==============================
==============================
====================
# 1. SUBMISSION DETAILS

_publ_contact_author_name
;
Gustavo Henrique de Magalh\~aes Gomes
;
_publ_contact_author_address
;
Rua Conselheiro Dantas 82, Ap 302, Calafate, Belo
Horizonte, Minas Gerais -
 Brazil
;

_publ_contact_author_email
gustavo.ghmg@gmail.com
_publ_contact_author_fax        ?
_publ_contact_author_phone      +5531989408570

_publ_contact_letter
;
;

_publ_requested_journal                'Acta
Crystallographica Section C'
_publ_requested_coeditor_name    ?
_publ_requested_category         FI


# 3. TITLE AND AUTHOR LIST

_publ_section_title
;
Unraveling the crystal structure of TT-Nb~2~O~5~
using X-ray powder diffraction
;

_publ_section_title_footnote
.

# The loop structure below should contain the names
and addresses of all
# authors, in the required order of publication.
Repeat as necessary.

loop_
_publ_author_name
_publ_author_address
_publ_author_footnote
_publ_author_email
```

'M. Gomes, Gustavo Henrique'
;
Universidade Federal de Minas Gerais - UFMG
Nanostructured Materials Laboratory
Chemistry Department
Av. Pres. Ant\^onio Carlos, 6627
Pampulha
Belo Horizonte
Brazil
;
.
;
gustavo.ghmg@gmail.com
;
'D. S. Mohallem, Nelcy'
;
Universidade Federal de Minas Gerais - UFMG
Nanostructured Materials Laboratory
Chemistry Department
Av. Pres. Ant\^onio Carlos, 6627
Pampulha
Belo Horizonte
Brazil
;
.
;
nelcydsm@gmail.com
;

loop_

#==========
==========
==========
5. OVERALL REFINEMENT & COMPUTING DETAILS

_refine_special_details 'Rietveld extraction method'
_pd_proc_ls_special_details
?

The following items are used to identify the programs used.
_computing_molecular_graphics 'VESTA, JEMS, DigitalMicrograph'
_computing_publication_material 'Word, printCIF'

_refine_ls_weighting_scheme ?
_refine_ls_weighting_details ?
_refine_ls_hydrogen_treatment ?
_refine_ls_extinction_method ?
_refine_ls_extinction_coef ?
_refine_ls_number_constraints ?

_refine_ls_restrained_S_all ?
_refine_ls_restrained_S_obs ?

#==========
==========
==========
6. SAMPLE PREPARATION DATA

(In the unusual case where multiple samples are used in a single
Rietveld study, this information should be moved into the phase
blocks)

The following three fields describe the preparation of the material.
The cooling rate is in K/min. The pressure at which the sample was

prepared is in kPa. The temperature of preparation is in K.

_pd_prep_cool_rate 10
_pd_prep_pressure 101
_pd_prep_temperature 773

_pd_char_colour White
_refine_ls_shift/su_max 0.00
_refine_ls_shift/su_mean 0.00
_computing_structure_refinement GSAS
_refine_ls_number_parameters 20
_refine_ls_goodness_of_fit_all 1.70
_refine_ls_number_restraints 0
_refine_ls_matrix_type full
#==========
==========
==========

7. CHEMICAL, STRUCTURAL AND CRYSTAL DATA

_pd_char_particle_morphology 'Fine powder, white'

_chemical_name_systematic 'dioxoniobiooxy(dioxo)niobium'

_chemical_name_common 'Niobium Pentoxide'
_chemical_formula_moiety 'Nb8 O21'
_chemical_formula_structural 'Nb8 O21'
_chemical_formula_analytical ?
_chemical_melting_point ?
_chemical_compound_source 'Explained in the synthesis procedure'
_symmetry_space_group_name_Hall '-P 2 2ab'

_exptl_crystal_F_000 ?
_exptl_crystal_density_diffrn 4.93
_exptl_crystal_density_meas ?
_exptl_crystal_density_method ?

_cell_measurement_temperature 298

_cell_special_details
?

_geom_special_details ?

The following item identifies the program(s) used (if appropriate).
_computing_structure_solution GSAS/EXPGUI

#==========
==========
==========

8. Phase information from GSAS

_pd_phase_name "from C:/UFMG/Doutorado/CIF TT/Ref_TT_fev.cif"
_cell_length_a 6.2086(5)
_cell_length_b 28.9988(24)
_cell_length_c 3.92256(19)
_cell_angle_alpha 90.0
_cell_angle_beta 90.0
_cell_angle_gamma 90.0
_cell_volume 706.22(6)
_symmetry_cell_setting orthorhombic
_symmetry_space_group_name_H-M "P b a m"
loop_ _symmetry_equiv_pos_site_id
_symmetry_equiv_pos_as_xyz
1 +x,+y,+z

2 -x+1/2,+y+1/2,+z
3 +x+1/2,-y+1/2,+z
4 -x,-y,+z
-1 -x,-y,-z
-2 +x+1/2,-y+1/2,-z
-3 -x+1/2,+y+1/2,-z
-4 +x,+y,-z

ATOMIC COORDINATES AND DISPLACEMENT PARAMETERS

loop_
_atom_site_type_symbol
_atom_site_label
_atom_site_fract_x
_atom_site_fract_y
_atom_site_fract_z
_atom_site_occupancy
_atom_site_thermal_displace_type
_atom_site_U_iso_or_equiv
_atom_site_symmetry_multiplicity
Nb Nb1 0.27486 0.03698 0.5 1.0 Uiso 0.00066 4
Nb Nb2 0.23351 0.1581 0.5 1.0 Uiso 0.0011 4
Nb Nb3 0.25386 0.27885 0.5 1.0 Uiso 0.00053 4
Nb Nb4 0.23359 0.40649 0.5 1.0 Uiso 0.00022 4
O O1 0.14595 0.03595 0.0 1.0 Uiso 0.00086 4
O O2 0.19997 0.17065 0.0 1.0 Uiso 0.02397 4
O O3 0.20774 0.27799 0.0 1.0 Uiso 0.0213 4
O O4 0.25421 0.40819 0.0 1.0 Uiso 0.00537 4
O O5 0.02074 0.09264 0.5 1.0 Uiso 0.01484 4
O O6 0.06646 0.2273 0.5 1.0 Uiso 0.00766 4
O O7 0.37936 0.33881 0.5 1.0 Uiso 0.0058 4
O O8 0.12787 0.47973 0.5 1.0 Uiso 0.00878 4
O O9 0.38946 0.1202 0.5 1.0 Uiso 0.00523 4
O O10 0.37633 0.20157 0.5 1.0 Uiso 0.0056 4
O O11 0.0 0.0 0.5 1.0 Uiso 0.03852 2

If you change Z, be sure to change all 3 of the following
_chemical_formula_sum "Nb8 O21"
_chemical_formula_weight 1079.23
_cell_formula_units_Z 2

MOLECULAR GEOMETRY

```
loop_
   _geom_bond_atom_site_label_1
   _geom_bond_atom_site_label_2
   _geom_bond_distance
   _geom_bond_site_symmetry_1
   _geom_bond_site_symmetry_2
   _geom_bond_publ_flag
  Nb1   Nb4   3.28622(22)  .   3_555  n
  Nb1   O1    2.11851(9)   .   1_555  n
  Nb1   O1    2.11851(9)   .   1_556  n
  Nb1   O5    2.25717(14)  .   1_555  n
  Nb1   O8    1.76647(13)  .   2_545  n
  Nb1   O8    2.24460(18)  .   3_555  n
  Nb1   O9    2.51595(20)  .   1_555  n
  Nb1   O11   2.01542(13)  .   1_555  n
  Nb2   O2    2.00559(10)  .   1_555  n
  Nb2   O2    2.00559(10)  .   1_556  n
  Nb2   O5    2.31266(15)  .   1_555  n
  Nb2   O6    2.25886(16)  .   1_555  n
  Nb2   O7    2.20062(19)  .   3_455  n
  Nb2   O9    1.46479(9)   .   1_555  n
  Nb2   O10   1.54126(10)  .   1_555  n
  Nb3   O3    1.98223(10)  .   1_555  n
  Nb3   O3    1.98223(10)  .   1_556  n
  Nb3   O6    1.89427(12)  .   1_555  n
  Nb3   O6    1.94898(16)  .   3_555  n
  Nb3   O7    1.90544(14)  .   1_555  n
  Nb3   O10   2.36640(18)  .   1_555  n
  Nb3   O10   2.41172(19)  .   3_455  n
  Nb4   Nb1   3.28622(22)  .   3_455  n
  Nb4   O4    1.96607(10)  .   1_555  n
  Nb4   O4    1.96607(10)  .   1_556  n
  Nb4   O5    1.78295(15)  .   3_555  n
  Nb4   O7    2.16125(15)  .   1_555  n
  Nb4   O8    2.22304(17)  .   1_555  n
  Nb4   O9    2.27236(17)  .   3_455  n
  O1    Nb1   2.11851(9)   .   1_554  n
  O1    Nb1   2.11851(9)   .   1_555  n
  O2    Nb2   2.00559(10)  .   1_554  n
  O2    Nb2   2.00559(10)  .   1_555  n
  O3    Nb3   1.98223(10)  .   1_554  n
  O3    Nb3   1.98223(10)  .   1_555  n
  O4    Nb4   1.96607(10)  .   1_554  n
  O4    Nb4   1.96607(10)  .   1_555  n
  O5    Nb1   2.25717(14)  .   1_555  n
  O5    Nb2   2.31266(15)  .   1_555  n
  O5    Nb4   1.78295(15)  .   3_455  n
  O5    O7    2.17309(16)  .   3_455  n
  O6    Nb2   2.25886(16)  .   1_555  n
  O6    Nb3   1.89427(12)  .   1_555  n
  O6    Nb3   1.94898(16)  .   3_455  n
  O6    O10   2.06345(15)  .   1_555  n
  O7    Nb2   2.20062(19)  .   3_555  n
  O7    Nb3   1.90544(14)  .   1_555  n
  O7    Nb4   2.16125(15)  .   1_555  n
  O7    O5    2.17309(16)  .   3_555  n
  O8    Nb1   1.76647(13)  .   2_555  n
  O8    Nb1   2.24460(18)  .   3_455  n
  O8    Nb4   2.22304(17)  .   1_555  n
  O8    O8    1.97561(12)  .   4_565  n
  O9    Nb1   2.51595(20)  .   1_555  n
  O9    Nb2   1.46479(9)   .   1_555  n
  O9    Nb4   2.27236(17)  .   3_555  n
  O10   Nb2   1.54126(10)  .   1_555  n
  O10   Nb3   2.36640(18)  .   1_555  n
  O10   Nb3   2.41172(19)  .   3_555  n
  O10   O6    2.06345(15)  .   1_555  n
  O11   Nb1   2.01542(13)  .   1_555  n
  O11   Nb1   2.01542(13)  .   4_555  n

loop_
   _geom_angle_atom_site_label_1
   _geom_angle_atom_site_label_2
   _geom_angle_atom_site_label_3
```

_geom_angle
_geom_angle_site_symmetry_1
_geom_angle_site_symmetry_2
_geom_angle_site_symmetry_3
_geom_angle_publ_flag

O1	Nb1	O1	135.573(4)	1_555	1_556 n
O1	Nb1	O5	75.2847(21)	1_555	1_555 n
O1	Nb1	O8	96.6574(13)	1_555	2_545 n
O1	Nb1	O8	111.4602(20)	1_555	3_555 n
O1	Nb1	O11	70.8903(21)	1_555	1_555 n
O1	Nb1	O5	75.2847(21)	1_556	1_555 n
O1	Nb1	O8	96.6574(13)	1_556	2_545 n
O1	Nb1	O8	111.4602(20)	1_556	3_555 n
O1	Nb1	O11	70.8903(21)	1_556	1_555 n
O5	Nb1	O8	155.6440(12)	1_555	2_545 n
O5	Nb1	O8	146.8115(20)	1_555	3_555 n
O5	Nb1	O11	77.796(7)	1_555	1_555 n
O8	Nb1	O8	57.5445(8)	2_545	3_555 n
O8	Nb1	O11	77.848(5)	2_545	1_555 n
O8	Nb1	O11	135.392(4)	3_555	1_555 n
O2	Nb2	O2	155.8680(19)	1_555	1_556 n
O2	Nb2	O5	95.1413(14)	1_555	. 1_555 n

O2	Nb2	O6	77.9452(10)	1_555	O3	Nb3	O3	163.3253(16)	1_555
.	1_555	n			.	1_556	n		
O2	Nb2	O7	83.6193(6)	1_555	O3	Nb3	O6	84.3427(8)	1_555
.	3_455	n			.	1_555	n		
O2	Nb2	O9	101.8161(10)	1_555	O3	Nb3	O6	98.2051(8)	1_555
.	1_555	n			.	3_555	n		
O2	Nb2	O10	84.9133(14)	1_555	O3	Nb3	O7	94.0405(6)	1_555
.	1_555	n			.	1_555	n		
O2	Nb2	O5	95.1413(14)	1_556	O3	Nb3	O6	84.3427(8)	1_556
.	1_555	n			.	1_555	n		
O2	Nb2	O6	77.9452(10)	1_556	O3	Nb3	O6	98.2051(8)	1_556
.	1_555	n			.	3_555	n		
O2	Nb2	O7	83.6193(6)	1_556	O3	Nb3	O7	94.0405(6)	1_556
.	3_455	n			.	1_555	n		
O2	Nb2	O9	101.8161(10)	1_556	O6	Nb3	O6	122.650(4)	1_555
.	1_555	n			.	3_555	n		
O2	Nb2	O10	84.9133(14)	1_556	O6	Nb3	O7	166.2426(8)	1_555
.	1_555	n			.	1_555	n		
O5	Nb2	O6	117.833(6)	1_555	O6	Nb3	O7	71.1075(32)	3_555
.	1_555	n			.	1_555	n		
O5	Nb2	O7	57.5009(35)	1_555	O4	Nb4	O4	171.9989(7)	1_555
.	3_455	n			.	1_556	n		
O5	Nb2	O9	76.212(7)	1_555	O4	Nb4	O5	86.2465(4)	1_555
.	1_555	n			.	3_555	n		
O5	Nb2	O10	180.0	1_555	O4	Nb4	O7	89.7408(4)	1_555
.	1_555	n			.	1_555	n		
O6	Nb2	O7	60.3324(25)	1_555	O4	Nb4	O8	89.73060(30)	1_555
.	3_455	n			.	1_555	n		
O6	Nb2	O9	165.9546(6)	1_555	O4	Nb4	O9	93.9997(4)	1_555
.	1_555	n			.	3_455	n		
O6	Nb2	O10	62.454(6)	1_555	O4	Nb4	O5	86.2465(4)	1_556
.	1_555	n			.	3_555	n		
O7	Nb2	O9	133.7130(31)	3_455	O4	Nb4	O7	89.7408(4)	1_556
.	1_555	n			.	1_555	n		
O7	Nb2	O10	122.7866(35)	3_455	O4	Nb4	O8	89.73060(30)	1_556
.	1_555	n			.	1_555	n		
O9	Nb2	O10	103.500(7)	1_555					
.	1_555	n							

O4 Nb4 O9 93.9997(4) 1_556 3_455 n
O5 Nb4 O7 66.0573(27) 3_555 1_555 n
O5 Nb4 O8 106.3606(20) 3_555 1_555 n
O5 Nb4 O9 160.9035(21) 3_555 3_455 n
O7 Nb4 O8 172.4179(7) 1_555 1_555 n
O7 Nb4 O9 94.846(5) 1_555 3_455 n
O8 Nb4 O9 92.736(4) 1_555 3_455 n
Nb1 O1 Nb1 135.573(4) 1_554 1_555 n
Nb2 O2 Nb2 155.8680(19) 1_554 1_555 n
Nb3 O3 Nb3 163.3253(16) 1_554 1_555 n
Nb4 O4 Nb4 171.9989(7) 1_554 1_555 n
Nb1 O5 Nb2 100.818(7) 1_555 1_555 n
Nb1 O5 Nb4 135.1591(33) 1_555 3_455 n
Nb2 O5 Nb4 124.0224(33) 1_555 3_455 n
Nb2 O6 Nb3 114.774(6) 1_555 1_555 n
Nb2 O6 Nb3 112.0874(34) 1_555 3_455 n
Nb3 O6 Nb3 133.1384(27) 1_555 3_455 n
Nb2 O7 Nb3 116.4727(23) 3_555 1_555 n
Nb2 O7 Nb4 112.4194(29) 3_555 1_555 n
Nb3 O7 Nb4 131.108(5) 1_555 1_555 n
Nb1 O8 Nb1 122.4555(8) 2_555 3_455 n
Nb1 O8 Nb4 142.836(4) 2_555 1_555 n
Nb1 O8 Nb4 94.7082(34) 3_455 1_555 n
Nb2 O9 Nb4 151.2862(12) 1_555 3_555 n
Nb1 O11 Nb1 180.0 1_555 4_555 n

Powder diffraction data for histogram 1

#==========

==========

==========

9. INSTRUMENT CHARACTERIZATION

_exptl_special_details

?

if regions of the data are excluded, the reason(s) are supplied here:

_pd_proc_info_excluded_regions

?

The following item is used to identify the equipment used to record

the powder pattern when the diffractogram was measured at a laboratory

other than the authors' home institution, e.g. when neutron or synchrotron

radiation is used.

_pd_instr_location

?
_pd_calibration_special_details # description of the method used
to calibrate the instrument
?

_diffrn_ambient_temperature 298.15
_diffrn_source 'sealed X-ray tube'
_diffrn_source_target Cu
_diffrn_source_type ?
_diffrn_measurement_device_type 'Shimadzu XRD-7000'
_diffrn_detector ?
_diffrn_detector_type ? # make or model of detector
_pd_meas_scan_method step

The following two items identify the program(s) used (if appropriate).
_computing_data_collection ?
_computing_data_reduction ?

Describe any processing performed on the data, prior to refinement.
For example: a manual Lp correction or a precomputed absorption correction
_pd_proc_info_data_reduction ?

The following item is used for angular dispersive measurements only.

_diffrn_radiation_monochromator ?

The following items are used to define the size of the instrument.
Not all distances are appropriate for all instrument types.

_pd_instr_dist_src/mono ?
_pd_instr_dist_mono/spec ?
_pd_instr_dist_src/spec ?
_pd_instr_dist_spec/anal ?
_pd_instr_dist_anal/detc ?
_pd_instr_dist_spec/detc ?

10. Specimen size and mounting information

The next three fields give the specimen dimensions in mm. The equatorial
plane contains the incident and diffracted beam.

_pd_spec_size_axial 10 # perpendicular to
equatorial plane

_pd_spec_size_equat 10 # parallel to
scattering vector
in transmission

_pd_spec_size_thick 2 # parallel to
scattering vector
in reflection

_pd_spec_mounting # This field should be
used to give details of the
container.
'packed powder pellet'

```
_pd_spec_mount_mode
reflection       # options are 'reflection'
                                # or 'transmission'

_pd_spec_shape                  flat_sheet       #
options are 'cylinder'
                                #    'flat_sheet'    or
'irregular'



loop_ _atom_type_symbol
      _atom_type_number_in_cell
      _atom_type_scat_dispersion_real
      _atom_type_scat_dispersion_imag
      _atom_type_scat_Cromer_Mann_a1
      _atom_type_scat_Cromer_Mann_a2
      _atom_type_scat_Cromer_Mann_a3
      _atom_type_scat_Cromer_Mann_a4
      _atom_type_scat_Cromer_Mann_b1
      _atom_type_scat_Cromer_Mann_b2
      _atom_type_scat_Cromer_Mann_b3
      _atom_type_scat_Cromer_Mann_b4
      _atom_type_scat_Cromer_Mann_c
      _atom_type_scat_source
  Nb+5      16.0     0.000     0.000
 17.9163  1.12446  13.3417  0.02878  10.7990  9.28206
0.33790 25.7228 -6.3934
  International_Tables_Vol_C
  O-2       42.0     0.000     0.000
 3.76936  15.0797  2.53342  6.30430  1.91579  40.3445
1.55094 0.31291 0.22789
  International_Tables_Vol_C
_diffrn_radiation_probe               x-ray
_diffrn_radiation_polarisn_ratio      0.521

loop_
      _diffrn_radiation_wavelength
      _diffrn_radiation_wavelength_wt
      _diffrn_radiation_type
      _diffrn_radiation_wavelength_id
                  1.540500      1.000    CuK\a~1~  1
                  1.544300      0.474    CuK\a~2~  2
_pd_proc_ls_prof_R_factor             0.0499
_pd_proc_ls_prof_wR_factor            0.0646
_pd_proc_ls_prof_wR_expected          0.0382
_refine_ls_R_Fsqd_factor              0.07058


_pd_proc_ls_background_function
;    GSAS Background function number 1 with 20
terms.
 Shifted Chebyshev function of 1st kind
      1:   346.077    2:  -137.639    3:  -43.6128    4:
-14.6900
      5:  -43.0979    6:   44.3352    7:  -3.87429    8:
-40.3635
      9:   5.40018   10:   9.25914   11:  -33.4315
12:   20.1120
     13:   19.9481   14:   9.16627   15:   4.69533
16:  -4.66282
     17:   16.5009   18:  -5.75420   19:  -8.69921
20:   6.99730
;


_exptl_absorpt_process_details
;    GSAS Absorption/surface roughness correction:
function number 0
 No correction is applied.
;
_exptl_absorpt_correction_T_min       1.00000
_exptl_absorpt_correction_T_max       1.00000
# Extinction correction
_gsas_exptl_extinct_corr_T_min        1.00000
_gsas_exptl_extinct_corr_T_max        1.00000


_pd_proc_ls_profile_function
```

;
CW Profile function number 5 with 16 terms
GU = 0.000000E+00 , GV = -0.118728E+04 , GW = 0.477267E+03 , GP = 0.000000E+00
LX = 0.219064E+02 , LY = 0.766925E+02 , S/L = 0.113067E-01 , H/L =0.100557E-02
trns = 0.109088E+02 , shft = 0.121387E+02 , stec = 0.000000E+00
ptec = 0.000000E+00, sfec = 0.000000E+00, D1 = 0.000000E+00, D2 = 0.000000E+00
D3 = 0.000000E+00

;
_pd_proc_ls_peak_cutoff 0.01000
_pd_proc_info_datetime 2021-02-22T14:10:10
_pd_calc_method "Rietveld Refinement"

#---- raw/calc data loop -----
_pd_meas_2theta_range_min 15.02
_pd_meas_2theta_range_max 80.0
_pd_meas_2theta_range_inc 0.02
_pd_proc_2theta_range_min 15.02832
_pd_proc_2theta_range_max 80.00832
_pd_proc_2theta_range_inc 0.02

_pd_meas_number_of_points 3250
_pd_proc_number_of_points 3250

_reflns_number_total 526
_reflns_limit_h_min 0
_reflns_limit_h_max 5
_reflns_limit_k_min 0
_reflns_limit_k_max 25
_reflns_limit_l_min 0
_reflns_limit_l_max 3
_reflns_d_resolution_high 1.200
_reflns_d_resolution_low 5.707
#--eof--eof--eof--eof--eof--eof--eof--eof--eof--eof--eof--eof--eof--eof--eof--#

_publcif_info_exptl_table_max_cols 4
_publcif_info_exptl_table_use_headnotes n

loop_
_publcif_info_datablock.id
_publcif_info_datablock.publ_exptl
_publcif_info_datablock.publ_geom
_publcif_info_datablock.structure
'{b0119e8f-70c2-4d36-93be-efa11c8fd139}' y y y

loop_
_publcif_info_exptl_table_extra_item
?

loop_
_publcif_info_exptl_table_header_item
?

loop_
_publcif_info_tables.block_id
_publcif_info_tables.reference_item
"{b0119e8f-70c2-4d36-93be-efa11c8fd139}"
"_publcif_info_datablock.publ_exptl"

loop_
_publcif_info_cif.paper_type
CE

_publcif_funding_html
;
;

Annex I – Publication List

Published full-length Articles:

1. Lima, L. F. de S.; Coelho, C. R.; Gomes, G. H. M.; Mohallem, N. D. S. Nb_2O_5/SiO_2 mesoporous monoliths synthesized by sol-gel process using ammonium niobate oxalate hydrate as a porogenic agent. JOURNAL OF SOL-GEL SCIENCE AND TECHNOLOGY, v. 1, p. 1-7, 2019.
2. Gomes, G. H. M.; Andrade, R. R.; Mohallem, N. D. S. Investigation of phase transition employing strain mapping in TT- and T-Nb_2O_5 obtained by HRTEM micrographs. MICRON, v. 148, p. 103112, 2021.

Published Dataset:

1. Gomes, G. H. M., Mohallem, N. D. S., CCDC 2103847: Experimental Crystal Structure Determination, ICSD Communication, 2021. (TT-Nb_2O_5 CIF file).

Submitted full-Length Articles:

1. Gomes, G. H. M; Mohallem, N. D. S. Unraveling the crystal structure of TT-Nb_2O_5 using X-ray powder diffraction. Acta Crystallographica C. (Status: Rejected – Under reformulation for future submission).
2. Gomes, G. H. M.; Olusegun, S. J.; Filho, J. B. G.; Mohallem, N. D. S. The role of crystalline Nb_2O_5 nanoparticles for enhanced Crystal Violet dye adsorption and photodegradation. Materials Science and Engineering: B (Status: Submitted to Materials Science and Engineering: B).
3. Gomes, G. H. M; Filho, J. B. G; Bruziquesia, C. G. O.; Victoria, H. F. V.; Krambrock, K.; Oliveira, L. C. A.; Mohallem, N. D. S. Selective photocatalytic conversion of glycerol into solketal, starting from isopropyl alcohol, by TT-Nb_2O_5 nanoparticles with single-electron-trapped oxygen vacancies. Chemical Engineering Journal (Status: Submitted to Chemical Engineering Journal).